

**INTEGRATED POLYSILICON THERMISTORS
FOR MICROFLUIDIC SENSING**

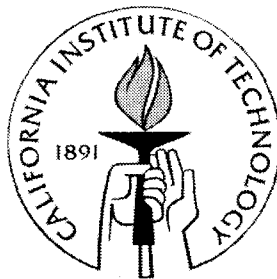
Thesis by

Shuyun Wu

In Partial Fulfillment of the Requirements

For the Degree of

Doctor of Philosophy



California Institute of Technology

Pasadena, California

2000

(Submitted April 14, 2000)

© 2000

Shuyun Wu

All Rights Reserved


INTEGRATED POLYSILICON THERMISTORS FOR MICROFLUIDIC SENSING

Thesis by

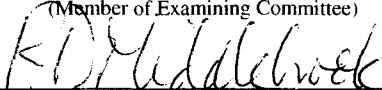
Shuyun Wu

Approved by
Dissertation Committee:

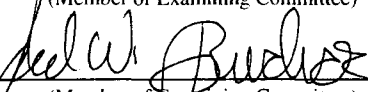
Date 4/14/00

Signed 
(Member of Examining Committee)

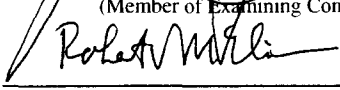
Date 4/14/00

Signed 
(Member of Examining Committee)

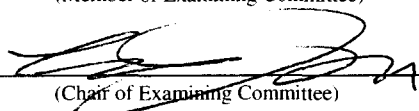
Date 4/14/00

Signed 
(Member of Examining Committee)

Date 4-14-00

Signed 
(Member of Examining Committee)

Date 4-14-'00

Signed 
(Chair of Examining Committee)

To my parents, wife, and daughters

Acknowledgements

On my journey to this key stage of my life, I have been extremely fortunate to be accompanied by many remarkable people. Without their encouragement, support and guidance, I would not be here writing my thesis. I would like to use this chance to express my great appreciation to them, in particular those mentioned below.

I started school after my father, Jianzhong Wu, sold his only heavy jacket for my tuition. I always saw his happy face when I was leaving for school even in a harsh winter. Tough life never stopped my parents' hope in me. Their love and support are my constant source of power. I must first thank them for everything.

Once I was frustrated with my future, but I was very lucky to know Dr. Denny Miu, who offered me a great chance to explore my potential in the United States. His life philosophy and wisdom helped me resolve many puzzles due to the different culture and society here. I greatly appreciate his friendship and help.

The most important turning point of my life was being introduced to the fantastic field of MEMS by my advisor, Professor Yu-Chong Tai. No words can express my deep gratitude to him. Without his inspiration, guidance, and support, what I have accomplished at Caltech would have been only a beautiful dream to me. Any success in my future will be a direct result of the knowledge and philosophy I learned from him. My special appreciation is also acknowledged to Professor Chi-Ming Ho of UCLA for his expert guidance and support for my research project.

I would like to deeply thank my research mentors, Yitshak Zohar of HKUST and Dr. Qiao Lin. The depth of their knowledge and their rigorous approaches in research and study amaze me. It is always a pleasure for me to work with them. I would like to offer

my particular thanks to Mr. Yin Yuen for his assistance with my research. My thanks also go to Mr. John Mai, who was the collaborator of my research project in UCLA.

I have had a wonderful experience in Caltech Micromachining Group. My appreciation is due to our former group members, Professor Chang Liu of UIUC, Dr. Thomas Tsao, Dr. Fukang Jiang, Dr. Xing Yang, and Dr. John Wright for their friendship and advice. I would like to thank all of people who worked closely with me in our laboratory, especially Mr. Wen Hsieh, Mr. Charles Grosjean, Mr. Xiang-Qi Wang, Mr. Tianxiang Weng, Dr. Amish Desai, Dr. Raanan Miller, Dr. Weilong Tang, Ms. Viktoria Temesvary, Mr. Ken Walsh, Mr. Yong Xu, and. I am also indebted to Mr. Trevor Roper and Mr. Hung Bui for their hard work and skills in the technique supporting of our laboratory. Furthermore, my special thanks to those who proofread my thesis and helped me improve the quality of my dissertation, in particular Dr. Qiao Lin, Dr. Tomas Tsao, Mr. Ken Walsh, Ms. Ellis Meng and Mr. Charles Grosjean.

My research project was sponsored by the Defense Advance Research Program Agency, Micro Technology Office (DARPA/MTO), and the Air Force Office of Scientific Research (AFOSR). I would like to present my acknowledgement for their support.

Finally, I would like to thank my wife, Ronghua Zhang, and my daughters, Lily Wu and Grace Wu, for their patience, understanding and support. My life is so wonderful because of them. Also, I would like to send my special appreciation to my parents-in-law in China for taking care of Lily and Grace for quite some time.

Limited space prevents me from listing the name of all the people who have helped me with their love, wisdom, and compassion. In return, I will do the same thing to whomever needs my help.

INTEGRATED POLYSILICON THERMISTORS FOR MICROFLUIDIC SENSING

Thesis by

Shuyun Wu

In Partial Fulfillment of the Requirements

For the Degree of Doctor of Philosophy

Abstract

This thesis documents results related to the design, fabrication, and testing of integrated polysilicon thermistors for microfluidic sensing in experimental investigations of micro impinging jet cooling and microchannel flow. Such experimental study has yielded fundamental understanding and practical design guidelines of these two microfluidic applications. Novel MEMS devices fabricated include temperature imagers, MEMS nozzles and nozzle arrays, and micro fluidic couplers. A technology for suspended microchannels with integrated polysilicon thermistors has been developed and used for microchannel flow study and flow-rate sensing. Theoretical models have been developed to analyze such micro thermal and fluidic phenomena.

In the micro impinging jet cooling study, a MEMS-based heat transfer measurement paradigm has been successfully developed for the first time. This includes technology for MEMS device fabrication, an experimental setup well suited for micro

scale thermal study, and accurate and efficient data processing techniques. Sensing and heating are integrated into a single thermal imager chip, which allows temperature measurement over a large area at very high spatial resolution. The heat transfer data demonstrate the excellent promise of micro-impinging-jet heat transfer, and provide useful rules for designing impinging-jet-based micro heat exchangers for IC packages.

In the investigation of micro channel flow, suspended microchannels with integrated thermistors have successfully been designed and fabricated to study the basic science of micro-scale channel flow. Considerable discrepancies between existing theory and experimental data have been observed, and an improved flow model that accounts for the effects of compressibility, boundary slip, fluid acceleration, non-parabolic fluid velocity profile and channel-wall bulging has been proposed to address such discrepancies.

In addition, micro fluidic couplers have been designed and fabricated as the fluidic interface connection between micro fluidic systems and the external macro environment. The experiments show that MEMS couplers are capable of handling pressures as high as 1200 psig.

Finally, this thesis presents the development of liquid flow sensors. Resolution of 0.4 nL/min and a capability of bubble detecting have been demonstrated. A numerical model is developed to understand device operation and to guide the design process. Excellent agreement has been found between numerical and experimental results.

Table of Contents

1. Introduction to MEMS and Its Applications in Microfluidics

1.1 Introduction to Micromachining Technology and MEMS	2
1.1.1 Introduction	2
1.1.2 Fabrication Techniques	3
1.2 Applications of MEMS in Microfluidics	8
1.3 Overview of Dissertation	9
References	11

2. Doped Polysilicon as a Thermistor Material

2.1 Introduction	21
2.2 Thin Film Deposition	23
2.2.1 Chemical Decomposition of Silane	23
2.2.2 LPCVD System for Polysilicon	24
2.2.3 Deposition Parameters	25
2.2.4 Doping Techniques	28
2.3 Material and Electrical Properties	29
2.3.1 Film Structure and Material Properties	29
2.3.2 Electrical Properties	31
2.3.3 Temperature Coefficient of Resistivity	35
2.4 Polysilicon Thin Film Thermistor	37
2.4.1 Design	37

2.4.2	Fabrication	39
2.4.3	Calibration	41
2.5	Summary	45
	References	46

3. MEMS Impinging-Jet Cooling Study with Thermal Imagers

3.1	Introduction	57
3.1.1	Background	57
3.1.2	Overview of Conventional Approaches	58
3.1.3	MEMS Impinging-Jet Cooling – A Novel Approach	64
3.2	Basics of Impinging-Jet Cooling	68
3.2.1	Basic Concepts	68
3.2.2	Flow Characteristics of Impinging Jets	72
3.2.3	Heat Transfer Characteristics of Impinging Jets	74
3.3	MEMS Jet-Cooling Study with Silicon Temperature Imager	77
3.3.1	Design and Fabrication of Devices	77
3.3.2	Instrumentation	83
3.3.3	Test Results and Discussion	88
3.4	Jet-Cooling Study with Quartz Temperature Imager	97
3.4.1	Design and Fabrication of Devices	98
3.4.2	Modification of Instrumentation	104
3.4.3	Data Processing	106
3.4.4	Heat Transfer Data and Discussion	110
3.5	Conclusion	117

References	120
 4. A Suspended Microchannel with Integrated Polysilicon Thermistors	
4.1 Introduction	126
4.2 Overview of Previous Work	127
4.3 Fundamentals	128
4.3.1 Governing Equations	128
4.3.2 Simplifications for Micro Channel Flow	129
4.3.3 Incompressible Micro Channel Flow	132
4.3.4 Compressible Micro Channel Gas Flow	132
4.3.5 Slip Boundary Gas Channel Flow	133
4.4 Design and Fabrication	134
4.4.1 Suspended Micro Channel with 1 st Generation Integrated Thermistors	134
4.4.2 Suspended Micro Channel with 2 nd Generation Integrated Thermistors	138
4.5 Experimental Setup	139
4.6 Test Results and Discussion	142
4.6.1 DI Water Flow in Microchannel	142
4.6.2 Low-pressure Gas Flow	148
4.6.3 High-pressure Gas Flow	150
4.6.4 Temperature Distribution for Microchannel Gas Flow	156
4.7 Conclusion	163
References	164

5. Micro Fluidic Couplers

5.1	Introduction	169
5.2	Concept and Design	171
5.3	Fabrication	177
5.3.1	Silicon Truncated Pyramidal Coupler	177
5.3.2	Molded Truncated Pyramidal Coupler	181
5.3.3	Post Coupler.....	182
5.4	Test Results and Discussion	184
5.5	Conclusion	186
	References	187

6. Integrated Micro Fluidic Flow Sensors

6.1	Introduction	190
6.2	Design	191
6.3	Fabrication	193
6.4	Experiment Setup	195
6.5	Test Results and Discussion	197
6.6	Error and Resolution Analysis	201
6.7	Micro Heat Transfer Modeling	203
6.8	Bubble Detection	206
6.9	Conclusion	207
	References	209

7. Conclusion	211
Appendix A: MOSIS Chip	215
Appendix B: 200-Channel Data Acquisition System	217

List of Illustrations

1.1.1	Bulk micromachining technology	5
1.1.2	Surface micromachining technology	7
2.2.1	Pictures of LPCVD systems in the Caltech Micromachining Laboratory	24
2.2.2	The illustration of a tube furnace for LPCVD polysilicon	25
2.2.3	Growth rate vs. $1/T$ for two different conditions	26
2.2.4	The effect of silane concentration on the polysilicon deposition rate	27
2.2.5	The effect of dopants on the polysilicon deposition rate at 610°C ...	28
2.3.1	An illustration of polysilicon grain boundaries	32
2.3.2	Room-temperature resistivity vs. doping concentration	33
2.3.3	Temperature coefficient of resistance for boron-doped polysilicon ..	35
2.4.1	Designs of heavily and lightly doped polysilicon thin film thermistors	38
2.4.2	Mask design of polysilicon heaters	39
2.4.3	Process flow of a polysilicon thin-film thermistor	40
2.2.4	Pictures of fabricated polysilicon thermistors	41
2.4.5	The illustration of four-point probe method	42
2.4.6	The picture of the four-contact method	42
2.4.7	The picture of the Van der Pauw method with a symmetrical sample	43
2.4.8	Temperature calibration of fabricated polysilicon thin-film thermistors	44
2.4.9	Polysilicon resistivity and temperature coefficient vs. doping concentration	44
3.1.1	Shrouded (a) plate and (b) pin fin arrays	59
3.1.2	Air-cooled, multichip modules	60

3.1.3	Schematic view of the compact heat sink incorporated into an integrated circuit chip	61
3.1.4	Range of heat transfer coefficients for various coolants	63
3.1.5	Conceptual illustration of MEMS impinging jet heat exchanger	65
3.1.6	The MEMS-based heat transfer measurement paradigm	67
3.2.1	An illustration of convection velocity and thermal boundary layers ..	69
3.2.2	Flow regions in a confined macro impinging jet	74
3.2.3	Distribution of local Nu number	76
3.3.1	A silicon temperature imager bonded on a PC board	78
3.3.2	Temperature sensor arrangement of the silicon temperature imager ..	78
3.3.3	Process flow of silicon temperature imager	79
3.3.4	Calibration curves of the sensors on a silicon temperature imager ..	79
3.3.5	Prototype MEMS nozzle	81
3.3.6	Nozzle fabrication process	81
3.3.7	Micromachined (a) nozzle and (b) slot arrays	81
3.3.8	MEMS jet array process flow	82
3.3.9	The illustration of experimental setup	83
3.3.10	Pictures of the experimental setup	84
3.3.11	The constant circuit used in the silicon temperature imager	85
3.3.12	The picture of the constant circuit used in the silicon temperature imager ..	87
3.3.13	A sample of the surface temperature profile	88

3.3.14	Contour temperature plots indicating that the sensor image correctly identifies and tracks an impinging jet	89
3.3.15	Composite illustration shows the effectiveness of impinging jet cooling	91
3.3.16	Average sensor chip temperature at various heights for a given inlet pressure of a single jet	93
3.3.17	Average chip temperature at various heights for a 500 μm diameter MEMS single nozzle	93
3.3.18	Cooling efficiency at various heights for a given inlet pressure of a free single jet	94
3.3.19	Cooling efficiency at various heights for a given inlet pressure of a MEMS single jet	94
3.3.20	Temperature distribution recorded from a nozzle array at 500 μm height, $P_{\text{in}} = 0.5$ psig, and power in = 1.12 W	95
3.3.21	Slot array temperature distribution at height = 1000 μm , $P_{\text{in}} = 1$ psig, and an input power of 1.12 W.....	95
3.4.1	A quartz temperature imager mounted onto a PC board	98
3.4.2	Picture of a sensor on the front side	99
3.4.3	Picture of a sensor on the back side	100
3.4.4	Sensor arrangement on the quartz temperature imager	101
3.4.5	Process flow of the Quartz temperature imager	101
3.4.6	MEMS (a) single and (b) 2 x 1 array nozzles	102
3.4.7	MEMS (a) 2 x 2 and (b) 10 x 10 array nozzles	103
3.4.8	Process flow of thin-wall nozzles	103

3.4.9	Conceptual diagram of 2 nd generation constant current circuit	105
3.4.10	The picture of a constant current circuit board	105
3.4.11	Data processing flow	107
3.4.12	Temperature distribution over the impingement surface	108
3.4.13	Fitted axisymmetric cubic spline vs. measured temperatures over the impingement surface ($p=1.8$ psi, $H/D=1$)	109
3.4.14	3-D plot of local h of a MEMS single jet ($p=1.8$ psi, $H/D=1$)	109
3.4.15	Local heat transfer coefficient of a MEMS thin-walled jet for different driving pressures	111
3.4.16	Local heat transfer coefficient of a MEMS thin-walled jet for fixed pressure for different jet heights	112
3.4.17	Average heat transfer coefficient of a MEMS single jet for different driving pressures	112
3.4.18	Local h of a 2x1 jet array ($Q=1.4$ SLPM, $H/D=3.3$, $a=1.5$ mm)	114
3.4.19	Dependence on jet-to-jet spacing of the average heat transfer coefficient of a 2 x 1 jet array at different flow rates	114
3.4.20	Dependence on jet-to-jet spacing of the average heat transfer coefficient of a 2 x 1 jet array for different jet heights	115
3.4.21	Average heat transfer coefficient of a 2 x 2 jet array for different driving pressures	116
3.4.22	Average heat transfer coefficient of a 10 x 10 jet array	117
4.3.1	Coordinates used in the derivation of equations	130
4.3.2	The coordinate system along the length direction	132

4.4.1	Conceptual illustration of MEM freestanding micro channel integrated with micro sensors	134
4.4.2	Fabrication process for suspended microchannel with integrated thermistors	135
4.4.3	Top view of suspended micro channel with integrated thermistors	137
4.4.4	Electron micrographs of suspended channel with an integrated sensor	137
4.4.5	A suspended micro channel with a broken part to show a freestanding thermistor inside	138
4.5.1	The illustration of experiment setup	140
4.5.2	The picture of the chip bonded on a packing holder	140
4.5.3	The top view of the vacuum chamber	141
4.5.4	The side view of the vacuum chamber	141
4.6.1	Comparison between the measurement data and the theory for a channel with constant cross section area	143
4.6.2	Illustration of channel deformation under pressurized flow	144
4.6.3	Bending beam model applied to the bulged channel wall	144
4.6.4	Measurement data fitted to the bulging model	146
4.6.5	Sample processed 3-D WYKO image showing beam deflection near the inlet at 300 psig	148
4.6.6	Theoretical and experimental results for low pressure N ₂ flow with outlet pressure at 1 atm	149
4.6.7	Theoretical curves and experimental data for low pressure N ₂ flow for 30 psig inlet pressure	150

4.6.8	Theoretical curve and experimental data for high pressure N ₂ flow for 1 atm outlet pressure	151
4.6.9	Mass flow rate vs. inlet pressures, with curves at various exit pressures, slip and no slip theoretical curves, and a curve with acceleration effects	153
4.6.10	Theoretical curves (for low and high inlet pressures) and experimental data for low pressure N ₂ flow for 1 atm outlet pressure	154
4.6.11	Mass flow rate vs. inlet pressure of experimental data and the curve plotted with our new model.....	156
4.6.12	Three working sensors on the packaged microchannel	157
4.6.13	Sensor sensitivity to temperature	158
4.6.14	Sensor sensitivity to pressure	158
4.6.15	Micro temperature sensors integrated inside a suspended channel ...	160
4.6.16	Temperature distribution within a micro channel at various inlet pressures	162
5.1.1	Pictures of the coupling with excessive epoxy	170
5.2.1	A micro fluidic system coupled with capillaries by micromachined fluidic couplers (not to scale)	171
5.2.2	The general concept of a coupler: an intermediate fitting between the capillary and micro fluidic system (not to scale)	172
5.2.3	A pyramidal pit, bounded by the four- (111) planes, anisotropically etched into (100) silicon through a square opening in the mask	173
5.2.4	A truncated pyramidal coupler can be used to connect a capillary to an inlet or outlet (not to scale)	174

5.2.5	A coupler fits into an inlet or outlet of two different sizes by adjusting the fitting depth	175
5.2.6	Three designs of truncated pyramidal couplers (not to scale)	175
5.2.7	A capillary connected to an inlet or outlet by a post coupler	176
5.3.1	Process flow of silicon truncated pyramidal coupler	178
5.3.2	SEM corner compensation results (a) & (b) with respective masks (c) & (d)	179
5.3.3	The picture of fabricated silicon truncated pyramidal couplers	180
5.3.4	The picture of fabricated silicon truncated pyramidal couplers bonded with silica capillary tubing	180
5.3.5	Process flow of a molded truncated pyramidal coupler	181
5.3.6	The picture of a molded coupler	182
5.3.7	Post coupler fabrication process flow	183
5.4.1	The pictures of fluidic chip with/without coupling to capillary tubing through silicon couplers	184
5.4.2	Illustration of the test setup for micro fluidic couplers	185
5.4.3	A picture of the test setup for micro fluidic couplers	185
6.2.1	A microchannel-based flow sensing approach	191
6.2.2	An improved flow sensing approach with a suspended microchannel	192
6.2.3	Three designs of flow sensors	193
6.3.1	Process flow of the microchannel flow sensor with a sensing element embedded in the channel wall	194

6.3.2	A fabricated flow sensor with polysilicon resistors and a micro channel on the silicon substrate	195
6.3.3	A fabricated flow sensor with polysilicon resistors and a micro channel suspended away from silicon substrate	195
6.4.1	Pictures of the chip packing: (a) top view, (b) bottom view	196
6.4.2	Schematic of the calibration system for MEMS flow sensors	197
6.5.1	Temperature dependence of three types of sensors	199
6.5.2	Characteristics of the flow sensors with three different designs	200
6.5.3	Temperature change of the sensors due to liquid flow	201
6.6.1	Histogram of a typical set of sensor measurements	202
6.7.1	Temperature distribution along the channel	203
6.7.2	Temperature distribution along the channel for four flow conditions (0, 0.05, 0.10, and 0.15 $\mu\text{L}/\text{min}$) at sensor #3 input power of 140 μW	204
6.7.3	Distribution of the flow-induced temperature change along the channel for sensor #3 at input power of 140 μW	205
6.7.4	Simulated vs. measured flow-induced temperature change for sensor #3	206
6.8.1	Real time output of the cold sensor next to heated sensor #1. Temperature spikes indicate passage of an air bubble	207
6.9.1	Temperature distribution, bubble generation, and pressure sensing capabilities for future flow sensors	208

List of Tables

TABLE 1 Material properties of polycrystalline and single-crystal silicon	30
TABLE 2 Typical ranges of the convection heat transfer coefficient	71
TABLE 3 Comparison of pressure required to cool the test chip to approximately 47 °C with $Q = 1.12$ W and height = 500 μm	97
TABLE 4 Temperature differences between the three sensors under two different flows	172
TABLE 5 A comparison of this work to other couplers	186
TABLE 6 TCR's, temperature-to-flow ratios and relative sensitivities	201

Nomenclature

A	area
B	constant depending on the boundary condition
C, C_1, C_2	constants
C_p	specific heat at constant pressure
D	diameter of a nozzle
E_a	activation energy
E_c	conduction band
E_v	valence band
E_f	Fermi level
E_{fi}	intrinsic Fermi level
h	heat transfer coefficient; height of a channel
H	spacing between a jet to the impingement surface
I	Current
k	Boltzmann's constant
k_s	thermal conductivity of solid
k_f	thermal conductivity of fluid
Kn	Knudsen number
L	polycrystalline silicon grain size
m^*	effective mass of carrier
n	a constant
N	number of samples
Nu	Nusselt number

p	pressure
p_o	the carrier concentration at center of a grain
P_{in}	inlet pressure
P_{out}	outlet pressure
Pr	Prandtl number
q	electronic charge
q''	heat flux density
Q	electrical charge
Q_m	mass flow rate
Q_{mi}	mass flow rate without compressible effect
Q_v	volumetric flow rate
r	distance from impingement center
r_{eff}	effective cooling range
R	specific gas constant
R_d	deposition rate
Re	Reynolds number
t	film thickness
T	temperature
T_s	temperature of solid surface
T_∞	fluid temperature
TCR	temperature coefficient of resistivity
S_V	ratio of voltage to flow rate
S_T	ratio of temperature to flow rate

S_V/V_0	relative sensitivity
u	velocity
u_j	jet velocity
V	voltage
V_b	space-charge potential barrier
V_{BE}	base-emitter voltage
I_E	emitter current
I_B	base current
I_C	load current
w	width
α	temperature coefficient of resistivity
α_{diff}	thermal diffusivity
β	pressure sensitivity of integrated thermistors
δ	thickness of grain boundary or flow velocity boundary
δ_t	thermal boundary thickness
λ	a constant
$\bar{\lambda}$	mean free path
η	a constant
η_c	compressible effect of mass flow rate
η_a	flow acceleration effect of mass flow rate
η_p	velocity profile effect of mass flow rate
η_s	slip boundary effect of mass flow rate

ρ_r	resistivity
ρ	fluid density
ρ_C	bulk resistivity of silicon crystal
σ	standard deviation
μ	fluid viscosity
ν	fluid kinematic viscosity
χ	scattering barrier height

CHAPTER 1

INTRODUCTION TO MEMS AND MEMS APPLICATIONS IN MICROFLUIDICS

Microfabrication started in the 1950s when the first integrated circuit (IC) was developed, and its rapid development has significantly changed modern industry and society. While such technology was focused on IC devices, similar batch fabrication technology, i.e., micromachining, was applied to mass-produce micro integrated electro-mechanical devices [1]. In the 1980s, Micro-Electro-Mechanical Systems (MEMS) were developed by integration of micro devices, including sensors, actuators, and microelectronics, that are batch fabricated on the same chip using micromachining and IC fabrication processes. The emerging MEMS technology has had a great impact on many fields including chemistry, biology, medicine, optics, and engineering. These broad applications imply a promising future for MEMS to revolutionize the design and fabrication of products in nearly every category.

1.1 Introduction to Micromachining Technology and MEMS

1.1.1 Introduction

Micromachining refers to the batch fabrication technology of large numbers of three-dimensional devices that consist of both electrical and mechanical components with typical sizes ranging from micrometers to millimeters. It originated from microelectronic fabrication techniques in the early 1970s, and gradually developed into a hybrid technology highly compatible with IC technology in the 1980s. During the past two decades, numerous micro electrical and mechanical devices were developed using micromachining technology, such as pressure sensors [2-5], ink-jet nozzles [6,7], chromatographic air analyzers [8], thermal sensors [9-12], accelerometers [12-16], and electrostatic actuators [17, 18].

Starting in the early 1990s, a dramatic increase of government-sponsored research in micromachining promoted the technological revolution that has brought us fully integrated Micro-Electro-Mechanical Systems (MEMS). By the integration of micromachined sensors and actuators with microelectronics fabricated using IC processing, MEMS makes it possible to realize complete systems-on-chip. Such micro systems are able to couple the full operation of sensing, information processing and manipulating actuation to the physical world on a scale that has never been possible before. The applications of MEMS have already had a major impact on many scientific fields such as biology and chemistry - biochemistry [19-22], optics [23, 24], and almost every aspect of engineering [25-28]. The constant effort in developing MEMS technology promises future revolutions in the manufacturing of commercial products [1, 29].

1.1.2 Fabrication Techniques

Generally, micromachining, which is vastly different from conventional machining, has been regarded as having originated from IC technology. In fact, because of the use of many of the same microfabrication processes, including photolithography patterning, thin film deposition, chemical wet etching, and plasma dry etching, micromachining shares the same virtues as IC technology, i.e., high precision and batch fabrication. However, there are still many differences between these two technologies. For instance, in micromachining, selective etching is applied in order to generate 3-D mechanical structures while in IC fabrication, planar processes are preferred to achieve smaller and smaller feature sizes of electronic devices on a wafer. Micromachining has been very useful in many applications because of its possibility of creating 3-D or even freestanding mechanical structures.

Micromachining generally has been classified into three major groups of techniques: bulk micromachining [30], surface micromachining [31, 32] and LIGA Technology [33], that we briefly discuss in the following.

Bulk micromachining refers to the fabrication of 3-D mechanical structures from a substrate by selectively removing a portion of the substrate material. Although there are many choices of substrate material and methods of material removal, historically single-crystalline silicon has been used as the major substrate material, which usually is selectively removed by chemical etching, either isotropically or anisotropically depending on the selection of etching chemicals [1, 30].

Mixtures with different ratios of hydrofluoric acid, nitric acid, and acetic acid (HNA) have been the most common aqueous chemical for silicon isotropic etching [1,

34-36], while xenon difluoride (XeF_2) [37] and bromine trifluoride (BrF_3) [38] have been used for silicon isotropic dry etching. Isotropic bulk etching is illustrated in Figure 1.1.1 (a). On the other hand, aqueous solutions, such as potassium hydroxide (KOH) [39-42], ethylene diamine pyrocatechol (EDP) [43, 44], tetramethylammonium hydroxide (TMAH) [45, 46], and ammonium hydroxide (NH_4OH) [47], have been employed for anisotropic silicon etching. Interestingly, the etching anisotropy exhibited in these chemical-etching processes is due to the different chemical reactivities of certain crystal plane of silicon. The etching rates are much faster silicon in the (100) and (110) silicon crystallographic directions than in the (111) direction. This allows mechanical components to be designed as the microstructures naturally bounded by {111} crystalline planes as illustrated in Figures 1.1.1 (b) and (c). Moreover, the etching rate can be decreased by heavily doping boron into silicon [42, 48] as well as electrochemically biasing a silicon p-n junction [49]. This adds an additional way of etching control besides the concentration and temperature of the etching solution. Anisotropic etching has been applied to fabricate many MEMS devices and structures such as pressure sensors, ink-jet nozzles, accelerometers, neural probes and wells, microgimbals and suspension for hard disk drives, flow sensors, fluidic filters and mixers, micro pumps, and air-jet nozzles, etc.

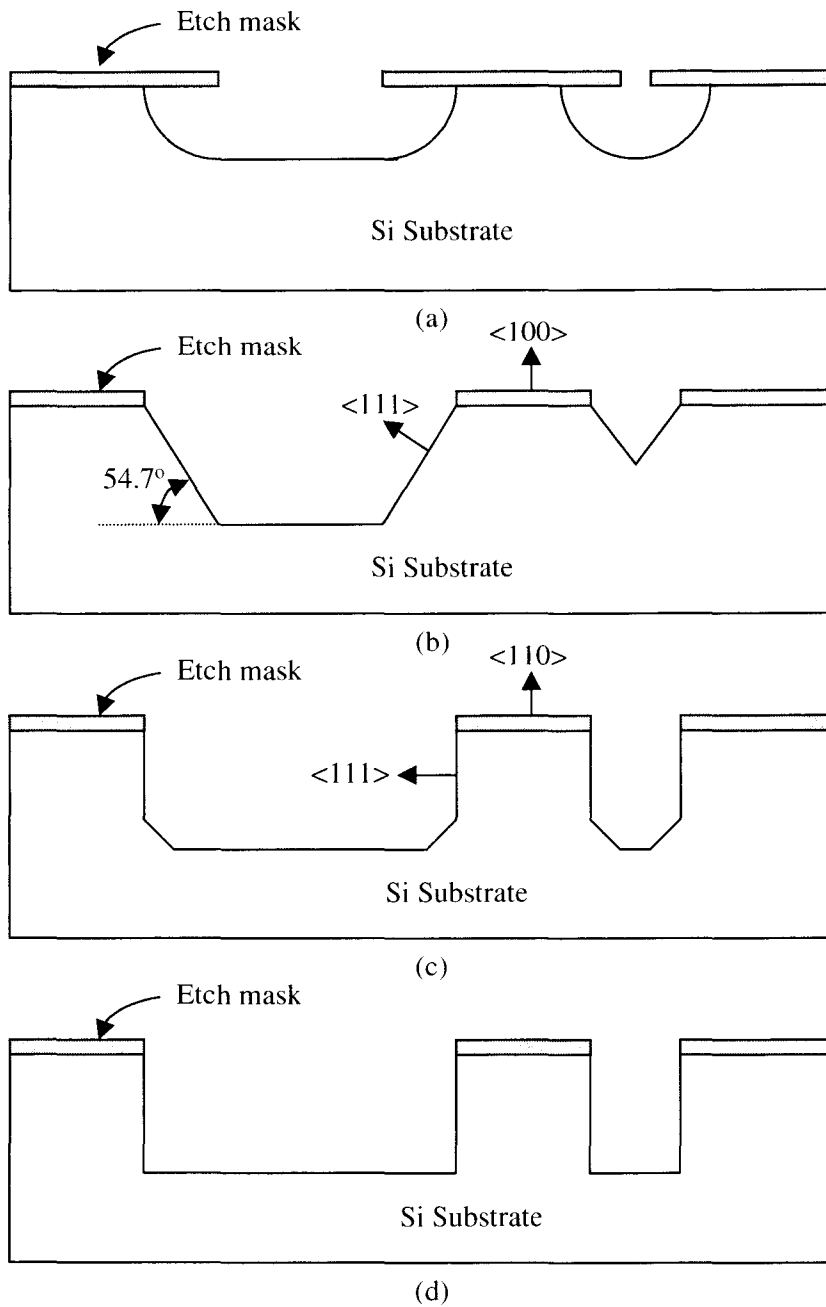


FIGURE 1.1.1 Bulk micromachining technology: (a) Isotropic etching, (b) Silicon anisotropic etching on (100) surface, (c) Silicon anisotropic etching on (110) surface, (d) Deep reactive ion etching (DRIE).

In addition to chemical etching, plasma-enhanced etching such as plasma etching [50], reactive ion etching (RIE) [51], and deep reactive ion etching (DRIE), illustrated in Figure 1.1.1 (d) [52, 53], have been widely applied to bulk silicon etching. Meanwhile, other physical machining techniques like silicon fusion bonding [54], silicon to glass anodic bonding [55], electrode discharge machining (EDM) [56, 57], and laser machining [58], have been introduced to silicon bulk micromachining as well.

Surface micromachining allows the fabrication of microstructures on the substrate surface. The substrate only provides mechanical support, and can be made up of silicon, quartz, glass, and even metal. In surface micromachining, a series of thin film depositions and patterning steps are performed to form microstructures using various standard methods similar to IC fabrication. As illustrated in Figure 1.1.2, selective etching is often performed to remove certain sacrificial layers and free other structural layers by taking advantage of high etching selectivity of the sacrificial layers and structure layers. In the hydrofluoric acid etching process, silicon dioxide and phosphor silicate glass (PSG) are popular sacrificial materials, and polycrystalline silicon and low stress silicon nitride are the commonly used structural materials [11, 15, 17, 18, 31, 32, 59, 60]. Numerous MEMS devices are fabricated using this sacrificial etching technique. Among them, micro digital mirrors, electrostatic motors, polysilicon resonators, accelerometers, gyroscopes, microchannels, pressure sensors, and flow sensors are the representative devices. Occasionally, polycrystalline silicon [61], photoresist [62], and even electroplated copper [63] has been used as a sacrificial material, with TMAH, acetone and a mixture of H_2SO_4 , acetic acid and H_2O_2 as the etchant, respectively.

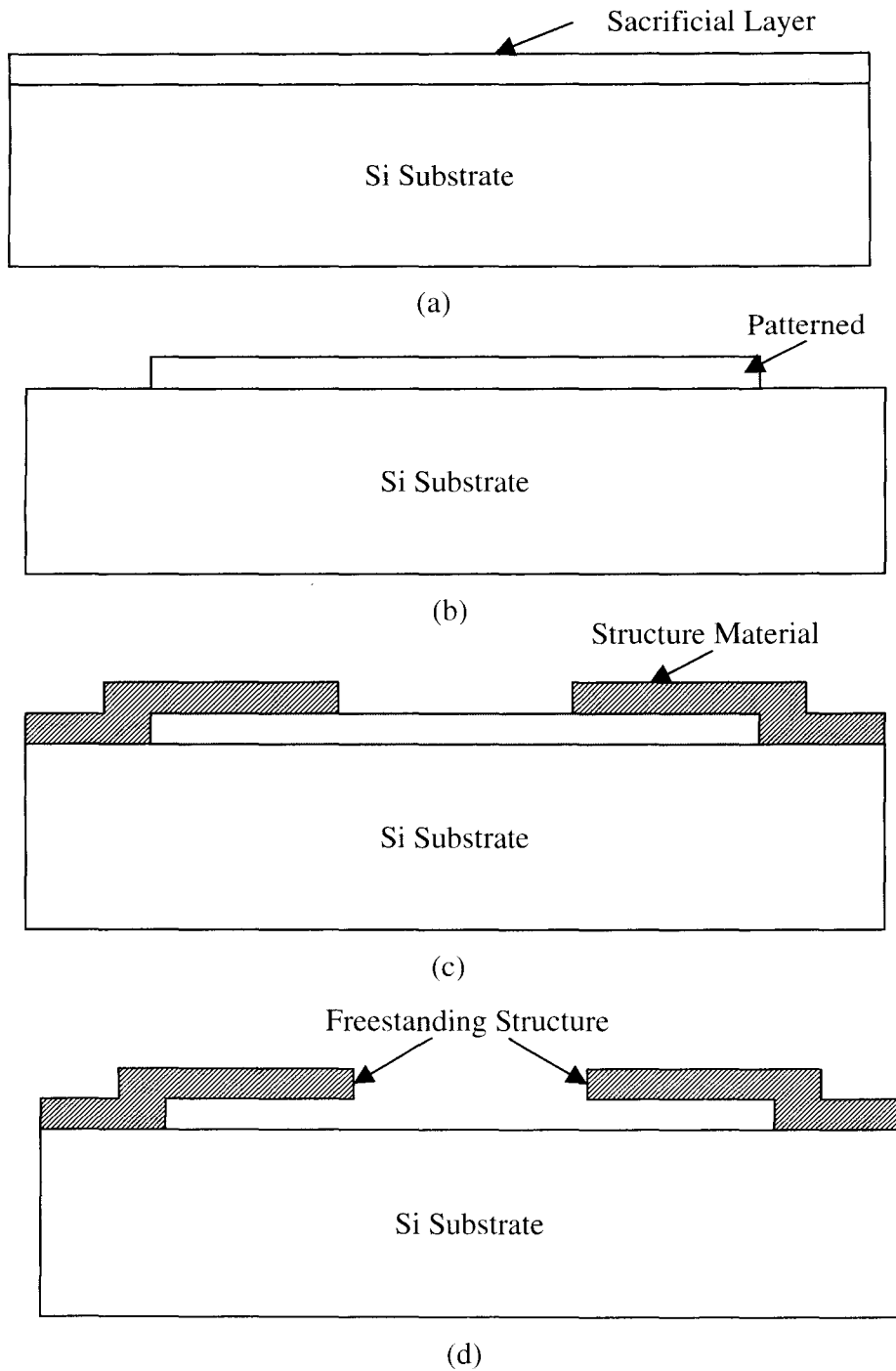


FIGURE 1.1.2 Surface micromachining technology: (a) Sacrificial layer deposition, (b) sacrificial layer patterning, (c) structural material deposition and patterning, (d) sacrificial layer etching.

LIGA technology was introduced to the micromachining community in the late 1980s. This technology involves X-ray lithography and thick electroplating, and it is useful for some special applications requiring a very fine spatial resolution and high aspect ratio [29, 30]. However, it is not popular so far due to the requirement for an expensive X-ray source that needs a high-energy synchrotron.

1.2 Applications of MEMS in Microfluidics

Microfluidics is a multidisciplinary research area involving disciplines such as engineering, physics, chemistry, biology, and medicine. It has been drawing a tremendous amount of interest and effort from its beginning because of its wide potential applications. MEMS technology has greatly accelerated the development of microfluidics in both device fabrication technology and fundamental investigation methods.

Microfluidic devices started to receive extensive attention since pressure transducers [2,3,4] and ink jet printing miniature structures [6, 7] were successfully demonstrated in the 1970s. The subsequent development of microfluidics, including gas chromatography systems [8], micro cryogenic refrigerators [64], heat sinks for VLSI [65], and microfluidic amplifiers [66], indicated its huge potential in the future. The emergence of Micro Electro Mechanical System (MEMS) is the main drive behind the fast development of microfluidics. Using advanced micromachining fabrication techniques, numerous microfluidic devices, such as microchannels, valves, flow sensors, filter and pumps [25, 27], have been created. More complicated microfluidic systems under development include microfluidic labs-on-chip [67-70] and chemical reaction systems [71] that consist of many individual single microfluidic devices.

In addition to device fabrication, MEMS technology provides a novel means for micro flow study. Because of the orders of magnitude of reduction in sizes, the dominating fundamental principles that govern flow at the micro scale may be different than those at macro scale. Many assumptions in classic fluid mechanics require re-examination for validity when applied to microfluidics. For instance, when the characteristic length scale of the gas flow system is on the same order of magnitude as the mean free path of gas molecules, the continuum gas flow model may be inappropriate, and the assumption of zero velocity at walls (non-slip boundary condition) may become invalid. Many micro gas flow phenomena associated with microchannels have been observed and studied [72-75]. While tremendous efforts have been focused on micro gas flow, many issues related to micro liquid flow, such as diffusion and separation [76], mixing [77], bubble detection [78], and phase transition [79], have been carefully studied with micromachined devices and systems as well. With the dramatically increasing demand for microfluidic devices and systems, MEMS technology based micro flow study is essential for understanding physical governing laws in micro scale and the operational principles of micro devices.

1.3 Overview of Dissertation

This thesis focuses on the design, fabrication and testing of integrated polysilicon thermistors for microfluidic sensing, and also documents experimental results related to MEMS impinging-jet cooling, micro flow sensors, and high-pressure channel flow.

Chapter 2 reports deposition techniques and properties of doped polysilicon, and then discusses issues related to the design, fabrication and calibration of polysilicon thin film thermistors.

Chapter 3 describes design and fabrication of MEMS thermal imagers and nozzles, explains the details of the experimental setup and data processing, and presents the testing results on MEMS impinging-jet cooling.

Chapter 4 addresses the design and fabrication of freestanding microchannels with integrated polysilicon thermistors, and presents the experimental results related to high-pressure flow in microchannel.

Chapter 5 discusses robust microfluidic couplers produced with a high yield and compatible with existing MEMS fluidic devices.

Chapter 6 presents the results related to the design, fabrication, testing, and simulation of micro flow sensors that have a resolution up to 1 nL/min and are capable of microbubble detection.

The thesis is finally summarized in Chapter 7.

References:

- [1] K. E. Petersen, "Silicon as a mechanical material," *Proceeding of the IEEE*, vol. No. 5, pp. 420-457, May, 1982.
- [2] Samaun, K. D. Wise, and J. B. Angell, "An IC piezoresistive pressure sensor for biomedical instrumentation," *IEEE Trans. Biomed. Eng.*, vol. BME-20, pp. 101, 1973.
- [3] A. C. M. Gieles and G. H. J. Somers, "Miniature pressure transducer with silicon diaphragm," *Phillips Tech. Rev.*, vol. 33, pp. 14, 1973.
- [4] W. K. Ko, J. Hynccek, and S.F. Boettcher, "Development of a miniature pressure transducer for biomedical applications," *IEEE Trans. Electron Devices*, vol. ED-26, pp.1896, 1979.
- [5] H. Guckel and D. W. Burns, "Planner processed polysilicon sealed cavities for pressure transducer arrays," in Tech. Dig. IEEE int. Electron Devices Meeting, San Francisco, CA, Dec. 1984, pp. 223-225.
- [6] E. Bassous, H.H. Taub, and L. Kuhn, "Ink jet printing nozzle arrays etched in silicon," *Appl. Phys. Lett.*, vol. 31, pp.135-137, 1977.
- [7] K. E. Petersen, "Fabrication of an integrated planar silicon ink-jet structure," *IEEE Trans. Electron Devices*, vol. ED-26, pp. 135-137, 1979.
- [8] S. C. Terry, "A gas chromatographic air analyzer fabricated on a silicon wafer using integrate circuit technology," Ph.D. dissertation, Department of Electrical Engineering, Stanford University, Stanford, CA, 1975.
- [9] C. C. Williams and H. K. Wickramasinghe, "High resolution thermal microscopy," *Proc. IEEE Ultrasonics Symposium*, Williamsburg, vol., pp. 393-397, 1986.

- [10] A. W. Van Herwaarden and P. M. Sarro, "Thermal sensors based on the seebeck effect," *Sensor and Actuator*, vol. 10, 1986, pp. 321-346.
- [11] Y. C. Tai and R. S. Muller, "Lightly doped polysilicon bridge as an anemometer," *Tech. Digest, Transducers '87*, 4th int. Conf. On Solid-state Sensors and Actuators, Tokyo, Japan, pp. 360-363, 1987.
- [12] I.H. Choi and K. D. wise, "A silicon-thermopile-based Infrared sensing array for use in automated manufacturing," *IEEE Trans. Electron Devices*, vol. ED-33, No.1, pp. 72-79, Jan. 1986.
- [13] L. M. Roylance and J. B. Angell, "A batch-fabricated silicon accelerometer," *IEEE Trans. Electron Devices*, vol. ED-26, pp.1991, 1979.
- [14] W. D. Frobenius, S. A. Zeitman, M. H. White, D. D. O. Sullivan, and R. G. Hamel, "Microminiature ganged threshold accelerometer compatible with integrated circuit technology," *IEEE Trans. Electron Devices*, vol. ED-19, pp. 37, 1972.
- [15] P. Chen, R. S. Muller, T. Shiosaki, and R. M. White, "Silicon cantilever beam accelerometer utilizing a PI-FET capacitive transducer," *IEEE Trans. Electron Devices*, vol. ED-26, pp.1857, 1979.
- [16] K. E. Petersen, A. Shartel, and N. Ralay, "Micromachanical accelerometer integrated MOS detection circuitry," *IEEE Trans. Electron Devices*, vol. ED-29, pp. 23, Jan. 1982.
- [17] L. S. Fan, Y. C. Tai, and R. S. Muller, "IC-processed electrostatic micromotor," *Technical Digest, IEDM*, pp. 666-669, 1988.
- [18] W. C. Tang, T. C. H. Nguyen, and R.T. How, "Laterally driven for polysilicon resonate microstructures," *Sensor and Actuators*, vol. 20, pp. 25-32, 1989.

- [19] C. L. Colyers, T. Tang, N. Chiem, and D. J. Harrison, "Clinical potential of microchip capillary electrophoresis systems," *Electrophoresis* 1997, 18, pp. 1733-1741.
- [20] C. H. Mastrangelo, M. A. Burns, and D. T. Burke, "Microfabricated devices for Genetic Diagnostics," Proceedings of IEEE, vol. 86, No. 8, Aug. 1998.
- [21] D. Figeys, S. P. gygi, G. Mckinnon, and R. Aebersold, "An integrated microfluidics-tandem mass spectrometry system for automated protein analysis," *Anal. Chem.*, 1998, vol. 70, pp. 3728-3734.
- [22] E. S. Kolesar and R. R. Reston, "Review and summary of a silicon micromachined gas chromatography system," *IEEE T COMPON PACK B* 21: (4), pp. 324-328 Nov. 1998.
- [23] B. E. Jones and J. S. Mckenzie, "A review of optical actuators and the impact of micromachining," *SENSOR ACTUAT A-PHYS* 37-8, pp. 202-207 Jun.-Aug. 1993.
- [24] M. C. Wu, "Micromachining for optical and optoelectronic systems," *P IEEE* 85: (11), pp. 1833-1856, Nov. 1997.
- [25] M. Elwenspoek, T. S. J. Lammerink, R. Miyake, et al., "Towards integrated microliquid handling systems," *J MICROMECH MICROENG* 4: (4), pp. 227-245, Dec. 1994.
- [26] C. M. Ho and Y. C. Tai, "Review: MEMS and its applications for flow control," *J FLUID ENG-T ASME* 118: (3), pp. 437-447, Sep. 1996.
- [27] S. Shoji, "Fluids for sensor systems," *TOP CURR CHEM* 194: 163-188, 1998.
- [28] G. A. Urban and G. Jobst, "Sensor systems," *TOP CURR CHEM* 194: 189-213, 1998.

- [29] M. Gad-el-Hak, "The fluid mechanics of microdevices - The Freeman Scholar Lecture," *J FLUID ENG-T ASME* 121: (1) pp. 5-33, Mar. 1999.
- [30] G. T. A. Kovacs, N. I. Maluf, and K. E. Petersen, "Bulk Micromachining of Silicon," *P IEEE* 86: (8) 1536-1551, Aug. 1998.
- [31] J. M. Bustillo, R. T. Howe and R. S. Muller, "Surface micromachining for microelectromechanical systems," *P IEEE* 86: (8) 1552-1574 AUG 1998.
- [32] Y. C. Tai, "IC-Processed Polysilicon micromechanics: technology, Materials and devices," *Ph.D. Thesis*, University of California, Berkeley (1989).
- [33] E. W. Becker, W. Ehrfeld, et al., "Fabrication of microstructure with high-aspect ratio and great structure heights by synchrotron radiation lithography, galvanofarming, and plastic molding (LIGA process)," *Microelectronic Engineering*, vol. 4, pp. 35-36.
- [34] H. Robbins and B. Schwartz, "Chemical etching of silicon, II. The system HF, HNO₃, HC₂H₃O₂," *J. Electrochem. Soc.*, vol. 106, pp. 505, 1959.
- [35] B. Schwartz and H. Robbins, "Chemical etching of silicon, VI. Etching technology," *J. Electrochem. Soc.*, vol. 123, pp. 1903, 1976.
- [36] K. R. Williams and R. S. Muller, "Etch rate for micromachining process," *J. Microelectromech. Syst.*, vol. 5, No. 4, pp. 256-269, Dec. 1996.
- [37] H. F. Winters and J. W. Coburn, "The etching of silicon with XeF₂ vapor," *Appl. Phys. Lett.*, vol. 34, No. 1, pp. 70-73, 1979.

- [38] X.Q. Wang, X. Yang, K. Walsh, and Y.C Tai. "Gas Phase Silicon Etching with Bromine Trifluoride," *Transducer*, 97.
- [39] J. B. Price, "Anisotropic etching of silicon with potassium hydroxide-water-isopropyl alcohol," in *Semiconductor Silicon*, H. R. Huff and R. R. Burgess, Eds. Princeton, NJ: *Electrochemical Society*, 1973, pp. 339.
- [40] K. E. Bean, "Anisotropic etching of silicon," *IEEE Trans. Electron Devices*, vol. ED-25, pp. 1185-1193, Oct. 1978.
- [41] H. Seidel, L. Csepregi, A. Heuberger, et al., "Anisotropic etching of crystalline silicon in alkaline-solutions. 1. Orientation dependence and behavior of passivation layers," *J ELECTROCHEM SOC* 137: (11) 3612-3626, Nov. 1990.
- [42] H. Seidel, L. Csepregi, A. Heuberger, et al., "Anisotropic etching of crystalline silicon in alkaline-solutions. 2. Influence of dopants," *J ELECTROCHEM SOC* 137: (11) 3626-3632, Nov. 1990.
- [43] R. M. Finne and D. L. Klein, "A water-amine-complexing agent system for etching silicon," *J ELECTROCHEM SOC* 114: (11), pp. 965, Nov. 1967.
- [44] D. Moser, "CMOS flowsensors," Doctoral dissertation, Swiss Federal Institute of Technology, Zurich, Switzerland, 1993.
- [45] O. Tabata, R. Asahi, H. Funabash, K. Shimaoka, and S. Sugiyama, "Anisotropic etching of silicon in TMAH solutions," *Sensors and Actuators*, vol. A34, No. 1, pp. 51-57, July 1992.

- [46] A. Merlos, M. Acero, M. H. Bao, J. Bausells, and J. Esteve, "TMAH/IPA anisotropic etching characteristics," *Sensors and Actuators*, vol. A37-38, pp. 737 - 743, June/Aug. 1993.
- [47] U. Schnakenberg, W. Benecke, and B. Lochel, "NH₄OH-based etchants for silicon micromachining," *Sensors and Actuators*, vol. A23, No. 1-3, pp. 1031-1035, Apr. 1990.
- [48] N. F. Raley, Y. Sugiyama, and T. Van Duzer, "(100) silicon etching rate dependence on boron concentration in ethylenediamine pyrocatechol water solutions," *J ELECTROCHEM SOC* 131: (11), No.1, pp.161-171, Jan. 1984.
- [49] T. N. Jackson, M. A. Tischler, and K. D. Wise, "An electrochemical p-n junction etch-stop for the formation of silicon microstructure," *IEEE Electron Device Letters*, vol. EDL-2, No. 2, pp. 44-45, Feb. 1981.
- [50] J. W. Coburn and H. F. Winters, "Plasma etching – A discussion of mechanisms," *J. Vac. Sci. Technol.*, vol. 16, No. 2, pp. 391-403, Mar./Apr. 1979.
- [51] G. C. Schwartz and P. M. Schaible, "Reactive ion etching of silicon," *J. Vac. Sci. Technol.*, vol. 16, No. 2, pp. 410-413, Mar./Apr. 1979.
- [52] K. Murakami, Y. Wakabayashi, K. Minami, and M. Esashi, "Cryogenic dry etching for high aspect ratio microstructures," in *Proc. IEEE Microelectromech. Syst. Conf.*, Fort Lauderdale, FL., Feb. 1993, pp. 65-70.
- [53] E. H. Klaassen, K. Petersen, J. M. Noworolski, et al., "Silicon fusion bonding and deep reactive ion etching: A new technology for microstructures," in *Dig. Tech. Papers transducers'95/Eurosensors IX*, Stockholm, Sweden, June 25-29, 1995, vol. 1, pp. 556-559.

- [54] P. W. Barth, "Silicon fusion bonding for fabrication of sensors, actuators and microstructures," *SENSOR ACTUAT A-PHYS* 23: (1-3) 919-926, Apr. 1990.
- [55] T. Rogers and J. Kowal, "Selection of glass, anodic bonding conditions and material compatibility for silicon-glass capacitive sensors," *SENSOR ACTUAT A-PHYS* 46: (1-3) 113-120, Jan.-Feb. 1995.
- [56] P. H. Heeren, D. Reynaerts, H. VanBrussel, et al., "Microstructuring of silicon by electro-discharge machining (EDM) .2. applications," *SENSOR ACTUAT A-PHYS* 61: (1-3) 379-386, Jun. 1997.
- [57] D. Reynaerts, W. Meeusen, and H. Van Brussel, "Machining of three-dimensional microstructures in silicon by electrodischarge machining," *SENSOR ACTUAT A-PHYS* 67: (1-3) 159-165 May 15, 1998.
- [58] T. M. Bloomish and D. J. Ehrlich, "Laser Stereo Micromachining at one-half million cubic micrometers per second," *Solid-state Sensors and Actuators Workshop, Technical Digest*, June 13-16, Hilton Head, North Carolina, pp. 142-144.
- [59] L. S. Fan, Y. C. Tai, and R. S. Muller, "Integrated movable micromechanical structures for sensors and actuators," *IEEE Trans. Electron Devices*, vol. ED-35, pp. 724-730, Jan. 1988.
- [60] J.Q. Liu, Y. C. Tai, J. Lee, K. C. Pong, Y. Zohar, and C. M. Ho, "In Situ Monitoring and Universal Modelling of Sacrificial PSG Etching Using Hydrofluoric Acid," *Proceedings, IEEE Micro Electro Mechanical Systems Workshop (MEMS '93)*, Fort Lauderdale, FL, pp. 71-76, Feb. 7-10 (1993).
- [61] O. Tabata, H. Funabashi, K. Shimaoka, R. Asahi, and S. Sugiyama, "Surface Micromachining Using Polysilicon Sacrificial Layer," *Proceedings of International*

- Symposium on Micromachine and Human Science*, pp. 163-172, Nagoya, Japan, Oct. 1991.
- [62] P. Man, D. Jones, and C. Mastrangelo, "Microfluidic Plastic Capillaries on Silicon Substrates: A New Inexpensive Technology for Bio Analysis Chips," *Proceedings of IEEE Workshop on Micro Electro Mechanical Systems Workshop (MEMS '97)*, pp. 311-316, Nagoya, Japan, Jan. 1997.
- [63] T. R. Tsao, T. Y. Hsu, and Y. C. Tai, "Copper Sacrificial Layer Technology for Use in Surface Micromachining," *Micromachining Workshop III, Southern California Chapter of American Vacuum Society*, Anaheim, CA, September 1996.
- [64] W. A. Little, "Design and construction of microminiature cryogenic refrigerator," in *AIP Proc. Of Future Trends of Superconductive Electronics* (University of Virginia, Charlottesville, 1978).
- [65] D. B. Tuckerman and R. F. W. Pease, "High-performance heat sinking for VLSI," *IEEE Electron Device Lett.*, vol. EDL-2, pp. 126, 1981.
- [66] M. J. Zdeblick, P. W. Barth, and J. A. Angell, "Microminiature fluidic amplifier," in *Tech. Digest IEEE Solide-State Sensor and Actuator Workshop* (Hilton Head Island, SC), 1986.
- [67] G. Dutton, "Hewlett Packard and Caliper launch microfluidics lab-on-chip - HP 2100 bioanalyzer debuts for biotech and pharmaceutical industries," *Genetic Engineering News*, vol. 19: (16) 1, Sep 15 1999.
- [68] K. Meldrum, "Microfluidics-based products for nucleic acid analysis," *American Laboratory*, vol. 31: (18) 20, Sep. 1999.
- [69] J. M. Ruano, D. Ortega, J. R. Bonar, A. J. McLaughlin, M. G. Jubber, J. M. Cooper, and J. S. Aitchison, "Fabrication of integrated microanalytical chambers and channels for biological assays using name hydrolysis deposition glass," *Microelectronic Engineering*, vol. 46: (1-4) 419-422, May 1999.

- [70] Q. Fang, F. R. Wang, S. L. Wang, S. S. Liu, S. K. Xu, and Z. L. Fang, "Sequential injection sample introduction microfluidic-chip based capillary electrophoresis system," *ANALYTICA CHIMICA ACTA*, vol. 390: (1-3) 27-37 May 19, 1999.
- [71] M. Koch, C. G. J. Schabmueller, A. G. R. Evans, and A. Brunnschweiler, "Micromachined chemical reaction system," *SENSORS AND ACTUATORS A-PHYSICAL*, vol. 74: (1-3) 207-210, Apr. 20, 1999.
- [72] J. Pfahler, J. Harley, H. Bau, J. Zemel, "Gas and liquid flow in small channels," Symp. Micromechanical Sensors, Actuators, and Systems (ed. D. Cho, R. Warrington, et al.) ASME DSC vol. 32, pp. 49-60, 1991.
- [73] E.B. Arkilic, M.A. Schmidt, K.S. Breuer, "Gaseous flow in microchannels," Application of Microfabrication to Fluid Mechanics, ASME Winter Annual Meeting, pp. 57-65, Chicago, IL, Nov. 1994.
- [74] K.C. Pong, C.M. Ho, J. Liu, and Y.C. Tai, "Non-linear pressure distribution in uniform microchannels," Application of Microfabrication to Fluid Mechanics, ASME Winter Annual Meeting, pp. 51-56, Chicago, IL, Nov. 1994.
- [75] S. Wu, J. Mai, Y. Zohar, Y. C. Tai, and C.M. Ho, "A suspended microchannel with integrated temperature sensors for high-pressure flow studies," in *Proc. of The Eleventh IEEE International Micro Electro Mechanical System (MEMS '98)*, Heideberg, Germany, pp. 87-92, Jan. 25-29, 1998.
- [76] B. H. Weigl and P. Yager, "Microfluidics - Microfluidic diffusion-based separation and detection," *SCIENCE* 283: (5400) 346-347, Jan. 15, 1999.
- [77] A. Desai, D. Bokenkamp, X. Yang, E. Marzluff, Y.C.Tai, and S. Mayo, "Microfluidic Sub-millisecond mixers for the study of chemical reaction kinetics,"

1997 International Conference on Solid-State Sensors and Actuators (Transducers '97), May 1997.

- [78] S. Wu, Q. Lin, Y. Yuen, and Y.C. Tai, "MEMS flow sensors for nano-fluidic applications," in *Proc. of The Thirteenth IEEE International Conference on Micro Electro Mechanical Systems (MEMS2000)*, Miyazaki, Japan, Jan. 23-27, 2000.
- [79] L. Jiang, M. Wong, and Y. Zhohar, "A micro-channel heat sink with integrated temperature sensors for phase transition study," in *Proc. of The Twelfth IEEE International Conference on Micro Electro Mechanical Systems (MEMS'99)*, Orlando, Florida, USA, Jan. 17-21, 1999, pp. 159-164.

CHAPTER 2

DOPED POLYSILICON AS A THERMISTOR MATERIAL

2.1 Introduction

Thin film polysilicon is a key electronic material in integrated-circuit technology [1,2]. Polysilicon films heavily doped with impurities, such as phosphorus, arsenic, or boron, offer relatively low resistivities and are commonly used as the gate electrodes and interconnections in silicon-gate MOS integrated circuit. On the other hand, lightly doped polysilicon films have high resistivity and are frequently employed for large-resistance resistors in static memory circuits. Polysilicon can also be used as a semiconductor in field-effect devices such as thin film transistors (TFT) for flat panel displays [1, 3-8]. In addition, large-grain polysilicon shows the potential for mass production of low-cost and high efficiency solar cells [9-14]. Due to many important applications of polysilicon, extensive research efforts have been devoted to polysilicon thin film formation [15-23],

impurity doping [24-27], annealing and crystallization [28-34], electrical properties [24,35-41], and device design and fabrication [1,2, 42-46].

In the 1980s, the emergence of the surface micromachining technology [47] has provided new application opportunities for polysilicon thin film as a mechanical material. Freestanding polysilicon beams were first successfully fabricated by etching away sacrificial layers (e.g., PSG) [48]. By repeatedly invoking this technique, many movable structures have been created [49]. For instance, electrostatic force has been applied to drive freestanding movable polysilicon structures. Electrostatic micromotors [50], micro comb drives [51] and microgrippers [52] are typical examples of micromachined actuators.

Polysilicon is used in microsensors such as pressure sensors, accelerometers, gyroscopes, and thermal sensors [53-59]. Among them, thermal sensors have drawn extensive attention because of their wide range of applications [59-63]. Doped polysilicon elements have temperature sensitive resistivities that allow for temperature sensing, which may be used to relate to the fluid flow and heat transfer characteristics. Such thermal sensors have been developed to measure flow velocity [64, 65], shear stress [66], flow rates [67,68], thermal effects of channel flow [69,70], and heat transfer coefficients of micro impinging jets [71]. Since polysilicon technology is compatible with many fabrication processes of microsystems, thermistors or thermistor arrays can be easily integrated. This solves the common problems arising from the relative large sizes of conventional sensors and the difficulties in implementing separate individual sensors. The fabrication technology and the characteristics of doped polysilicon thin film are discussed in the following sections.

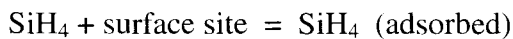
2.2 Thin Film Deposition

Low-pressure chemical vapor deposition (LPCVD) [72-74], plasma-enhanced chemical vapor deposition (PECVD) [75] and sputtering [76,77] have been reported for polysilicon thin film deposition. Among them, LPCVD is the most common method because of its uniformity, impurity, and system availability (LPCVD has been widely used in silicon epitaxy, and other thin film deposition such as silicon nitride and low-temperature oxide LTO) and high throughput (batch fabrication). The following focuses on LPCVD, which is used to prepare polysilicon thin films for integrated thermistors used in this work.

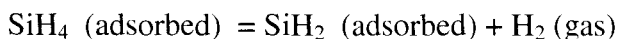
2.2.1 Chemical Decomposition of Silane

Polysilicon is generally deposited by the thermal decomposition of silane (SiH_4) in the temperature range 580-650 °C and total pressure range 0.2-1 torr. There are three reaction sequences involved in the deposition process [74]:

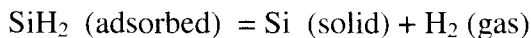
1. SiH_4 adsorption:



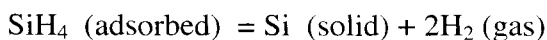
2. Decomposition to SiH_2 :



3. SiH_2 Further Decomposition:



Then the overall reaction is generally written as:



While 100% pure silane gas has been commonly used in LPCVD polysilicon deposition, 20% to 30% silane diluted in nitrogen or hydrogen is very popular as well.

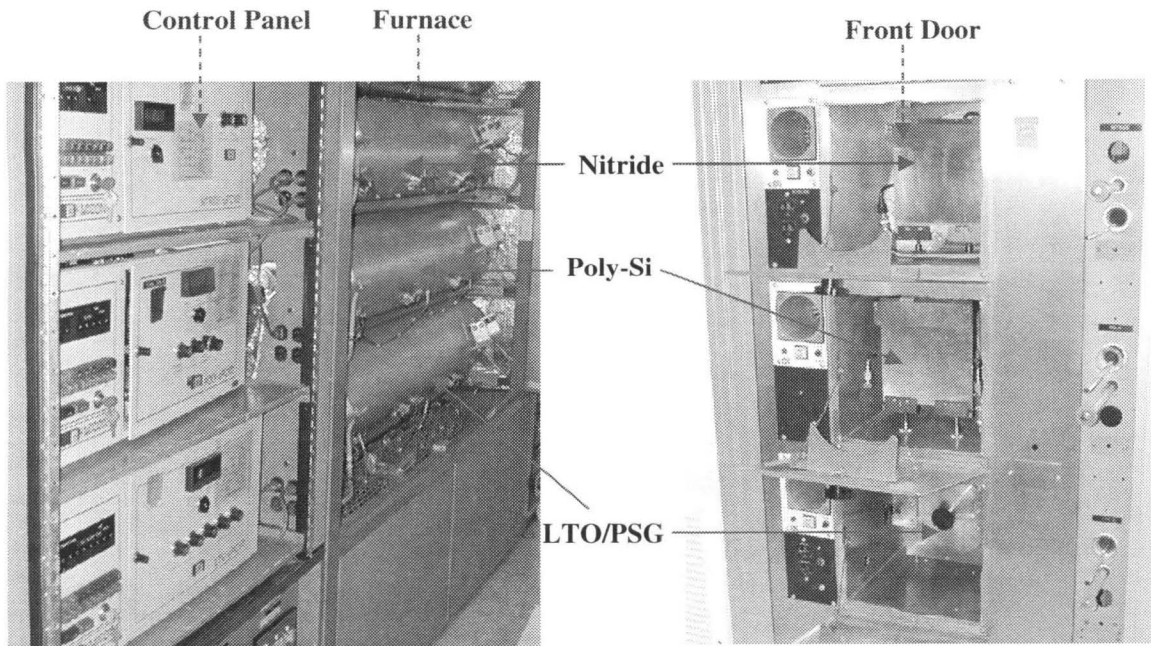


FIGURE 2.2.1 Pictures of LPCVD systems in the Caltech Micromachining Laboratory.

2.2.2 LPCVD System for Polysilicon

Figure 2.2.1 shows the LPCVD systems in the Caltech Micromachining Group. There are three reactors: nitride, polysilicon, and LTO or PSG. Figure 2.2.2 is the illustration of a tube furnace of LPCVD polysilicon. Inside the tube, wafers are sitting vertically in a quartz boat and radiantly heated by resistive heating coils which surround the quartz reaction tube. Silane is fed into the quartz tube in the front and the byproducts are pumped out to establish the required deposition pressure. Many pressure meters, mass flow controllers and valves are included in this system.

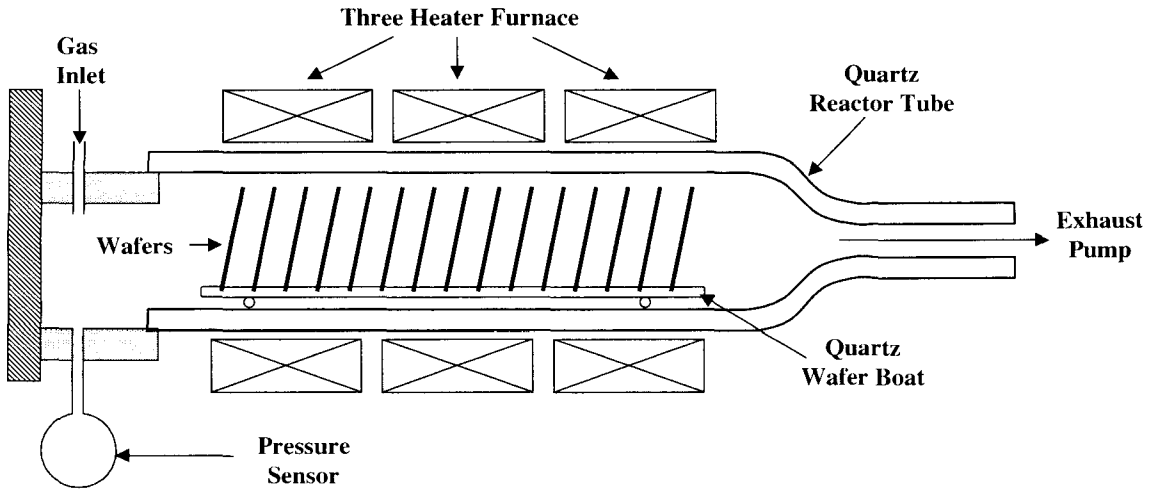


FIGURE 2.2.2 The illustration for a tube furnace of LPCVD polysilicon.

2.2.3 Deposition Parameters

Temperature, pressure, silane concentration, and dopant concentration are the important process parameters in polysilicon deposition. Wafer spacing and loading size have minor effects as well [78].

The deposition rate usually follows the Arrhenius Equation [78, 79]:

$$R_d = C \exp(-qE_d/kT) \quad (2.1)$$

where R_d is the deposition rate, E_d is the activation energy in eV , T is the absolute temperature in K , C is a constant depending on pressure and concentrations, k is Boltmann's constant, and q is the electronic charge.

The temperature dependence is an exponential function of the negative ratio between the activation energy and the thermal energy because the reaction is a thermodynamic process. Figure 2.2.3 provides the data of growth rate vs. reciprocal deposition temperature $1/T$ for two different conditions [74]. The activation energies

calculated from the slopes of fitted lines are found to depend on the silane pressure and range from 1.36 to 1.7 eV. The deposition temperature is usually limited to 580-650°C. If the temperature is too high, gas phase reactions occur and this leads to rough and loosely adhering films. On the other hand, if the temperature is below 580°C, the deposition rate is too low for practical applications (<50 Å/min).

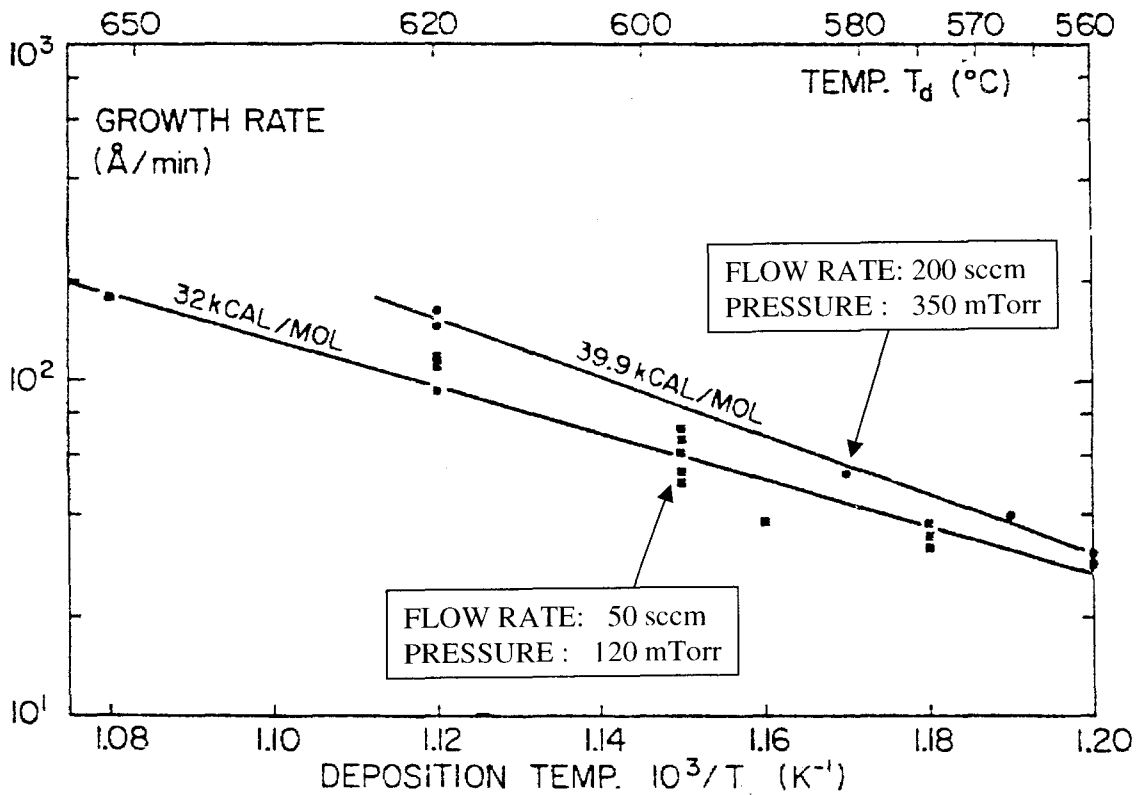


FIGURE 2.2.3 Growth rate vs. $1/T$ for two different conditions [74].

Varying the silane flow rate, silane concentration, and pumping speed can control the deposition pressure and hence control the deposition rate. Practically, changing the pumping speed while fixing silane concentration and flow rate provides the best control of the deposition pressure and deposition rate. Figure 2.2.4 shows the nonlinear dependence of polysilicon deposition rate on the silane pressure. This may be due to

homogeneous reactions, adsorption of hydrogen on the surface site, or transportation effects [74].

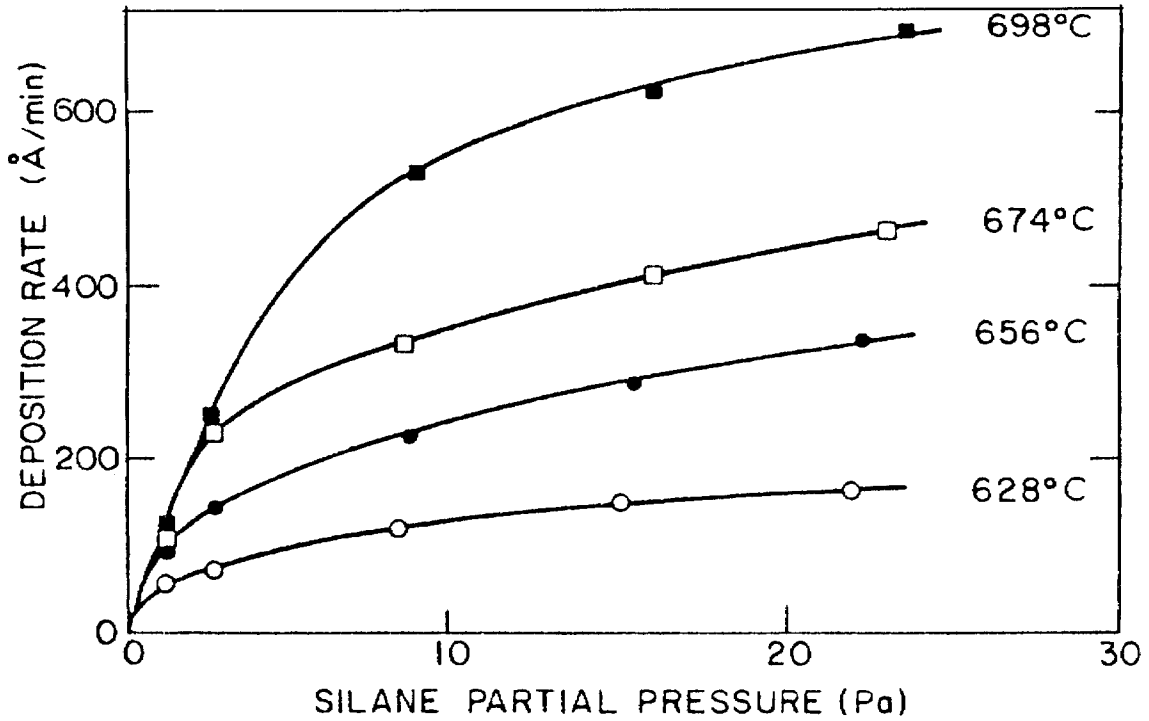


FIGURE 2.2.4 The effect of silane concentration on the polysilicon deposition rate [74].

The dopant and its gas concentration affect the deposition rate as well. As shown in Figure 2.2.5, the addition of diborane to the silane during deposition for boron doping causes dramatic increase in the deposition rate, but the addition of phosphine or arsine to silane results in significant reduction in the growth rate. Such phenomena may be attributed to the adsorption of the dopant gas on the substrate [80].

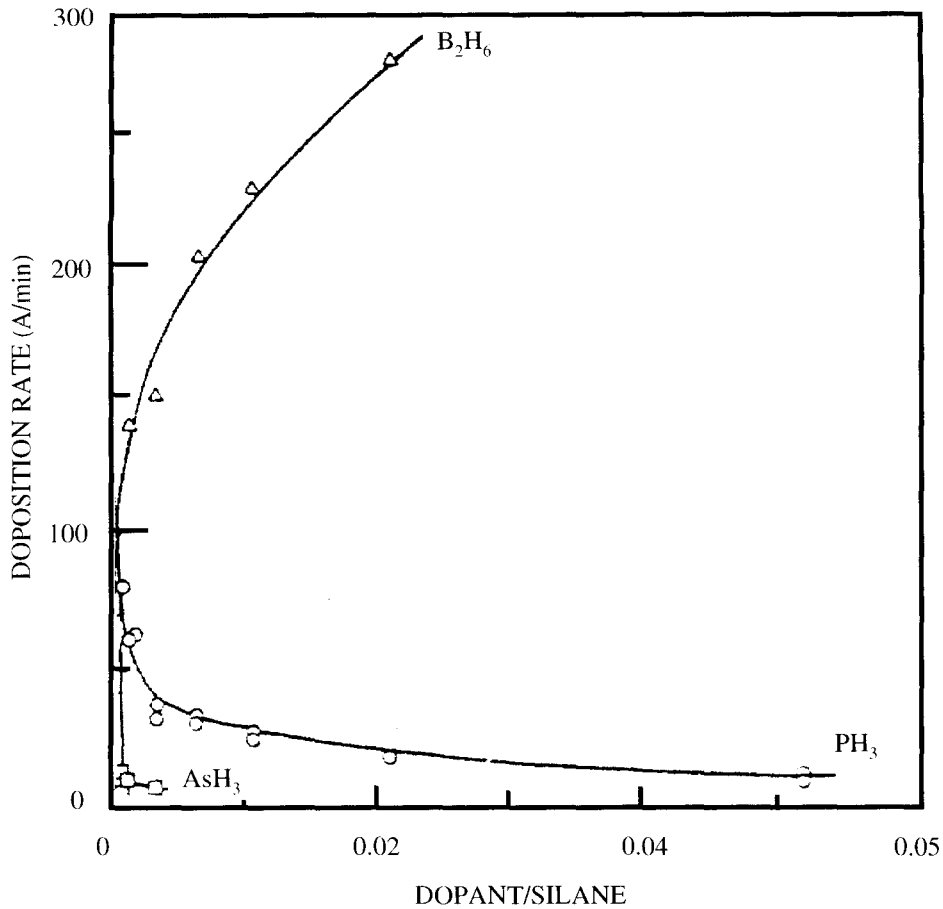


FIGURE. 2.2.5 The effect of dopants on the polysilicon deposition rate at 610°C [74].

2.2.4 Doping Techniques

In situ doping, diffusion, and ion implantation are three basic techniques to dope polysilicon with impurities.

In situ doping involves adding dopant gases such as diborane and phosphine to the silane and combines doping and deposition into one process. The control of film thickness, dopant uniformity, and deposition rate is extremely complicated because of the addition of the dopant gases. In addition, in situ doping affects the film structure, such as grain size and orientation.

Diffusion doping uses relatively high temperatures to drive dopants into the polysilicon film from a source such as heavily doped glass that is grown, deposited or even attached on the polysilicon surface. This high-temperature process can also serve as an annealing process. Very high concentrations (even above the solid-solubility limit because of boundary segregation effects) can be introduced into polysilicon films, resulting in high conductivity. But the surface roughness may increase due to the its high temperature.

Ion implantation doping involves high-energy dopant ions bombarding the polysilicon films and subsequent annealing to redistribute and activate the dopants. The implantation energy is usually chosen so that the maximum distribution of dopants is located at the center of the film, and the ion implantation current and time are controlled according the precise required dosage. A typical annealing process is at $\sim 900^{\circ}\text{C}$ for 30 minutes. But rapid thermal processing (at 1150°C for less than 30 seconds) has also been used as annealing and activation techniques.

2.3 Material and Electrical Properties

2.3.1 Film Structure and Material Properties

The structure of polysilicon depends very much on the deposition temperature, the type and concentration of its dopant, and subsequent thermal cycling. Silicon is amorphous if deposited below 580°C , and the film is polycrystalline if the deposition temperature is above 580°C . It was found that the grain structure and grain size are highly reproducible in films crystallized from the amorphous phase, and the average grain size is generally larger than that in films deposited as polycrystalline directly. In addition, the films in the

amorphous phase tend to have smoother surfaces even after annealing at 900-1000°C. This smoother surface is attributed to the slower deposition rate below 580°C of amorphous silicon. Furthermore, the average grain size has been observed to increase with film thickness. More interestingly, the resistivity in boron doped films has been found to increase exponentially as the film thickness decreases.

Inside each grain, atoms are arranged in a periodic structure and behave similar to single crystal silicon. But there are large numbers of defects due to the incomplete bonds at the grain boundaries that are formed by disordered atoms. These defects behave as trapping centers, and the impurity atoms tend to move to and stay at the grain boundaries. In addition, diffusion constants are much larger in the grain boundary regions than in single crystal regions. Hence, impurity atoms travel much faster along grain boundaries.

Polycrystalline silicon films have many mechanical material properties close to those of single crystal silicon. Table 2.1 lists important mechanical properties of both polycrystalline silicon and single crystal silicon.

TABLE 1 Material properties of polycrystalline and single-crystal silicon [81,82].

	Yield Strain	Young's Modulus	Density	Specific Heat	Thermal Conductivity	Thermal Expansion
	(%)	(dyne/cm ²)	g/cm ³	(J/g°C)	(W/cm°C)	(10 ⁻⁶ /°C)
Single Crystal	3.5	1.9 x 10 ¹²	2.3	0.7	1.57	2.3
Polycrystalline	1.7	1.2 x 10 ¹²	2.3	0.7	0.32	2.0

2.3.2 Electrical Properties

Seto developed the first comprehensive theory of carrier transport in polysilicon based on the trapping model shown in Figure 2.3.1 [35]. In his model, he assumed that the trapping state are monoenergetic (E_t) and are located below the intrinsic level while the thermionic emission (TE) process dominates the carrier transport across the grain-boundary potential barrier (E_b). Based on Seto's model, many modifications have been made to account for experimental results. Lu *et al.* [37] concluded that the carrier transport includes thermionic field emission through the space-charge potential barrier resulting from trapping effects (TFE) and through the grain-boundary scattering potential barrier (TFES), as well as the thermionic emission over these barriers. By assuming a voltage applied to each grain boundary falls in series across the grain-boundary material, space-charge potential barrier, and crystal bulk, they derived the resistivity formula of doped polysilicon [37] as

$$\rho_r = \frac{(2\pi m^* kT)^{1/2}}{Lq^2 p_o} \exp(\chi^{1/\eta} \delta^{1/\lambda}) \exp(qV_b / nkT) + \rho_c \left(1 - \frac{2w}{L} - \frac{\delta}{L}\right) \quad (2.1)$$

where m^* is the effective mass of the carrier, p_o is the carrier concentration at center of a grain, χ is the scattering barrier height, δ is the scattering barrier width, V_b is the space-charge potential barrier, w is the space-charge width, and ρ_c is the bulk resistivity of silicon crystal as shown in Figure 2.3.1. η , λ and n are constant slightly larger than or equal to one. As we can find from Equation 2.1, the doped polysilicon resistivity depends

on the dopant, doping concentration and the film grain structure, which related to deposition temperature and annealing temperature.

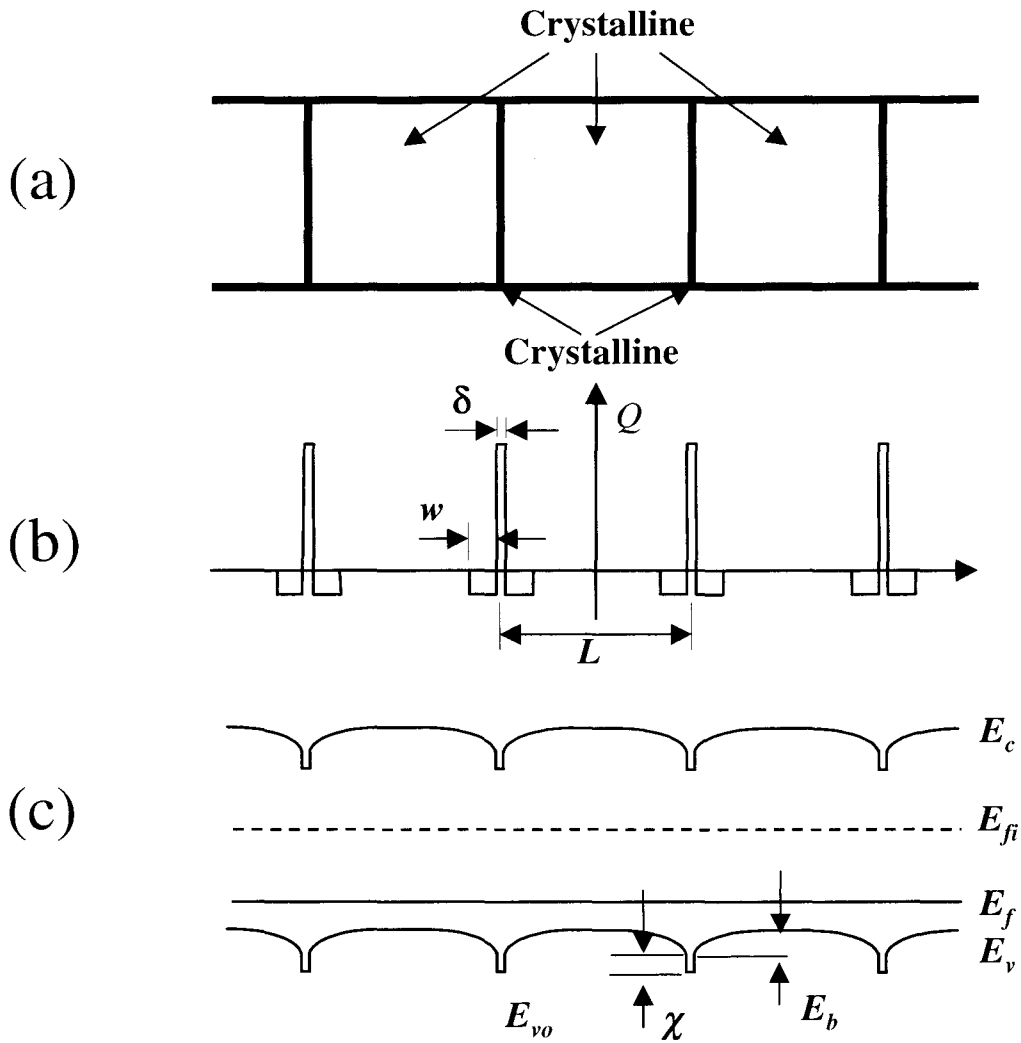


FIGURE 2.3.1 An illustration of polysilicon grain boundaries (a) Model for the crystal structure of polysilicon films. (b) The charge distributions inside the grains and at the grain boundaries. (c) Energy band structure for polysilicon. E_c is the conduction band, E_v is the valence band, E_f is the Fermi level, and E_{fi} is the intrinsic Fermi level.

The behavior of electrons or holes inside each crystal grain is basically similar to that in bulk single crystal silicon, and the electrical properties of polysilicon films mainly depend on their polycrystalline structure and doping.

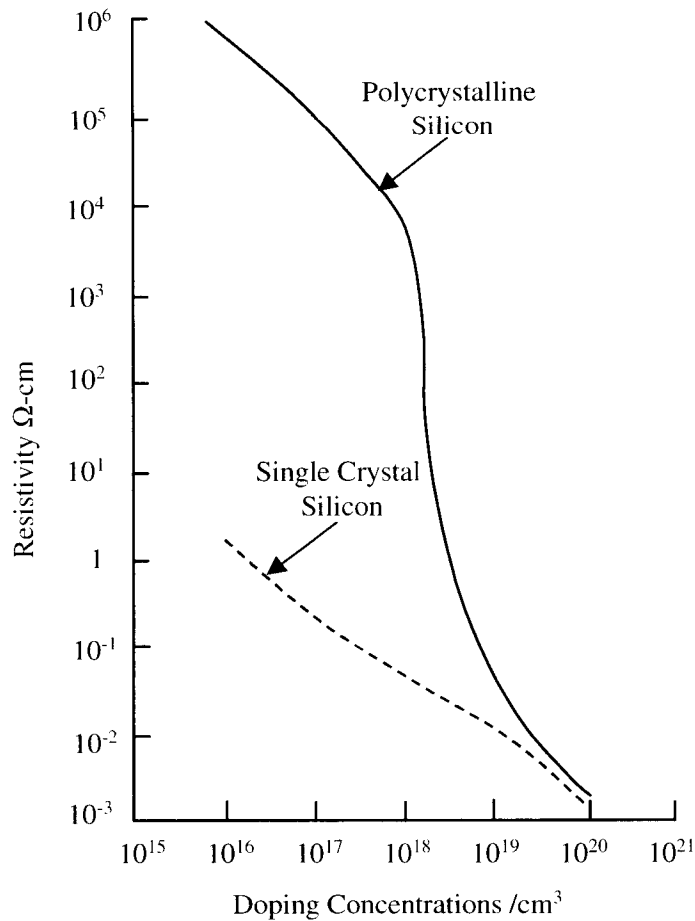


FIGURE 2.3.2 Room-temperature resistivity vs. doping concentration of both single crystal and polycrystalline silicon [35, 79].

As shown in Figure 2.3.2, at the same doping concentrations ($<10^{18}/\text{cm}^3$), polysilicon exhibits significantly larger resistivity than single crystal silicon. This is primarily due to grain boundary effects. First, some dopant atoms (e.g., As and P, but not B) are trapped and segregated in the grain boundaries, such that they do not effectively

generate free carriers. The number of dopant atoms inside the grains, where they are able to contribute free carriers, is reduced, and thus yields a higher resistivity. Second, the grain boundaries with many incomplete bonds can trap free carriers as well. Such trapping not only decreases the overall number of effective free carriers inside the grains, but also creates local potential barriers and depletion regions for the free carriers as shown in Figure 2.3.1. Hence the resistivity is further increased. Finally, the defects in the grain boundary lower the free carrier mobility and increase the resistivity.

As doping concentration increase, the boundaries are saturated with impurity atoms, and more dopant atoms stay inside the single crystal grains to generate a higher concentration of the free carriers. Moreover, a high concentration of the free carriers inside the grains reduces the depletion width significantly so that the free carriers are able to tunnel through, and the resistivity basically depends on the bulk crystal resistivity, which is usually very small for a high concentration doping. Hence, we can see a sharp transition region from a high resistivity region to a low resistively region as shown in Figure 2.3.2.

As we can find from Equation 2.1, the grain structure and size (L) have great effects on film resistivity. Films with larger grain sizes have proportionally smaller grain boundary densities, hence less resistivity deviation from that of bulk single-crystal silicon. Very small grains are easier to fully deplete such that the resistivity increases dramatically. The significant increase of resistivity in boron doped films as the film thickness decreases is due to the decrease of the grain sizes.

2.3.3 Temperature Coefficient of Resistivity

As we can see in Equation 2.1, the resistivity of doped polysilicon is a strong function of temperature. The temperature coefficient of resistivity (*TCR*) mainly depends on both dopant and doping concentration, as well as deposition and annealing temperature. The effect of the doping concentration is briefly discussed here and other effects can be founded from the literature [83, 84].

The temperature coefficient of resistivity is defined as

$$TCR \equiv \frac{1}{\rho_r} \frac{d\rho_r}{dT} \quad (2.2)$$

Figure 2.3.3 shows the *TCR* of boron-doped polysilicon as function of doping concentration.

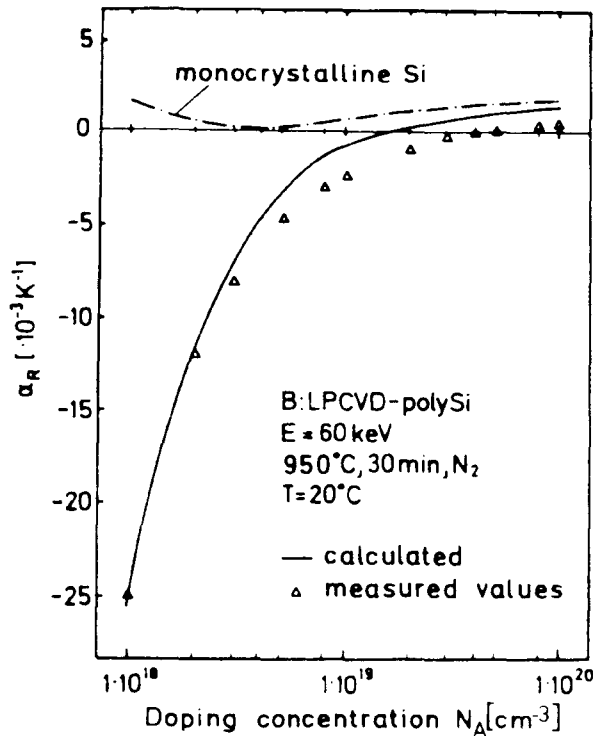


FIGURE 2.3.3 Temperature coefficient of resistance for boron-doped LPCVD [83] polysilicon for $T=20^\circ C$ as a function of doping concentration.

As we can see, there are three regions:

- (1) $TCR < 0$ (doping concentration $< 10^{19} \text{ cm}^{-3}$): The grains are fully (or partially) depleted, and the resistivity is dominated by the first term in Equation 2.1 so that we have

$$\rho_r = \frac{(2\pi n^* kT)^{1/2}}{Lq^2 p_o} \exp(\chi^{1/\eta} \delta^{1/\lambda}) \exp(qV_b / nkT) \quad (2.3)$$

Substitute Equation 2.3 into 2.3, we obtain

$$TCR = \frac{1}{2T} - \frac{qV_b}{nkT^2} = -\left(\frac{qV_b}{nkT} - \frac{1}{2}\right) \frac{1}{T} \quad (2.4)$$

Usually $\frac{qV_b}{nkT} > \frac{1}{2}$ and TCR is negative with relative larger magnitudes compared to boron-dope single crystal silicon.

- (2) $TCR > 0$ (doping concentration $< 10^{20} \text{ cm}^{-3}$): The doping is so heavy that degeneration happens and the film behaves like a metal film. The resistivity depends on the scattering effects at the grain boundaries and inside crystal grains. Such scattering effects increase with increasing temperature, hence the TCR is positive.

- (3) $TCR \approx 0$ (doping concentration somewhere close to $5 \times 10^{19} \text{ cm}^{-3}$): When the doping concentration is between 10^{19} and 10^{20} cm^{-3} , both terms in Equation 2.1 are of the same order of magnitude. The effects on both depletion and scattering exist but act in two opposite trends, and it is possible to cancel each other to give zero TCR around the doping concentration at $5 \times 10^{19} \text{ cm}^{-3}$.

As one can see in Figure 2.3.3, lowering doping concentration can increase the temperature sensitivity. But there are problems including nonlinearity, instability and noise if the doping concentration is too low ($<10^{18} \text{ cm}^{-3}$) [64, 83]. A tradeoff is usually needed in order to achieve the best performance. In the meantime, heavily boron doped polysilicon is often chosen as a sensing material because of its good linearity and stability. On the other hand, doping concentrations are chosen close to $5 \times 10^{19} \text{ cm}^{-3}$ for strain gauge material to minimize errors or noise caused by temperature fluctuations of the environment. This is essential to applications such as polysilicon strain gauges for pressure sensors, accelerometers, and shock sensors.

2.4 Polysilicon Thin Film Thermistors

Doped polysilicon has been widely used as a material for thermistors because of the temperature dependence of its resistivity [61-71, 83-84], which can be carefully calibrated using standard methods. General design, fabrication and calibration of polysilicon thin film thermistors are discussed in this section.

2.4.1 Design

Typical commercial temperature sensors such as thermocouples, resistive temperature detectors (RTD) are millimeter scale. Such individual sensors are very difficult to integrate with the microsystems that have sub-millimeter dimensions. Micromachining provides the technology to fabricate and integrate thin film polysilicon thermistors with microelectromechanical systems (MEMS).

As shown in Figure 2.4.1, polysilicon thermistors can be made from both heavily and lightly doped polysilicon thin films. The lightly doped sensor can be designed as small as a few microns square, which is suitable for the measurement of local temperatures. The zigzag shape of the heavily doped sensor can be arranged to cover a larger area, which is appropriate for the measurement of average temperatures over relatively large areas. In many cases, polysilicon sensors are passivated with a dielectric thin film such as nitride or oxide, and contact holes are opened to expose the heavily doped leads for metal ohmic contact (usually with Al). The resistance of the sensor is normally larger than a few hundreds ohms so that the resistance from contacts and leads can be ignored. In some special cases, such designs are used for both sensing and heating as well. Many physical parameters (heat transfer coefficient, flow velocity, fluid flow rate, etc.) are evaluated by measuring the sensor's temperature and power dissipation.

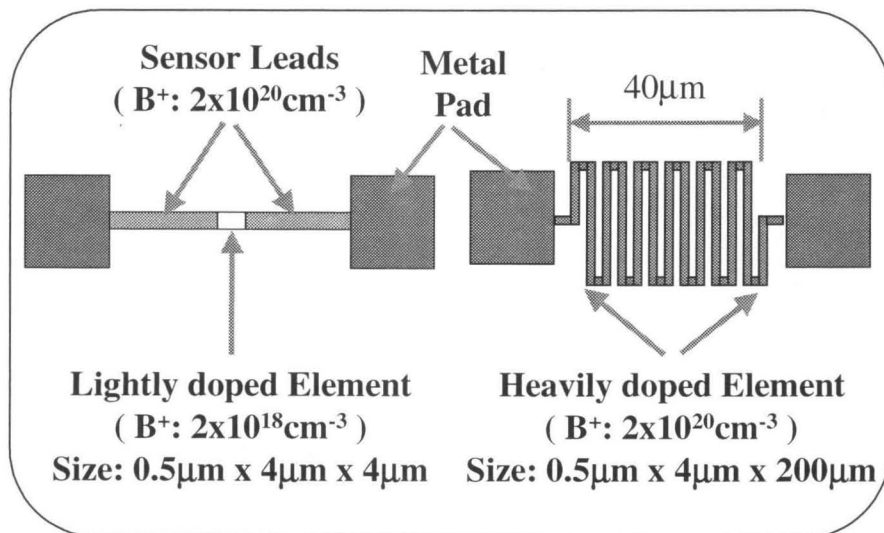


FIGURE 2.4.1 Designs of heavily and lightly doped polysilicon thin film thermistors.

Figure 2.4.2 shows two polysilicon thin film heaters for larger area uniform heating: (a) A heater formed by polysilicon thin film sheet ($0.5 \mu\text{m}$ thick), and (b) A

heater formed by many zigzag shaped polysilicon resistors in parallel. Heavily doped polysilicon ($2 \times 10^{20} \text{ cm}^{-3}$ for this work) is used to provide low resistance (50Ω) for the heaters so that a high thermal power is generated without using a very high voltage. The temperature variance across $1 \text{ cm} \times 1 \text{ cm}$ is demonstrated to be less than 0.1°C when the substrate is heated up to more than 80°C .

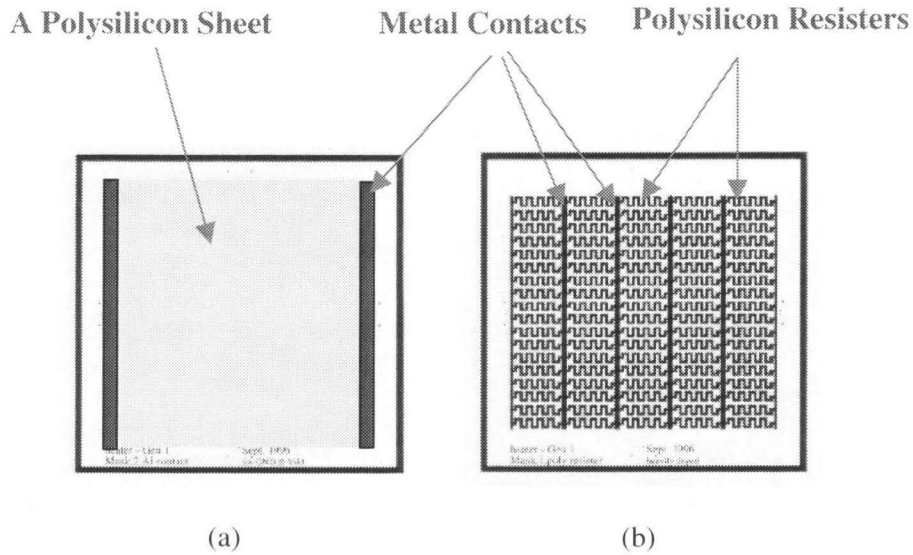


FIGURE 2.4.2 Mask design of polysilicon heaters (a) Polysilicon thin film sheet heater. (b) Parallel polysilicon resistor heater.

2.4.2 Fabrication

Figure 2.4.3 shows the typical fabrication process of a polysilicon thin-film sensor built on a silicon wafer. Starting from a bare silicon wafer, $0.5 \mu\text{m}$ thick thermal oxide is grown for electrical isolation and then $0.2 \mu\text{m}$ thick low stress LPCVD silicon nitride is deposited as a passivation layer. A $0.5 \mu\text{m}$ thick LPCVD polysilicon is deposited as the sensor material, then selectively doped with B^+ implantation followed by activation annealing at temperatures between 900 to 1100°C for 30 minutes. After patterning by

RIE, the sensor is protected by the deposition of another layer of 0.2 μm thick low stress LPCVD silicon nitride. Finally, the contact area is opened by dry etching such as reactive ion etching or plasma enhanced etching, and 1 μm thick Al is deposited and patterned to provide leads for the sensor.

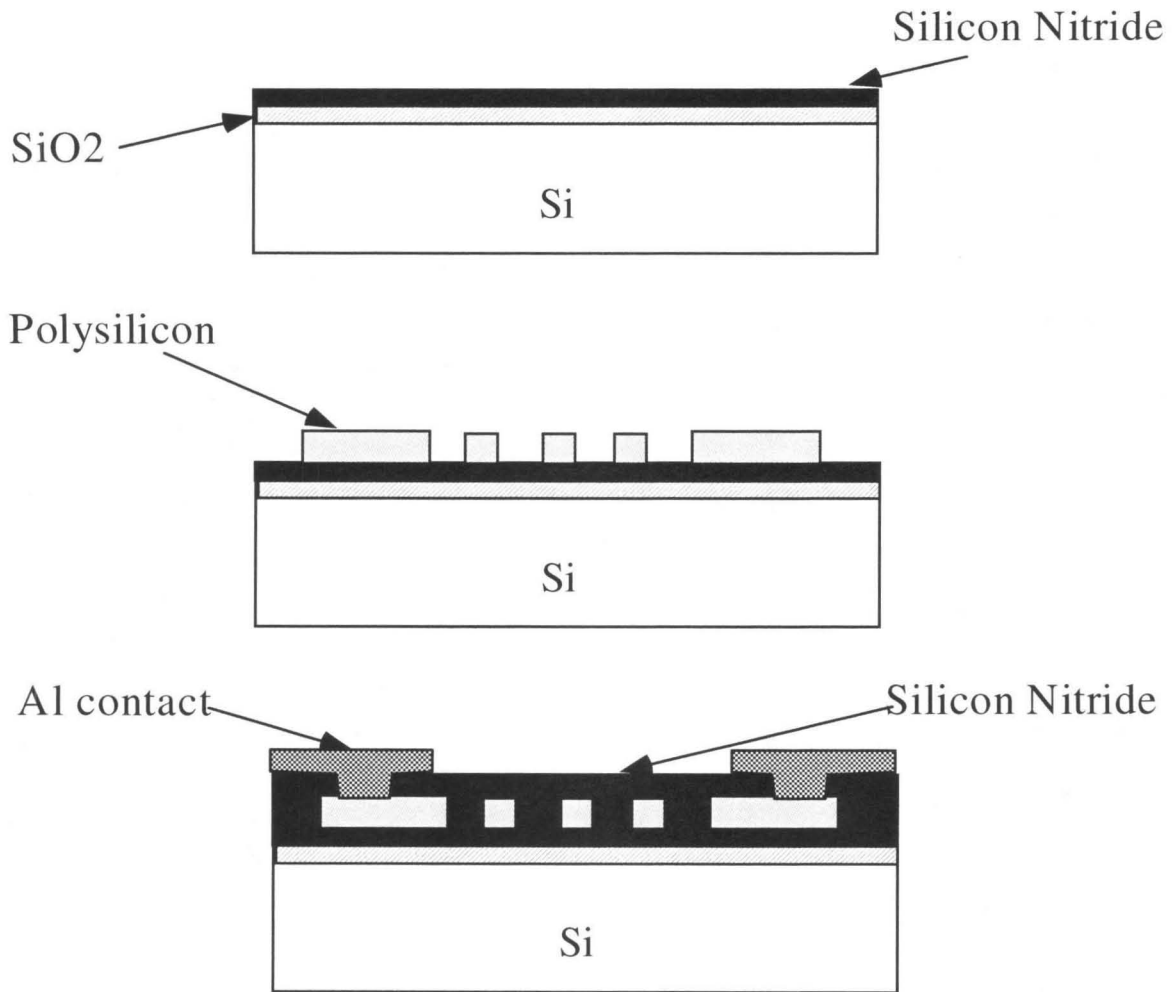


FIGURE 2.4.3 Process flow of a polysilicon thin-film thermistor.

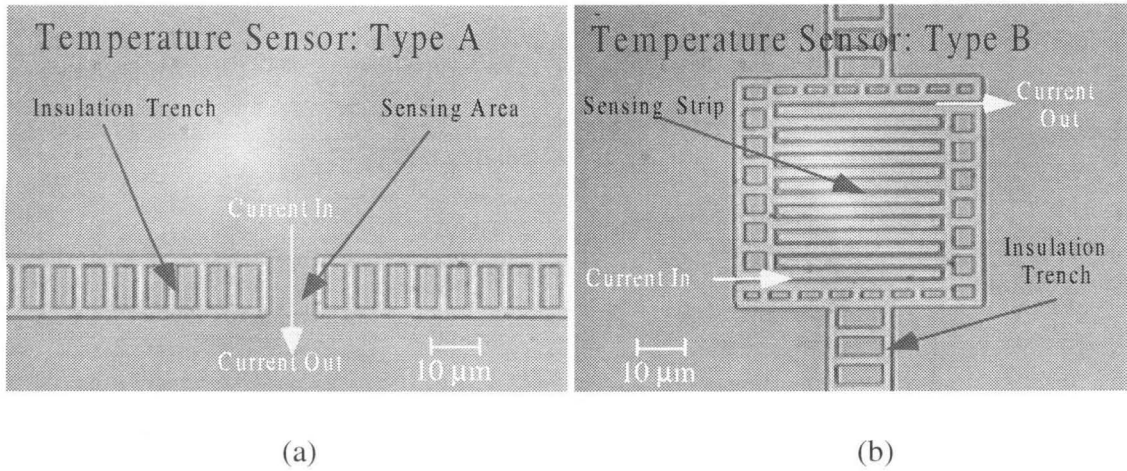


FIGURE 2.4.4 Pictures of fabricated polysilicon thermistors (a) The picture of sensor type A with a lightly boron-doped polysilicon sensing element. (b) The picture of sensor type B with a heavily boron-doped polysilicon sensing zigzag sensing strip.

2.4.3 Calibration

Polysilicon resistivity is usually measured by a four-point probe as shown in Figure 2.4.5. Four evenly spaced probes are brought into contact with the surface of a polysilicon sample, then a current I is passed through the outer two probes and potential V is measured between two inner probes. The resistivity of the polysilicon sample is calculated from

$$\rho = 4.53 \frac{V}{I} t \quad (s \gg t) \quad (2.5)$$

where s is the spacing and t is the film thickness [85].

Practically, test patterns of polysilicon films are often arranged on the wafers to monitor the quality and doping concentration of the film by measuring the resistivity of the samples. Figures 2.4.6 and 2.4.7 shows two typical test patterns used on a wafer.

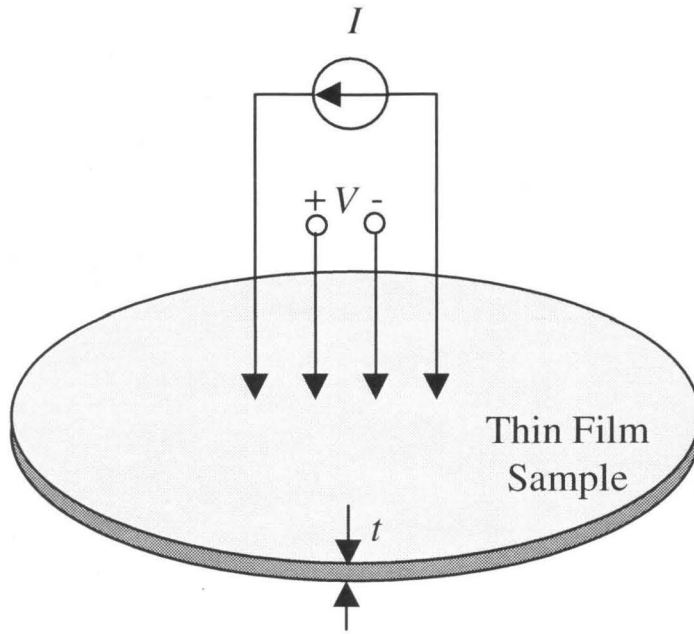


FIGURE 2.4.5 The illustration of the four-point probe method.

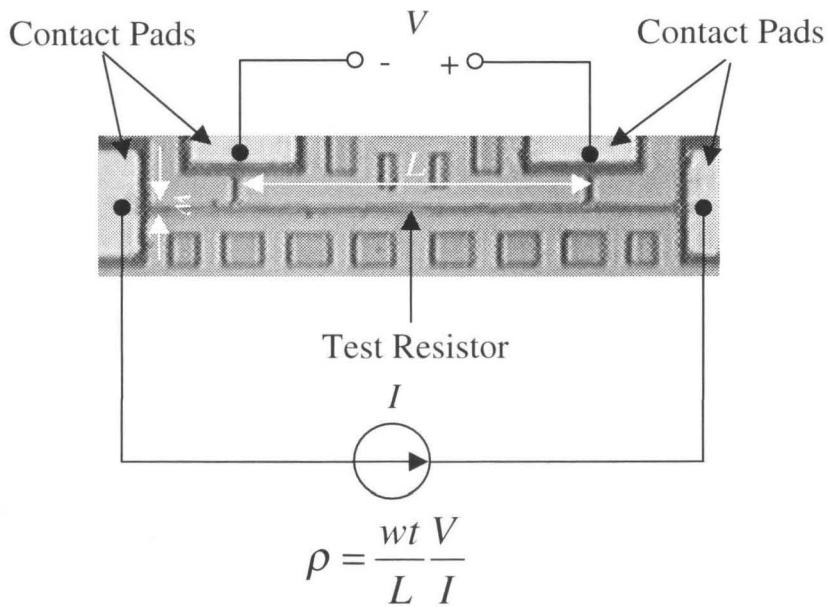
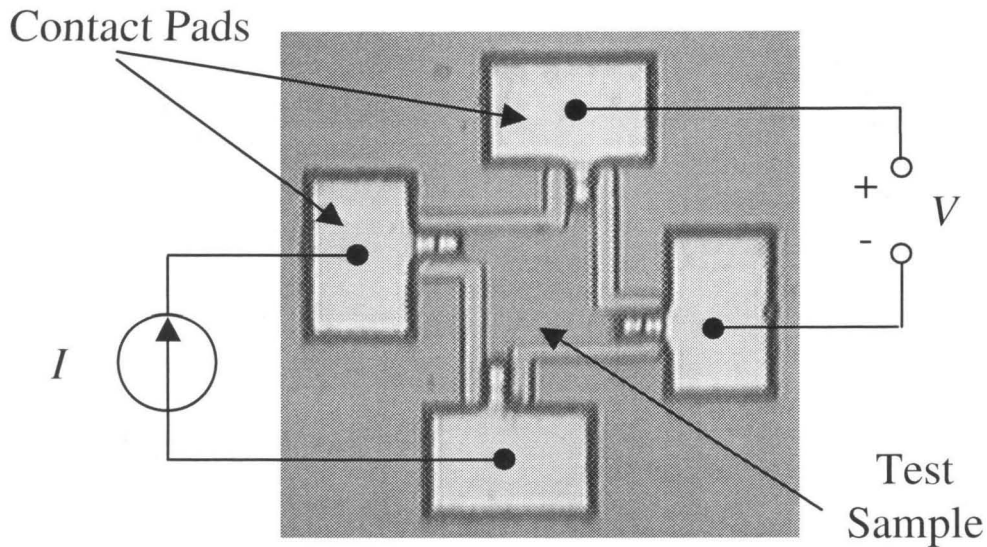


FIGURE 2.4.6 The picture of the four-contact method.



$$\rho = 4.53 \frac{V}{I} t$$

FIGURE 2.4.7 The picture of the Van der Pauw method with a symmetrical sample.

Figure 2.4.8 shows the temperature dependence of resistance and TCR measured from both lightly ($2 \times 10^{18} \text{ cm}^{-3}$) and heavily ($2 \times 10^{20} \text{ cm}^{-3}$) boron-doped polysilicon test samples. As we can see, the resistance of heavily boron-doped polysilicon is rather linear with temperature and the *TCR* is constant, while the resistance of lightly boron-doped polysilicon shows non-linear behavior with temperature and the *TCR* increases with the increasing temperature. More comprehensive data of the polysilicon fabricated at the Caltech Micromachining Laboratory are present in Figure 2.4.9 [86]. They are consistent with the results available from many published references [24,35-41, 83, and 84].

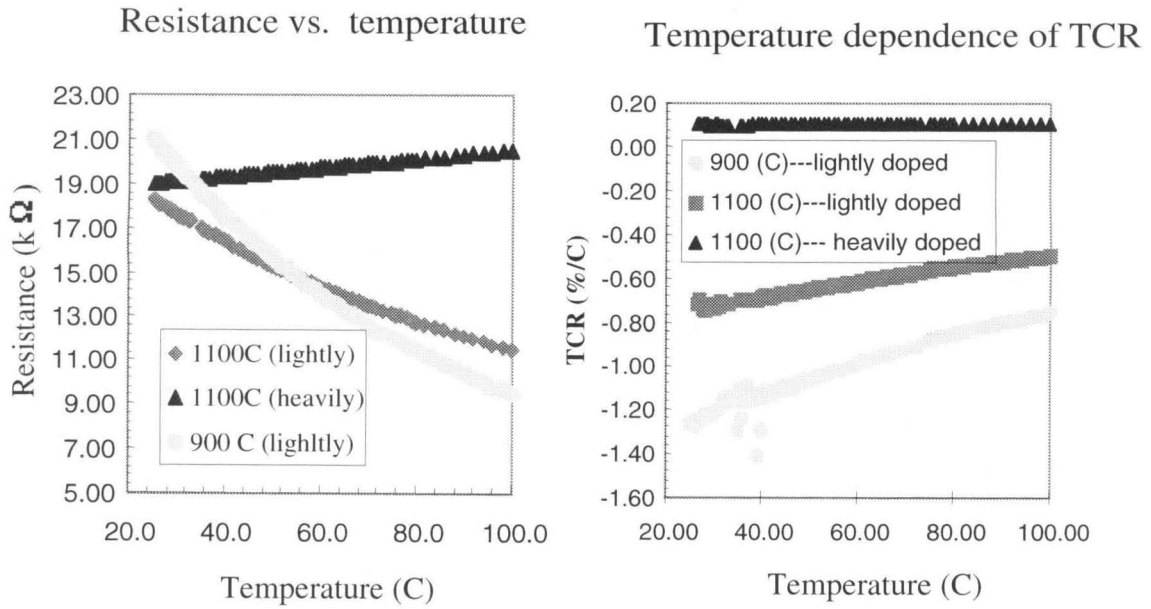


FIGURE 2.4.8 Temperature calibration of fabricated polysilicon thin-film thermistors.

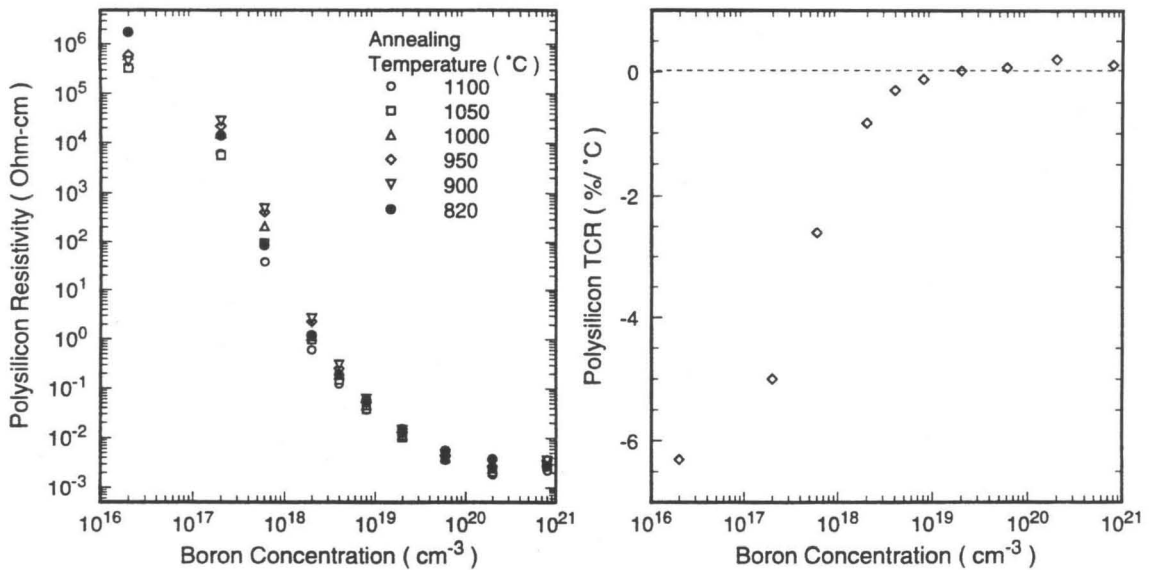


FIGURE 2.4.9 Polysilicon resistivity and temperature coefficient vs. doping concentration. The polysilicon thin film is fabricated and tested in the Caltech Micromachining Laboratory [86].

2.5 Summary

LPCVD Polysilicon has been widely used in both IC's and MEMS technology. It is deposited by thermal decomposition of silane in a low-pressure furnace. Its material and electrical properties mainly depend on deposition temperature, grain structure, dopant type and doping concentration. Lightly doped polysilicon has very large resistivity and large negative TCR, while heavily doped polysilicon exhibits very low resistivity with positive TCR. For general thermal sensor design, a small square sensing element made from lightly doped polysilicon can be used for local temperature measurement, and a zigzag heavily doped polysilicon strip can be designed for sensing average temperature covering a relatively large area. Finally, boron-doped polysilicon thin films fabricated in the Caltech Micromachining Laboratory have been tested and the results agree with published data.

References:

- [1] T. Kamins, "Polysilicon for integrated circuits and displays," *Kluwer, Boston*, 1998.
- [2] P. R. Gray and R. G. Meyer, "Analysis and Design of Analog Integrated Circuit,"
New York: Wiley, 1997, ch. 2.
- [3] H. Ohshima and Y. Matsueda, "Poly-si TFT and driver integration technology,"
ELECTRONICS AND COMMUNICATIONS IN JAPAN PART II-ELECTRONICS, 77:
(7) 46-55, Jul. 1994
- [4] S. D. Brotherton, "Polycrystalline silicon thin film transistors," *SEMICONDUCTOR
SCIENCE AND TECHNOLOGY*, 10: (6) 721-738, Jun. 1995.
- [5] N. Yamauchi and R. Reif, "Polycrystalline silicon thin films processed with ion
implantation and subsequent solid-phase crystallization: Theory, experiments, and
thin-film transistor applications," *J. Appl. Phys.* 75(7), 1, April 1994.
- [6] K. Y. Choi and M. K. Han, "A novel gate-overlapped LDD poly-si thin-film
transistor," *IEEE ELECTRON DEVICE LETTERS*, 17: (12) 566-568, Dec. 1996.
- [7] D. N. Kouvatso, A. T. Voutsas, and M. K. Hatalis, "High-performance thin-film
transistors in large grain size polysilicon deposited by thermal decomposition of
disilane," *IEEE TRANSACTIONS ON ELECTRON DEVICES*, 43: (9) 1399-1406,
Sep. 1996.
- [8] K. H. Lee, J. K. Park, and J. Jang, "A high-performance polycrystalline silicon thin
film transistor with a silicon nitride gate insulator," *IEEE TRANSACTIONS ON
ELECTRON DEVICES*, 45: (12) 2548-2551, Dec. 1998.

- [9] M. A. M. Shaltout, A. A. El-Hadad, M. A. Fadly, A. F. Hassan, and A. M. Mahrous, "Determination of suitable types of solar cells for optimal outdoor performance in desert climate," *RENEWABLE ENERGY*, 19: (1-2) 71-74, Jan.-Feb. 2000.
- [10] M. Ohashi, Y Iida, and S. Wada, "Mullite-based substrates for polycrystalline silicon thin-film solar cells," *Journal of the Ceramic Society of Japan*, 108: (1) 105-107, Jan. 2000.
- [11] H Morikawa, Y. Nishimoto, H. Naomoto, Y. Kawama, A. Takami, S. Arimoto, T. Ishihara, and K. Namba, "16.0% efficiency of large area (10 cm x 10 cm) thin film polycrystalline silicon solar cell," *SOLAR ENERGY MATERIALS AND SOLAR CELLS*, 53: (1-2) 23-28, May 1998.
- [12] T. Machida, A. Miyazawa, M. Nishida, Y. Yokosawa, H. Nakaya, S. Tanaka, S. Moriuchi, and T. Nunoi, "Efficiency improvement in polycrystalline silicon solar cells and development of basic technologies for large scale mass production," *SHARP TECHNICAL JOURNAL*, (63) 26-29, Dec. 1995.
- [13] M. A. C. Wais, "The potential attractiveness and efficiency of amorphous-silicon solar-cells as compared with polycrystalline silicon solar-cells," *RENEWABLE ENERGY*, 6: (5-6) 579-587, Jul.-Sep. 1995.
- [14] C. A. Dimitriadis, "Effect of doping concentration on the performance of large-grain polycrystalline silicon solar-cell," *JOURNAL OF APPLIED PHYSICS*, 59: (6) 2259-2261, Mar. 15, 1986.
- [15] T. A. Badgwell, T. F. Edgar, I. Trachtenberg, and J. K. Elliott, "Experimental-verification of a fundamental model for multiwafer low-pressure chemical vapor-

- deposition of polysilicon,” *JOURNAL OF THE ELECTROCHEMICAL SOCIETY*, 139: (2) 524-532, Feb. 1992.
- [16] H. Kuhne, “On the chemical-reaction mode of polysilicon deposition from silane,” *CRYSTAL RESEARCH AND TECHNOLOGY*, 28: (1) 39-52 1993.
- [17] C. Azzaro, P. Duverneuil, and J. P. Couderc, “Comments on the influence of the entrance zone in lpevd reactors for insitu phosphorus-doped polysilicon deposition,” *CHEMICAL ENGINEERING SCIENCE*, 48: (10) 1915-1922, May 1993.
- [18] A. J. Toprac, T. F. Edgar, and I. Trachtenberg, “Modeling of gas-phase chemistry in the chemical-vapor-deposition of polysilicon in a cold-wall system,” *JOURNAL OF THE ELECTROCHEMICAL SOCIETY*, 140: (6) 1809-1813, Jun. 1993.
- [19] G. Depinto, “Optimizing polysilicon deposition for film uniformity and particles,” *JOURNAL OF THE IES*, 36: (4) 31-38, Jul.-Aug. 1993.
- [20] E. Ibok and S. Garg, “A characterization of the effect of deposition temperature on polysilicon properties - morphology, dopability, etchability, and polycide properties,” *JOURNAL OF THE ELECTROCHEMICAL SOCIETY*, 140: (10) 2927-2937, Oct. 1993
- [21] W. Ahmed, E. Ahmed, and M. L. Hitchman, “An overview of the deposition chemistry and the properties of in-situ doped polysilicon prepared by low-pressure chemical-vapor-deposition,” *JOURNAL OF MATERIALS SCIENCE*, 30: (16) 4115-4124, Aug. 15, 1995.
- [22] A. Theodoropoulou, R. A. Adomaitis, and E. Zafiriou, “Model reduction for optimization of rapid thermal chemical vapor deposition systems,” *IEEE*

TRANSACTIONS ON SEMICONDUCTOR MANUFACTURING, 11: (1) 85-98, Feb. 1998.

- [23] H. Lim, S. S. Kim, and K. S. Chung, "Influence of polysilicon deposition conditions on the characteristics of oxide-nitride-oxide memory capacitors," *JOURNAL OF THE KOREAN PHYSICAL SOCIETY*, 33: (4) 501-506, Oct. 1998.
- [24] F. S. Becker, H. Oppolzer, I. Weitzel, Eichermuller, and H. Schaber, "Low resistance polycrystalline silicon by boron or arsenic implantation and thermal crystallization of amorphously deposited films.
- [25] A. Tounsi, E. Scheid, C. Azzaro, P. Duverneuil, and J. P. Couderc, "Elaboration of in-situ phosphorus-doped polysilicon films under LPCVD conditions - process modeling and characterization," *JOURNAL DE PHYSIQUE IV*, 3: (C3) 123-130, Aug. 1993.
- [26] C. M. Ransom, T. N. Jackson, J. F. Degelormo, D. Kotecki, C. Graitmann, and D. K. Sadana, "Arsenic gas-phase doping of polysilicon," *JOURNAL OF VACUUM SCIENCE & TECHNOLOGY B*, 12: (3) 1390-1393, May-Jun. 1994.
- [27] G. Fresquet, C. Azzaro, and J. P. Couderc, "Analysis and modeling of in-situ boron-doped polysilicon deposition by LPCVD," *JOURNAL OF THE ELECTROCHEMICAL SOCIETY*, 142: (2) 538-547 FEB 1995
- [28] P. Kwizera and R. Reif, "Annealing Behavior of thin polycrystalline silicon film damage by silicon ion implantation in the critical amorphization range," *Thin Solid Films*, 100 (1983) 227-233.
- [29] K. Nakazawa, "Recrystallization of amorphous films deposited by low-pressure chemical vapor deposition from Si₂H₆ gas," *J. Phys.* 69 (3), 1 February 1991.

- [30] S. Hasegawa, S. Sakamoto, T. Inokuma, and Y. Kurata, "Structure of recrystallized silicon film prepared from amorphous silicon deposited using disilane," *Appl. Phys. Lett.* 62 (11), 15 March 1993.
- [31] R. Ruther, J. Livingstone, and N. Dytlewski, "Large-grain polycrystalline silicon thin film obtained by low-temperature stepwise annealing of hydrogenated amorphous silicon," *Thin Solid Films*, 310 (1997) 67-74.
- [32] J. P. Guilemet, B. de Mauduit, B. Pieraggi, D. Bielle-Daspert, and E. Scheid, "Crystallization of amorphous thin LPCVD Si films: "in situ" TEM measurement of nucleation and grain growth rates," *Materials Science and Engineering*, A173 (1993) 379-382.
- [33] D. K. Sohn, J. N. Lee, S. W. Kang, and B. T. Ahn, "Low-temperature crystallization of amorphous Si films by metal adsorption and diffusion," *Jpn. J. Appl. Phys.*, vol. 35 (1996) Pt. 1, No. 2B.
- [34] Z. G. Meng, M. X. Wang, and M. Wong, "High performance low temperature metal-induced unilaterally crystallized polycrystalline silicon thin film transistors for system-on-panel applications," *IEEE Transactions on Electron Devices*, 47: (2) 404-409, Feb. 2000.
- [35] J. Y. W. Seto, "The electrical properties of polycrystalline silicon films," *J. Appl. Phys.*, vol. 46, No. 12, pp. 5247-5254, Dec. 1975.
- [36] M. M. Mandurah, K. C. Saraswat, and T. I. Kamins, "A model for conduction in polycrystalline silicon," *IEEE Transactions on Electron Devices*, 28: (10) 1163-1176, Oct. 1981.

- [37] N. C. C. Lu, L. Gerzberg, C. Y. Lu, and J. D. Meindl, "A conduction model for semiconductor-grain-boundary barriers in polycrystalline-silicon films," *IEEE Transactions on Electron Devices*, 30: (2) 137-149, Feb. 1983.
- [38] D. P. Joshi and R. S. Srivastava, "A model of electrical conduction in polycrystalline silicon," *IEEE Transactions on Electron Devices*, 31: (7) 1163-1176, July 1984.
- [39] N. C. C. Lu, C. Y. Lu, M. K. Lee, C. C. Shih, C. S. Wang, W. Reuter, and T. T. Sheng, "The effect of film thickness on the electrical properties of LPCVD polysilicon films," *J. Electromecham. Soc.: Solid-State Science and Technology*, Vol. 131, No. 4, pp. 897-901.
- [40] G. Harbeke, L. Krausbauer, E. F. Steigmeier, A. E. Widmer, H. F. Kappert, and G. Neugebauer, "Growth and physical properties of LPCVD Polycrystalline Silicon Films," *J. Electromecham. Soc.: Solid-State Science and Technology*, vol. 131, No. 3, pp. 675-681.
- [41] S. N. Singh, R. Kishore, and P. K. Singh, "Thermionic emission diffusion model of current conduction in polycrystalline silicon and temperature dependence of mobility," *J. Appl. Phys.*, vol. 57, No. 8, pp. 2793-2801, 15 April 1985.
- [42] K. Kato, T. Ono, and Y. Amemiya, "Electrical trimming of polycrystalline silicon resistors and its application to analog IC's," *IEEE Trans. Electron Devices*, vol. ED-27, pp. 2194, Nov. 1980.
- [43] W. A. Lane and G. T. W., "The design of thin-film polysilicon resistors for analog IC applications," *IEEE Trans. Electron Devices*, vol. ED-36, pp. 738, April 1980.

- [44] P. X. Ma, L. C. Zhang, B. Y. Zhao, and Y. Y. wang, "An analytical model for determining carrier transport mechanism of polysilicon emitter bipolar-transistors," *IEEE TRANSACTIONS ON ELECTRON DEVICES*, 42: (10) 1789-1797, Oct. 1995.
- [45] C. M. Park and M. K. Han, "Fabrication of the buried channel polycrystalline silicon TFT," *SOLID-STATE ELECTRONICS*, 43: (9) 1785-1789, Sep. 1999.
- [46] S. I. Jun, Y. H. Yang, J. B. Lee, and D. K. Choi, "Electrical characteristics of thin-film transistors using field-aided lateral crystallization," *APPLIED PHYSICS LETTERS*, 75: (15) 2235-2237, Oct. 11, 1999.
- [47] J. M. Bustillo, R. T. Howe and R. S. Muller, "Surface micromachining for microelectromechanical systems," *P IEEE* 86: (8) 1552-1574, Aug. 1998.
- [48] R. T. Howe and R. S. Muller, "Polycrystalline silicon micromechanical structure beams," *J. Electrochem. Soc.* 130, 1420-1423 (1983).
- [49] L. S. Fan, Y. C. Tai, and R. S. Muller, "Integrated Movable Micromachanical Structures for sensors and actuators," *IEEE Trans. Electron Devices*, Vol. 35, No. 6, pp. 724-730, June 1988.
- [50] L. S. Fan, Y. C. Tai, and R. S. Muller, "IC-processed electrostatic micromotor," *Technical Digest, IEDM*, pp. 666-669, 1988.
- [51] W. C. Tang, T. C. H. Nguyen, and R.T. How, "Laterally driven for polysilicon resonate microstructures," *Sensor and Actuators*, vol. 20, pp. 25-32, 1989.
- [52] C. J. Kim, A. P. Pisano, R. S. Muller, and M. G. Lim, "Polysilicon microgripper," *SENSORS AND ACTUATORS A-PHYSICAL*, 33: (3) 221-227, Jun. 1992.

- [53] R. S. Hijab and R. S. Muller, "Micromechanical thin-film cavity structures for low pressure and acoustic transducer application," *Transducers 85 Digest of Technical Papers*, June 1985, Philadelphia, USA, pp. 178-181.
- [54] H. Guckel, "Surface micromachined pressure transducers," *SENSORS AND ACTUATORS A-PHYSICAL*, 28: (2) 133-146, Jul. 1991.
- [55] W. P. Eaton and J. H. Smith, "Micromachined pressure sensors: Review and recent developments," *SMART MATERIALS & STRUCTURES*, 6: (5) 530-539, Oct. 1997.
- [56] D. W. Burns, J. D. Zook, R. D. Horning, W. R. Herb, and H. Guckel, "Sealed-cavity resonant microbeam pressure sensor," *SENSORS AND ACTUATORS A-PHYSICAL*, 48: (3) 179-186, May 30, 1995.
- [57] D. W. Burns, J. D. Zook, R. D. Horning, W. R. Herb, and H. Guckel, "Sealed-cavity resonant microbeam accelerometer," *SENSORS AND ACTUATORS A-PHYSICAL*, 53: (1-3) 249-255, May 1996.
- [58] R. T. Howe, B. E. Boser, and A. P. Pisano, "Polysilicon integrated microsystems: Technologies and applications," *SENSORS AND ACTUATORS A-PHYSICAL*, 56: (1-2) 167-177, Aug. 1996.
- [59] S. M. Sze, "Semiconductor sensors," *John Wiley & Sons, Inc.*, 1994.
- [60] K. S. Udell, A. P. Pisano, R. T. Howe, R. S. Muller, and R. M. White, "Microsensors for heat-transfer and fluid-flow measurements," *EXPERIMENTAL THERMAL AND FLUID SCIENCE*, 3: (1) 52-59, Jan. 1990.
- [61] C. M. Ho and Y. C. Tai, "Micro-electro-mechanical-systems (MEMS) and fluid flows," *ANNUAL REVIEW OF FLUID MECHANICS*, 30: 579-612 1998.

- [62] C. M. Ho and Y. C. Tai, "Review: MEMS and its applications for flow control," *JOURNAL OF FLUIDS ENGINEERING-TRANSACTIONS OF THE ASME*, 118: (3) 437-447, Sep. 1996.
- [63] N. T. Nguyen, "Micromachined flow sensors - a review," *FLOW MEASUREMENT AND INSTRUMENTATION*, 8: (1) 7-16, Mar 1997.
- [64] Y. C. Tai and R. S. Muller, "Lightly-doped polysilicon bridge as a flow meter," *SENSORS AND ACTUATORS*, 15: (1) 63-75, Sep. 1988
- [65] F. Jiang, Y. C. Tai, C. H. Ho, and W. J. Li. "A Micromachined Polysilicon Hot-Wire Anemometer," *Solid-State Sensor and Actuator Workshop*, Hilton Head, SC, pp. 264-267, 1994.
- [66] F. Jiang, Y. C. Tai, B. Gupta, R. Goodman, S. Tung, and C. H. Ho, "A Micromachined Shear Stress Imager," *MEMS-96*, San Diego, pp. 110-115, 1996.
- [67] N. T. Nguyen and R. Kiehnscherf "Low-cost silicon sensors for mass-flow measurement of liquids and gases," *SENSORS AND ACTUATORS A-PHYSICAL*, 49: (1-2) 17-20, Jun. 1995.
- [68] S. Wu, Q. Lin, Y. Yuen, and Y.C. Tai, "MEMS flow sensors for nano-fluidic applications," in *Proc. of The Thirteenth IEEE International Conference on Micro Electro Mechanical Systems (MEMS2000)*, Miyazaki, Japan, Jan. 23-27, 2000.
- [69] L. Jiang, M. Wang, and Y. Zohar, "A micro-channel heat sink with integrated temperature sensors for phase transition study," *Proc. 12th Annual International Workshop on Micro Electro Mechanical System*, pp. 159-164, January 17-21, 1999, Orlando, Florida.

- [70] S. Wu, J. Mai, Y. Zohar, Y. C. Tai, and C.M. Ho, "A suspended microchannel with integrated temperature sensors for high-pressure flow studies," in *Proc. of The Eleventh IEEE International Micro Electro Mechanical System (MEMS '98)*, Heideberg, Germany, pp. 87-92, Jan. 25-29, 1998.
- [71] S. Wu, J. Mai, Y.C. Tai, and C.M. Ho, "Micro Heat Exchanger by Using MEMS Impinging Jets," *Proc. 12th Annual International Workshop on Micro Electro Mechanical System*, pp. 171-176, Jan. 17-21, 1999, Orlando, Florida.
- [72] G. Harbeke, L. Krausbauer, E. F. Steigmeier, A. E. Widmer, H. F. Kappert, and G. Neugebauer, "Growth and physical-properties of lpcvd polycrystalline silicon films," *JOURNAL OF THE ELECTROCHEMICAL SOCIETY*, 131: (3) 675-682, 1984.
- [73] G. Harbeke, L. Krausbauer, E. F. Steigmeier, A. E. Widmer, H. F. Kappert, and G. Neugebauer, "LPCVD polycrystalline silicon - growth and physical-properties of insitu phosphorus doped and undoped films," *RCA REVIEW*, 44: (2) 287-312, 1983.
- [74] S. Wolf and R. N. Tauber, "Silicon processing for the VLSI era," Vol. 1, Chapter 6, *Sunset Beach, CA.: Lattice Press*, c1986.
- [75] S. Hasegawa, M. Morita, and Y. Kurata, "Structural and electrical-properties of p-doped and b-doped polycrystalline silicon by plasma-enhanced CVD at 700-degrees-C," *JAPANESE JOURNAL OF APPLIED PHYSICS PART 2-LETTERS*, 28: (4) L522-L524, Apr. 1989.
- [76] W. A. Turner, and G. Lucovsky, "Electrical-properties of microcrystalline silicon prepared by reactive magnetron sputtering from crystalline silicon targets," *JOURNAL OF NON-CRYSTALLINE SOLIDS*, 166: 997-1000, Part 2, Dec. 1993.

- [77] Z. Sun, K. Y. Tong, and W. B. Lee, "Properties of furnace crystallized polysilicon films prepared by rf sputtering," *THIN SOLID FILMS*, 288: (1-2) 224-228, Nov. 15, 1996.
- [78] S. M. Sze, "VLSI Technology," 2nd Edition, McGraw-Hill publishing Company, 1988.
- [79] W. R. Runyan and K. E. Bean, "Semiconductor Integrated Circuit Processing Technology," Addison –Wesley Publishing Company, Inc., 1990.
- [80] B. S. Meyerson and W. Olbricht, "Phosphorus-doped poly-Si via LPCVD," *J. Electrochem. Soc.* 131, 2361 (Oct. 1984).
- [81] Y. C. Tai, "IC-Processed polysilicon micromechanics: technology, materials and devices," *Ph.D. Thesis*, University of California, Berkeley (1989).
- [82] K. E. Petersen, "Silicon as a mechanical material," *Proceeding of the IEEE*, vol. No. 5, pp. 420-457, May, 1982.
- [83] E. Obermeier and P. Kopystynski, "Polysilicon as a material for microsensor applications," *Sensors and Actuators A*, 30 (1992) 149-155.
- [84] S. Marco, O. Ruiz, J. Samitier, and J. R. Morante, "Relation between electrical conductivity and structural characteristics in boron-doped LPCVD polycrystalline silicon used in sensor devices," *Sensors and Actuators A*, 37-38 (1993) 68-73.
- [85] A. Bar-Lev, "Semiconductor and electronic devices," 3rd edition, Prentice Hall, 1993.
- [86] J. Q. Liu, "Integrated micro devices for small scale gaseous low study," *Ph.D. Thesis*, Electrical Engineering Department, California Institute of Technology, 1994.

CHAPTER 3

MEMS IMPINGING-JET COOLING STUDY WITH TEMPERATURE IMAGERS

3.1 Introduction

3.1.1 Background

The rapid development of very large scale integrated (VLSI) circuit technology has revolutionized the electronic industry by continuously increasing the density and operating speed of microelectronic devices. Now, state-of-the-art IC technology achieves feature sizes smaller than 0.2 micrometers and allows millions of transistors to be fabricated on a single IC chip. For example, an Intel Pentium III chip has about 20 million transistors and a clock rate up to 1GHz. In fact, under the strong demands of information technology, the trend of fabricating faster ICs with higher transistor density has been predicted to continue for another two decades. While the challenges in microfabrication absorbed much of the attention in manufacture of high-performance IC

chips, thermal management for IC packages has also appeared as an important problem that needs to be solved. For instance, for the Intel Pentium III, an extra fan cooling system with a huge size and weight compared to the chip itself is required to keep chip temperature below the threshold (normally at 75°C) allowed for normal operation of transistors. Although the power supply of Intel Pentium III has been lowered to 2.5 V, the maximum power dissipation can be up to 34.5 W with a maximum local power density of 36.4 W/cm² [33]. Moreover, projections from current trends suggest that power dissipation increases with the increases in the number and speed of transistors, and can reach a density up to 100 W/cm². Hence, it can be foreseen that chip cooling will be the bottleneck for the next generation of personal computers. It is apparent that highly efficient, reliable and low-cost cooling systems need to be developed in order to meet the requirements of rapid IC technology development.

3.1.2 Overview of Previous Work

Heat transfer in electronic equipment cooling may be categorized as being based on natural convection, forced convection, and heat transfer with phase change (these basic heat transfer concepts are explained in 3.2.1).

In the natural convection approach, heat-dissipating components are mounted on a PCB plate and heat is transferred to the coolant by natural convection, to the plate by conduction, as well as to the surroundings by radiation. In most cases, the majority of heat is dissipated by natural convection due to the poor thermal conductivity of the PCB plate and extremely small amount of radiation at the chip operation temperature. In order to increase the surface area of free convection, fin arrays (as shown in Figure 3.1.1) made

from a thermally conductive material are widely used for cooling electronic components [4].

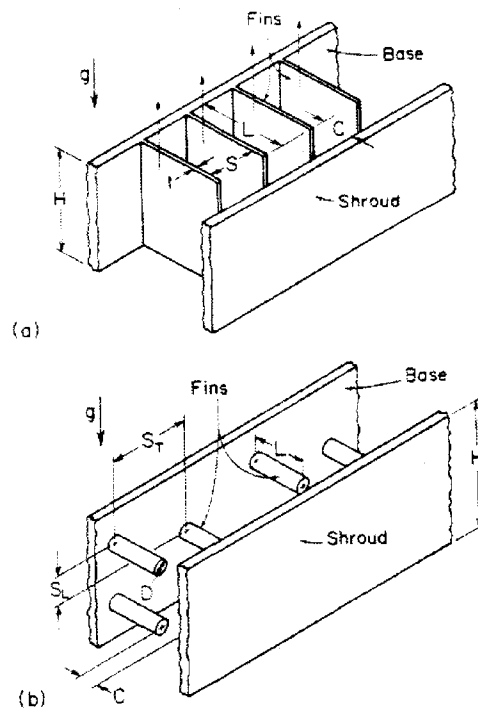


FIGURE 3.1.1 Shrouded (a) plate and (b) pin fin arrays [4].

In the forced convection approach, a coolant is driven by a pressure generated by external means, such as a fan or a pump. The heat transfer coefficient is much higher than that of natural convection due to the higher kinetic motion of the coolant. Multi-chip thermal modules with fins are also used to enhance the convection between the electronic components and the coolant.

As examples, two air-cooled multi-chip modules are shown in Figure 3.1.2. In the Hitachi silicon-carbide module [11], heat is transferred from each chip through solder posts to a silicon circuit board, and through a high-thermal-conductivity gold eutectic bond layer to a SiC heat spreader and then to an aluminum heat sink with longitudinal

fins. The heat is finally removed by the forced flow of air. In the IBM 4381 module [12], chips are attached to a multi-layer ceramic by solder posts and to a ceramic cap through a layer of thermal grease. Most of the heat generated by the chips is transferred to the ceramic cap directly through the grease or indirectly through the solder bumps and the substrate. The aluminum heat sink consists of an array of hollow pin fins, which are cooled by air jet impingement. Compared to the Hitachi module, the IBM module is more effective for heat removal due to the use of high-velocity impinging air jets.

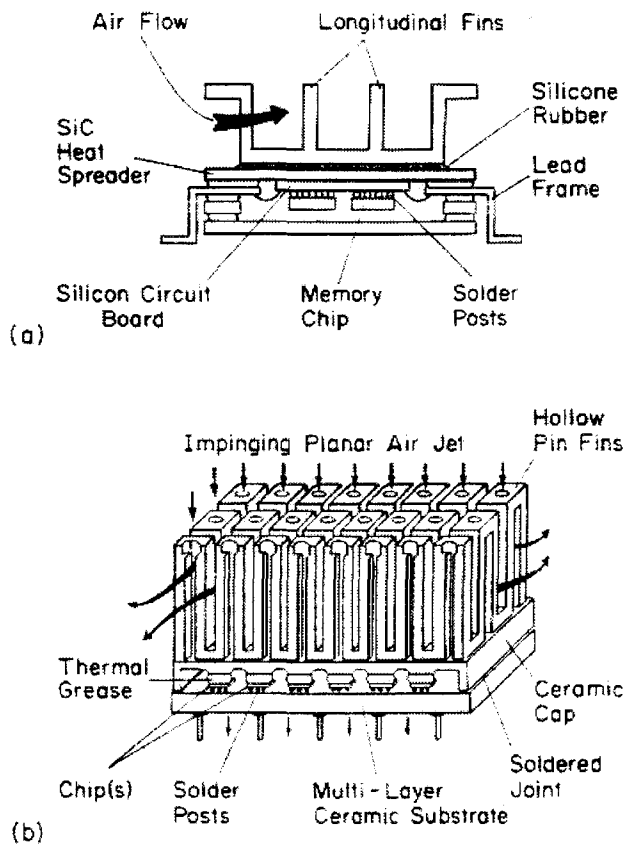


FIGURE 3.1.2 Air-cooled, multichip modules: (a) Hitachi silicon carbide module [11], (b) IBM 4381 jet impingement module [12].

Cooling effectiveness can be further enhanced by a heat sink incorporated directly into an integrated circuit [13], which is shown in the Figure 3.1.3. Using silicon anisotropic wet etching, microchannels were fabricated on the IC substrate. The heat generated by an individual electronic device is directly removed away by the coolant through these channels in the substrate. Because of high thermal capacity of the water and short thermal path, the heat transfer coefficient is more than one order of magnitude higher than previous two air modules.

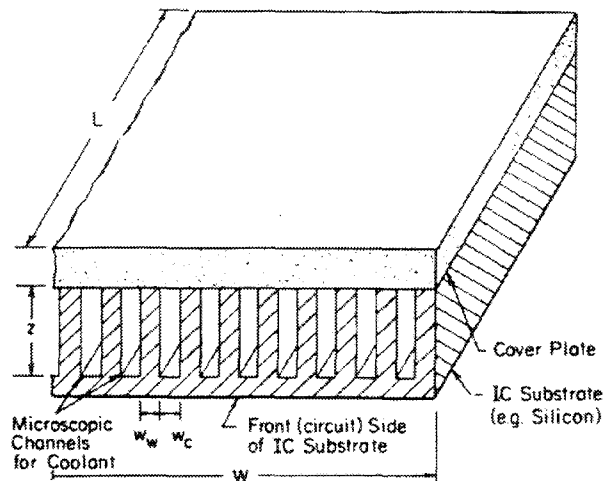


FIGURE 3.1.3 Schematic view of the compact heat sink incorporated into an integrated circuit chip [13].

Cooling efficiency can be even higher with techniques that are based on heat transfer with phase change, since a large amount of heat is taken away by coolant evaporation. In pool boiling heat transfer, a chip surface alteration is applied to reduce or eliminate the temperature overshooting for chemically inert coolant. Such surface alteration includes laser-drilled holes at the chip surface, sandblast/KOH treatment,

electrolytic deposition, and porous metallic coating or even a copper stud attached to the surface. In **forced convection boiling**, both boiling and convection (such as impingement, channel flow, and film falling) contribute to cooling and is extremely effective. A critical heat flux (CHF) achieved can be up to 100 W/cm^2 and temperature overshoots were observed to be negligible [14]. A **two-phase thermosyphon** with complete encapsulation has been used for high power components and airborne electronic packaging [15, 16], as well as densely populated PCBs and chip arrays [17, 18]. Usually, it creates saturated or subcooled boiling at the surfaces of the electronic components and condensation within the liquid and/or at an encapsulated cold plate.

As shown in Figure 3.2.4, Simons [19] summarizes the range of heat transfer coefficients of different cooling methods with various coolants. This data is consistent with Table 3.1 [4]. As we can see, **natural convection** is the simplest thermal management approach, but the corresponding heat transfer coefficients are the lowest. In particular, the heat transfer coefficient of natural convection by air is only 0.0002 to $0.0025 \text{ W/cm}^2\text{K}$, and is suitable only for the packaging of discrete electronic devices with low power dissipation. Heat transfer with phase change (i.e., boiling or condensation) is the most complicated despite being the most effective cooling method with heat transfer coefficient as high as $10 \text{ W/cm}^2\text{K}$. It is usually designed for high power components and densely populated chip arrays with extremely high power dissipation. Forced convection by air is the most common approach for thermal management. The heat transfer coefficient is in the range of 0.0025 to $0.025 \text{ W/cm}^2\text{K}$. Many CPUs and PC boards of computers are cooled by this approach with fan blowers and metal heat sinks. Carefully

designed forced convection thermal packaging may have a good balance between the structural complexity and heat removal capability.

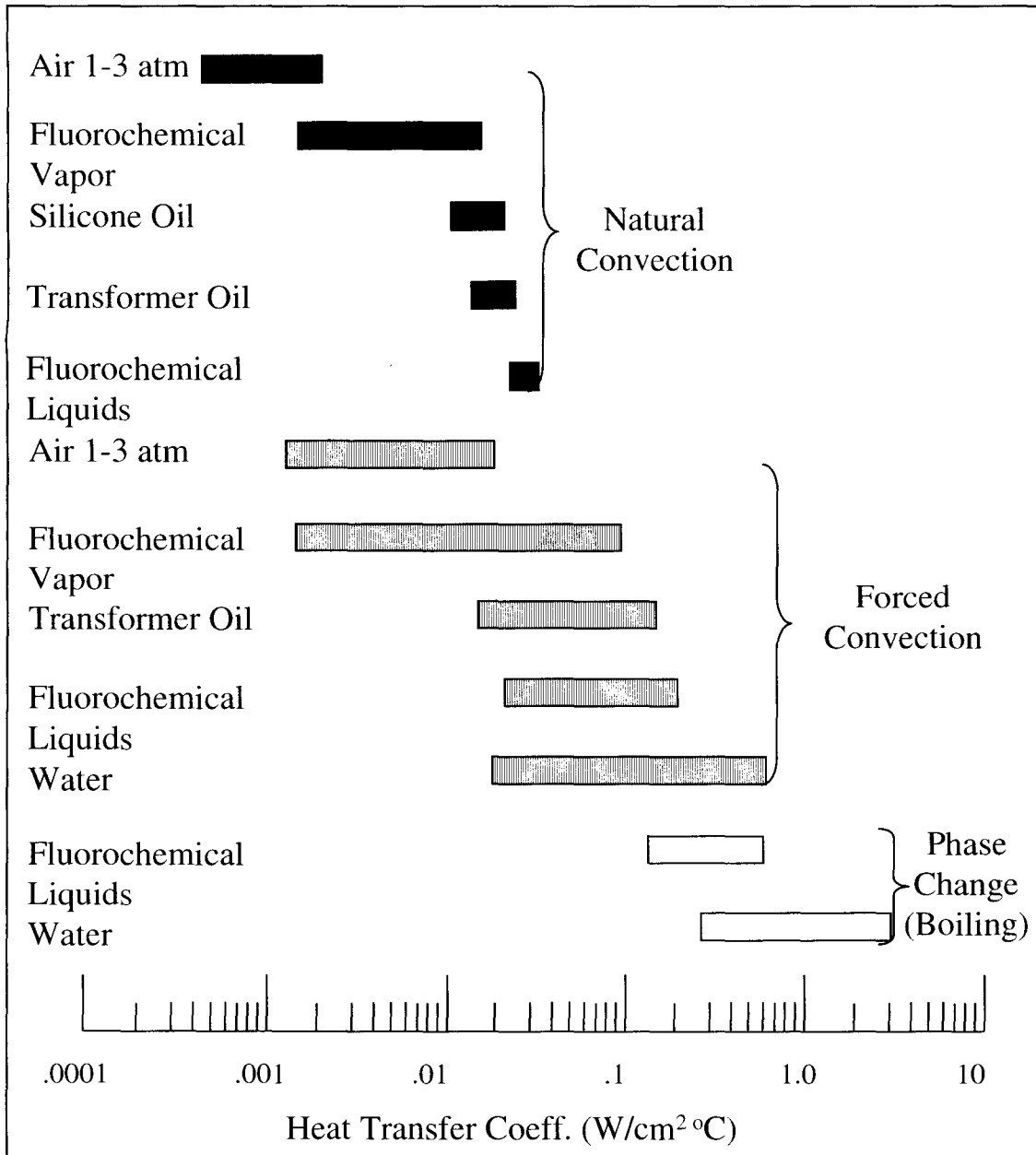


FIGURE 3.1.4 Ranges of heat transfer coefficients for various coolants [19].

3.1.3 MEMS Impinging-Jet Cooling - A Novel Approach

Currently, most electronic thermal packages use forced air convection for heat removal. This is due to the convenience of air as the coolant source, simplicity of the packaging and single-phase operation, as well as highly reliable thermal management. It is interesting to note that for a chip under a given heat flux and a maximum allowable chip temperature increase, the tangential forced-convection heat transfer coefficient, h , is on the order of $0.001 \text{ W/cm}^2\text{K}$ [4, 20]. This may be insufficient for future requirements of electronic thermal management and therefore it is necessary to investigate better thermal cooling methods. For impinging-jet cooling, on the other hand, the heat transfer coefficient can be one or two orders of magnitude larger, i.e., from 0.01 up to $0.1 \text{ W/cm}^2\text{K}$ [21]. Furthermore, because the thermal conductivity of thin films can be one to two orders of magnitude lower than the bulk thermal conductivity, IC's and MEMS will suffer severe local heating problems even if only a very small amount of power is dissipated in a thin-film region [14]. Arranging jets impinging directly on the local hot spots may solve the local heating problem. Thus, impinging-jet cooling is a promising cooling method with the advantage of single-phase (gas phase) cooling and local cooling.

Impinging-jet cooling experiments reported in the literature to date have mainly used macro-scale impinging jets. In addition, these works focused largely on turbulent jets with H/D ratios greater than 1.0, where H is the spacing between the nozzle and impingement surface (also called the height of the jet) and D the diameter of the jet. Interestingly, the regime with H/D ratios less than 1.0 can now be studied using MEMS technology to produce micro-scaled jets. Naturally, a more efficient micro heat exchanger

may become possible, because micro jets can be placed much closer to the hot surface than macro jets.

Figure 3.1.5 illustrates the conception of MEMS impinging-jet cooling for electronics. A high-speed cooling gas directly impinges on the hot surface through a MEMS nozzle/slot array, and penetrates deep into the boundary layer to form a sharp temperature gradient. Approximately one nozzle length downstream, the coherent structures in the jets induce an unsteady separation [15] that has a strong upward motion to carry the heat away from the surface. The distance between the nozzle plane and the hot surface is much smaller than that in a macro scale model so that a much higher heat flux can be achieved. The cooling efficiency can be further improved by direct micro jet impingement on the local hot spots. Furthermore, MEMS heat exchanger will be economical due to the mass production capability of MEMS technologies. Finally, this approach will be easy to implement because only cold air is required, so that technical difficulties and reliability problems in liquid-phase or multi-phase heat exchanger can be avoided.

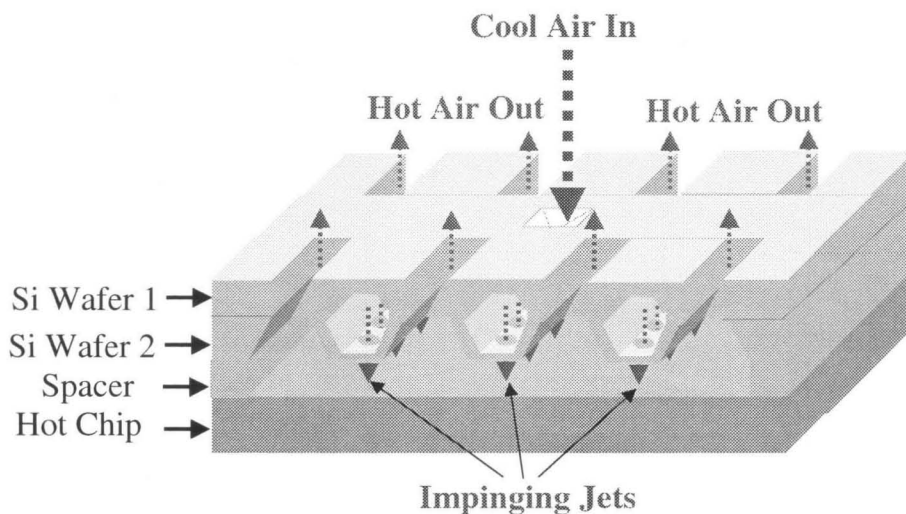


FIGURE 3.1.5 Conceptual illustration of MEMS impinging jet heat exchanger.

The characteristics of MEMS impinging-jet cooling have to be studied to develop an efficient and economical heat exchanger that will meet present and future integrated circuit microchip cooling requirements. The MEMS-based heat transfer measurement paradigm (shown in Figure 3.1.6) includes a technology for MEMS device fabrication, an experimental setup well suited for micro scale thermal study, and an accurate and an efficient data processing technique. In the technology aspect, we have developed silicon nozzles and nozzle arrays for jet generation, as well as temperature imagers with integrated micro heaters and thermistors made of polysilicon thin films (shown in Figure 3.1.6). The heaters have excellent heating uniformity, while the thermistors are very small in size ($4\ \mu\text{m} \times 4\ \mu\text{m}$), are distributed over a significantly large impingement surface area and offer good temperature resolution (0.1°C). Due to the integration of the heaters and sensors, the temperature imagers are highly reliable, and cause virtually no disturbances to the flow. The small size of temperature sensors enables the temperature imagers to have unmatched spatial resolution for accurate measurement of microscale local temperature distributions. This was never possible before with conventional thermistors, whose large size and demanding assembly requirements only allow for measurements in an average sense, with limited reliability and possibly significant disturbances to the jet flow.

In terms of the experimental setup, a vacuum chamber thermally insulated the backside of the temperature imagers. This thermal insulation was very important for eliminating the heat loss from the backside to media other than the imager chip, and insures measurement accuracy. The jet nozzles and imager chip were placed inside a

metal enclosure to eliminate disturbances to the jet flow. As for the data processing technique, we determined the axisymmetric temperature distribution on the front side of the temperature imager due to single-jet impingement by performing a spline-based least-squares curve fitting. The front side temperature distribution (for both single- and array-jet impingement) and backside uniform heating were used as input for finite element analysis to compute the heat transfer coefficient, which is the most important heat transfer data for micro impinging jets.

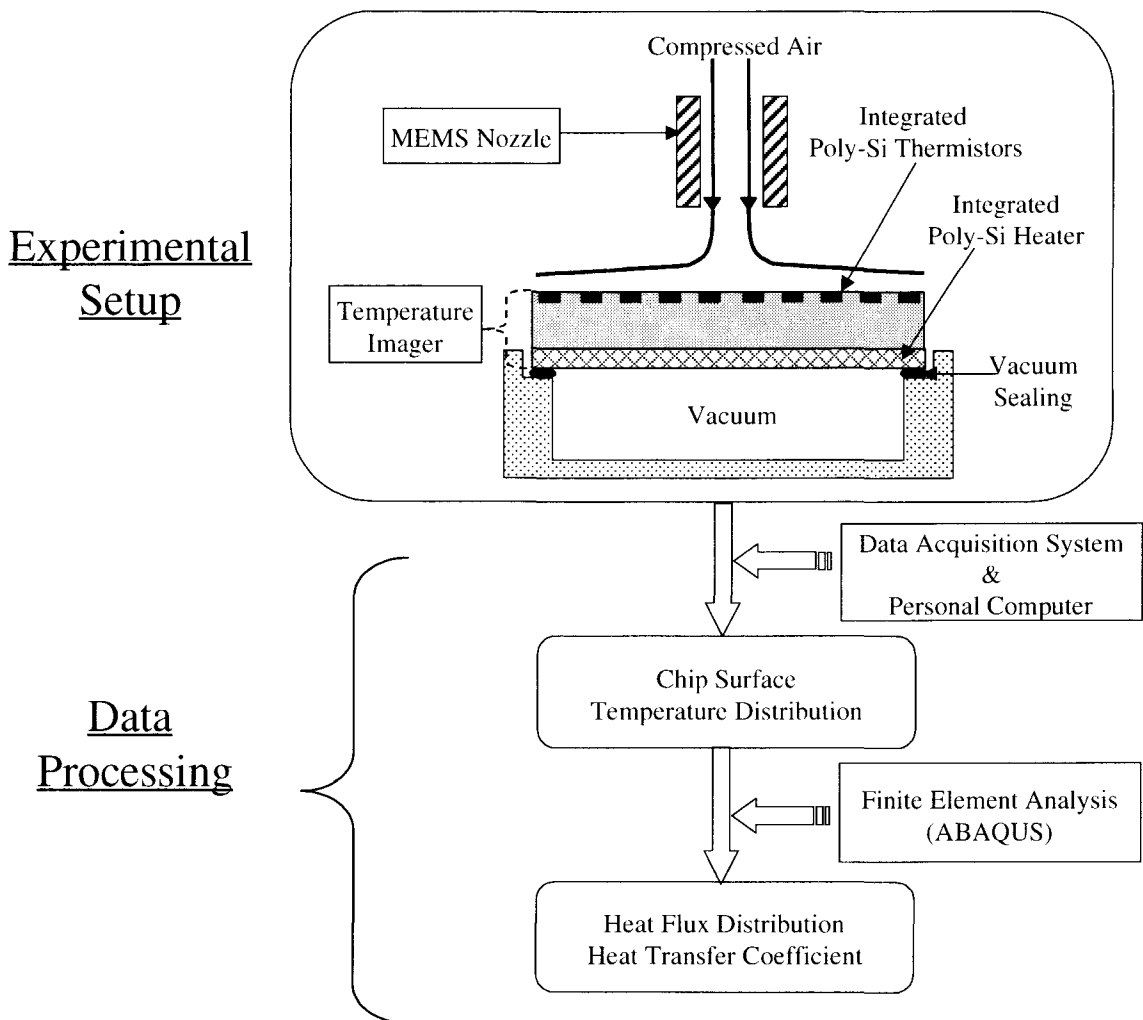


FIGURE 3.1.6 The MEMS-based heat transfer measurement paradigm.

3.2 Basics of Impinging-Jet Cooling

In many impinging-jet cooling systems, heat is taken away through a fluid that impinges directly upon a hot surface from nozzles or nozzle arrays. The impinging flow generates a very thin boundary layer near the impingement center and provides high local heat transfer coefficients [1-4]. By directing impinging jets to the especially hot regions where the maximum cooling is needed, the cooling efficiency is greatly enhanced. In fact, impinging jets have been widely used in the cooling of electric components, turbine engines, and dicing blades. Suitable design for such practical applications requires the knowledge of impinging-jet heat and mass transfer. Usually, the transfer characteristics depend on nozzle geometry, nozzle spacing, nozzle-to-target distance, and exhaust locations.

3.2.1 Basic Concepts

Impinging-jet heat transfer is closely related to fluid flow characteristics, which generally has been classified into laminar, turbulent, and transition flow regimes. In **laminar flow**, fluid motion is highly ordered and smooth, and it is possible to identify streamlines of the flow. The agitation of fluid particles is of molecular nature only, and the flow is stable. In **turbulent flow**, fluid motion is highly irregular, and the fluid particles slide past and collide with other particles. The flow is characterized by rapid and continuous mixing and velocity fluctuations of the fluid. Such mixing and fluctuations greatly enhance transfer momentum and energy so that the heat transfer coefficient in turbulent flow is much higher than that in laminar flow. The flow that is in development from laminar flow to turbulent flow is **transition flow**.

The **Reynolds number**, a dimensionless parameter that generally measures the ratio of fluid inertial viscous forces, is defined by

$$Re \equiv \frac{uL}{\nu} \quad (3.6)$$

where u is the characteristic velocity, L is the characteristic length, and ν is the kinematic viscosity of the fluid. This parameter is commonly used to identify the appropriate flow regimes. For instance, any fluid flow in cylindrical pipes will be laminar if the Reynolds number is less than 2100 and turbulent if the Reynolds number is larger than 4000.

The notion of boundary layers is an important tool for flow analysis. As shown in Figure 3.2.1, as fluid passes over a solid surface, the fluid particles that are in contact with the surface are brought to rest. Away from the surface, the velocities of fluid particles increase with increasing the distance from the surface until reaching the free stream velocity. Such a layer of slower moving fluid close to the solid surface is known as a **velocity boundary layer**. The thickness of the layer typically refers to the distance from the surface where the local velocity is 99% of the free stream velocity.

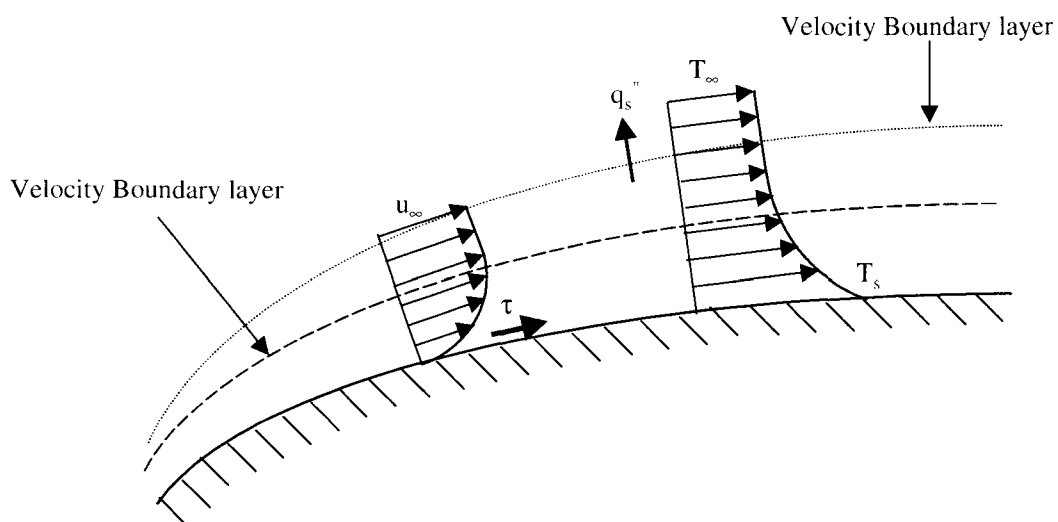


FIGURE 3.2.1 An illustration of convection velocity and thermal boundary layers.

If the free stream temperature is different from the temperature of the surface, convection heat transfer occurs, and the fluid temperature varies from the surface temperature (T_s) on the surface to the free stream temperature far enough from the surface. The thin layer of temperature transition is known as a **heat boundary layer**. Similar to the case of velocity boundary layers, the thickness of thermal boundary layer typically refers to the distance from the surface to the point where the local fluid temperature T satisfies the following equation,

$$\frac{T_s - T}{T_s - T_\infty} = 0.99 \quad (3.3)$$

At the solid surface, there is no fluid motion and the heat transfer occurs by **thermal conduction**, which can be expressed as

$$q_s'' = -k_f \left. \frac{\partial T}{\partial y} \right|_{y=0} \quad (3.4)$$

where k_f is the fluid thermal conductivity. Conduction can be viewed as the transfer of energy from more energetic (at a higher temperature) to less energetic (at a lower temperature) particles of a substance due to interaction between the particles, i.e., diffusion of energy.

Away from the solid surface, heat transfer is due to a superposition of energy transport by the random motion of the molecules (energy diffusion) and by bulk motion of the fluid. Such heat transfer between a fluid flow and a solid surface when they are at different temperatures is **thermal convection** (shown in Figure 3.1.2), and is of the form

$$q'' = h(T_\infty - T_s) \quad (3.2)$$

where q'' is the convective heat flux, T_s is the temperature of solid surface, and T_∞ is the fluid temperature. Table 2 lists the typical values of the convection heat transfer coefficient.

TABLE 2 Typical ranges of the convection heat transfer coefficient [4].

Process	h (W/cm²•K)
Free convection Gases	0.0002 - 0.0025
Liquids	0.005 - 0.1
Forced convection Gases	0.0025 - 0.0250
Liquids	0.005 - 2.0
Convection with phase change Boiling or condensation	0.025 - 10

In the thermal boundary layer, the heat transfer by conduction is equal to the heat transfer by the flow convection. By combining Equation 3.2 and 3.4, we then obtain

$$h = -k_f \frac{\partial T / \partial y|_{y=0}}{T_s - T_\infty} \quad (3.5)$$

So the behavior of the thermal boundary layers, which strongly influences the surface temperature gradient $\partial T / \partial y|_{y=0}$, determines the heat transfer rate through the boundary layers. When the thickness of the thermal boundary layer decrease, the magnitude of the

surface temperature gradient $\partial T / \partial y|_{y=0}$ generally increases, hence convective heat transfer increases. This is the basic principle of heat transfer enhancement by fluid impingement.

In addition to heat transfer coefficient (i.e., h), the **Nusselt number**, a dimensionless parameter measuring the ratio between the heat transfer rates by convection and by conduction, is often used for the analysis of convection heat transfer. It is defined as

$$Nu \equiv \frac{hL}{k_f} \quad (3.9)$$

h is the convection heat transfer coefficient, L is the characteristic length, and k_f is the thermal conductivity of the fluid. Usually the Nusselt number is much larger than 1 since conduction is smaller than convection. For the same fluid, the larger the Nusselt number, the larger the convection heat transfer rate.

3.2.2 Flow Characteristics of Impinging Jets

For an air jet impinging perpendicularly upon a flat surface, the flow pattern of a single nozzle can be divided into four characteristic regions as shown in Figure 3.2.2 [1, 2]:

- (1) **Potential core region:** the part of flow where the axial velocity remains almost equal to the nozzle exit velocity. The boundary of the potential core region is commonly defined as the area where the fluid speed is equal to 95% of exit velocity. Because the fluid from the surroundings is mixed into the jet, the region reduces with the increasing distance from the nozzle exit plane, and eventually

shrinks to a point. The length of this potential core region is determined by the growth rate of layers, and is about five or six times the nozzle diameters according to a survey that covers a large range of Reynolds numbers [5].

- (2) **Free jet region:** the part of developing flow where the axial velocity decays and the jet spreads to the surroundings. Eventually, lateral profiles of the axial velocity approach a bell shape. In the fully developed free jet region, similar axial velocity profiles exist at different jet lengths.
- (3) **Stagnation flow region:** this flow region is characterized by an increased static pressure as a result of the sharp decrease in mean axial velocity. Upon impingement, the flow deflects and starts to accelerate along the impingement surface. At this location, the vertical jet velocity component is decelerated and transformed into an accelerated horizontal component, also known as the wall bounded flow. Measurements show that this region extends about $2D$ from the impingement center along the plate surface [6] and $1.2D$ from the plate surface [7]. Here D is the nozzle diameter shown in Figure 3.2.2.
- (4) **Wall jet region:** near the beginning of this region, the local transverse velocity rises very quickly to a maximum, and then falls with increasing the transverse distance. The wall jet flow usually has higher heat transfer rates than parallel flow due to the turbulence generated by the shear between the wall jet and the surrounding air that reduces the boundary layer at the impingement surface. In

this region, the boundary layer grows along the impingement surface and the heat transfer decreases.

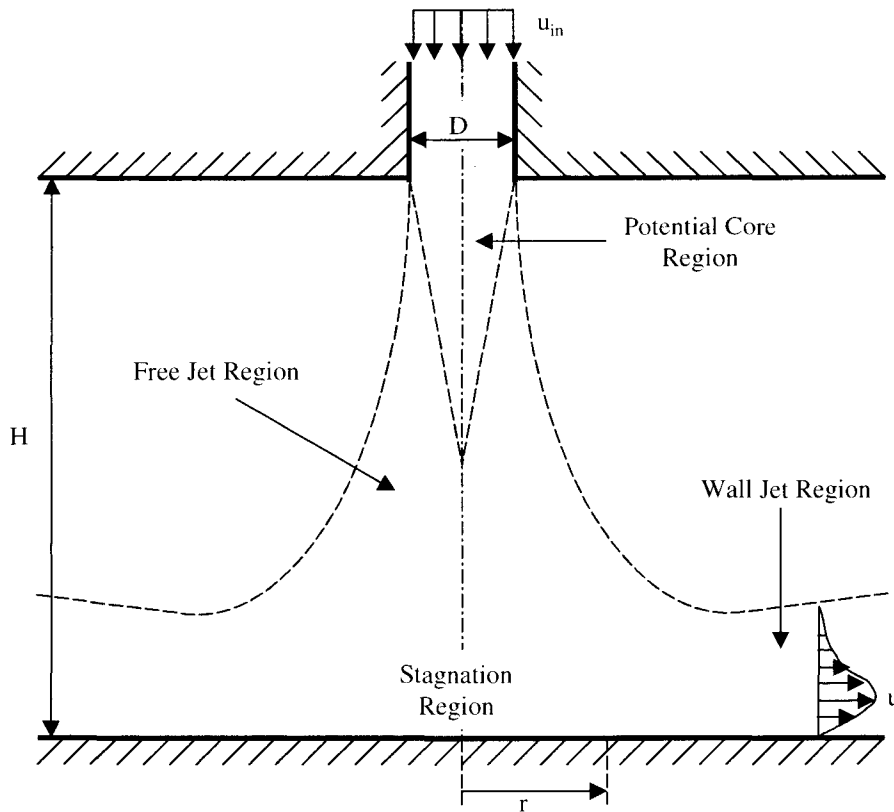


FIGURE 3.2.2 Flow regions in a confined macro impinging jet [1, 2].

3.2.3 Heat Transfer Characteristics of Impinging Jets

As shown in Figure 3.2.2, assume the gas jet exits a round nozzle with a uniform velocity u_j and temperature T_e that is equal to the ambient temperature T_∞ . Convective heat transfer occurs on the impingement surface if the surface temperature is different from the ambient temperature. The non-uniform flow characteristics of impingement result in non-uniform distributions of the surface temperature $T_s(r)$, heat flux $q''(r)$ and heat

transfer coefficient $h(r)$. According to Newton's law of cooling, the convection heat transfer coefficient follows

$$h(r) = \frac{q''(r)}{T_\infty - T_s(r)} \quad (3.10)$$

In the impinging jet flow, the characteristic length is taken to be the hydraulic diameter of the nozzle, in particular the diameter of the nozzle D if the shape is circular. Hence the Reynolds number and the local Nusselt number are given respectively by

$$Re_j = \frac{u_j D}{\nu} \quad (3.10)$$

$$Nu(r) = \frac{h(r)D}{k_f} \quad (3.12)$$

The average Nusselt number \overline{Nu} may be obtained by integration of the local result over the appropriate surface area A as

$$\overline{Nu} = \frac{\overline{h}D}{k_f} \quad (3.13)$$

where

$$\overline{h} = \frac{\int h dA}{A} \quad (3.14)$$

In 1977, H. Martin reviewed impinging gas jets with extensive data of heat transfer coefficients [1]. For a single round or slot nozzle under large nozzle-to-plate separations ($H/D > 5$), the local Nusselt number distribution is characterized by a bell-shaped curve for which Nu monotonically drops from a maximum at the stagnation point, $r/D = 0$, as shown in Figure 3.2.3 (a). For small separations ($H/D \leq 5$), the distribution is characterized by a 2nd maximum, which increases with increasing Re_j and may exceed the 1st maximum. The threshold separation at $H/D = 5$ is most likely related to the

length of the potential core of the impinging jet shown in Figure 3.2.3 (b). The appearance of the 2nd maximum is caused by a rapid rise in the turbulent level in the transition from an accelerating stagnation region flow to a decelerating wall jet flow [1]. Additional maxima have been observed and associated with the formation of the vortices in the stagnation zone [8], and the transition to a turbulent wall jet [9], as well as the adjoining wall jet regions of jet arrays [1, 10].

Generally, the heat transfer correlations of impinging jets have the form of

$$Nu(r) = f(Re, Pr, r/D, H/D) \quad (3.15)$$

$$\overline{Nu} = \overline{f}(Re, Pr, r/D, H/D) \quad (3.16)$$

Empirical data and analytic functions of the Nusselt numbers for both single jets and jet arrays have been given in several extensive review articles [1, 2, 3, 4].

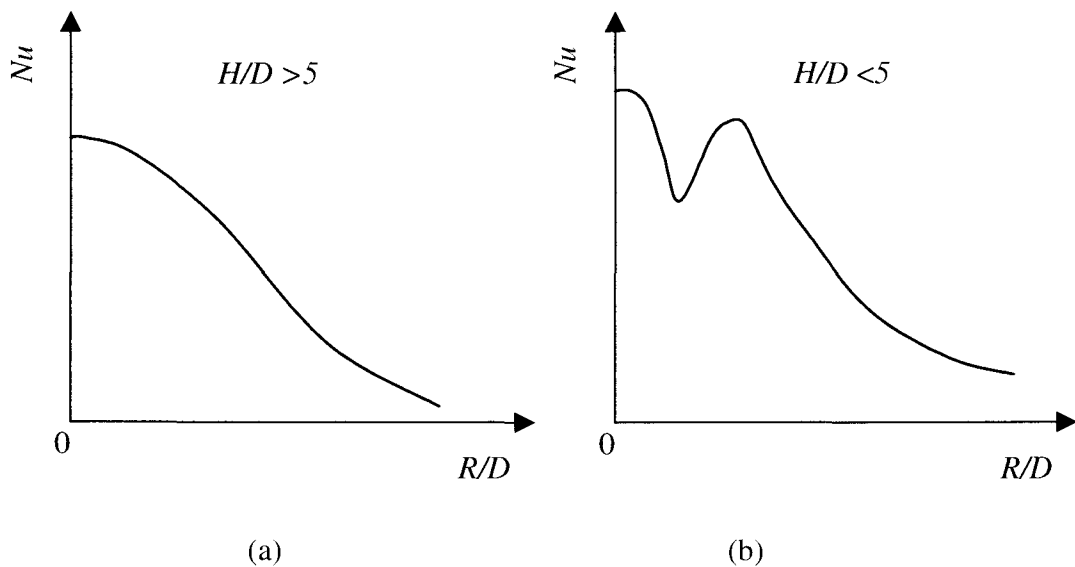


FIGURE 3.2.3 Distribution of local Nu number associated with a single round or slot jet nozzle for (a) large and (b) small relative nozzle-to-plate spacing.

3.3 MEMS Jet-Cooling Study with Silicon Temperature Imager

An experimental study of MEMS impinging-jet cooling with a silicon temperature imager is presented in this section. Using a specially designed experimental setup, the cooling effect of MEMS impinging single jet and array jets has been tested under various driving pressures and spacings between the nozzle exit surface and impingement surface. The 2-D temperature distributions on the impingement surface have been obtained with the silicon temperature imager. The heat transfer analysis includes cooling efficiency, driving pressure, and cooling uniformity.

3.3.1 Design and Fabrication of Devices

I. Silicon Temperature Imager

A temperature imager or sensor-array chip, shown in Figure 3.3.1, was fabricated in order to serve as a test target for the impinging jets. This 2 cm x 2 cm chip has an integrated polysilicon heater on the backside and an 8x8 array of temperature sensors on the front side. The 64 thermistor-type polysilicon sensors, each 4 μm x 4 μm , are 500 μm apart and are placed in a 4 mm x 4 mm area at the center of the top surface shown in Figure 3.3.2. These polysilicon temperature sensors have a nominal room-temperature resistance of about 20 k Ω and a temperature resolution of 0.1°C.

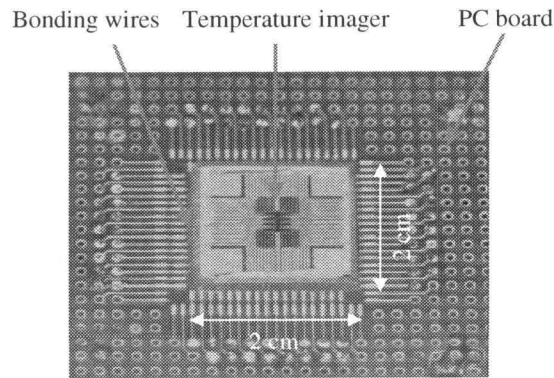


FIGURE 3.3.1 A silicon temperature imager bonded on a PC board.

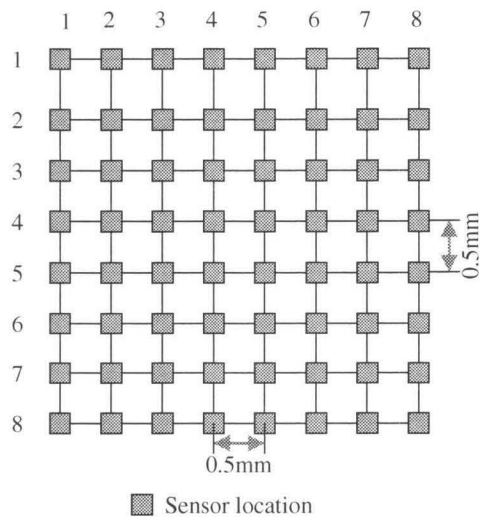


FIGURE 3.3.2 Temperature sensor arrangement of the silicon temperature imager.

The fabrication process of the sensor chip is given in Figure 3.3.3. Starting with bare <100> silicon, a 5000 Å thick layer of dry thermal oxide and a 2000 Å thick layer of LPCVD nitride are deposited. Then 5000 Å of LPCVD polysilicon is deposited for the sensors and doped with boron to a concentration of $5 \times 10^{18} \text{ cm}^{-3}$. The sensors are then encased in another 2000 Å thick nitride layer that electrically isolates and protects the sensors. Finally contact holes are opened in the nitride by RIE and aluminum metalization finishes the sensor process. Here, the backside heater is fabricated similarly,

with the only differences in masking and the backside polysilicon doping, i.e., heavily boron doped at $5 \times 10^{20} \text{ cm}^{-3}$.

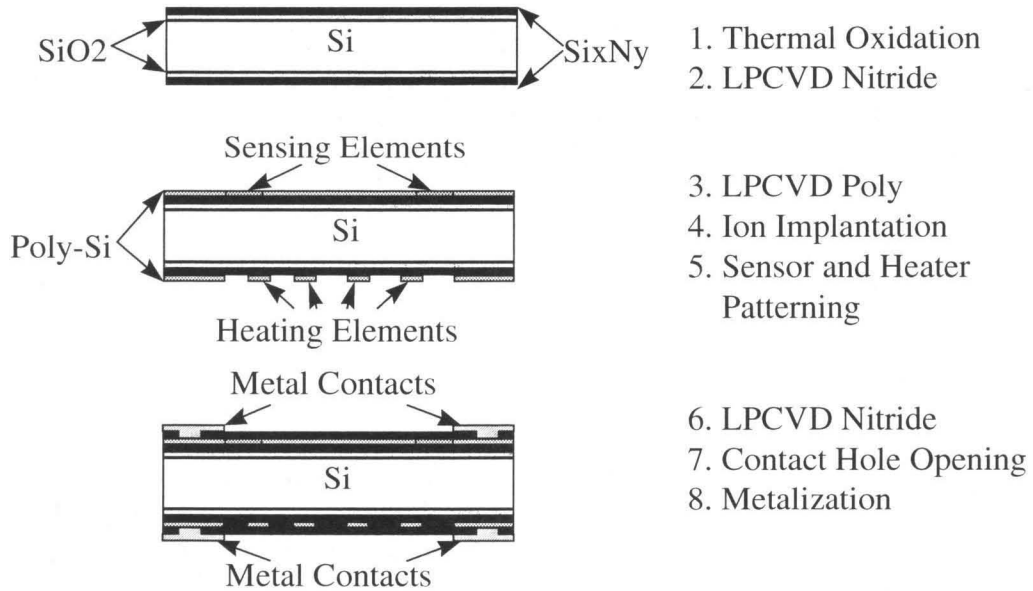


FIGURE 3.3.3 Process flow of silicon temperature imager.

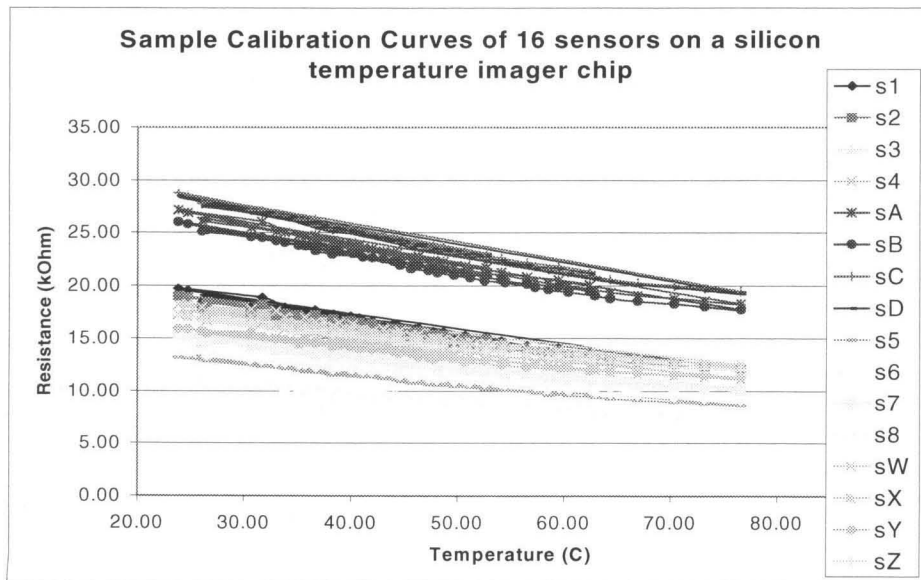


FIGURE 3.3.4 Calibration curves of the sensors on a silicon temperature imager.

Figure 3.3.4 shows preliminary calibration of 16 randomly selected sensors on the chip. Due to non-uniformities in the ion implantation or over etching of some sensors, the room temperature resistance ranges from approximately 12 k Ω to 28 k Ω at room temperature. Thus every sensor must be calibrated individually in an isothermal oven.

II. MEMS Nozzles

Precisely formed nozzles with exit diameters in the range from 1 μm to 500 μm are not commercially available. In addition, glass pipettes and plastic tubing cannot be formed to the exact contours necessary for them to act as contraction region for sonic nozzles. This leaves MEMS as the leading technology candidate for the fabrication of micro nozzles. The following outlines the design and fabrication steps of micro nozzles.

MEMS Single Nozzle

MEMS single nozzles shown in Figure 3.3.5 have been fabricated. The fabrication process, illustrated in Figure 3.3.6, begins with a nitride layer deposited on both sides of a bare <100> Si wafer. Etch holes are patterned and opened in the backside nitride using RIE, and the 500 μm thick wafer is then anisotropically etched in KOH. An RIE etch is used to open a circular nozzle pattern on the front side nitride. This process is used to produce circular single jets with inlet diameters of 1.5 mm and outlet diameters ranging from 0.5 mm to 1.5 mm.

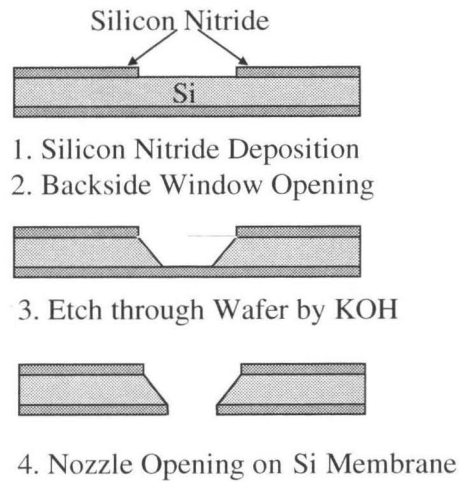
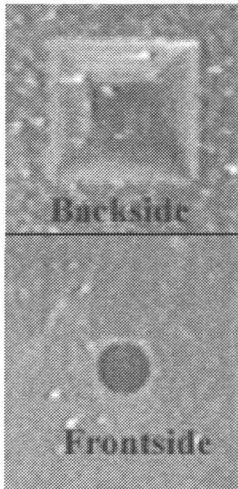


FIGURE 3.3.5 Prototype MEMS nozzle. **FIGURE 3.3.6** Nozzle fabrication process.

MEMS Nozzle and Slot Arrays

MEMS nozzle and slot arrays have also been fabricated. These arrays are made by bonding two separate chips together using silicon fusion bonding technology. Figure 3.3.7 shows the finished nozzle and slot arrays. In the figure, the circular nozzles are 1 mm in diameter, and the slots are 1 mm wide and 8 mm long. Rows of nozzles/slots are spaced 2.5 mm apart from center to center. The entire structure is approximately 1mm thick.

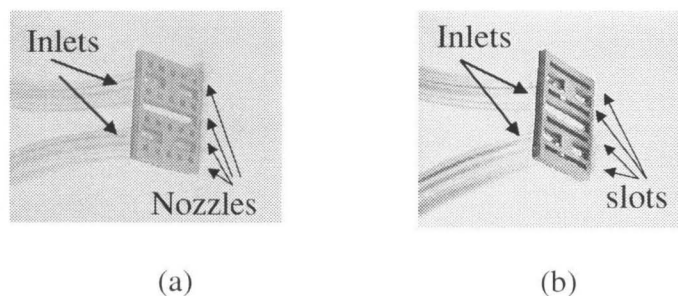


Figure 3.3.7 Micromachined (a) nozzle and (b) slot arrays.

The fabrication process of both chips is shown in Figure 3.3.8. The wafer on the left defines the nozzles/slots and the wafer on the right defines the gas inlets. The two

pieces are fabricated with the same process. Starting with <100> Si wafers, openings for the nozzles/slots are first etched in KOH. Then a 5000 Å thick thermal oxide is grown on both sides over the openings as a protective layer. Etching windows are then opened in the oxide, and followed by KOH through-wafer etching. After dicing, the thermal oxide is removed using BHF. To make a final array chip, a pair of matching chips are then aligned and fusion bonded. Finally, the bonded array chip is coated with a 4-µm-thick layer of Parylene. This Parylene layer serves two purposes. One is to seal any unbonded surfaces, and the other is to increase thermal insulation from ambient.

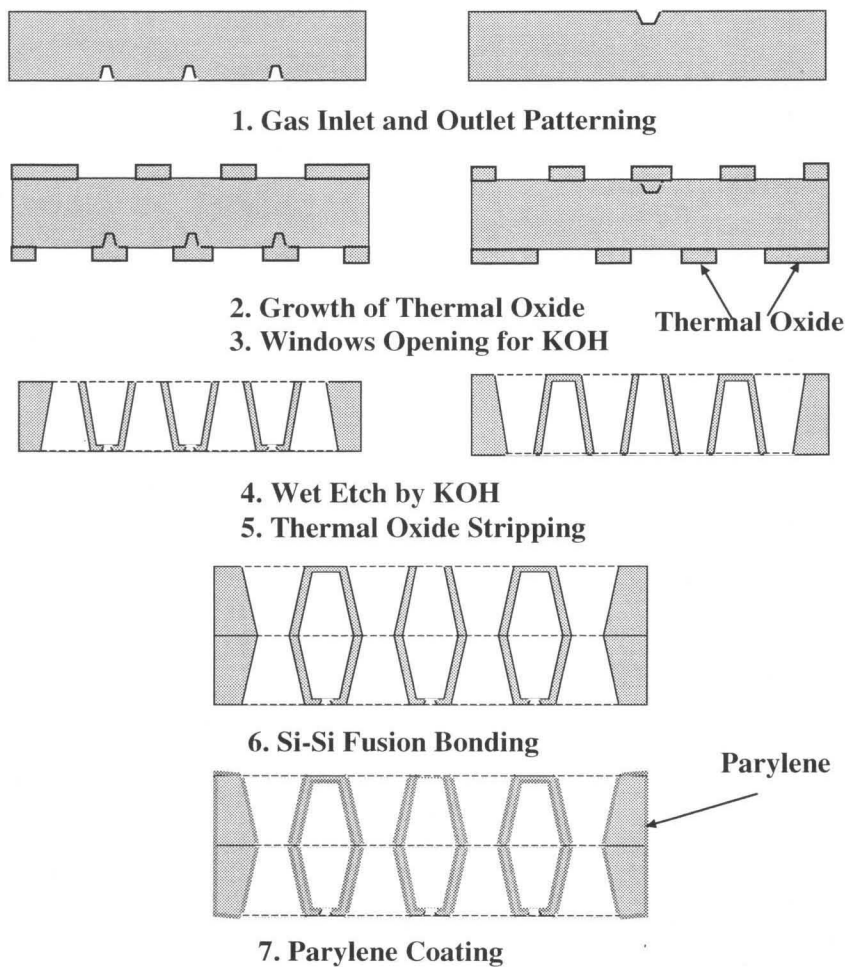


FIGURE 3.3.8 MEMS jet array process flow.

3.3.2 Instrumentation

I. Experimental Setup

The experimental setup is illustrated in Figure 3.3.9. The chip is mounted on a Plexiglas chuck for thermal isolation. The backside polysilicon heater has a nominal resistance of 55Ω , and by varying the input voltage, we have a precisely controllable heat source using the Joule heating of this resistor. Most tests are conducted with approximately 1W of power. As shown, vacuum is always present on the backside of the chip to prevent backside heat loss. This is important because it is desirable to have all the heat transferred to the top surface. Above the sensor chip, filtered air is applied to drive an impinging-jet nozzle or array chip, which is then held above the sensor chip by an aluminum L-block that is attached to a 3-axis micro-positioner (Figure 3.3.10). The inlet air/gas system has sensors and valves to monitor and control the inlet pressure and the mass flow rate.

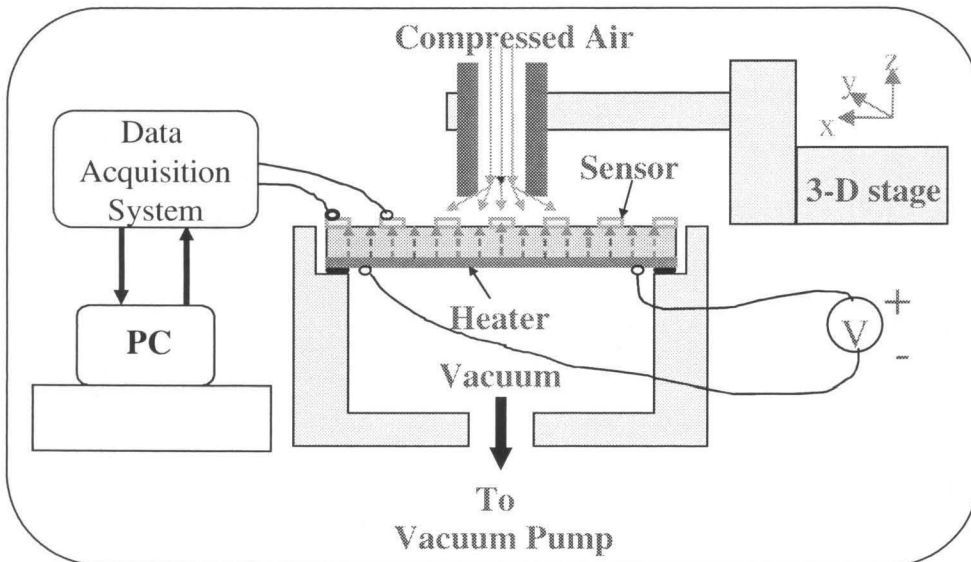


FIGURE 3.3.9 The illustration of experimental setup.

Each sensor on the chip is wire bonded to the leads on a PCB mounted on the top surface of the Plexiglas chuck. The PCB is connected to an HP 34970A data acquisition system that has been set up to measure resistance. An environmental chamber is used to obtain sensor temperature calibration curves (second-order polynomial) used for data processing. These sensors are calibrated from room temperature to 80 °C.

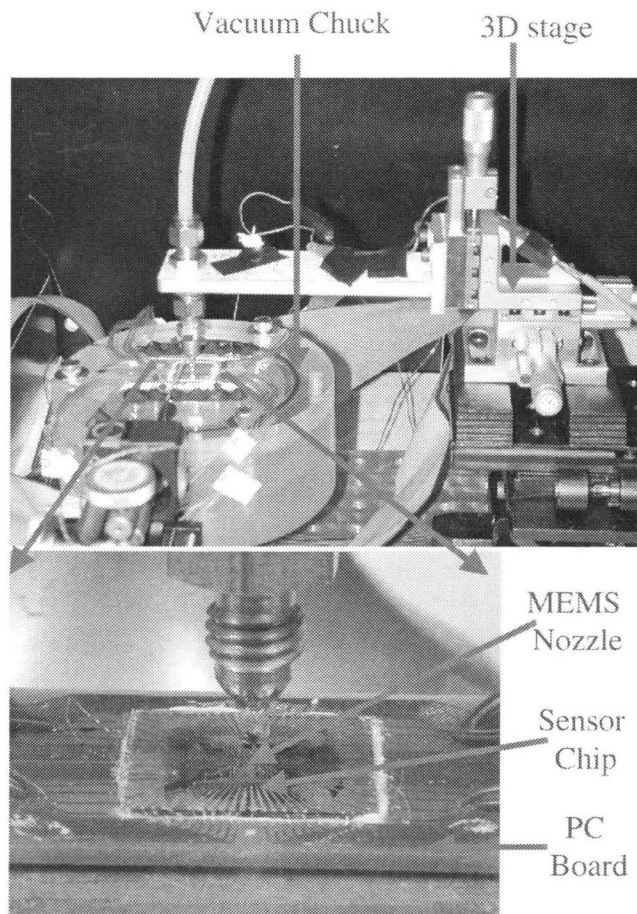


FIGURE 3.3.10 Pictures of the experimental setup.

II. Constant Current Circuit for the Silicon Temperature Imager

Figure 3.3.11 shows the circuit for the silicon temperature imager. The voltage divider on the left side sets the base bias voltage for the transistors. The voltage follower (Op-Amp) is used to buffer the rest of the circuit, from which the constant current is provided. The output of the operational amplifier can supply a very stable voltage regardless of changes in load (sensor resistance $\gg Z_{output}$). The voltage across the emitter resistor and the base-emitter line of every PNP-transistor thus stays constant. If the base-emitter voltage (V_{BE}) is assumed to be constant ($V_{BE} = 0.6V$), the voltage across the emitter resistor is also constant. This provides a constant emitter current (I_E) and, by neglecting the little base current (I_B), it also provides a constant load current (I_C).

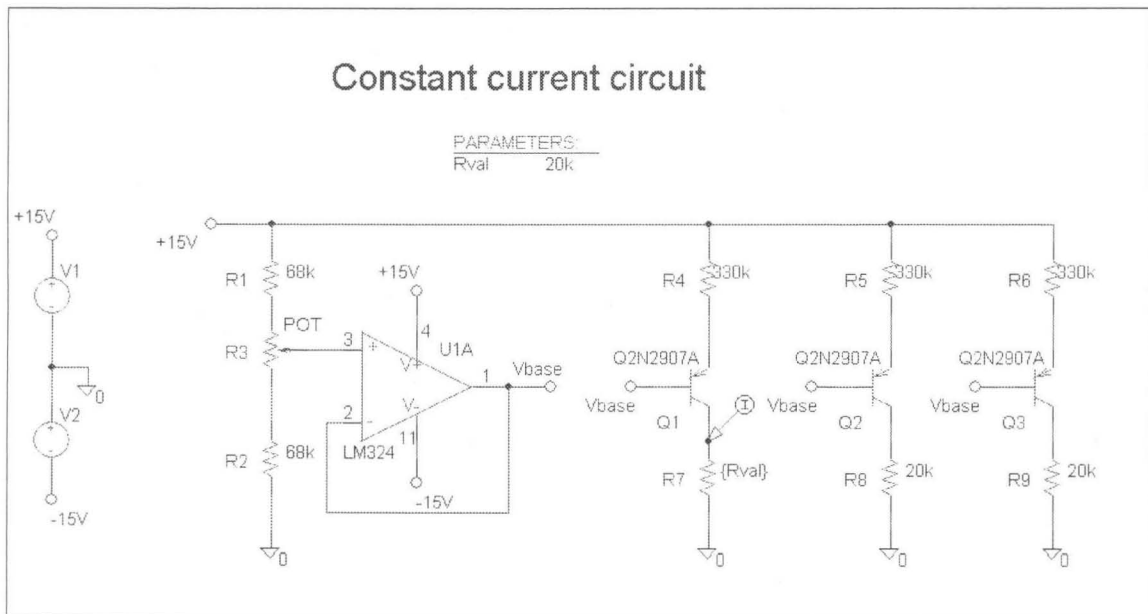


FIGURE 3.3.11 The constant circuit used in the silicon temperature imager.

With this circuit all the nodes can share a common potential. Another advantage is that the potentiometer, needed to adjust the current I_C , is used only once which decreases calibration effort.

To provide a current $I_E=20\mu\text{A}$, the voltage across the emitter resistor (V_{RE}) is chosen to be about 7V. This will provide a very stable current (the higher this voltage, the more stable the load current). To maintain the required value of $I_E=20\mu\text{A}$, the value for the emitter resistor (R_E) (e.g., R_4 in Figure 3.3.11) is calculated to be

$$R_E = \frac{V_{RE}}{I_E} = \frac{7}{20 \cdot 10^{-6}} = 350\text{k}\Omega$$

By using two resistors in parallel (1 M Ω and 500 k Ω), the overall resistor value of $R_E=333.3\text{k}\Omega$ is obtained. The actual voltage V_E calculates to be

$$V_E = +15\text{V} - R_E \cdot I_E = 15 - 333.3 \cdot 10^3 \cdot 20 \cdot 10^{-6} = 8.3\text{V}$$

As mentioned earlier, the base voltage can be calculated to be

$$V_B = V_E - 0.6 = 8.3 - 0.6 = 7.7\text{V}$$

The values of the resistors for the voltage divider are calculated to be $R_1=R_2=68\text{k}\Omega$. The potentiometer (POT- R_3) is chosen to be 10k Ω . Thus the requested value of V_B is within the adjusting range of R_3 .

Since there is a rather large number of channels (64) driven by one voltage follower, the issue of achievable output current has to be discussed: One OpAmp output can sink a maximum output-current of about 20mA. If there is a load with very high resistance, the transistor will operate in the saturation region, meaning that the emitter-collector voltage (V_{EC}) is lower than about 0.3V. In this operation mode, the base current can no longer be neglected. If even the load resistance is infinite, i.e., no sensor is

connected to the transistor, the base current becomes equal to the emitter current: $I_E=I_B$. If too many of the sensor- collector junctions are left open, the OpAmp will no longer provide the stable voltage. The base voltage will drop, and the output current will no longer remain constant. In order to avoid this situation, one operation amplifier is used for at most 10 sensors (Figure 3.3.12). With this design, such improper operation will not occur.

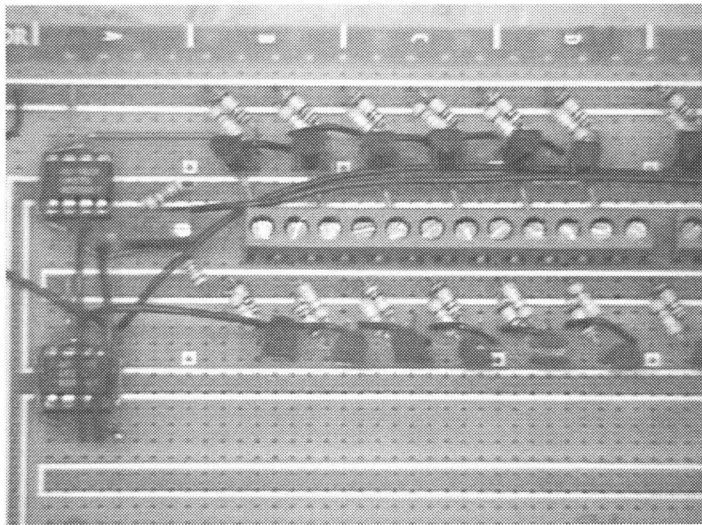


FIGURE 3.3.12 The picture of the constant circuit used in the silicon temperature imager.

III. HP 34970A Data Acquisition System

A HP34970A data acquisition/switch unit was used to sample experimental data for the sensors on a temperature imager. Along with three HP 34901A channel multiplexers, it can scan as many as 60 channels. Using the HP BenchLink Data Logger software, a PC will control the HP data acquisition system and store sampled data into its hard disk. The system can be configured to measure voltage, current and resistance. It has a 6.5-digit (22bits) DMM and 0.01% basic 1-year accuracy.

3.3.3 Test Results and Discussion

A single glass nozzle, a MEMS single nozzle, a MEMS nozzle array and a MEMS slot array were tested over a range of height from 100 μm to 3000 μm and a pressure range from 0.5psi to 5psi.

I. Temperature Distribution Measurement

The temperature sensors measure the temperatures shown in Figure 3.3.13. These sample-point temperatures are input to the Surface Mapping System from Golden Software, Inc., to plot the temperature distribution over the impingement surface (4 mm x 4 mm). Figure 3.3.2 is a sample temperature distribution taken with a silicon target chip. The MEMS jet is 500 μm in diameter and 750 μm above the target surface. The inlet pressure is 5 psig and there is a controlled heat flux of 1.12 W into the entire 4 cm^2 area of the silicon target chip.

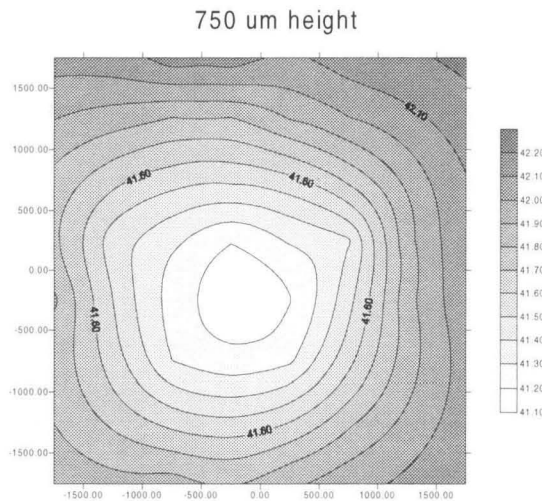
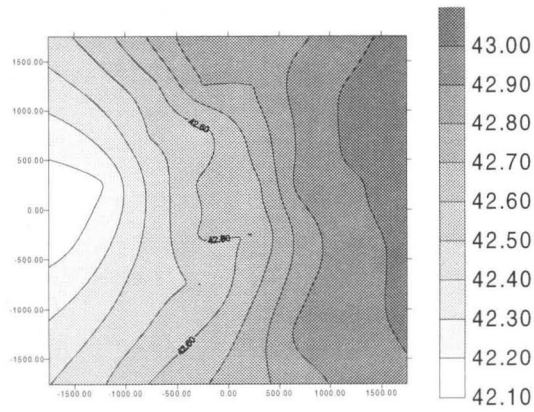
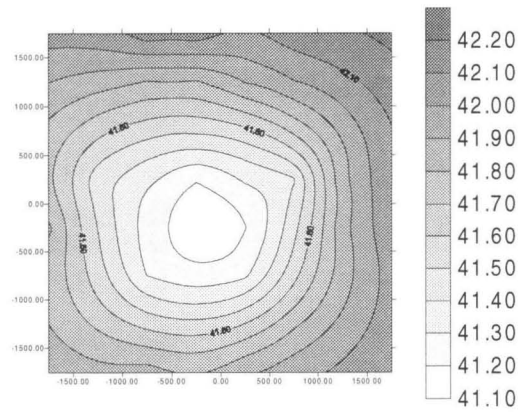


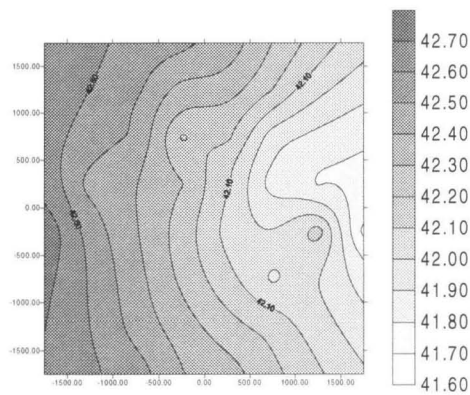
FIGURE 3.3.13 A sample of the surface temperature profile.



(a) Jet on the left



(b) Jet at center



(c) Jet on the right

FIGURE 3.3.14 Contour temperature plots indicating that the sensor image correctly identifies and tracks an impinging jet.

As we can see from the figure, the coolest center region corresponds to the stagnation region right under the nozzle. In addition, the temperature gradient on the right is larger than that on the left. This is because the impinging jet was tilted to the left, instead being normal to the surface. Furthermore, instead of being circular or elliptical, the isothermal profile shows a certain degree of squareness, and this can be explained by the effect of the square nozzle surface.

Temperature distribution measurements must be performed first to confirm the functionality of the sensor chip by using a MEMS single jet which is 750 μm away from the sensor chip and driven by 2 psig compressed air. Figure 3.3.13 shows some typical data imaged in this fashion. The sensor chip must be able to identify and track the jet as it is moved around as in Figure 3.3.14. Otherwise, the chip does not function properly.

II. Single Impinging-Jet Cooling

Figure 3.3.15 is a composite of the sensor chip temperature profiles constructed from instantaneous sensor array data for each of the three cases. First, the temperature profile, shown as the bottom plane, was measured at room temperature without any heating and cooling. The uniformity (± 0.1 $^{\circ}\text{C}$) of the measured temperatures from time to time shows good system reliability. The top plane is the temperature profile measured with 1.12 W applied via the backside heaters and no cooling on the frontside. The uniform temperature implies heat was evenly generated by the MEMS heater across the chip. The middle plane is the temperature profile under cooling by a 500 μm diameter MEMS nozzle which is 750 μm above the surface and driven by 5 psi compressed air. A large total temperature drop (>35 $^{\circ}\text{C}$) after the applied cooling shows the high cooling effectiveness

by an impinging jet. A small temperature variation across the sensing area implies a large effective cooling area, enough to cause a measureable temperature profile even considering the large thermal conductivity of silicon.

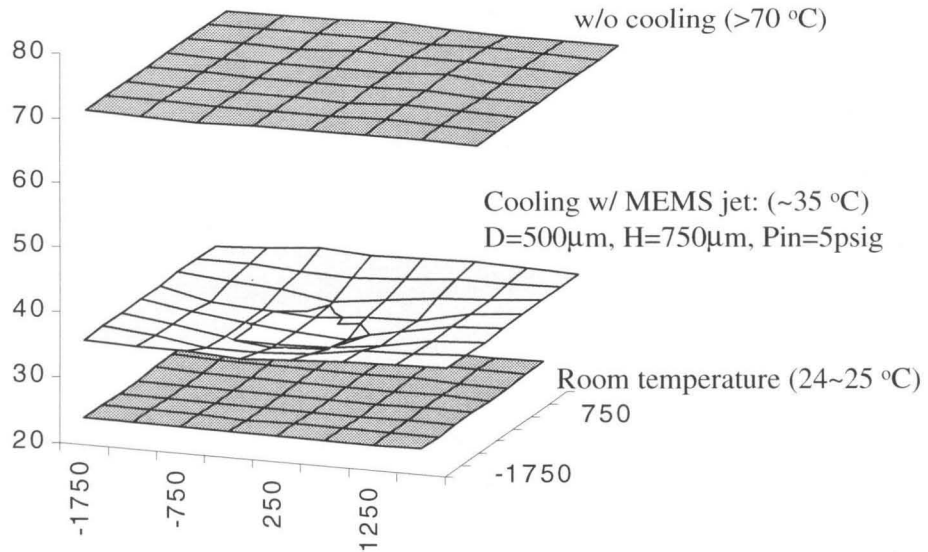


FIGURE 3.3.15 Composite illustration shows the effectiveness of impinging jet cooling.

Figures 3.3.16 and 3.3.17 show the average temperature vs. spacing between a jet and the sensor chip at different air pressure conditions. The backside heater powered by 8V gave about 1.12W of heat generation. The surface temperature distribution due to the free jet at various heights is relatively stable. This is due to the fact that the free jet can easily entrain local cold air and circulate it over the heated test chip. In the case of the MEMS jet, it is more of a confined jet situation [3, 26-28]. Since the MEMS jet is a hole fabricated into an approximately 4 mm by 4 mm silicon chip, at heights less than 1mm the top wall combines with the bottom sensor chip to produce a channel flow effect. This

reduces the volume of cold air available next to the MEMS nozzle to be entrained and circulated past the heated bottom chip. This leads to a higher measured surface temperature for similar height and pressure conditions when compared to the free jet. However, at larger heights, this confined flow effect is greatly reduced and the MEMS jet cooling effectiveness is comparable to the free jet, as evident from the heat transfer coefficients calculated in Figure 3.3.17 for the MEMS jet. The heat transfer coefficient for the free jet is approximately constant at $0.032 \text{ W/cm}^2\text{K}$ at 5 psi and $0.025 \text{ W/cm}^2\text{K}$ at 3 psi. Thus the MEMS jet (with an approximately 16 mm^2 chip area) has similar cooling characteristics to a free jet when the H/D ratio is greater than 3. Comparison of Reynolds numbers indicates the observed results agree with the expected flow regime. The Reynolds number for H/D less than 1/2 for the MEMS jet should scale with the height since it is now the minimum opening in the system. These yield values of Re as low as 1300, which is in the lower end of the transition region near laminar flow [2], which is known to have poorer heat transfer qualities than turbulent flow.

Jet cooling efficiency, defined as heat transfer coefficient normalized by the kinetic energy of the impinging gas, has been calculated and plotted in Figure 3.3.18 and 3.3.19 for the single free jet and MEMS jet respectively. For both types of jet, a low gas driving pressure gives a high cooling efficiency. This gives us a practical guide for cooling system design: Low gas pressure is preferred if the gas source and power limitation is the constraint. Otherwise, high pressure and high-speed jets can be used to achieve low surface temperature.

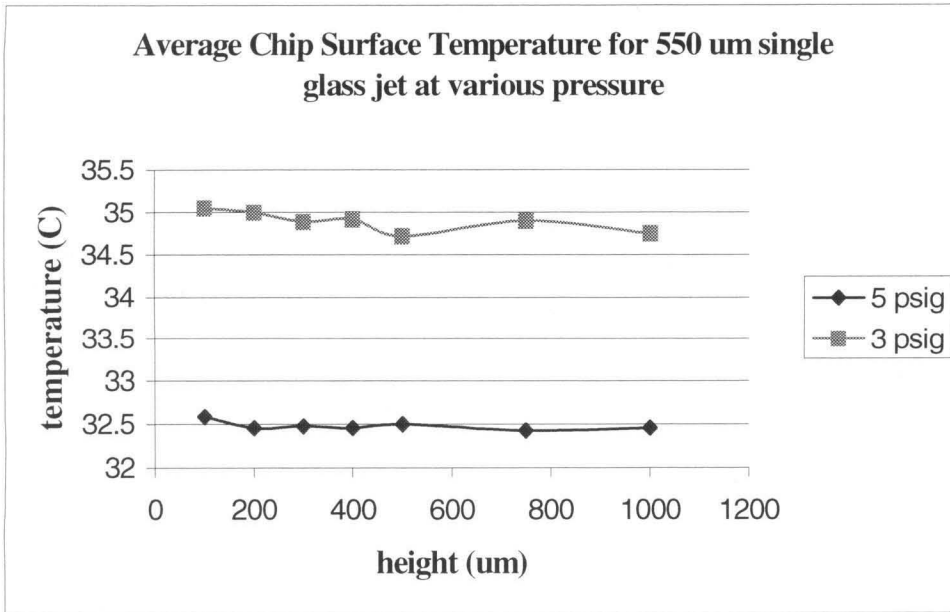


FIGURE 3.3.16 Average sensor chip temperature at various heights for a given inlet pressure of a single jet.

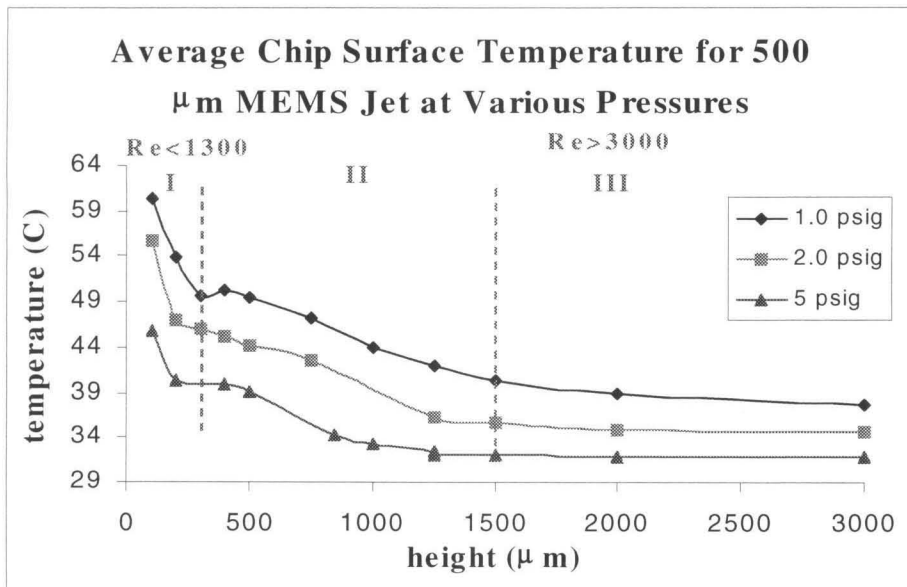


FIGURE 3.3.17 Average chip temperature at various heights for a 500 μm diameter MEMS single nozzle.

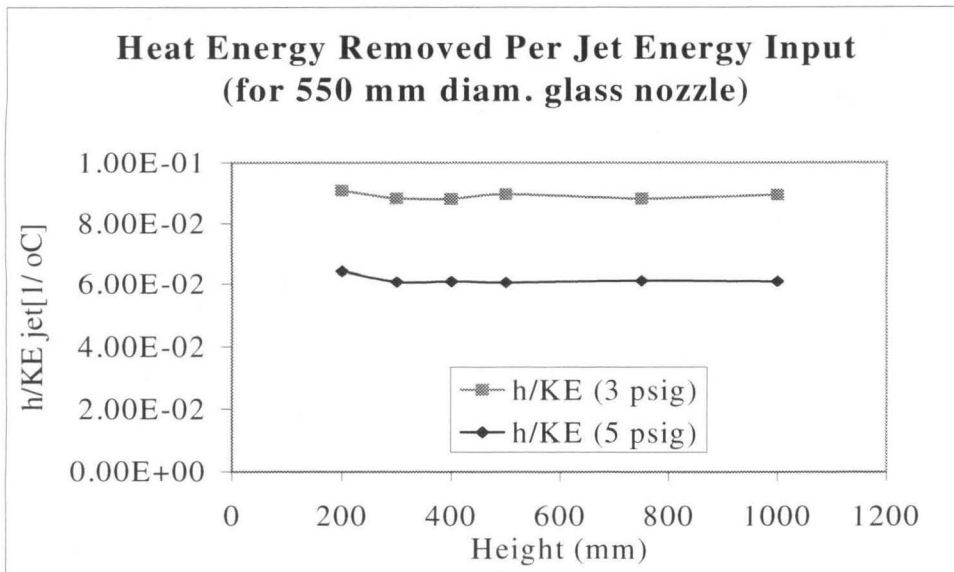


FIGURE 3.5.18 Cooling efficiency at various heights for a given inlet pressure of a free single jet.

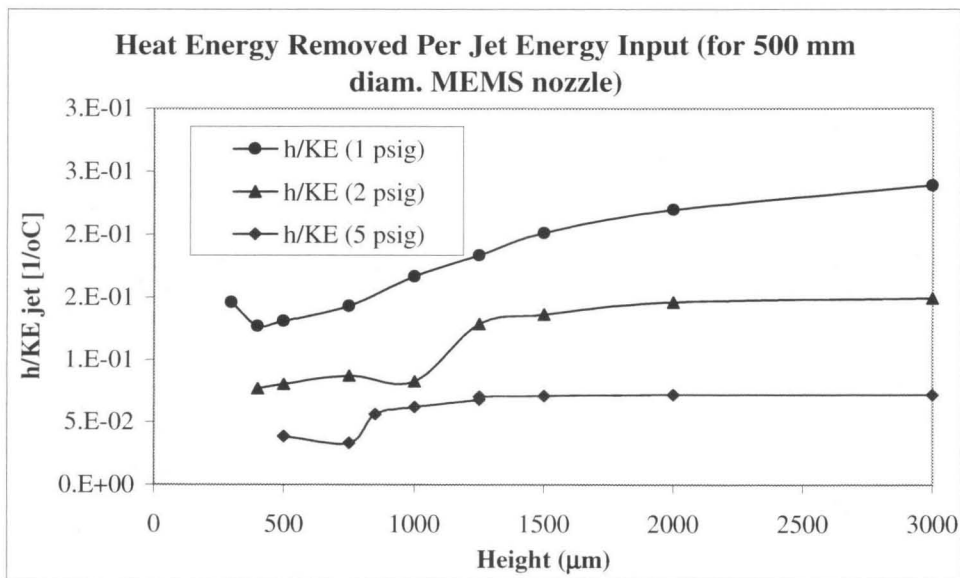


FIGURE 3.5.19 Cooling efficiency at various heights for a given inlet pressure of a MEMS single jet.

III. Jet-Array Cooling

Preliminary data images with a nozzle array and slot array are presented in Figures 3.3.20 and 3.3.21. Although the temperature images are not as simple as the image of a single jet because of the more complicated gas flow pattern, the temperature distribution is more uniform than any single jet.

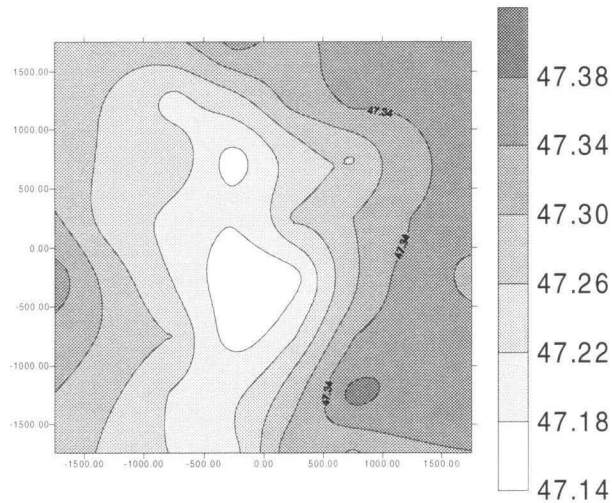


FIGURE 3.3.20 Temperature distribution recorded from a nozzle array at 500 μm height, $P_{in} = 0.5$ psig, and power in = 1.12 W.

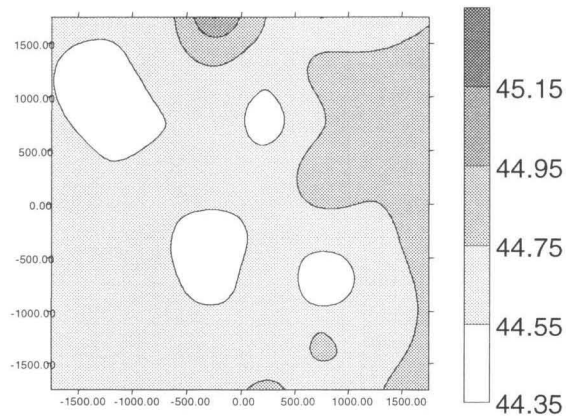


FIGURE 3.3.21 Slot array temperature distribution at height = 1000 μm, $P_{in} = 1$ psig, and an input power of 1.12 W.

There seems only one major minimum in temperature. This is due to the fact that the 2-mm gas inlet on the backside of the chip is centered only over the center exit jet in each row. Since there is only 1 temperature sensor every 500 μm , we do not have enough spatial resolution so most of the exit flow from the two center jets appears as a single larger elliptical impingement region.

The slot nozzle data in Figure 3.3.21 also indicates peculiarities in the prototype nozzle design. It seems that the inlets are acting as nozzles and the slots serve to confine the flow along the slot direction. According to turbulent impinging jet theory, boundary layer flow separation and recirculation can occur 2 nozzle diameters down from the centerline inlet [23]. This region can give rise to secondary maximums in heat transfer [4] and corresponds to the smaller cool regions. The lack of symmetry in the secondary cooling peak can be explained by the fact that the inlet is not precisely aligned with the exit slots, so the jet from the inlet is deflected, creating an oblique exit jet which is then confined by the slot. Hence there should be local secondary minimums on the left side, but they appear to be on the low momentum side of the oblique jet so separation occurs at a larger distance away from the impingement point, which is out of the sensor area.

In practice, cooling fans can only provide a limited pressure gradient for electronic cooling. Since it is assumed that standard PC-level cooling fans will be eventually interfaced with these MEMS devices, in practice, it is reasonable to evaluate cooling effectiveness by comparing surface temperature as a function of inlet pressure, regardless of total mass flow rate. With this consideration in mind, a quick comparison method between the single nozzle and nozzle array is available, as evident in Table 3.

From Table 3, it is apparent that if one design parameter is a small pressure drop, then a MEMS nozzle array is the optimal cooling configuration.

TABLE 3 Comparison of pressure required to cool the test chip to approximately 47°C with $Q = 1.12$ W and height = 500 μm .

	Single MEMS Jet	Single Glass Jet	Slot Array	Nozzle Array
Gas Pressure (psig)	2.0	1.0	0.7	0.5

3.4 Jet-Cooling Study with a Quartz Temperature Imager

The heat transfer measurement using the silicon thermal imager, as described previously, yielded interesting results. However, the results also indicated that the silicon target chip did not provide sufficient information on the temperature distribution because of the limited coverage area covered by the sensor array. In addition, the high thermal conductivity of silicon produced only a small temperature difference (about 1 °C, see Figure 3.3.13) across the measurement area (4mm x 4mm), significantly reducing the relative precision of temperature measurement. Furthermore, the cooling effect of the MEMS nozzle jet reduces dramatically when flow confinement effect appears. In view of these observations, a quartz temperature imager, thin-walled MEMS nozzles and nozzle arrays have been designed and fabricated, and used to perform further experimental investigation of impinging-jet cooling.

3.4.1 Design and Fabrication of Devices

I. Quartz Temperature Sensor Array Chip

A 2nd generation temperature-sensor-array chip was successfully fabricated and used as a test target for the impinging jet system. This 2 cm x 2 cm device, fabricated on a quartz substrate, has integrated heating resistors on the bottom and 84 temperature sensors on the top. Figure 3.4.1 shows a completed quartz temperature imager chip mounted on a PC board, which provides the necessary electrical interconnects, and the entire setup is ready to be mounted on a vacuum chuck for impinging jet testing. The uniformity of the surface temperature distribution produced by these backside heaters was verified by direct measurement from the calibrated surface sensors.

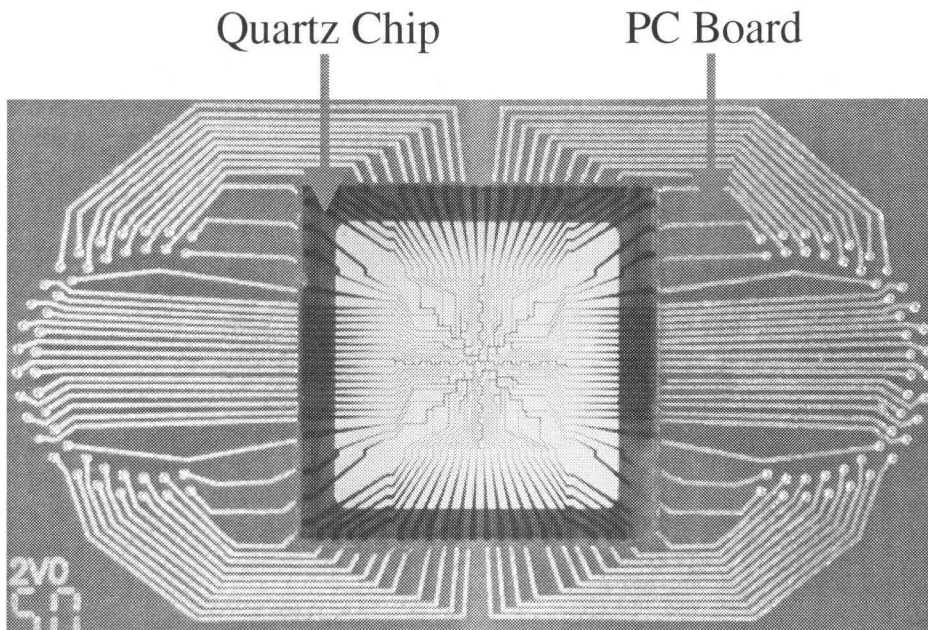


FIGURE 3.4.1 A quartz temperature imager mounted onto a PC board.

Quartz was used as a substrate because its thermal conductivity is two orders of magnitude lower than silicon (1.4 W/m K versus 148 W/m K) [25]. This should

increase the thermal isolation of each temperature sensor embedded on the surface, as well as improve the acquisition of local temperature measurements. Each individual sensor is $4\ \mu\text{m} \times 4\ \mu\text{m}$ in area, as pictured in Figure 3.4.2. In addition, similar silicon based target chips were also fabricated. These chips incorporated all the integrated sensors and heaters of the quartz design, plus the added bonus of having backside temperature sensors for heat flux measurements. The backside sensors are pictured in Figure 3.4.3. Benefiting from experience with previous target chip designs, we arranged the sensors in a semi-radial array from the center. As shown in Figure 3.4.4, near the center, the sensors are regularly spaced in a 5×5 square array. Further away, the remaining 59 sensors are separated in the theta-direction every 22.5 degrees. Their radial spacing has also been staggered in order to increase the concentration of sensors near the center, the jet impingement point. Also, the radial spacing gradually increases away from the center.

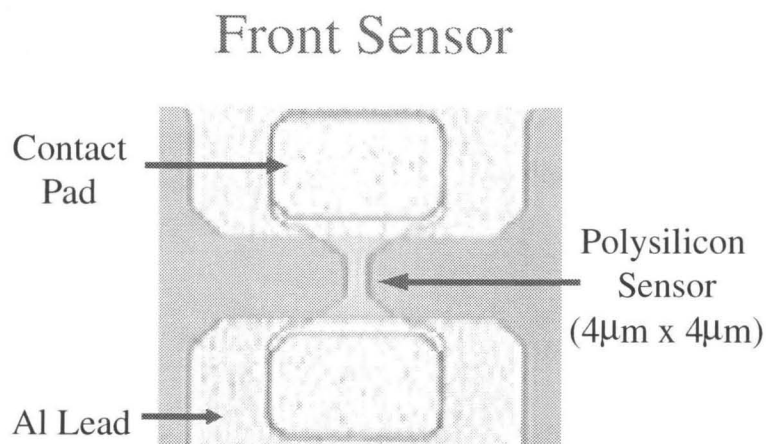


FIGURE 3.4.2 A picture of a sensor on the front side.

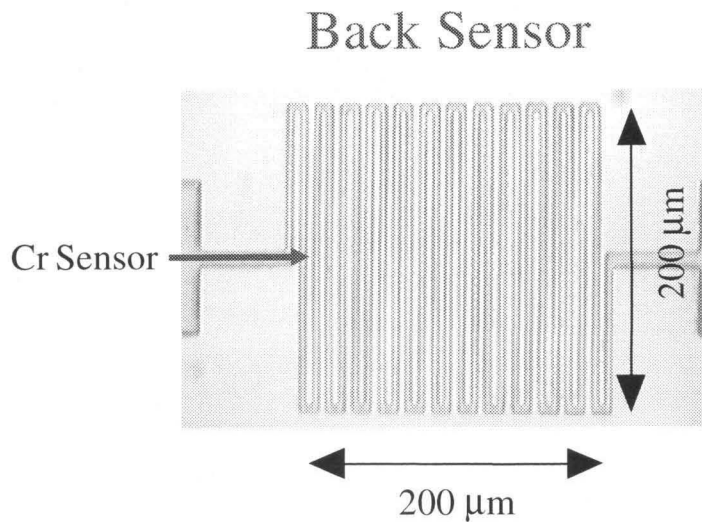


FIGURE 3.4.3 A picture of a sensor on the front side.

As illustrated in Figure 3.4.5, the process flow for the quartz based sensor array is similar to previous designs. Starting with a bare 4 in. diameter, 0.5mm thick quartz wafer, 0.5 μm of polysilicon is LPCVD deposited. The polysilicon is then masked and boron ions are implanted. The lightly doped polysilicon, defining the sensors, is then remasked and ion implantation is repeated to yield the heavily doped, lower resistance contact leads for each sensor. The excess polysilicon is then patterned and removed by RIE. Next, an approximately 1.5 μm-thick layer of LTO is LPCVD deposited. The entire wafer is then annealed at 1050°C for 30 minutes. Then, RIE is used to open contact openings on the topside in the oxide. Processing of the topside is finished after the deposition of a 1 μm thick layer of aluminum contact pattern. Backside processing is then done with RIE that opens contacts through the oxide layer to the polysilicon. Then, a Cr(0.1 μm)/Cu (0.5 μm) metalization is done. Finally, the metal is patterned to define the heaters in the case of the quartz chip, or the backside sensors and heater in the case of the silicon chip.

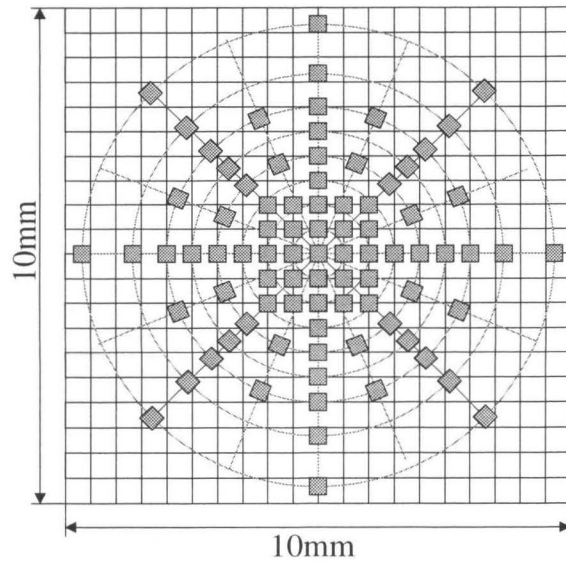


FIGURE 3.4.4 Sensor arrangement on the quartz temperature imager.

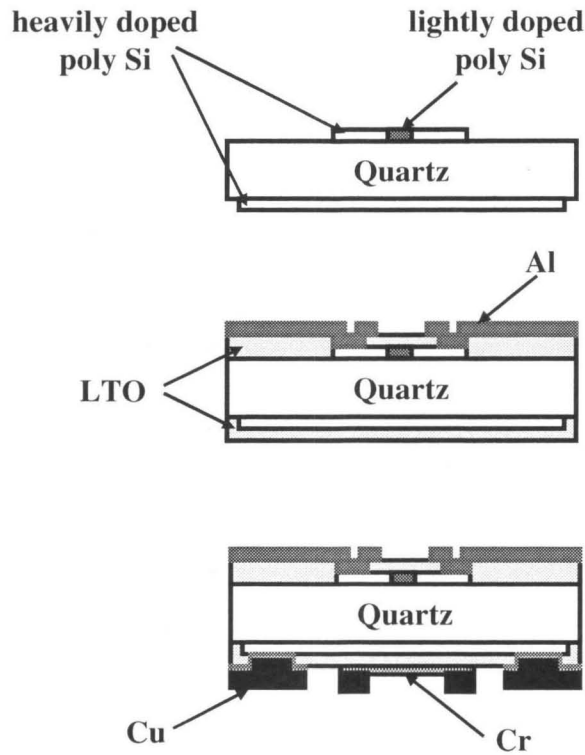


FIGURE 3.4.5 Process flow of the quartz temperature imager.

II. MEMS Single Thin-Wall Nozzle and Thin-Wall Nozzle Arrays

As discussed in Section 3.3.3, heat transfer effectiveness tends to be reduced by the confinement of flow between the nozzle and impingement surfaces. In order to reduce the confinement effect, the second generation MEMS single nozzles and nozzle arrays have been fabricated [24]. Figures 3.4.6 and 3.4.7 show such thin-wall single nozzle and thin-wall nozzle arrays in 1 x 2, 2 x 2 and 10 x 10 arrangements. The nozzles (diameter $D=0.5$ mm) are made with two DRIE steps and have a thin wall (0.1 mm) to eliminate flow confinement between the nozzle and chip, improving heat transfer effectiveness. The fabrication process is shown in Figure 3.4.8. Starting with a thermal oxide layer grown on both sides of a bare $\langle 100 \rangle$ Si wafer, thermal oxide was patterned to define nozzles. Then photoresist was spin coated and patterned for the nozzle wall. After the first DRIE for 200mm to initiate nozzles, thermal oxide was removed from most of the wafer except underneath the photoresist, which defines the nozzle wall. The second step of DRIE is then applied to etch through the wafer to complete the nozzles.

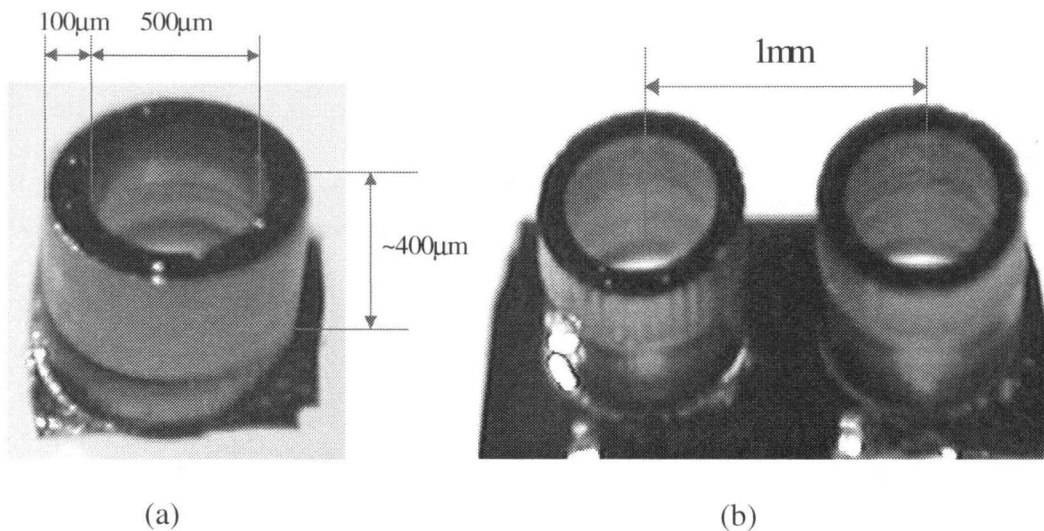


FIGURE 3.4.6 MEMS (a) single and (b) 2 x 1 array nozzles.

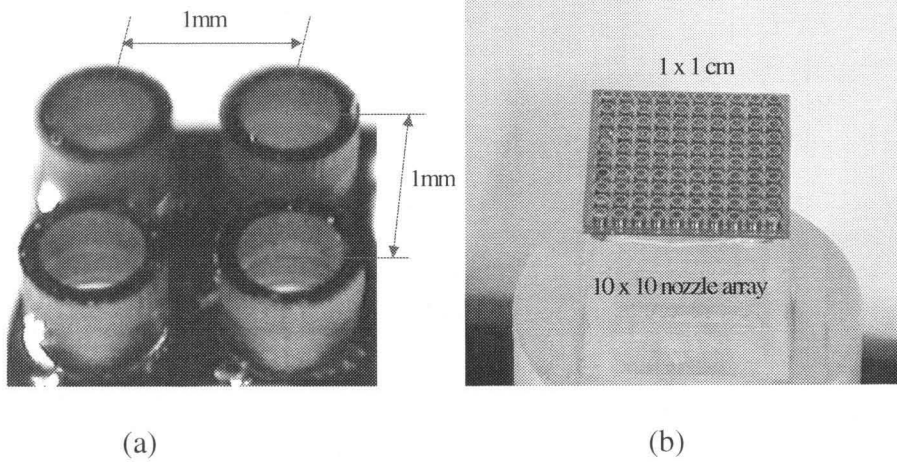
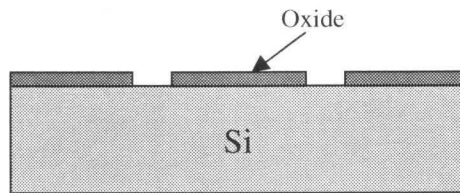
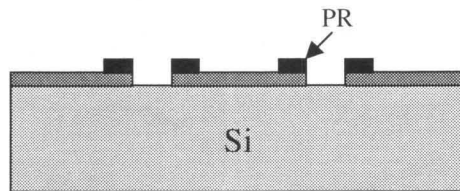


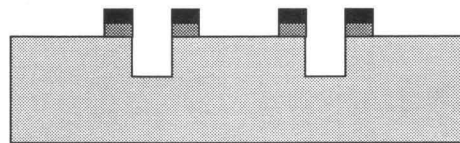
FIGURE 3.4.7 MEMS (a) 2 x 2 and (b) 10 x 10 array nozzles.



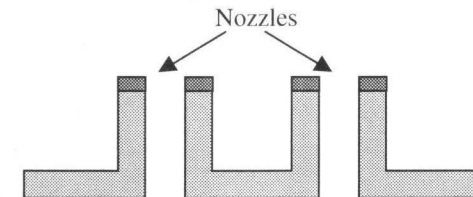
1. Thermal Oxidation.
2. Patterning oxide defines nozzles.



3. PR spinning and patterning nozzle wall.



4. DRIE 200 μm to initiate nozzles.
5. Oxide etching.



6. DRIE through-etching to complete nozzles.

FIGURE 3.4.8 Process flow of thin-wall nozzles.

3.4.2 Modification of Instrumentation

A few modifications of the experimental investigation in this section have been included. A more stable and compact constant current circuit has been designed, and a 200-channel Data Acquisition system has been used to provide enough channels for the quartz temperature imager. In addition, the data for 2-D temperature distribution on the impingement surface has been further processed to obtain the 2-D distribution of heat transfer coefficient or local heat transfer coefficient.

I. Constant Current Circuit

In our setup for the silicon and quartz temperature imagers, we used the LM334 constant current source IC and IC current mirrors (MOSIS Chip, which is originally developed for the UAV project [1]) to provide constant current bias to the sensors (as shown Figure 3.4.9). Since the LM334 has a positive temperature coefficient, we used an extra resistor and diode to cancel out the temperature drift. $R1$ and $R2$ set the current for the IC. The feature summary of the MOSIS chip is described in appendix A. Figure 3.4.10 shows the picture of a constant current circuit board. This design provides constant current sources that are less sensitive to the environmental temperature, and the circuit board is more compact because of the MOSIS chip.

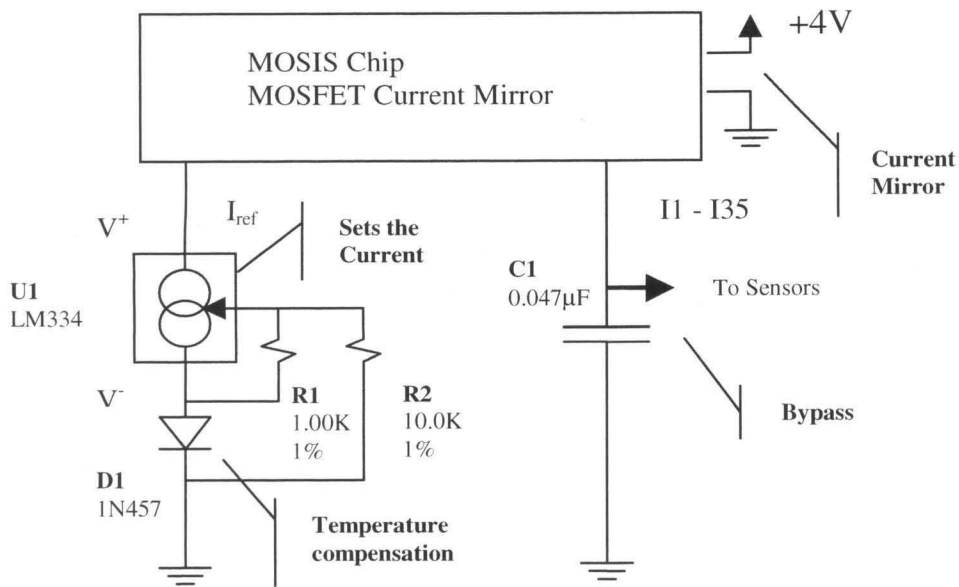


FIGURE 3.4.9 Conceptual diagram of 2nd generation constant current circuit.

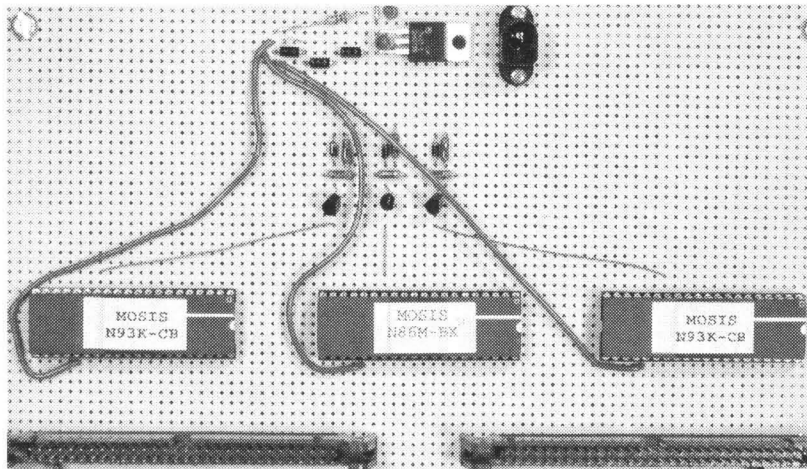


FIGURE 3.4.10 The picture of a constant current circuit board.

II. Data Acquisition System

In addition, a 200-Channel Data Acquisition System replaces the HP349 Data Acquisition System in order to provide enough channels for the quartz imager chip (84 temperature sensors on the front side). It was built by Mr. Tianxiang Weng of the Caltech

Micromachining Laboratory [30]. Appendix B summarizes the features of this data acquisition system.

3.4.3 Data Processing

The temperature sensor readings give the temperatures at a collection of sample points (Figure 3.4.4). As shown in Figure 3.4.11, these sample-point temperatures from thermistors are used to obtain the temperature distribution over the impingement surface, which is in turn used as input to a finite element simulation for calculating the heat flux, and finally the heat transfer coefficient.

For an array of micro impinging jets, the temperature distribution over the impingement surface is two-dimensional. In this case, the interpolation package in MATLAB is used to find the temperatures at points other than the temperature sensor locations. When a single round jet impinges upon the quartz chip, the ideal temperature distribution is axisymmetric, i.e., the temperature on the impingement surface only depends on the distance from the jet impingement center. Figure 3.4.12 shows a typical temperature distribution on the quartz impingement surface of a single MEMS thin-wall nozzle. However, since the nozzle surface is not precisely aligned with the impingement surface due to placement imperfections, there are errors in the axisymmetry of the sample point temperatures. In addition, the location of the jet center is not precisely known, especially because of the small jet size. To address this issue, we use the least-squares method to fit an axisymmetric cubic spline [31] to the sample-point temperatures. The center of the axisymmetric cubic spline is chosen by an optimization procedure such that

the least-squares curve fitting error is minimized. Figure 3.4.13 shows a typical fitted axisymmetric temperature distribution.

Once the temperature distribution on the quartz chip's front side (i.e., the impingement surface) is known, the ABAQUS finite element package is used for analysis of heat conduction in the quartz chip. This analysis is performed on the $10 \times 10 \text{ mm}^2$ section of the quartz chip whose front side is covered by the temperature sensors. Thus, in the finite element model the front side has a prescribed temperature distribution. Assuming uniform heating of the polysilicon heater, the heat flux onto the back side is uniform and given by the total power divided by the chip area. Since the chip's thickness (0.5 mm) is far less than its transverse dimension (10 mm), the boundary conditions at the peripheral faces (normal to the front and back sides) of the $10 \times 10\text{-mm}^2$ chip section are unimportant. Figure 3.4.14 shows a 3-D plot of the heat transfer coefficient of a thin-wall MEMS single jet (see Figures 3.4.6).

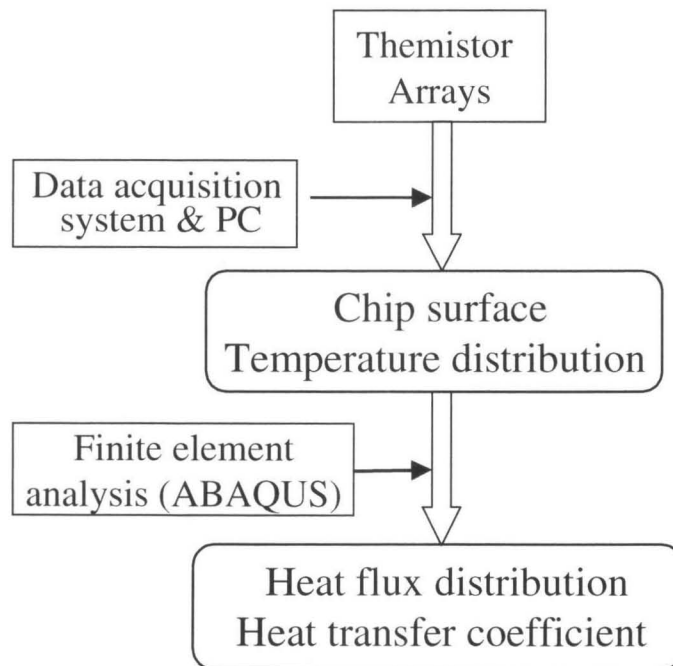


FIGURE 3.4.11 Data processing flow.

Thus, from measurement and finite element analysis, we find the temperature, T , and heat flux q , on the impingement surface. The heat transfer coefficient is then computed from the formula

$$h = \frac{q}{T - T_{\infty}},$$

where T_{∞} is the ambient temperature.

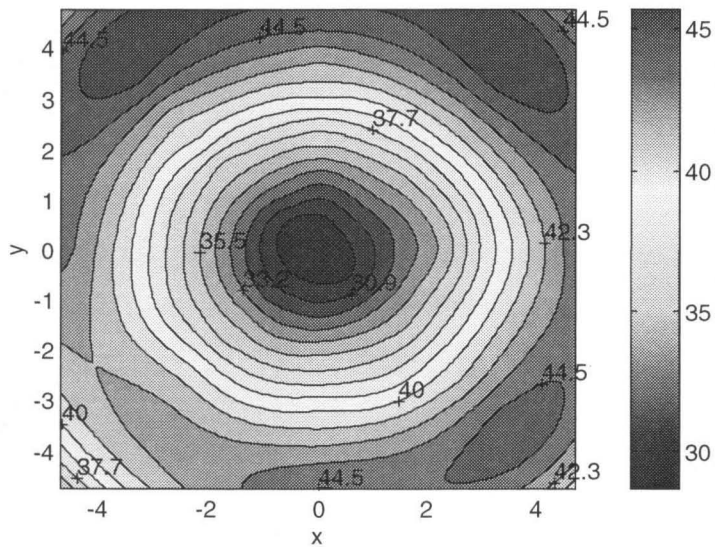


FIGURE 3.4.12 Temperature distribution over the impingement surface ($p=1.8$ psi, $H/D=1$).

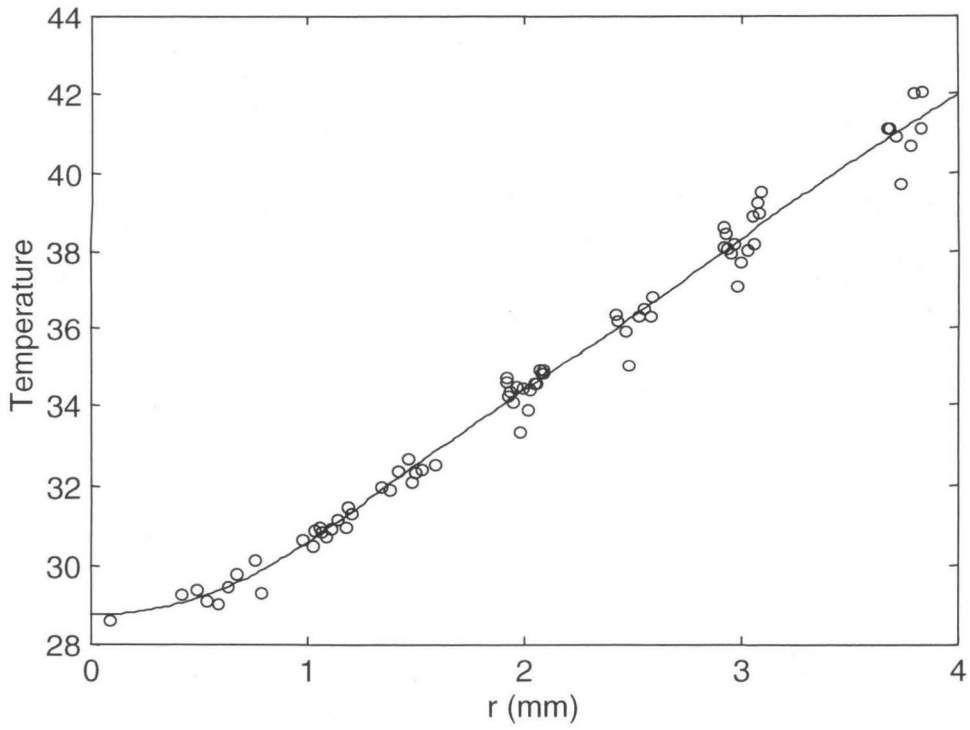


FIGURE 3.4.13 Fitted axisymmetric cubic spline vs. measured temperatures over the impingement surface ($p=1.8$ psi, $H/D=1$).

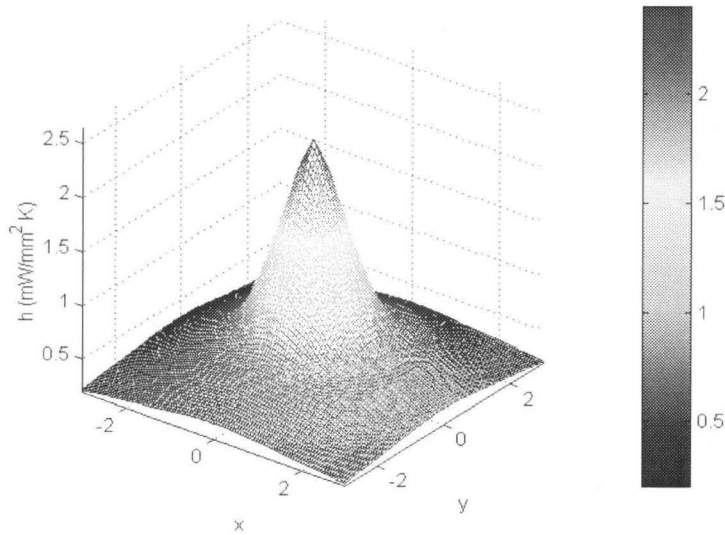


FIGURE 3.4.14 3-D plot of local h of a MEMS single jet ($p=1.8$ psi, $H/D=1$).

3.4.4 Heat Transfer Data and Discussion

We have studied single and array jets, each of which was discharged from a MEMS nozzle of diameter $D=500\ \mu\text{m}$ for different jet heights, H , and driving pressures, p , across the nozzle. Note that, equivalent to the driving pressure, the flow rate could be used as a parameter. Most tests were conducted with approximately 1.5 W of power.

I. Impingement Heat Transfer of MEMS Single Thin-Wall Nozzle

In the single impinging jet case, a typical measured temperature distribution is shown in Figures 3.4.12. It can be seen that the temperature distribution over the impingement surface is, as expected, highly axisymmetric. The corresponding axisymmetric cubic spline is shown in Figure 3.4.13. We see that there is reasonably good agreement between the fitted spline and measured temperatures.

Temperature distributions obtained from measurements and curve fitting were then used to perform finite element computation of the heat flux, q , from the impingement surface to the impinging micro jet. The heat transfer coefficient, h , was then computed from the formula given in the previous section. Figure 3.4.14 depicts a 3D plot of h over the chip surface. The variation of h with the distance from the jet center, r , is shown in Figure 3.4.15 for driving pressures (p) from 0.4 psi to 2.0 psi. This pressure range corresponded to a flow rate between 0.4 and 1.1 SLPM. The corresponding Reynolds number, defined as $Re=uD/\nu$ (u is the average air velocity at the nozzle exit and ν the kinematic viscosity of air), took on a value between 1800 and 2900. It can be seen that as the pressure drop increases, the heat transfer coefficient h also increases. In addition, the maximum of h occurs at the jet center at lower pressures, while shifting off

center at the highest pressure studied (2.0 psi). This is in agreement with macro-jet data [3], as h for macro turbulent jets achieves its maximum off jet center for $H/D < 4$. Note that at $p=2.0$ psi and $Re=2900$, the micro jet is just entering the turbulent flow regime.

Figure 3.4.16 shows the heat transfer coefficient distribution for different jet heights (H). We can see that except in a region very close to the jet center, h is very insensitive to H for H/D between 1 and 6. This insensitivity can be more clearly observed in Figure 3.4.17, which illustrates the average heat transfer coefficient, denoted h_{av} and computed over a disk of radius $2D$, as a function of H/D for different driving pressures. In addition, maximum peak of h was observed off the center (Figures 3.4.15 and 3.4.16) with a high driving pressure (>2 psig) and a small height ($H/D \neq 3$). It may correspond to the actual secondary maximum peak of h which exists for turbulent macro jets [1, 23], while the first maximum peak of h could be missed or averaged away because of its small diameter. Further investigation with a denser array of thermistors is necessary to examine the heat transfer characteristics around the small impingement center.

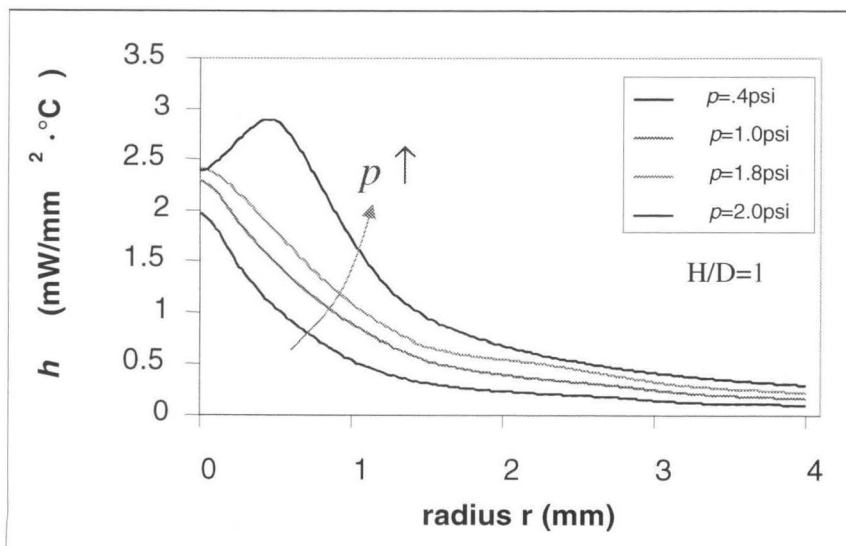


FIGURE 3.4.15 Local heat transfer coefficient of a MEMS thin-walled jet for different driving pressures.

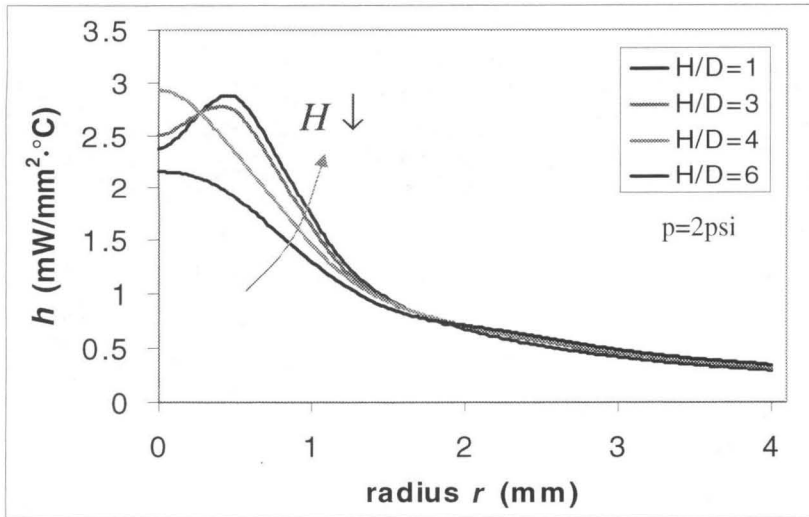


FIGURE 3.4.16 Local heat transfer coefficient of a MEMS thin-walled jet for fixed pressure for different jet heights.

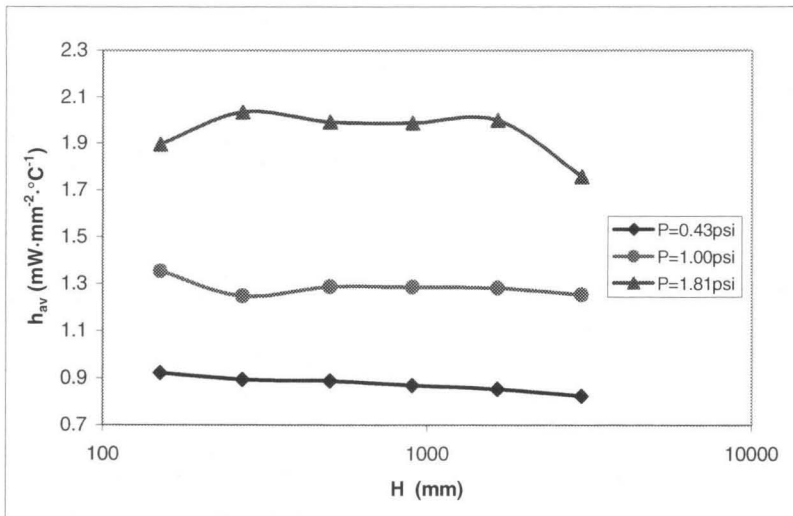


FIGURE 3.4.17 Average heat transfer coefficient of a MEMS single jet for different driving pressures.

The effective cooling range r_{eff} can be defined as the location where the heat transfer coefficient is only half of the maximum value, i.e.,

$$\frac{h(r_{eff})}{h_{max}} = \frac{1}{2} \quad (3.17)$$

As we can find for Figures 3.4.15 and 3.4.16, r_{eff} changes from one jet diameter to two times the jet diameter as the pressure changes from 0.4 psig to 2.0 psig, but is far less sensitive to the spacing between the jet and impinged surface if $H/D < 6$. This provides the reference spacing between the individual single jet for jet arrays that are studied in the following.

II. Impingement Heat Transfer of MEMS Thin-Wall Nozzle Array

In addition to single jets, arrays of micro impinging jets have also been investigated. The MEMS nozzles were arranged in 2×1 and 2×2 , as well as 10×10 arrays. Figure 3.4.18 shows a representative distribution of h , the heat transfer coefficient, for a 2×1 jet array. We can clearly see that h has two maxima corresponding to the individual jets that make up the array, and quickly levels off as one moves away from the jet array. The local heat transfer coefficient of the other types of jet arrays exhibited a similar qualitative behavior.

With the relatively simple geometry of 2×1 micro impinging jet arrays, we were able to investigate the dependence of the average heat transfer coefficient, h_{av} , on the jet-to-jet spacing. Figures 3.4.19 and 3.4.20 depict this dependence for different flow rates and jet heights, respectively. It can be seen that while the influence of the jet spacing on the average heat transfer coefficient is generally insignificant, h_{av} does increase slightly as the jet spacing is decreased from 2 mm to 1 mm (arranged for $r_{eff}/D = 1-2$). This

increase in h_{av} is more noticeable at larger flow rates or smaller jet heights. This may have been caused by the enhanced interaction between the individual jets at higher flow rates or lower jet heights.

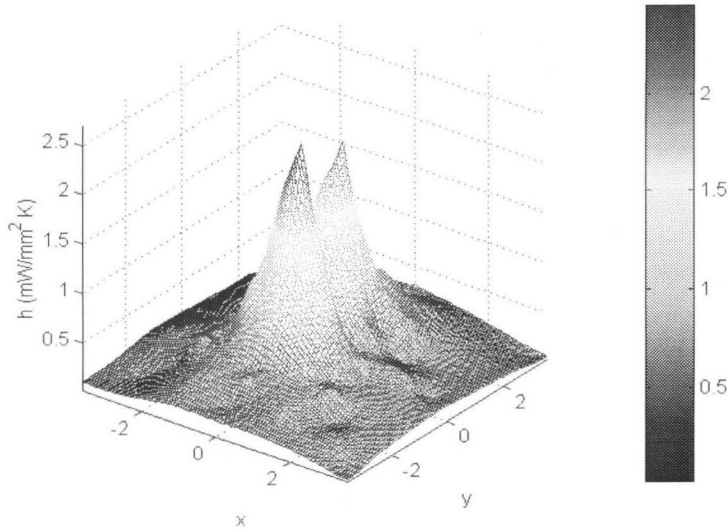


FIGURE 3.4.18 Local h of a 2x1 jet array ($Q=1.4$ SLPM, $H/D=3.3$, $a=1.5$ mm).

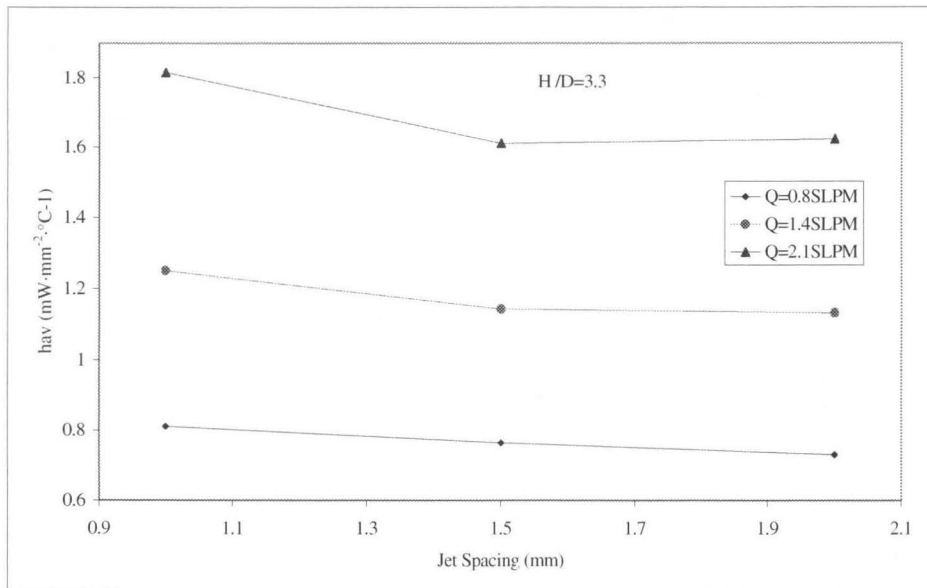


FIGURE 3.4.19 Dependence on jet-to-jet spacing of the average heat transfer coefficient of a 2 x 1 jet array at different flow rates.

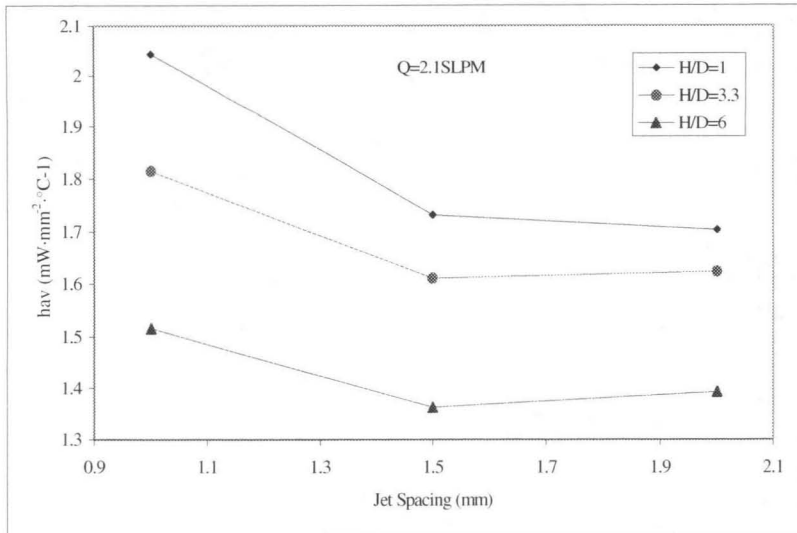


FIGURE 3.4.20 Dependence on jet-to-jet spacing of the average heat transfer coefficient of a 2 x 1 jet array for different jet heights.

By using 2x1 and 2x2 jet arrays, the effects of the driving pressure or flow rate, as well as the jet height, on the average heat transfer coefficient have been studied. Shown in Figure 3.4.21 is h_{av} as a function of jet height for different driving pressures for a 2x2 jet array (with a jet-to-jet spacing of 1 mm). It is clear from Figures 3.4.21 and 3.4.22 that higher driving pressures or flow rates resulted in enhanced heat transfer. As for the effect of the jet height, Figure 3.4.21 indicates that the average heat transfer coefficient increases as H decreases to an optimum (between $H=0.25$ to 0.5 mm), after which h_{av} drops slightly. Note that the heat transfer enhancement effect of smaller jet heights can

also be observed in Figure 3.4.20. Thus, the interaction between the jets facilitated heat transfer. Further investigation is needed to understand the mechanism of this interaction.

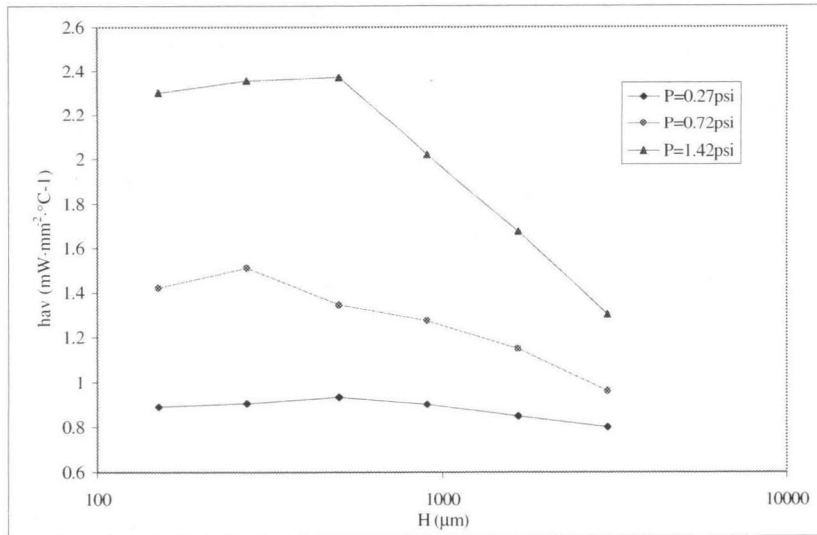


FIGURE 3.6.21 Average heat transfer coefficient of a 2 x 2 jet array for different driving pressures.

Finally, to assess the viability of using micro impinging arrays to build MEMS heat exchangers, we have been investigating heat transfer characteristics of micro impinging jet arrays in more complicated MEMS nozzle arrangements. Our preliminary results from a 10×10 MEMS jet array (with a jet-to-jet spacing of 1 mm and a jet height between 0.25 mm and 0.5 mm) indicate that at a driving pressure 0.2 and a flow rate of 6 SLPM, one can achieve $h_{av} = 1 \text{ mW/mm}^2$ over the 1-cm² area covered by the array (as shown in Figure 3.6.22). For comparison, consider a macro single jet, which has the same flow rate (6 SLPM) and total cross-sectional area ($100\pi D^2/4$) as the 10×10 micro jet array. (The macro jet diameter is thus 5 mm.) According to the correlation formula given

in Ref. [1], the macro jet's average heat transfer coefficient over a 1-cm² area is approximately 0.17 mW/mm². It follows that the heat transfer rate of the 10×10 micro jet array, in addition to being more uniform, is 6 times that obtainable by the macro single jet. We can thus see that MEMS heat exchangers using micro impinging jet arrays can provide highly effective and uniform cooling.

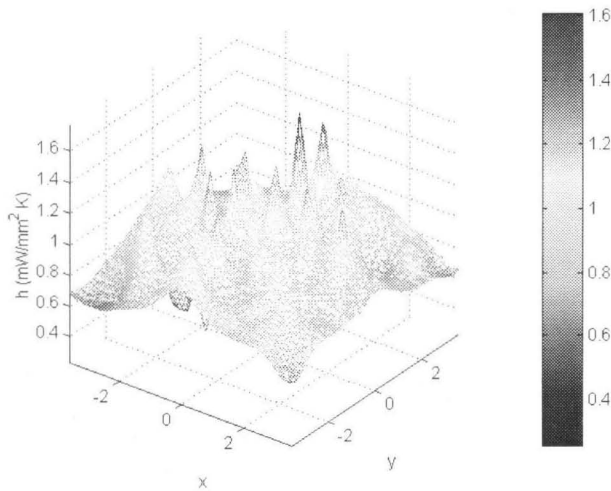


FIGURE 3.6.22 Average heat transfer coefficient of a 10 x 10 jet array ($Q = 6$ SLPM, $H = 0.25$ mm, $P = 11$ W).

3.5 Conclusion

MEMS impinging-jet cooling has been studied using temperature imagers with integrated micro heaters and thermistors made of polysilicon thin films. The study has yielded a MEMS-based heat transfer measurement paradigm, as well as extensive experimental data on jet-impingement heat transfer. The MEMS-based measurement paradigm successfully integrates sensing and heating, and for the first time allows high-resolution measurements of the 2-D temperature distribution over an adequately large impingement

surface area. The heat transfer data demonstrates the excellent promise of micro-impinging-jet heat transfer, and provides useful rules for designing impinging-jet-based micro heat exchangers.

In single-jet cooling, the higher the driving pressure, the higher the heat transfer coefficient. The reason is that the mass flow rate increases with the driving pressure, allowing the heat to be removed more effectively. The stronger turbulence level due to an increase of the gas speed also enhances the heat transfer. On the other hand, the heat transfer rate of a impinging jet with a single MEMS nozzle starts to decrease significantly when the jet height is lowered from three times the nozzle diameter due to the confinement effect between the nozzle and impinged surfaces. Such confinement effect has been successfully eliminated with a thin-walled MEMS nozzle, and hence a relatively large tolerance in the jet height (H/D varied from 1 to 6) was allowed. Finally, the heat transfer coefficient of single impinging jets with a thin-walled nozzle show the peak values as high as $0.3 \text{ W/cm}^2\text{K}$ (several times larger than conventional jets), as well as an approximate effective cooling range of one to two times nozzle diameters. This demonstrates the excellent effectiveness of micro impinging jets for local spot cooling, and provides a guideline for designing practical micro heat exchangers.

The experiments with micro impinging-jet arrays have yielded useful results on the influence of the jet-to-jet spacing, the flow rate, as well as the jet height on the heat transfer rate. The jet-to-jet spacing appears to have an insignificant effect on the heat transfer, while higher flow rates result in higher heat transfer rates. It has been shown that the jet height influences the heat transfer quite significantly. As the jet height decreases down to an optimal value, the average heat-transfer coefficient increases. This

phenomenon is in contrast to the single-jet case, where the jet height has a much less *significant effect*. The interaction between adjacent jets is believed to contribute favorably to enhance the heat transfer. To demonstrate applications of impinging-jet arrays to micro heat exchangers, we experimented with a 10 x 10 jet array. The resulting data show that a considerably uniform heat transfer coefficient, on the order of 0.1 W/cm²K, can be achieved. This rate, approximately 6 times that achievable by a comparable macro single jet, shows that micro impinging-jet-array based heat exchangers are quite promising.

References:

- [1] H. Martin, "Heat and mass transfer between impinging gas jets and solid surfaces," in *Advances in Heat Transfer*, vol. 13 (Edited by T. Irvine and J. P. Harnett), pp. 1-60, Academic Press, New York (1977).
- [2] S. Polat, B. Huang, A.S. Mujumdar, and W. J. M. Douglas, "Numerical flow and heat transfer under impinging jets: a review," in *Annual Review Of Numerical Fluid Mechanics And Heat Transfer*, vol. 2, pp. 157-197, 1989.
- [3] K. Jambunathan, E. Lai, M. A. Moss, and B. L. Button, "A review of heat transfer data for single circular jet impingement," *International Journal Of Heat And Fluid Flow*, pp. 106-115, vol.13, No. 2, June 1992.
- [4] F. P. Incropera and D. P. Dewitt, "Impinging jets," in *Fundamentals of Heat and Mass Transfer*, 4th edition, pp. 387-396, JOHN WILEY & SONS.
- [5] J. W. Gauntner, J. N. B. Livingood, and P. Harycak, "Survey of literature on flow characteristics of a single turbulent jet impinging on a flat plate," NASA, TN D-5652 NTIS N70-18963, 1970.
- [6] I. Tani, and Y. Komatsu, "Impingement of a round jet on a flat surface," *Proc. Of the Eleventh International Congress of Applied Mechanics* (H. Gortler, Ed.), Springer-Verlag, New York, pp. 672-676, 1966.
- [7] F. Giralt, C. J. Chia, and O. Trass, "Characterization of the impingement region in an axisymmetric turbulent jet," *Ind. Eng. Chem. Fundam.*, vol. 16, pp. 21-28, 1977.
- [8] N. Didden and C. M. Ho, "Unsteady separation in a boundary-layer produced by an impinging jet," *Journal of Fluid Mechanics*, vol. 10, pp. 235-256, 1985.

- [9] Cz. O. Popiel and L. Boguslawski, "Mass or heat transfer in impinging single round jets emitted by a bell-shaped nozzle and sharp-ended orifice," in C. L. Tien, V. P. Carey, and J. K. Ferrell, Eds., *Heater Transfer* 1986, vol. 3, Hemisphere Publishing, New York, 1986.
- [10] R. J. Goldstein and J. F. Timmers, "Visualization of heat-transfer from arrays of impinging jets," *International Journal Of Heat And Mass Transfer*, 25: (12) 1857-1868, 1982.
- [11] K. Okutani, K. Otsuka, K. Sahara, and K. Satoh, "Packaging design of a SiC ceramic multi-chip RAM modules," *Proceedings of Fourth Annual International Electronics Packaging Conference*, 1984, pp. 229-304.
- [12] R. G. Biskeborn, J. L. Horvath, and E. B. Hultmark, "Integral Cap Heat Sink Assembly for the IBM 4381 Processor," *Proceedings of Fourth Annual International Electronics Packaging Conference*, 1984, pp. 468-474.
- [13] D. B. Tuckerman and R. F. W. Pease, "High-performance Heat Sink for VLSI," *IEEE Electron Device Letters*, May 1981, vol.2, No. 5, pp. 126-129.
- [14] M. Monde and Y. Katto, "Burnout in High Heat-Flux Boiling System with An Impinging Jet," *International Journal of Heat and Mass Transfer*, vol. 21, pp. 295-305, 1978.
- [15] M. Mark, M. Stephenson, and C. E. Goltsos, "An Evaporative Gravity Technique for Airborne Equipment Cooling," *IRE Transactions*, vol. ANE-5, 1958, pp. 47-52.
- [16] C. E. Goltsos and M. Mark, "Packaging with a Flexible Container for Oil-Filled or Evaporative Cooled Electronic Equipment," *IRE Transportations*, vol. PEP-6, 1962, pp. 44-48.

- [17] F. E. Megerlin and P. Ningerhoet, "Thermal Control of Densely Packaged Microelectronics in Dielectric Fluids," *Proceedings National Aeronautical Electronics Conference*, 1971, pp. 254-259.
- [18] N. G. Aakalu, R. C. Chu, and R. E. Simons, "Liquid Encapsulated Air Cooling Module," *U.S. Patent* No. 3,741,292.
- [19] R.E. Simons, "Thermal Management of Electronic Packages," *Solid State Technology* 26: (10) 131-137, 1983.
- [20] B. Hollworth, and M. Durbin, "Impinging Cooling of Electronics," *J. Heat Transfer*, v. 114, pp. 607-613, August 1992.
- [21] J. Seyed-Yagoobi, "Enhancement of Heat and Mass Transfer with Innovative Impinging Jets," *Drying Technology*, 14(5), pp. 1173-1196 (1996).
- [22] C-L. Tien, A. Majumdar, F. Gerner, ed., "Microscale Energy Transport," *Series in Chemical and Mechanical Engineering*, Taylor & Francis, 1998.
- [23] N. Didden and C. M. Ho, "Unsteady Separation in a Boundary-Layer Produced by an Impinging Jet," *Journal of Fluid Mechanics*, 160: (NOV) 235-256 1985.
- [24] S. Wu, J. Mai, Y.C. Tai, and C.M. Ho, "Micro Heat Exchanger by Using MEMS Impinging Jets," *Proc. 12th Annual International Workshop on Micro Electro Mechanical System*, pp. 171-176, January 17-21, 1999, Orlando, Florida.
- [25] D. R. Lide, ed., "Handbook of chemistry and physics," 77th edition, 1996-1997.
- [26] O. A. Moreno, R. H. Katyl, J. D. Jones, and P. A. Moschak, "Mass transfer of an impinging jet confined between parallel plates," *IBM J. Res. Develop.*, vol. 37, No. 2, pp. 143-155, March 1993.

- [27] D. W. Colucci and R. Viskanta, "Effect of nozzle geometry on local convective heat transfer to a confined impinging air jet," *Experimental Thermal and Fluid Science*, vol. 13, pp. 71-80, 1996.
- [28] A. Huber and R. Viskanta, "Effect of jet-jet spacing on convective heat transfer to confined, impinging arrays of axisymmetric air jets," *Int. J. Heat Mass Transfer*, vol. 37, No. 18, pp. 1859-2869, 1994.
- [29] J. Y. San, C. H. Huang, and M. H. Shu, "Impingement cooling of a confined circular air jet," *International Journal Of Heat And Mass Transfer*, vol. 40: (6) 1355-1364, Apr. 1997.
- [30] F. Jiang, Y. Xu, T. Weng, Z. Han, Y. C. Tai, A. Huang, C. M. Ho, and S. Newbern, "Flexible shear stress sensor skin for aerodynamics applications," *Proc. 13th Annual International Workshop on Micro Electro Mechanical System*, pp. 364-369, January 23-27, 1999, Miyazaki, Japan.
- [31] P. Dierckx, *Curve and Surface Fitting with Splines*, Clarendon Press, 1993.
- [32] D. Lytle, and B.W. Webb, "Secondary Heat Transfer Maxima for Air Jet Impingement at Low Nozzle-to-Plate Spacings," *Proc. 2nd World Conf. on Experimental Heat Transfer, Fluid Mechanics, and Thermodynamics*, pp. 776-783, Dubrovnik, Yugoslavia, 1991.
- [33] Pentium® III Processors – Datasheets, available at
<http://developer.intel.com/design/pentiumiii/datashts/>

CHAPTER 4

SUSPENDED MICRO CHANNELS WITH INTEGRATED POLYSILICON THERMISTORS

ABSTRACT

A freestanding microchannel, with integrated thermistors, has been developed for high-pressure flow studies. These microchannels are approximately $20\mu\text{m} \times 2\mu\text{m} \times 4400\mu\text{m}$, and are suspended above $80\mu\text{m}$ deep cavities, bulk micromachined using a BrF_3 dry etch. Volumetric flow rates of N_2 in the microchannel were measured at inlet pressures up to 578 psig. Discrepancies between the data and theory resulted from the flow acceleration in the channel, the non-parabolic velocity profile, and the bulging of the channel. Bulging effects were evaluated by using incompressible water flow measurements, which also led to a measurement of $0.001045 \text{ N}\cdot\text{s}/\text{m}^2$ for the viscosity of DI water. The temperature data from sensors along the channel shows isothermal flow in microchannel at inlet pressures up to 300 psig.

4.1 Introduction

Micromachining is a rapidly emerging technology in which micron-scaled fluidic devices are possible for the first time. For example, microchannels may be used in a variety of applications such as transport of fluid in micro chromatography [1] and electrophoreses [2-6], microfluidic control systems (micro pumps, micro valves, micro filter, micro flow meters) [7-8], micro reaction systems [9], and micro total analysis systems [10-12]. In order to design and fabricate such micro devices effectively, the physical laws governing fluid flow in small conduits needs to be understood. Such flow differs from its macroscopic counterpart in that non-continuum effects for a gas or polar mechanics effects for a liquid may not be negligible due to the small scale of the flow.

Furthermore, the characteristics of the fluid flow along its path (from the reservoir to the jet nozzle, to impingement surface and finally exit to the ambient) will have a significant impact on the heat exchanger's performance [13]. At the micro scale, such flow paths often take the form of micro channels. Therefore, the study of micro channel flow will greatly facilitate the understanding of fundamental operation principles of micro heat exchangers, and provide for an effective tool in practical micro heat exchanger design.

4.2 Overview of Previous Work

In recent years, microchannel flow has attracted considerable attention. Pfahler, et al. [14] estimated experimentally the friction factor for gas and liquid flow in small channels. Nevertheless, Arkilic et al. [15] considered the effect of compressibility in a microchannel flow. The most detailed studies up-to-date were conducted by Pong et al. [16], Shih et al. [17], and C. W. Chiu [18] who measured not only the overall pressure drop and flow rate, but also the pressure distribution along the microchannel. However, they were only able to obtain data for relatively low inlet pressures because of the low operating pressure in these devices [19]. They showed that by considering slip and compressible effects, the flow rate could be accurately determined.

There are only a few theoretical studies addressing compressible, viscous, steady laminar flow in small uniform conduits. Prud'homme et al. [20] calculated the mass flow rate of gas through a long tube for an ideal gas. Van den Berg [21] presented a detailed study using perturbation methods to calculate the mass flow rate of a gas through a cylindrical capillary. They clearly identified the effects of compressibility, acceleration and non-parabolicity of the velocity profile. Harley et al. [22] attempted to analyze the same flow in a microchannel, but as they stated, their model is mathematically inconsistent. Here we present an experimental study of gas and liquid flow through a microchannel under high inlet pressures. We compare the results with an analytical model developed for capillary flow that accounts for 2-D, slip and compressibility and corrects for flow acceleration and non-parabolicity. We show that under very high pressures, the resulting change in channel geometry needs to be considered.

Data for liquid flow through a microchannel is rare since not only a much higher pressure is required to obtain measurable values but also the channels are easily blocked by particles. This project then shows that the robust design of the present microchannels, together with the careful set-up of the external flow handling system, allows us to carry out accurate measurement of a liquid flow rate under high inlet pressure.

In addition, several investigations have been done to study heat transfer in microchannels [16], but no experimental data on the temperature distribution along a microchannel is available. This information is required to understand the heat transfer process and to develop a complete set of analytical models. This is the motivation behind the development of a suspended microchannel with integrated temperature sensors.

4.3 Fundamentals

This section reviews basic fluid mechanics results as relevant to microchannel flow [24-28]. Starting from the governing equations, i.e., the continuity, momentum and energy equations, the mass flow rate formulas are derived for incompressible liquid flow and compressible gas flow with several appropriate simplifications for micro channel flow.

4.3.1 Governing Equations

Fundamental studies of fluid mechanics [24-28] give the governing equations of fluid flow. The following list the differential equations of continuity, momentum, and energy:

$$\text{Continuity: } \frac{1}{\rho} \frac{D\rho}{Dt} + \nabla \cdot \bar{\mathbf{u}} = 0 \quad (4.1)$$

$$\text{Momentum: } \rho \frac{D\bar{u}}{Dt} + \nabla p = \rho G + \mu \nabla^2 \bar{u} + \left(\mu_v + \frac{1}{3}\mu\right) \nabla(\nabla \cdot \bar{u}) \quad (4.2)$$

$$\text{Energy: } \delta E = \delta Q + \delta W \quad (4.3)$$

In these equations, ρ is fluid density, t is time, \bar{u} is fluid velocity, p is pressure, G is the specific body-force, E is the fluid energy, Q is the heat and W is the work done to fluid.

For a steady state viscous flow at a small Reynold's number, Equations 4.1 and 4.2 can be further simplified as

$$\text{Continuity: } \nabla \cdot (\rho \bar{u}) = 0 \quad (4.4)$$

$$\text{Momentum: } \nabla p = \mu \nabla^2 \bar{u} \quad (4.5)$$

where the body-force has been ignored.

4.3.2 Simplifications for Micro Channel Flow

The coordinate system shown in Figure 4.3.1 is arranged so that the origin is at the center of the channel cross section at the inlet, the x-axis is along the flow direction, the y-axis along the channel height direction, and z-axis along the channel width direction. The flow in a channel with constant height and width can be further simplified by assuming the flow velocity in the directions y and z to be zero (i.e., $v=0$, and $w=0$), as shown in Equations 4.6 and 4.7.

$$\text{Continuity: } \frac{\partial(\rho u)}{\partial x} = 0 \quad (4.6)$$

$$\text{Momentum: } \frac{\partial p}{\partial x} = \mu \left(\frac{\partial^2 u}{\partial x^2} + \frac{\partial^2 u}{\partial y^2} + \frac{\partial^2 u}{\partial z^2} \right) \quad (4.7)$$

$$\frac{\partial p}{\partial y} = 0 \quad (4.8)$$

$$\frac{\partial p}{\partial z} = 0 \quad (4.9)$$

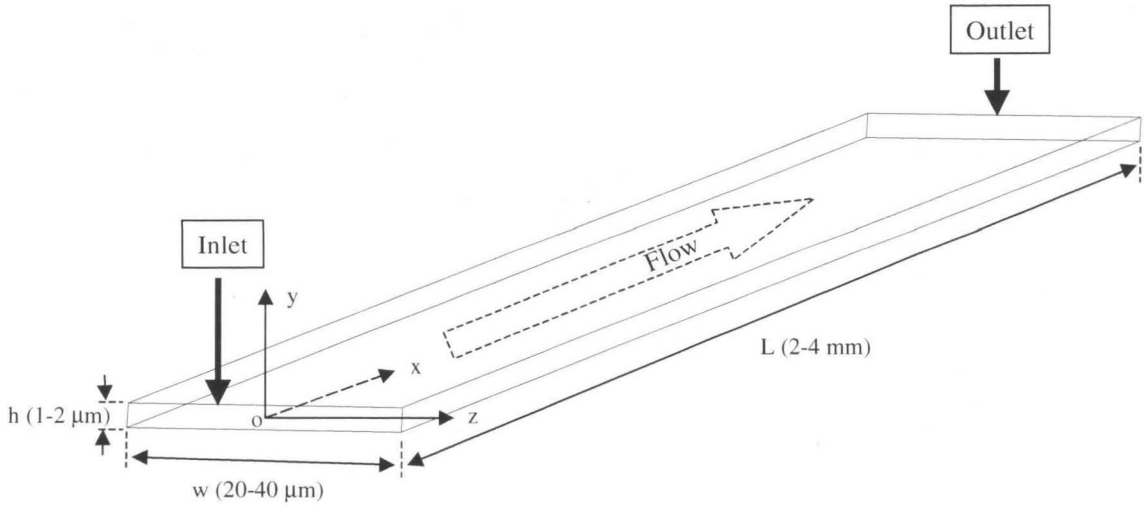


FIGURE 4.3.1 Coordinates used in the derivation of equations.

In our case, the channel height is much smaller than the width and length, and we have the following approximation:

$$\frac{\partial^2}{\partial y^2} \gg \frac{\partial^2}{\partial x^2}, \frac{\partial^2}{\partial z^2} \quad (4.10)$$

In addition, since the width is much larger than the height, the flow model can be approximated to 2-D flow as show in Figure 4.3.2. Applying such approximations to Equation 4.7, we have

$$\frac{\partial p}{\partial x} = \mu \frac{\partial^2 u}{\partial y^2} \quad (4.11)$$

From Equations 4.8 and 4.9, we know the pressure is only a function of x,

$$p = p(x) \quad (4.12)$$

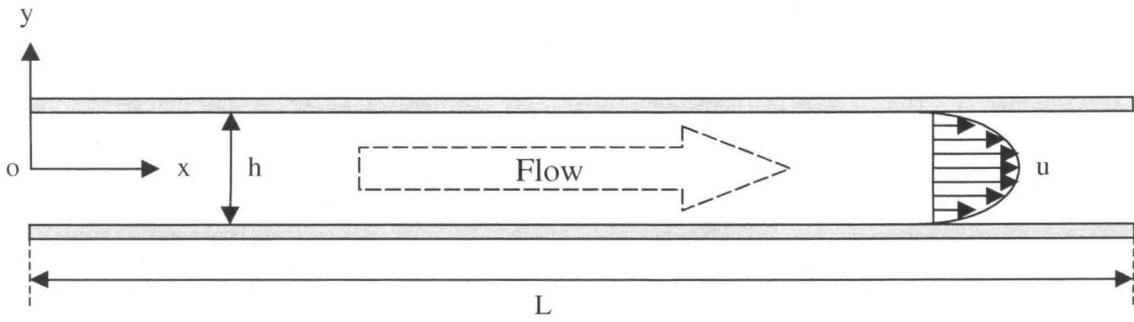


FIGURE 4.3.2 The coordinate system along the length direction.

Integrating Equation 4.11 twice along y direction, we get

$$u = \frac{1}{2\mu} \frac{\partial p}{\partial x} y^2 + C_1 y + C_2 \quad (4.13)$$

As we can see in Figure 4.3.2,

$$\left. \frac{du}{dy} \right|_{y=0} = C_1 = 0 \quad (4.14)$$

For non-slip boundary conditions, we have

$$u \Big|_{y=\pm \frac{h}{2}} = \frac{1}{2\mu} \frac{\partial p}{\partial x} \frac{h^2}{4} + C_2 = 0 \quad (4.15)$$

$$C_2 = -\frac{1}{8\mu} \frac{\partial p}{\partial x} h^2 \quad (4.16)$$

Substituting Equations 4.14 and 4.16 into Equation 5.13 then yields

$$u = -\frac{1}{2\mu} \frac{\partial p}{\partial x} \left(\frac{h}{2} \right)^2 \left(1 - \frac{y^2}{\left(\frac{h}{2} \right)^2} \right) \quad (4.17)$$

The mass flow rate can given by

$$\dot{m} = \int_{-\frac{h}{2}}^{\frac{h}{2}} \rho u dA = \rho w \int_{-\frac{h}{2}}^{\frac{h}{2}} u dy \quad (4.18)$$

Substituting Equation 4.17 into Equation 4.18, and integrating y from $-h/2$ to $h/2$, we have

$$Q_m = -\frac{1}{12\mu} \rho w h^3 \frac{\partial p}{\partial x} \quad (4.19)$$

4.3.3 Incompressible Micro Channel Flow

Assuming isothermal conditions for incompressible flow, we have

$$\rho \sim \text{constant} \quad (4.20)$$

$$\frac{\partial p}{\partial x} = -\frac{p_{in} - p_{out}}{L} \quad (4.21)$$

Applying above equations to Equation 4.19, we have equations for mass flow rate and volume flow rate,

$$Q_m = \frac{1}{12\mu} \rho w h^3 \frac{p_{in} - p_{out}}{L} = \frac{h^3 w \rho}{12\mu L} \Delta P \quad (4.22)$$

$$Q_v = \frac{Q_m}{\rho} = \frac{h^3 w}{12\mu L} \Delta P \quad (4.23)$$

4.3.4 Compressible Micro Channel Gas Flow

The state equation of gas can be expressed as the following,

$$p = \rho R T \quad (4.24)$$

where R is the specific gas constant. Then we can have

$$\rho = \frac{P}{RT} \quad (4.25)$$

Applying Equation 4.25 to Equation 4.19 and integrating x from 0 to L ,

$$\int_0^L Q_m dx = \int_0^L -\frac{1}{12\mu RT} wh^3 \left(P \frac{\partial P}{\partial x} \right) dx \quad (4.26)$$

Q_m is constant along the channel. Assuming isothermal flow, we have

$$Q_m = \frac{wt^3 P_{out}^2}{24\mu RTL} \left[\left(\frac{P_{in}}{P_{out}} \right)^2 - 1 \right] \quad (4.27)$$

4.3.5 Slip Boundary Gas Channel Flow

The assumption of no-slip boundary slip condition may not be accurate for micro channel flow, especially in low pressure micro channel flow [16, 18, 19, 22]. The Knudsen number for the channel flow can be defined as

$$Kn = \frac{\bar{\lambda}}{L} \quad (4.28)$$

Where $\bar{\lambda}$ is the mean free path of the gas molecules, and L is a characteristic length of the channel such as height. Under the standard condition, i.e., at the room temperature and atmospheric pressure, the Knudsen number for our channel (h : 1-2 μm) is about 0.02 to 0.04. In such a case, the slip boundary condition has been considered and the mass flow rate has been modified using the Knudsen number [29], which is described as

$$Q_m = \frac{wh^3 P_{out}^2}{24\mu RTL} \left[\left(\frac{P_{in}}{P_{out}} \right)^2 - 1 + 12Kn \left(\frac{P_{in}}{P_{out}} - 1 \right) \right] \quad (4.29)$$

4.4 Design and Fabrication

Figure 4.4.1 shows the micro channel flow study. Using surface micromachining techniques, we fabricate robust micro channels, which are able to withstand pressures up to several hundred pounds per square inch. Micro sensors are integrated with the micro channels so that we are able to obtain the temperature, pressure, and flow rate information during the fluid flows through the channels. Furthermore, undercutting the silicon underneath thermally isolates the channel, which allows us to study the thermal effects of micro channel flow [23].

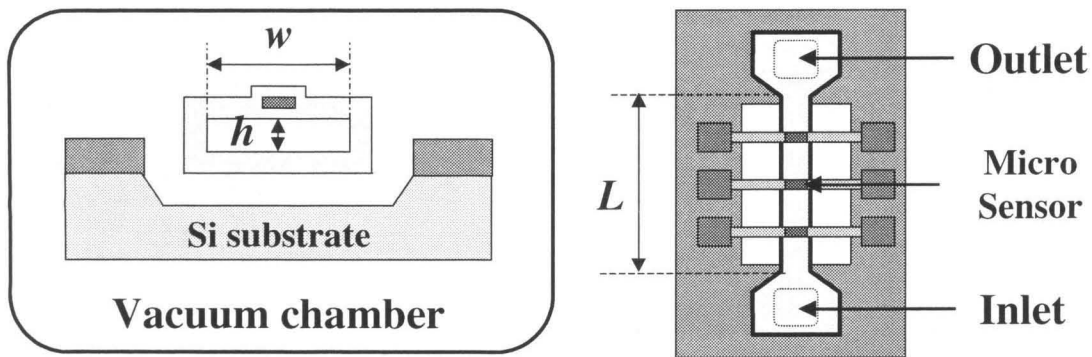


FIGURE 4.4.1 Conceptual illustration of MEM freestanding micro channel integrated with micro sensors.

4.4.1 Suspended Micro Channel with 1st Generation Integrated

Thermistors

The freestanding microchannels with integrated thermal sensors were fabricated using surface micromachining techniques, while the thermal isolation cavity as well as the inlet and outlet pits were bulk micromachined [23].

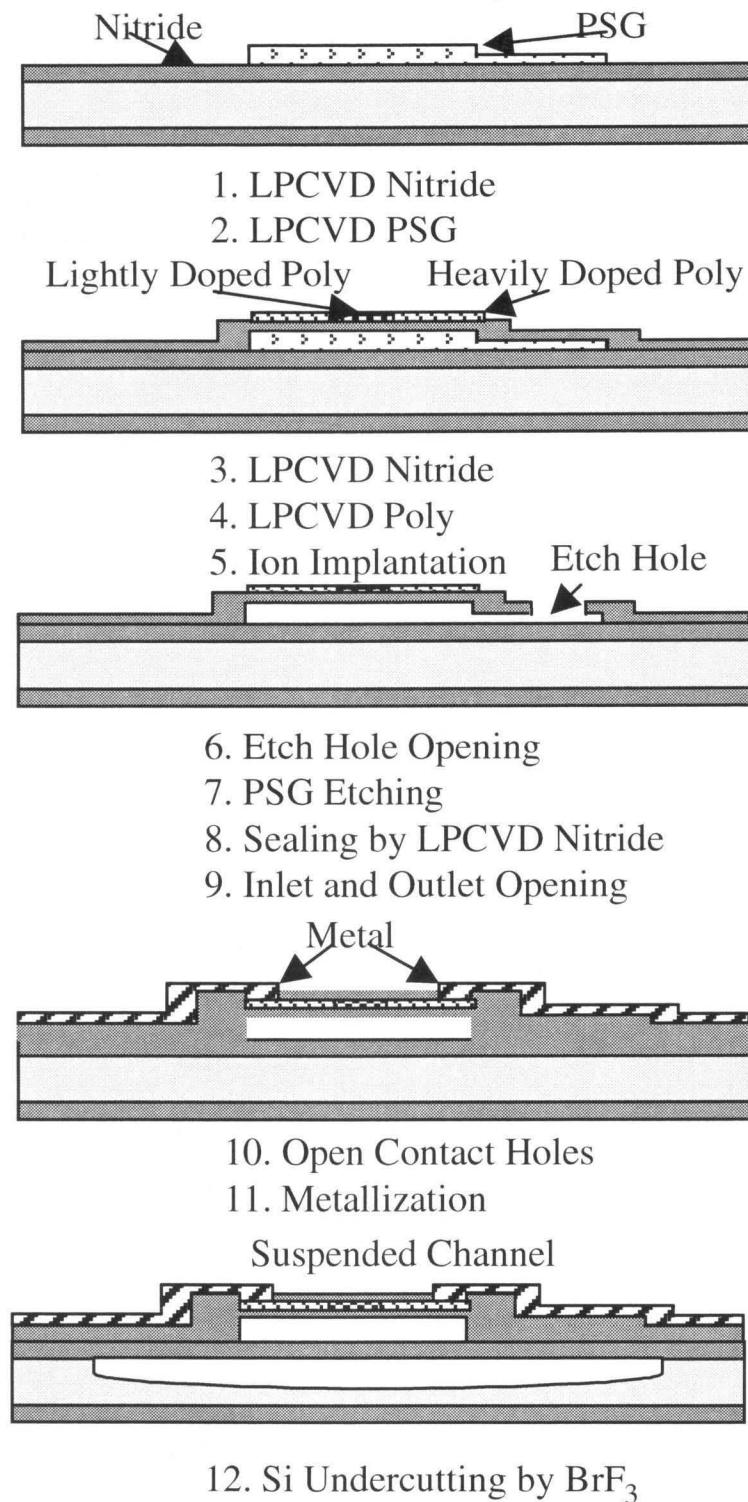


FIGURE 4.4.2 Fabrication process for suspended microchannel with integrated thermistors.

The fabrication process, schematically shown in Figure 4.4.2, starts with low pressure chemical vapor deposition (LPCVD) of a 1 μm thick nitride layer on a bare $\langle 100 \rangle$ oriented silicon wafer, followed by the patterning of the channel inlet and outlet. Next, a 2 μm LPCVD PSG sacrificial layer, which defines the microchannel length, width, and height, is deposited on the topside of the wafer. Another 0.5 μm thick layer of LPCVD nitride is deposited on the PSG to define the channel boundaries, i.e., sidewalls and ceiling. A 0.5 μm layer of LPCVD polysilicon is then deposited and patterned to form the temperature sensors on top of the microchannel. Selective boron ion implantation is used to control the electrical properties of the polysilicon. The sensor element, 4 μm x 4 μm in size, is lightly doped with boron ($2 \times 10^{18}/\text{cm}^3$) giving the sensor a nominal room temperature resistance of 30 k Ω . The polysilicon contact lines to the sensor are heavily boron doped ($2 \times 10^{20}/\text{cm}^3$) to reduce the resistance of the sensor leads. RIE is performed to open holes through the nitride to the PSG in order to facilitate etching. A sacrificial etching of the microchannels in a 49% HF solution to remove the PSG layer immediately follows.

The newly formed microchannels are re-sealed by uniformly depositing a 0.5 μm layer of LPCVD nitride. This completes the fabrication of the microchannels with the channels having 1 μm thick walls. An anisotropic TMAH solution is used to bulk etch the channel inlet and outlet pits, and a second RIE step is then used to open contacts through the nitride to the polysilicon underneath. Metallization forms bonding pads for connections between the macro-world and the sensor elements and, finally, thermal isolation of the channel is achieved by isotropically bulk micromachining the silicon underneath the channel. A photoresist mask is used to protect the channel and its

suspension stringers from a BrF_3 dry etch [30], which results in a cavity $80\ \mu\text{m}$ deep and about $400\ \mu\text{m}$ wide. The channel used in the experiments (Figure 4.4.3) was $4.4\ \text{mm}$ long, $1.85\ \mu\text{m}$ high, and $19\ \mu\text{m}$ wide. These dimensions were obtained using an Alpha Step profiler. The microchannels are suspended by $200\ \mu\text{m}$ long stringers on each side spaced approximately $500\ \mu\text{m}$ apart. The temperature sensor contact lines run from the center of the channel out along the stringers, as shown in Figure 4.4.4, and to the bonding pads next to the isolation cavity.

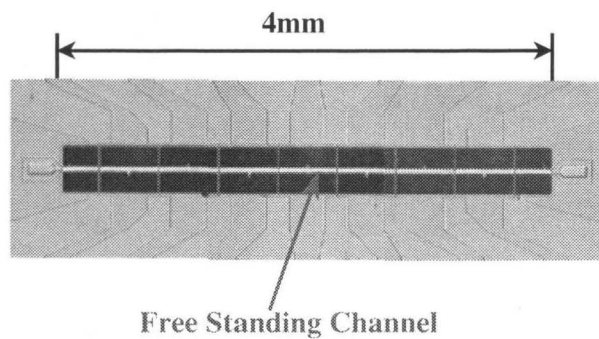


FIGURE 4.4.3 Top view of suspended micro channel with integrated thermistors.

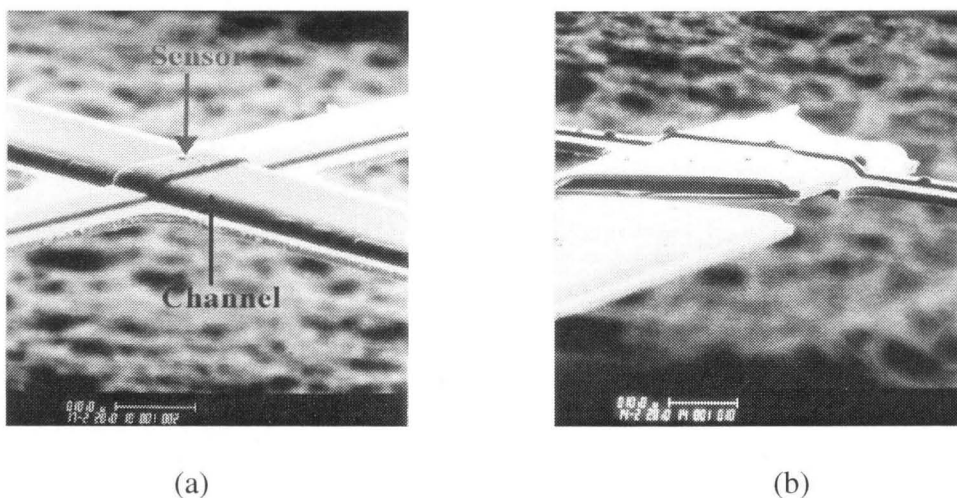


Figure 4.4.4 Electron micrographs of suspended channel with an integrated sensor: (a) Section where sensor locates, (b) Cross section shown from broken channel.

4.4.2 Suspended Micro Channel with 2nd Generation Integrated Thermistors

1st generation integrated thermistors embedded inside a channel wall measure the temperature in the wall, which may be different from the temperature inside the gas flow. 2nd generation integrated thermistors shown in Figure 4.4.5 have been designed and fabricated to measure the temperature of fluid flowing inside the channel.

The fabrication process is similar to the first generation design except the polysilicon layer is sandwiched between two low temperature oxide layers. The oxide is later sacrificially etched to produce the freestanding sensor inside of the nitride channel as shown in Figure 4.4.5.

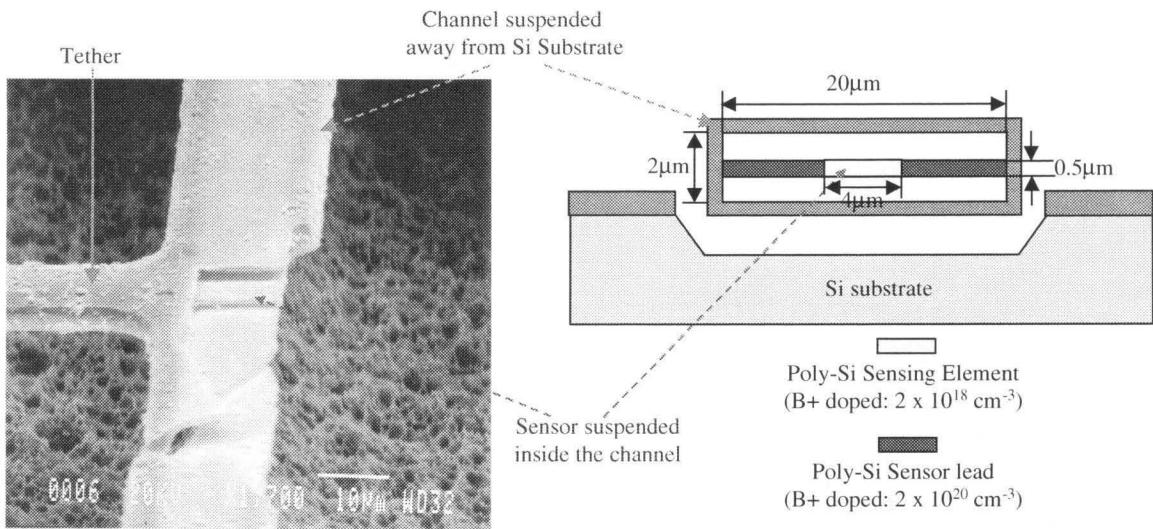


FIGURE 4.4.5 A suspended micro channel with a broken part to show a freestanding thermistor inside.

4.5 Experimental Setup

Gas and liquid flow measurements were conducted in the apparatus illustrated in Figure 4.5.1. The chip was bonded to a packaging holder (20 H/B, Plug In, 1.056 x 1.156 Cavity) from Spectrum Semiconductor Materials, Inc. (Figure 4.5.2). Figures 4.5.3 and 4.5.4 show the vacuum chamber where the high-pressure gas channel flow is tested. The temperature distribution along the pressurized channel was measured in a vacuum chamber, the chamber was evacuated to 10 mtorr in order to minimize heat loss due to convection effects.

As shown in Figure 4.5.1, microelectronic grade N₂ from a pressurized cylinder was passed through HPLC tubing into the suspended microchannel. An Omega type PX120 pressure transducer was used to monitor the inlet pressure. An Omega model HHP-3200 digital manometer measures the exit pressure. These transducers had an uncertainty of 1.0 and 0.1 psia, respectively. The volume flow rate is measured using various glass tubes approximately 1.1 meter in length, and from 3 mm to 8 mm in (outer) diameter, whichever is appropriate for the flow rate being investigated. These tubes were calibrated using water and a graduated cylinder. The volume flow rate in the tube was measured optically as a meniscus of water traveled past marked gradations versus time. Data for each set of flow parameters (at various inlet and outlet pressures) took from thirty minutes (for a gas) to four hours (for a liquid), depending on the relative flow rate. In addition, a vacuum/compressor pump is connected to the settling chamber at the end of the measurement tube. This allows the exit pressure to be lowered to a maximum vacuum of -12 psig, or pressurized to 20 psig.

Temperature calibrations of the embedded sensors were conducted inside a Delta Design Model 2300 isothermal oven. Resistances were measured by a HP Model 34401A multimeter, and accurate temperature measurements, better than 0.01 °C, were obtained using an Omega DP-251 precision thermometer using a calibrated RTD sensor element.

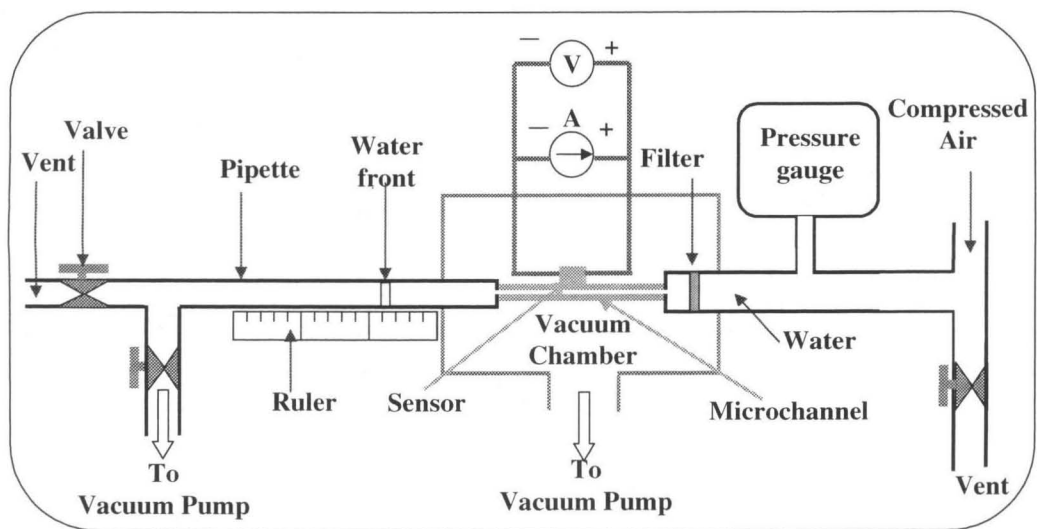


FIGURE 4.5.1 The illustration of experiment setup.

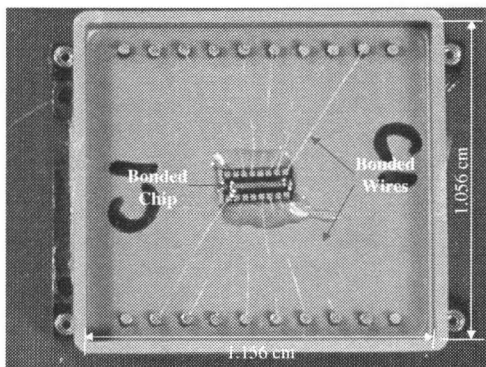


FIGURE 4.5.2 The picture of the chip bonded on a packing holder. The sensors are wire-bonded to the holder plugs.

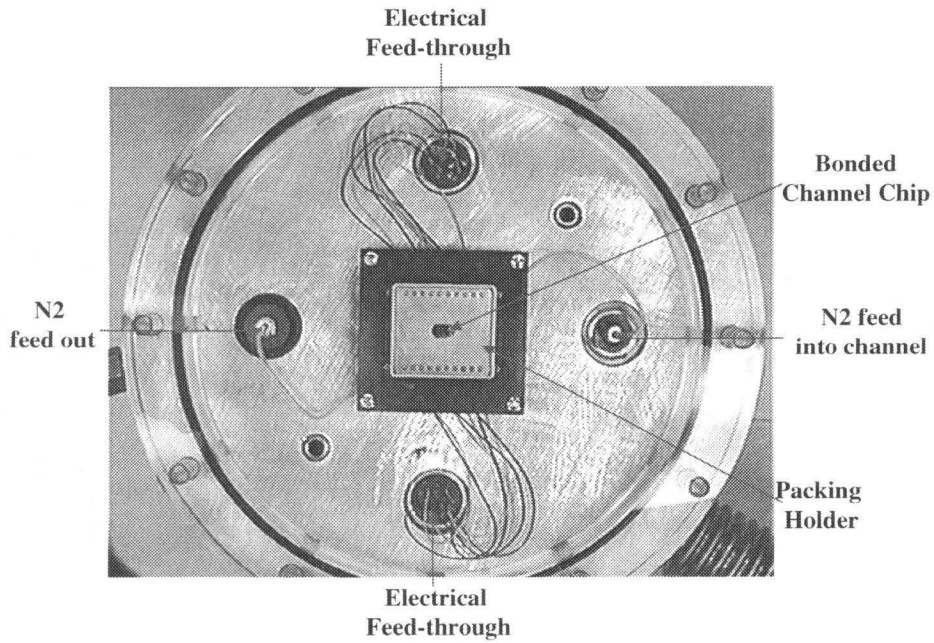


FIGURE 4.5.3 The top view of the vacuum chamber.

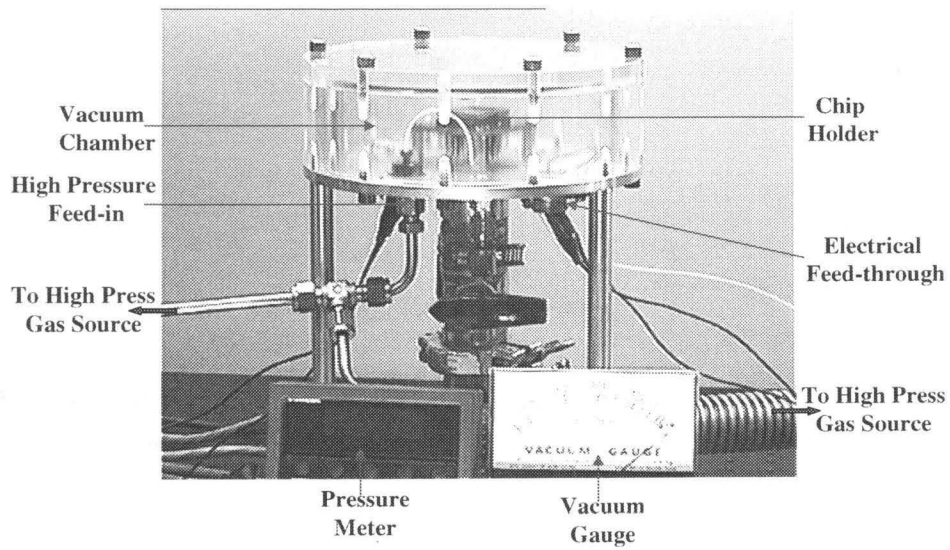


FIGURE 4.5.4 The side view of the vacuum chamber.

4.6 Test Results and Discussion

The flow rates through a channel ($4400 \times 19 \times 1.85 \mu\text{m}^3$) have been measured with a maximum driving pressure up to about 600psig. The discrepancy between the test results and theory comes from a flow acceleration and a non-parabolic velocity profile under high pressure, as well as the bulging effect of the channel wall. The temperature measurements confirm that the assumption of isothermal flow is appropriate for microchannel flow.

4.6.1 DI Water Flow in Microchannel

DI water flow in a microchannel has been measured. The discrepancy between the experimental data and theory is accounted for the bulging effect of the channel wall. Our new model based on the bending beam theory agrees with test results. In future channel design, if we can reduce the bulging by designing channels with thicker walls, we can then concentrate our studies on the flow properties such as viscosity, compressibility, slip boundary or even more complicated effects like those due to flow acceleration and a non-parabolic velocity profile under high pressure [1].

I. Flow Rate of DI Water through a Microchannel

Figure 4.6.1 displays data for the volume flow rate of DI water in the channel under various inlet pressures, which is nonlinear. According to the analysis in Section 4.3 and Equation 4.23, the flow rate of an incompressible liquid through a uniform microchannel is proportional to the pressure difference between the inlet pressure and outlet pressure. The measurement results indicate that the channel deforms under high pressure since the

experimental results deviate from the theoretical values calculated using Equation 4.23, as illustrated by the solid line in Figure 4.6.1.

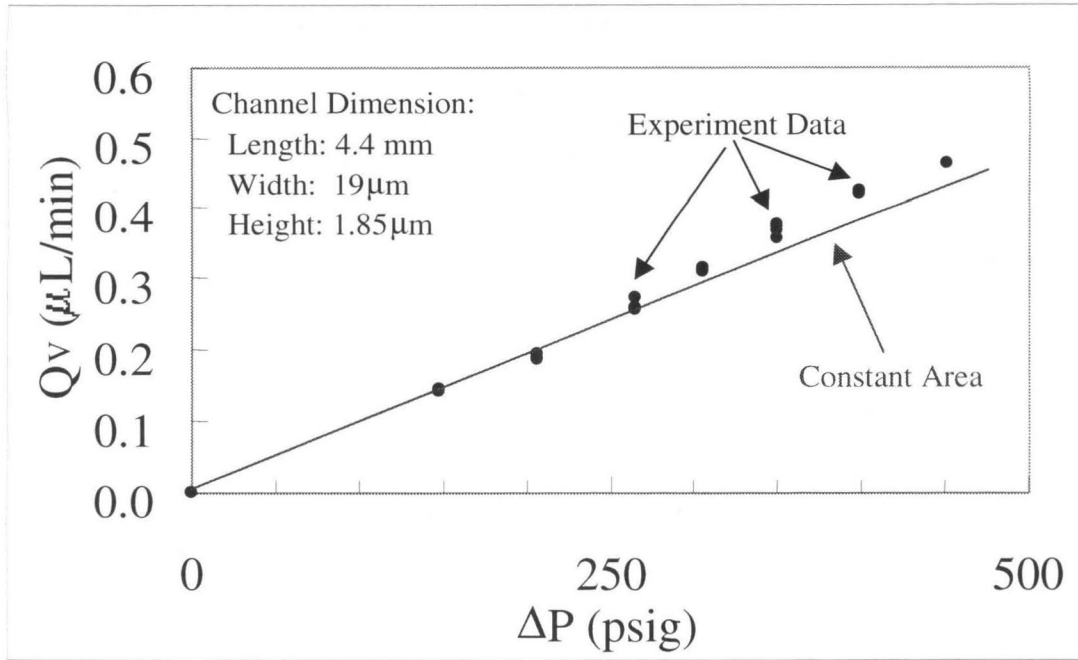


FIGURE 4.6.1 Comparison between the measurement data and the theory for a channel with constant cross section area.

II. Bulging Effect of a Microchannel under Pressurized Flow

We investigate this hypothesis by modifying the height term in the volume flow rate equation, accounting for the wall-deflection effect due to pressure. For small deflection under a pressure (uniform loading on the cross section), we assume the local deformation is linear with the local pressure $p(x)$ as shown in Figure 4.6.2.

Since the channel length is much larger than the height and width, we can treat the top or bottom wall as a single beam with the fixed angle boundary condition as shown in Figure 4.6.3. By applying bending beam theory [31, 32], we can find deflection curve is a parabolic curve and the maximum deflection is found by Equation 4.30.

$$\Delta(x) = \frac{B}{384} \frac{p(x)w^4}{Et^3/12} \quad (4.30)$$

Where B depends on the boundary condition. For example, $B=2$ in our case.

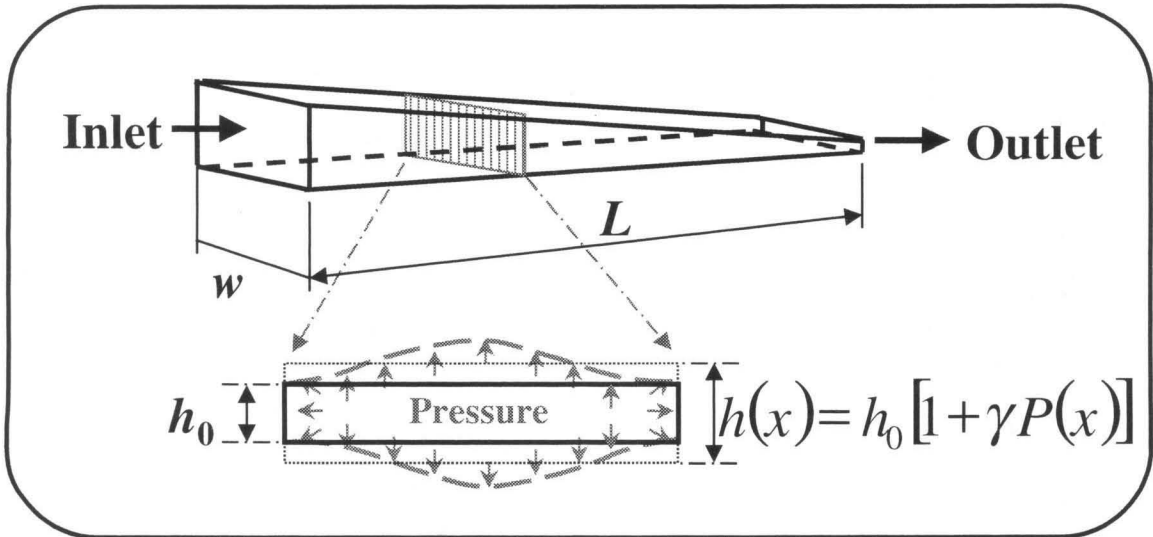


FIGURE 4.6.2 Illustration of channel deformation under pressurized flow.

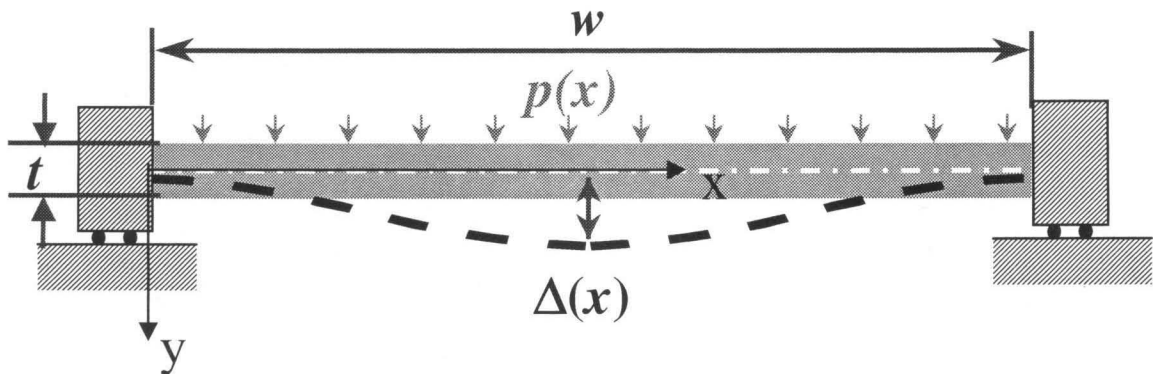


FIGURE 4.6.3 Bending beam model applied to the bulged channel wall.

The increased area of the cross section by bulging of both top and bottom walls is obtained as

$$\Delta A \approx w \cdot \Delta(x) = \frac{B}{384} \frac{p(x)w^5}{Et^3/12} \quad (4.31)$$

Then the equivalent change of height is

$$\Delta h = \frac{\Delta A}{w} = \frac{B}{384} \frac{p(x)w^4}{Et^3/12} = \gamma p(x)h_o \quad (4.32)$$

Where

$$\gamma = \frac{B}{384} \frac{w^4}{Et^3h_o/12} = \frac{B}{32} \frac{w^4}{Et^3h_o} \quad (4.33)$$

h_o is the nominal channel height of 1.85 μm at standard conditions, and $p(x)$ is the local pressure. Then the effect channel height is

$$h = h_o[1 + \gamma p(x)] \quad (4.34)$$

By substituting Equation 4.34 into Equation 4.23, and assuming that $\gamma p(x) \ll 1$ so that higher order terms can be ignored, we get:

$$Q_v = -\frac{1}{12\mu} wh_o^3(1 + \gamma p(x))^3 \frac{\partial p(x)}{\partial x} \approx -\frac{1}{12\mu} wh_o^3(1 + 3\gamma p(x)) \frac{\partial p(x)}{\partial x} \quad (4.35)$$

After integrating along the channel and assuming $\Delta P \gg P_{out}$ in the case of very high input pressure, the following approximation for volume flow rate is obtained:

$$Q_v = \frac{h_o^3 w}{12\mu L} (P_{in} - P_{out}) \left[1 + \frac{3}{2} \gamma (P_{in} + P_{out}) \right] \approx \frac{h_o^3 w}{12\mu L} \Delta P \left(1 + \frac{3}{2} \gamma \Delta P \right) \quad (4.36)$$

By comparing Equation (4.36) to Equation (4.23), we can define a correction term due to bulging as

$$Q_v = Q_{vo} (1 + \eta_{def}) \quad (4.37)$$

Where

$$\eta_{def} = \frac{3}{2} \gamma \Delta P \quad (4.38)$$

$$Q_{vo} = \frac{h_o^3 w}{12\mu L} \Delta P \quad (4.39)$$

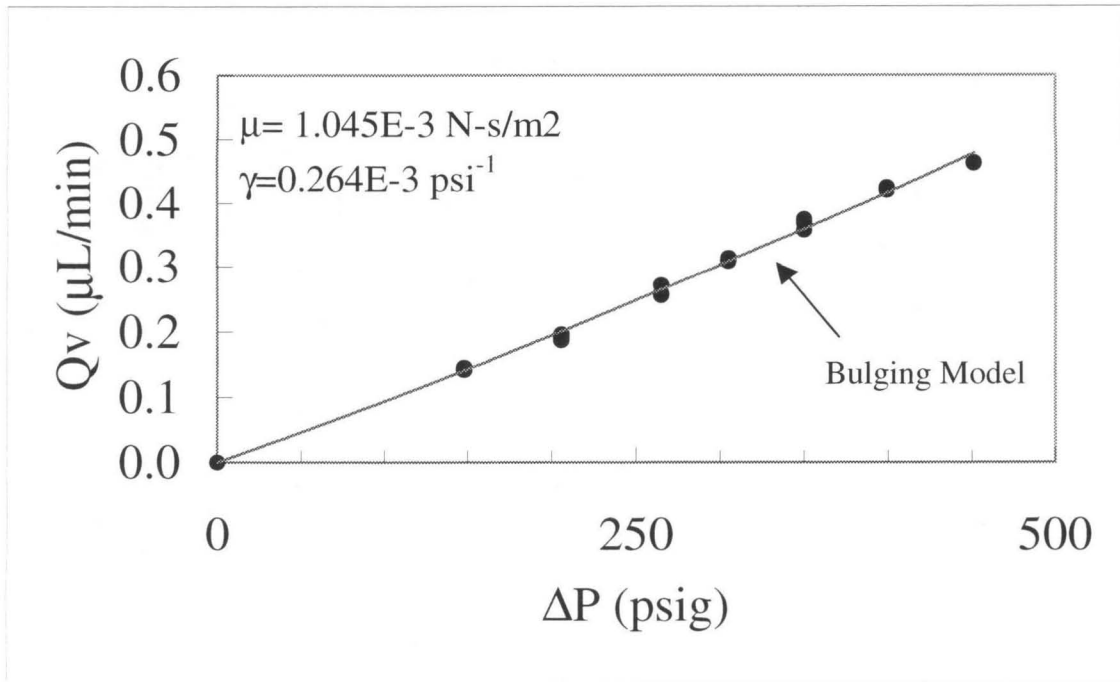


FIGURE 4.6.4 Measurement data fitted to the bulging model.

It is clear that this geometry correction is parabolic with respect to the pressure difference and explains the curvature of the data as seen in Figure 4.6.1. By fitting the experimental data with Equation 10.9, this yields $\mu=1.045 \times 10^{-3}$ N-s/m² and $\gamma = 0.000264$ psi⁻¹ as shown in Figure 4.6.4. Applying all of the channel dimensions to the Equation 10.8, we estimate the value of nitride Young's modulus as E=400Gpa. The reliability of the method can be seen by the fact that our estimated viscosity and nitride Young's modulus are consistent with the published values [33, 34] by taking into account the experimental error (less than 5%).

III. In Situ Deflection Measurements

The presence of bulging was confirmed using in-situ deflection measurements obtained from a WYKO model RST Plus optical profiler. Interferometric scans of magnified sections of the channel were taken in the WYKO's vertical scanning imaging (VSI) mode. A 30nm layer of Au-Pb was sputtered onto the channel in order to circumvent the detrimental transparency of the nitride roof. Images at different input pressures, but at identical locations, were digitally subtracted from each other in order to obtain the resulting deflection in the channel for a given pressure difference. The images were taken at 400 times magnification with an interrogation area CCD camera resolution of 256 x 256, yielding a resolution of about 0.24 μm per pixel. Figure 4.2.5 is a computer-calculated image, which illustrates the resulting beam deflection near the inlet when an image at 300 psig is subtracted from an image at 0 psig. The maximum deflection measured on one side is approximately 60 nm at $\Delta P = 300$ psig, which yields a $\gamma/2 = 0.0001426$ psig⁻¹, i.e., $\gamma = 0.0002852$ psig⁻¹. Here γ is close to the value from the fit of the incompressible water measurements. This shows that the model is suitable to modify the water flow rate through the channel under high pressure.

The maximum deflection measured, shown in Figure 4.6.5, is approximately 75 nm at $\Delta P = 300$ psig, which yields a $\gamma = 0.000178$ psig⁻¹. Here γ is close to the value from the fit of the incompressible water measurements [14]. Although the WYKO deflection results are consistently lower than values obtained from fits of the volumetric flow data, we now have experimental evidence that the model is suitable for explaining high pressure deflection effects on the suspended micro channel's dimensions to within reasonable error.

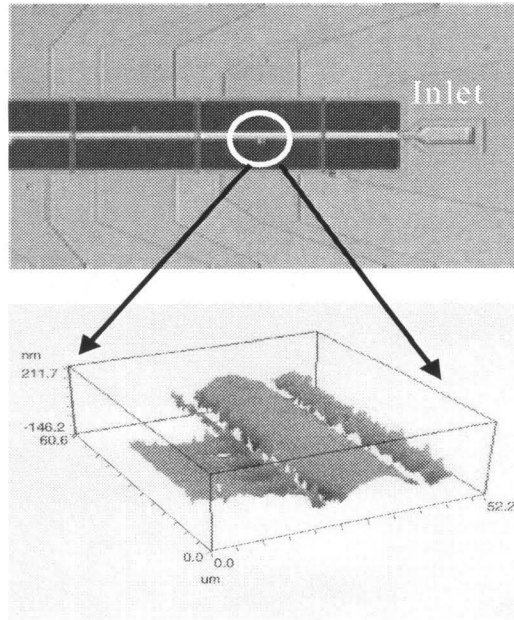


FIGURE 4.6.5 Sample processed 3-D WYKO image showing beam deflection near the inlet at 300 psig.

4.6.2 Low-pressure Gas Flow

Before proceeding to high-pressure gas flow, we tested the validity of the experimental procedure by investigating low pressure flow, in order to compare our results to previous results available in the literature. Nitrogen gas was passed through the microchannel at low and high pressures. We regard low pressure as being under 60 psia, which is comparable to the pressure range already investigated [15, 16, 17, 21, 22]. By assuming a parabolic velocity profile and neglecting the convection term, the mass flow rate for compressible flow with slip boundary condition is given by Equation 4.29 that is rewritten as:

$$Q_m = \frac{wh^3 p_{out}^2}{24\mu RTL} \left[\left(\frac{P_{in}}{P_{out}} \right)^2 - 1 + 12Kn \left(\frac{P_{in}}{P_{out}} - 1 \right) \right] \quad (4.29)$$

where Kn_{out} is the Knudsen number at the channel exit and R is the specific gas constant.

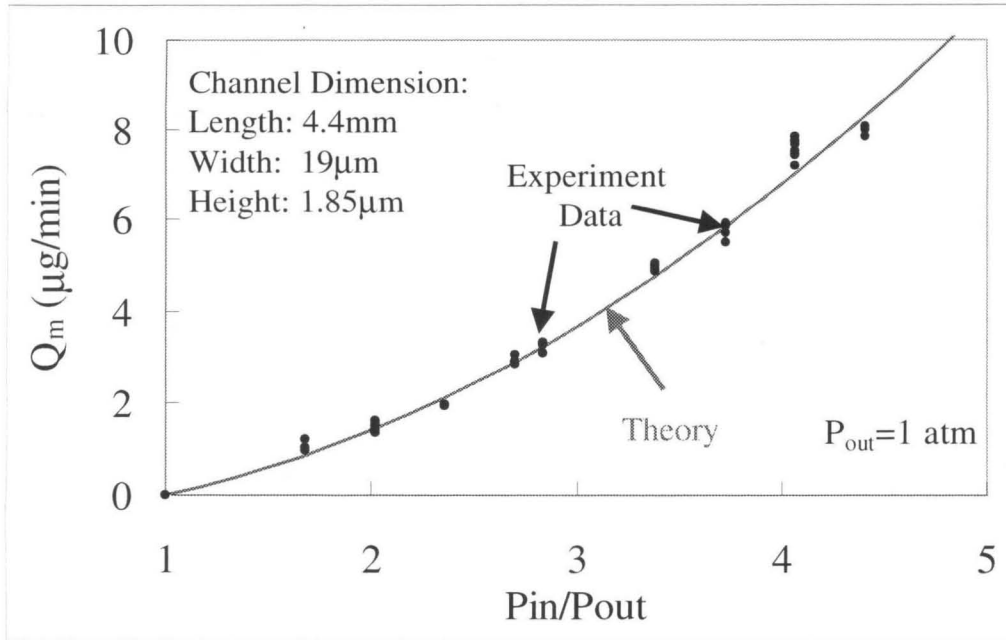


FIGURE 4.6.6 Theoretical and experimental results for low pressure N_2 flow with outlet pressure at 1 atm.

Figure 4.6.6 shows the mass flow rate of nitrogen flowing through a microchannel at 1 atmosphere pressure. The inlet pressure was controlled by connecting to a high-pressure cylinder through a valve. Figure 4.6.7 shows the mass flow data for a fixed inlet pressure of 30 psig. The outlet pressure was controlled by connecting to a vacuum pump through a valve.

As one can see from these two figures, within experimental error, these data points fit well to the generally accepted low-pressure theoretical predictions as in Equation 4.29. The agreement between the experimental results and the theoretical calculations verify that the present setup provides an appropriate system to reliably obtain

extremely small volume flow rate measurements. Furthermore, these results support the argument that flow acceleration and non-parabolicity effects are negligible at low pressures, and flow rate predictions taking into account only compressible and slip flow effects are accurate [23].

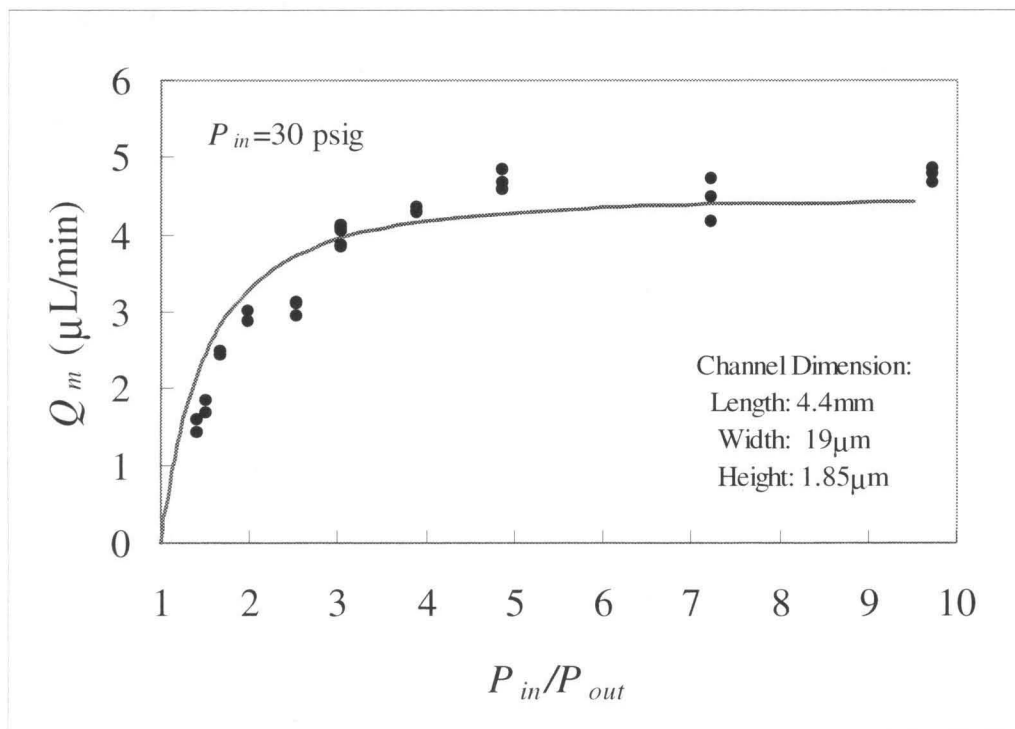


FIGURE 4.6.7 Theoretical curves and experimental data for low pressure N_2 flow for 30 psig inlet pressure.

4.6.3 High-Pressure Gas Flow

When the inlet pressure gets higher and higher, we notice that the experimental data deviates from the theoretical curve from Equation 4.29 (shown in Figure 4.6.8). It implies that it is no longer appropriate to ignore the effects of flow acceleration, non-parabolicity, as well as deformation of channel wall at high inlet pressure (>60 psia).

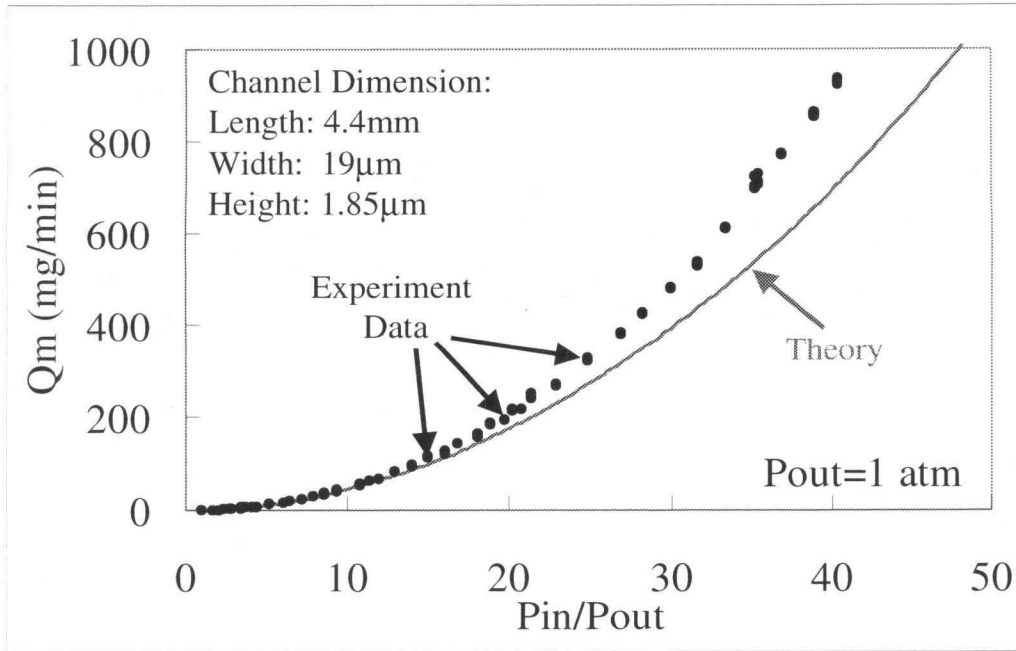


FIGURE 4.6.8 Theoretical curve and experimental data for high pressure N₂ flow for 1 atm outlet pressure.

In order to estimate the influence of the flow terms ignored so far in this analysis, we refer to the work of van den Berg, et al. [21] for guidance. They derived equations for mass flow rates which take into consideration the non-parabolicity of the velocity profile, as well as the convection (acceleration) term of the momentum equation. However, their analytical study was for a capillary with a circular cross section. Using hydraulic diameter arguments, we assume that the relative contributions of these effects for pipe flow are on the same order of magnitude for channel flow. Therefore, the factors contributing to the total mass flow rate can be estimated as follows:

$$Q_m = Q_{mi} [1 + \eta_c + \eta_s] (1 - \eta_a) (1 - \eta_p) \quad (4.40)$$

where Q_{mi} , which refers to the mass flow rate as in Equation 4.22 by assuming there is no compressible effect and the gas density constantly is equal to the density at the outlet, such as

$$Q_{mi} = \frac{1}{12\mu} \rho_{out} w h^3 \frac{P_{in} - P_{out}}{L} = \frac{1}{12\mu} w h^3 \frac{(P_{in} - P_{out})}{L} \frac{P_{out}}{RT} \quad (4.41)$$

If we compare Equations 4.40, 4.41, and 4.42, then we have the correction effect due to the gas compressibility

$$\eta_c = \frac{1}{2} \left(\frac{P_{in}}{P_{out}} - 1 \right) \quad (4.43)$$

The correction due to slip effects is

$$\eta_s = 6 \text{ Kn} \quad (4.44)$$

According to H.R. van den Berg, et al. [21], the contribution from the convection term is

$$\eta_a = \frac{Q_{mi}}{6\pi\mu L} \ln \frac{P_{in}}{P_{out}} \quad (4.45)$$

and the contribution of a non-parabolic velocity profile has an effect on the order of

$$\eta_p = \frac{Q_{mi}}{12\pi\mu L} \ln \frac{P_{in}}{P_{out}} \quad (4.46)$$

Substituting in values for η_a and η_p , it is apparent that these terms are much less than 1, so higher order terms can be neglected and Equation 5.40 can be rewritten as

$$Q_m = Q_{mi} [1 + \eta_c + \eta_s] (1 - \eta_a - \eta_p) \quad (4.47)$$

When the acceleration effect and the effect due to the non-parabolic velocity profile are taken into consideration, a lower theoretical mass flow rate should result. For example, the difference between the usual non-slip curve and the curve that takes into

account acceleration and non-parabolicity is about 6% at 600 psig (pressure ratio is about 40), as seen in Figure 4.6.9.

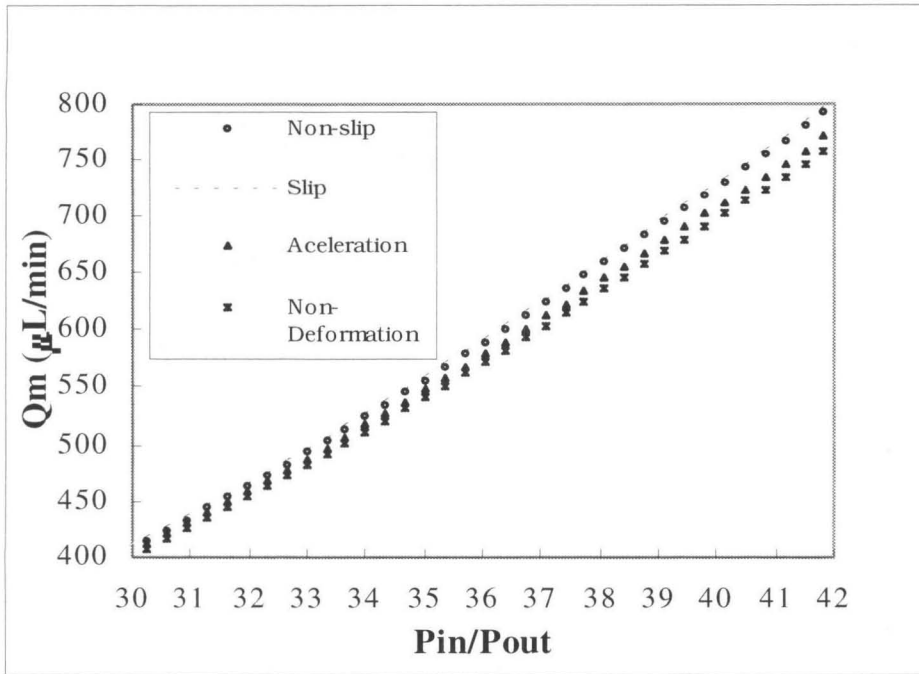


FIGURE 4.6.9 Mass flow rate vs. inlet pressures, with curves at various exit pressures, slip and no slip theoretical curves, and a curve with acceleration effects.

In Figure 4.6.10 at higher-pressure ratios the data deviates even more from the curve that takes into consideration acceleration and a non-parabolic velocity profile. This discrepancy between measured and theoretical values calculated from Equation 4.47 can only be attributed to deformations in the channel geometry due to high pressure of the channel. An effective mass flow rate can be written as Equation 4.48,

$$Q_{effective} = Q_m (1 + \eta_{def}) \tag{4.48}$$

where Q_m takes into consideration flow acceleration and non-parabolicity, as well as geometry. Again assuming small deflection of the channel wall, rewriting Equation 4.34 for the effective height under the pressure $p(x)$,

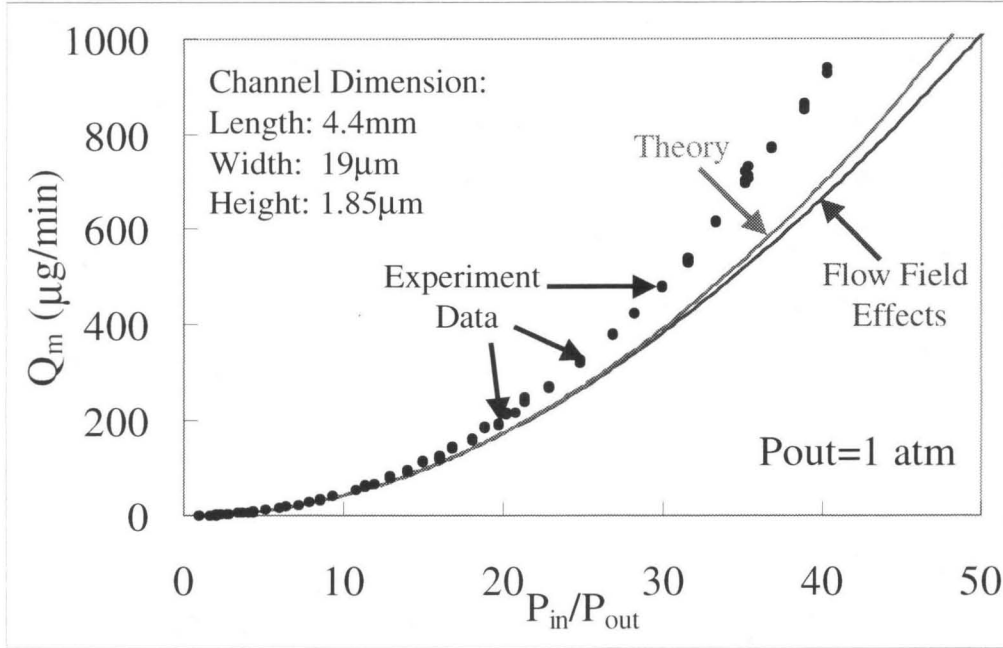


FIGURE 4.6.10 Theoretical curves (for low and high inlet pressures) and experimental data for low pressure N_2 flow for 1 atm outlet pressure.

$$h = h_o [1 + \gamma p(x)] \quad (4.34)$$

and substituting Equation 4.34 and gas state Equation 4.25, we have effective mass flow rate

$$Q_{eff} = -\frac{1}{12\mu RT} w h_o^3 (1 + 3\gamma p) \left(p \frac{\partial p}{\partial x} \right) \quad (4.49)$$

Integrating to Equation 4.49 for x from 0 to L , then we have

$$Q_m = \frac{wh^3 p_{out}^2}{24\mu RTL} \left[\left(\frac{p_{in}}{p_{out}} \right)^2 - 1 \right] \left(1 + 2\gamma P_{in} \left(1 + \frac{1}{\frac{p_{in}}{p_{out}} \left(1 + \frac{p_{in}}{p_{out}} \right)} \right) \right) \right) \quad (4.50)$$

For the high-pressure flow, we have

$$\frac{p_{in}}{p_{out}} \left(1 + \frac{p_{in}}{p_{out}} \right) \gg 1 \quad (4.51)$$

Then we obtain

$$Q_m \approx \frac{wh^3 p_{out}^2}{24\mu RTL} \left[\left(\frac{p_{in}}{p_{out}} \right)^2 - 1 \right] (1 + 2\gamma P_{in}) \quad (4.52)$$

Hence we have

$$\eta_{def} = 2\gamma P_{in} \quad (4.53)$$

Here γ only depends on the channel geometry and wall material, and it is given by Equation 4.33.

Figure 4.6.9 illustrates that the measured data fits the mass flow rate model when flow acceleration, non-parabolic flow velocity profile, and channel deformation due to high pressures is taken into consideration.

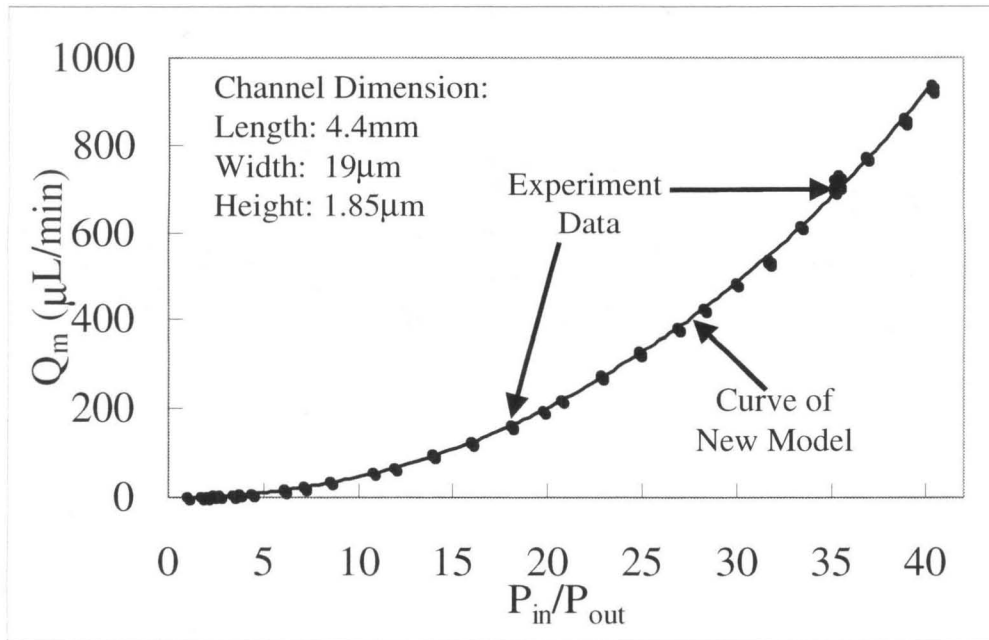


FIGURE 4.6.11 Mass flow rate vs. inlet pressure of experimental data and the curve plotted with our new model.

4.6.4 Temperature Distribution of Microchannel Gas Flow

I. Results From 1st Generation Integrated Temperature Sensors

Because of the problems of fabrication and packaging, three working sensors on the packaged microchannel (as shown on Figure 4.6.12) are calibrated for the effect on both temperature and pressure. Preliminary temperature measurements have been performed using these calibrated sensors.

Sensor calibration

The micro channel is intended for high-pressure heat transfer experiments, and lightly doped polysilicon displays piezoresistive properties. Therefore, it is important to not only

calibrate the sensor resistive output as a function of temperature, but also to compensate for any pressure effects. The data shows that the sensor temperature sensitivity is independent of pressure in the range between 0 and 300 psig. Figure 4.6.13 shows the nonlinear resistance dependence on temperature of both 1st and 2nd generation sensors. Furthermore, the curves converge to each other, showing good uniformity of sensitivity to temperature among different sensors. Similarly, Figure 4.6.14 shows the sensor resistance change due to variations in pressure. The resistance sensitivity of the sensor to pressure is almost linear in the tested range, and is independent of temperature between 10°C and 40°C. Thus, the overall sensor sensitivity, parabolic with temperature and linear with pressure, can be expressed as:

$$(R-R_0)/R_0 = \alpha_2(T-T_0)^2 + \alpha_1(T-T_0) + \beta(P-P_0) \quad (4.54)$$

where α_1 , α_2 , and β are experimentally calibrated to be approximately equal to $-0.009\text{ }^\circ\text{C}^{-1}$, $6 \cdot 10^{-5}\text{ }^\circ\text{C}^{-2}$, and 10^{-5} psi^{-1} , respectively.

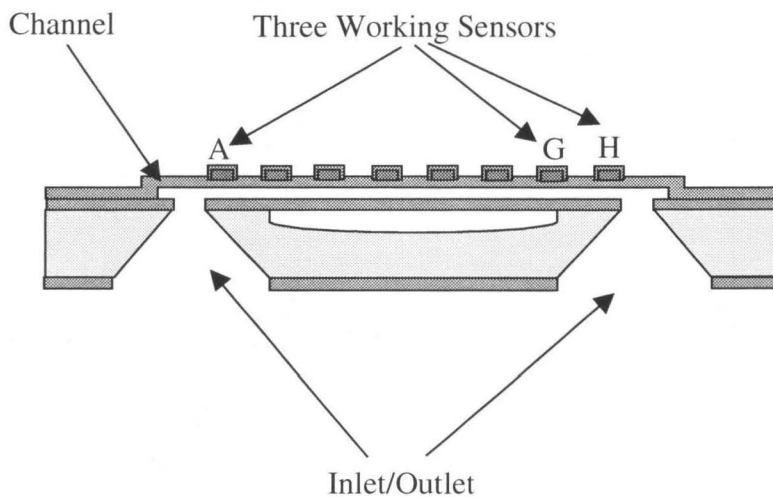


FIGURE 4.6.12 Three working sensors on the packaged microchannel.

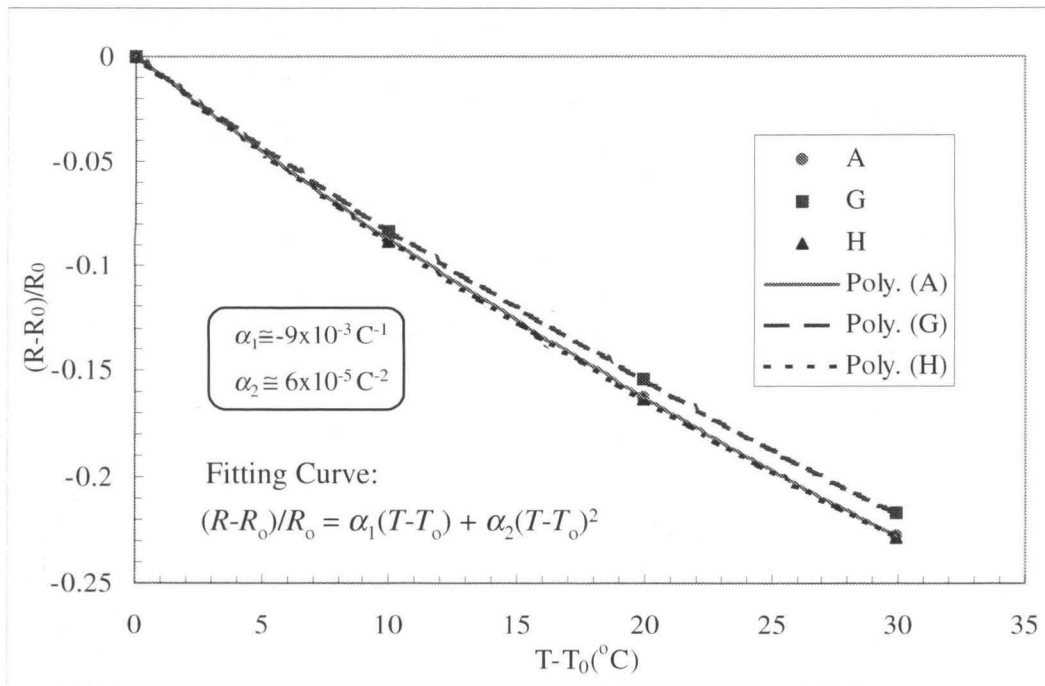


FIGURE 4.6.13 Sensor sensitivity to temperature.

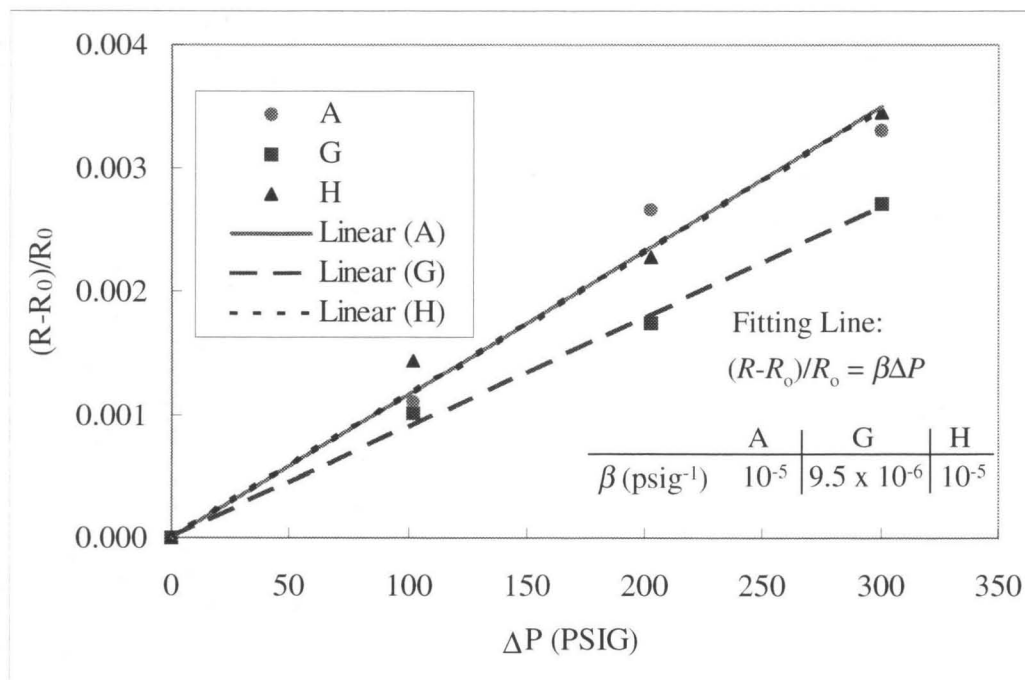


FIGURE 4.6.14 Sensor sensitivity to pressure.

Temperature Distributions

The measurements are taken under two flow cases: (a) 271 psig gas pressure applied to the inlet near Sensor A and the flow direction is A-G-H, (b) 305 psig gas pressure applied to the inlet near Sensor H and the flow direction is G-H-A. Assuming the parabolic pressure distribution of the compressible gas channel flow [18], the pressure effects of all three sensors for both cases are estimated. Then using Equation 4.54, the temperature is calculated from the measurement data by taking into account the pressure effects. Table 4 lists the results of two different flows.

TABLE 4 Temperature differences between the three sensors under two different flows.

Temperature Difference: $\Delta T = T - T_A (^{\circ}\text{C})$			
Sensor	A	H	G
Flow: A-H-G (271 psig)	0	0.07	-0.28
Flow: G-H-A (305 psig)	0	0.41	0.05

As one can see from the table, the temperature changes between the three sensors are smaller than 0.5°C . This indicates that the temperature calibration can be narrowed to a very small range (for example 5°C) for improved accuracy. In addition, the temperature dependence of sensors can be approximated by a linear function in a small temperature range because the contribution of the first term in Equation 5.54 is only about 3%. Of course, the three sensors are not sufficient to give complete information on the temperature distribution in the high-pressure gas flow. The problems with the fabrication

process need to be addressed and the channel chip has to be packaged carefully so that all eight sensors are functional.

II. Results From 2nd Generation Integrated Temperature Sensors

Unlike 1st generation sensors, all eight sensors along a channel (Figure 4.6.15) function appropriately. After calibration for both temperature and pressure effects, these sensors suspended inside the channel are used to take measurements under several high-pressure gas flows.

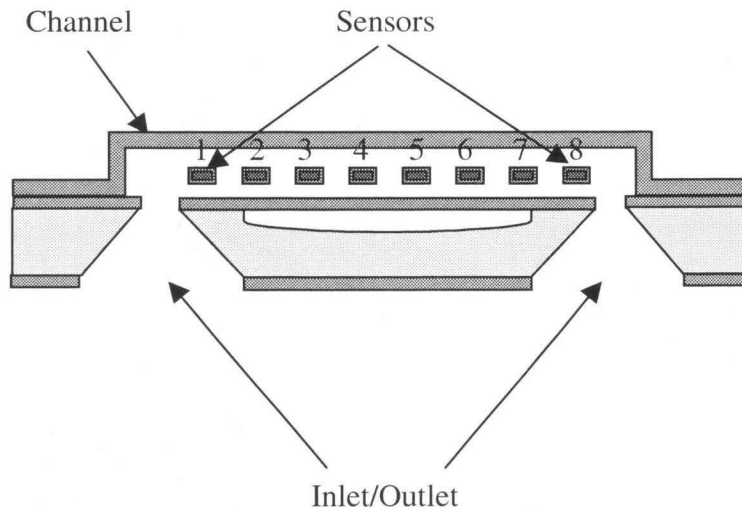


FIGURE 4.6.15 Micro temperature sensors integrated inside a suspended channel.

Sensor Calibration

All of the eight sensors are calibrated in the temperature range from 20 to 25 °C, and the pressure range from 0 to 300 psig. Instead of a parabolic function for temperature dependence in the calibration of the 1st generation sensors, we take a linear temperature relationship (i.e., $\alpha_2=0$) for the calibration of 2nd generation sensors in the small

temperature range. We still use a linear function for the pressure dependence as before. Table 5 lists the calibration results of the eight sensors, and the definitions of α_1 and β are the same as in Equation 4.54.

In contrast to the case of 1st generation sensors, β is negative for 2nd generation sensors. This is most likely caused by the opposite stress induced by the bulging of the wall under pressure. When a channel wall bulges, 1st generation sensors experience tensile stress since they lie on the wall, but 2nd generation sensors have compressive stress because they are suspended inside the channel.

Table 5 Calibration results of the eight 2nd generation sensors along a suspended channel.

Sensor	#1	#2	#3	#4	#5	#6	#7	#8
α_1 ($^{\circ}\text{C}^{-1}$)	-0.0060	-0.0044	-0.0041	-0.0046	-0.0040	-0.0040	-0.0044	-0.0036
$\beta(10^{-5} \text{ psig}^{-1})$	-2.3	-1.6	-1.3	-1.5	-2.0	-1.4	-2.1	-1.3

Temperature Distributions

Having discussed methods to take measurements and consider the pressure effect, we proceed to examine the temperature profile along the channel for various inlet pressures. Figure 4.6.16 shows the temperature profile at various inlet pressures, as measured by the eight free standing temperature sensors within the 2nd generation micro channel. Even at 300 psig, there is no appreciable temperature difference (less than 0.1 $^{\circ}\text{C}$) along the entire length of the channel. This would indicate that either heat conduction in thin film nitride is greater than heat generation by the flow or that the energy loss due to the conversion of

flow energy into viscous frictional energy is negligible in this micro channel configuration.

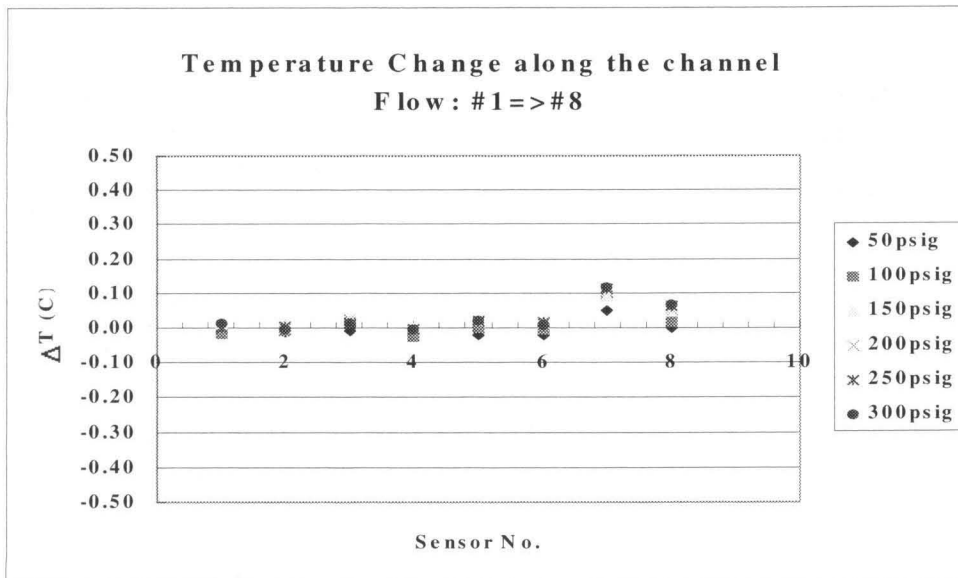


FIGURE 4.6.16 Temperature distribution within a micro channel at various inlet pressures.

III. Summary

Both 1st generation and 2nd generation integrated sensors have been calibrated considering temperature and pressure effects. While high-pressure gas flows through a channel, measurements have been performed by these calibrated sensors. The measuring data have been converted to temperature results by taking into account the pressure effect on the sensors. The results from both 1st generation and 2nd generation integrated sensors show insignificantly small changes of temperature along the channel and confirm that the isothermal assumption is appropriate for gas flow in a microchannel even for a driving pressure up to 300 psig.

4.7 Conclusion

The robust nature of silicon micromachined microchannels facilitated high-pressure measurements for both DI water and N_2 gas. Mass flow data at unprecedented high inlet pressures has been successfully obtained, and the deviation of this data from theory is attributed to fluid flow effects such as local flow acceleration and a non-parabolic velocity profile, as well as to bulging in the channel. This bulging effect was isolated and measured using incompressible liquid flow. In addition, at a fixed inlet pressure, a complete saturation flow rate curve has been obtained by evacuating and pressurizing the exit of the channel. Furthermore, we obtained coefficients for the parabolic dependence of the resistance of the imbedded thermal sensors to temperature, as well as the coefficient for the sensor's linear dependence on pressure. Finally, our temperature distribution shows negligible temperature change data along the channel with a high-pressure gas flow, and for the first time directly provides evidence validating the treatment of micro channel flow as isothermal flow.

References:

- [1] S. C. Terry, "A gas chromatographic air analyzer fabricated on a silicon wafer using integrate circuit technology," Ph.D. dissertation, Department of Electrical Engineering, Stanford University, Stanford, CA, 1975.
- [2] A. Desai, Y.C.Tai, M. T. Davis, and T. D. Lee, A MEMS Electro Spray Nozzle for Mass Spectroscopy. 1997 International Conference on Solid-State Sensors and Actuators (Transducers '97), May 1997.
- [3] X.Q. Wang, A. Desai, Y.C Tai, L. Licklider, and T.D. Lee. "Polymer-Based Electro spray Chips for Mass Spectroscopy", *Proc. 12th Annual International Workshop on Micro Electro Mechanical System*, pp. 523-528, January 17-21, 1999, Orlando, Florida.
- [4] C. L. Coly, T. Tang, N. Chiem, and D. J. Harrison, "Clinical potential of microchip capillary electrophoresis system," *Electrophoresis 1997*, 18, 1733-1741.
- [5] N. H. Chiem and D. J. Harrison, "Monoclonal antibody binding affinity determined by microchip-based capillary electrophoresis," *Electrophoresis 1998*, 19, 3040-3044.
- [6] S. D. Mangru and D. J. Harrison, "Chemiluminescence detection in integrated postsparation reactors for microchip-bases capillary electrophoresis and affinity electrophoresis," *Electrophoresis 1998*, 19, 3040-3044.
- [7] X. Yang, C. Grosjean, and Y. C. Tai. "A MEMS Thermopneumatic Silicone Membrane Valve," *MEMS'97*, Nagoya, Japan, Feb. 1997.
- [8] S. Wu, Q. Lin, Y. Yuen and Y.C. Tai, "MEMS flow sensors for nano-fluidic applications," in *Proc. of The Thirteenth IEEE International Conference on Micro Electro Mechanical Systems (MEMS2000)*, Miyazaki, Japan, Jan. 23-27, 2000.
- [9] M. Koch, C. G. J. Schabmueller, A. G. R. Evans, and A. Brunnschweiler, "Micromachined chemical reaction system," *Sensor and Actuator*, 74(1999) 207-210.

- [10] K. Petersen, "From microsensors to microinstruments," *Sensor and Actuators A* 56 (1996), pp. 143-149.
- [11] C. H. Mastrengelo, M. A. Burns, and D. T. Burke, "Microfabricated devices, for genetic diagnostics," *Proceeding of the IEEE*, vol. 86, No. 8, August 1998.
- [12] B. H. Weigl and P. Yager, "Microfluidic diffusion-based separation and detection," *Science*, vol. 283, pp. 46-47, January, 1999.
- [13] S. Wu, J. Mai, Y.C. Tai, and C.M. Ho, "Micro Heat Exchanger by Using MEMS Impinging Jets," *Proc. 12th Annual International Workshop on Micro Electro Mechanical System*, pp. 171-176, January 17-21, 1999, Orlando, FL.
- [14] J. Pfahler, J. Harley, H. Bau, and J. Zemel, "Gas and liquid flow in small channels," *Symp. Micromechanical Sensors, Actuators, and Systems* (ed. D. Cho, R. Warrington, et al.) ASME DSC vol. 32, pp. 49-60, 1991.
- [15] E. B. Arkilic, M.A. Schmidt, and K.S. Breuer, "Gaseous flow in microchannels," *Application of Microfabrication to Fluid Mechanics*, ASME Winter Annual Meeting, pp. 57-65, Chicago, IL, Nov. 1994.
- [16] K. C. Pong, C.M. Ho, J. Liu, and Y.C. Tai, "Non-linear pressure distribution in uniform microchannels," *Application of Microfabrication to Fluid Mechanics*, ASME Winter Annual Meeting, pp. 51-56, Chicago, IL, Nov. 1994.
- [17] J. Liu, Y. C. Tai, K. C. Pong, and C. M. Ho, "Micromachine channel/pressure sensor system for microflow studies," *Transducers' 93*, pp. 995-997
- [18] C.W. Chiu, "Micro-channel Flow Studies and MEMS Flow Systems," *Master Thesis*, 1998, M.A.E. Department, UCLA.
- [19] J.C. Shih, C.M. Ho, J. Liu, and Y.C. Tai, "Monatomic and polyatomic gas flow through uniform microchannels," *Application of Microfabrication to Fluid Mechanics*, ASME Winter Annual Meeting, pp. 197-203, Atlanta, GA, Nov. 1996.
- [20] R.K. Prud'homme, T.W. Chapman, and J.R. Bowen, "Laminar compressible flow in a tube," *Appl. Sci. Res.* vol. 43, pp. 67-74, 1986.

- [21] H.R. van den Berg, C.A. Seldam, and P.S. Gulik, "Compressible laminar flow in a capillary," *J. Fluid Mechanics*, vol. 246, pp. 1-20, 1993.
- [22] J.C. Harley, Y. Huang, H. H. Bau, and J.N. Zemel, "Gas flow in micro-channels," *J. Fluid Mechanics*, vol. 284, pp. 257-274, 1995.
- [23] S. Wu, J. Mai, Y. Zohar, Y.C. Tai, and C.M. Ho, "A Suspended Microchannel with Integrated Temperature Sensors for High-pressure Flow Studies," *Proc. 11th Annual International Workshop on Micro Electro Mechanical System*, pp. 87-92, January 25-29, 1998, Heidelberg, Germany.
- [24] P. A. Thompson, "Compressible-Fluid Dynamics," *Advanced Engineering Series*, 1988.
- [25] J. D. Anderson, Jr., "Modern Compressible Flow," 2nd edition, *Series in Aeronautical and Aerospace Engineering*, McGraw-Hill, 1990.
- [26] M. J. Zucrow and J. D. Hoffman, "Gas Dynamics," John Wiley & Sons, Inc., 1976.
- [27] J. A. Owczarek, "Fundamentals of Gas Dynamics," *International Textbook in Mechanical Engineering*, International Textbook Company, 1964.
- [28] H. W. Liepman and A. Roshko, "Elements of Gasdynamics," *GALCIT Aeronautical Series*, John Wiley & Sons, Inc., 1957.
- [29] J. Q. Liu, "Integrated micro devices for small scale gaseous low study," *Ph.D. Thesis*, Electrical Engineering Department, California Institute of Technology, 1994.
- [30] X.Q Wang, X. Yang, K. Walsh, and Y.C. Tai, "Gas phase silicon etching with Bromine Triflouride," *Transducer '97*.
- [31] E. P. Popov, "Engineering Mechanics of Solids," *Prentic-Hall International Series In Civil Engineering and Engineering Mechanics*, Edited by W. J. Hall, 1990.
- [32] S. Timoshenko and S. Woinowsky-Krieger, "Theory of Plates and Shells," 2nd edition, *McGraw-Hill*, 1987.

- [33] J. K. Vennard and R. L. Street, "Elementary Fluid Mechanics," 5th Edition, John Wiley & Sons, Inc., 1975.
- [34] K. E. Petersen, " Silicon as a mechanical material," *Proceeding of the IEEE*, vol. No. 5, pp. 420-457, May, 1982.

CHAPTER 5

MICRO FLUIDIC COUPLERS

Abstract

Micromachined fluidic couplers capable of withstanding up to 1200 psi have been designed, fabricated, and tested. These couplers are robust, have high yield, and are compatible with existing MEMS fluidic devices.

5.1 Introduction

Rapidly developing Micro Electro Mechanical Systems (MEMS) technology makes micro fluidic systems very attractive for many applications, such as micro heat exchangers, micro chromatographs, biochemical detectors, micro mass spectrometers, micro reactors, and micro fluid control systems (e.g., microchannels, micro valves, micro pumps, and micro flow meters). It is quite challenging to transfer fluids between a micro fluidic system and its macroscopic environment because of micron-scale dimensions of

the system. There is no effective and simple way to apply conventional fluidic couplers to micro-scale fluidic systems at this time. Currently, to achieve coupling, a tube with an inside diameter significantly larger than the size of the inlet or outlet is directly glued to the opening as shown in Figure 5.1.1. The yield of this approach is usually very low due to tube misalignment and inlet or outlet blockage by excessive glue. In addition, the permissible number of couplings for a micro fluidic system is limited by the relatively large size of the tubing used, and may not be adequate for the system. Furthermore, such a coupling generally cannot withstand high pressures required in many applications.

Several different approaches have been developed [1-3]. However, they are still limited by many of the same critical issues. Micromachined rubber o-ring couplers [4] are reusable but feasible only for lower pressures.

In order to accommodate to the rapidly growing demand for micro fluidic systems, a novel, low-cost, and highly reliable coupling technique is needed. Micromachined fluidic couplers that have been developed at the Caltech Micromachining Laboratory can fulfill this requirement [5].

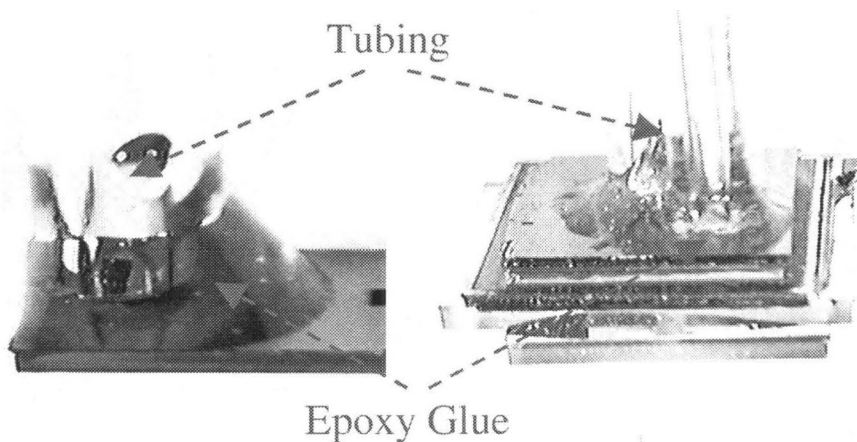


FIGURE 5.1.1 Pictures of the coupling with excessive epoxy.

5.2 Concept and Design

Micromachined fluidic couplers are used to connect fluidic capillaries to a micro fluidic system with inlets and outlets that may differ from the capillaries in both shape and size. By using such couplers, a fluidic interconnection with multiple channels is built for the micro fluidic system as shown in Figure 5.2.1.

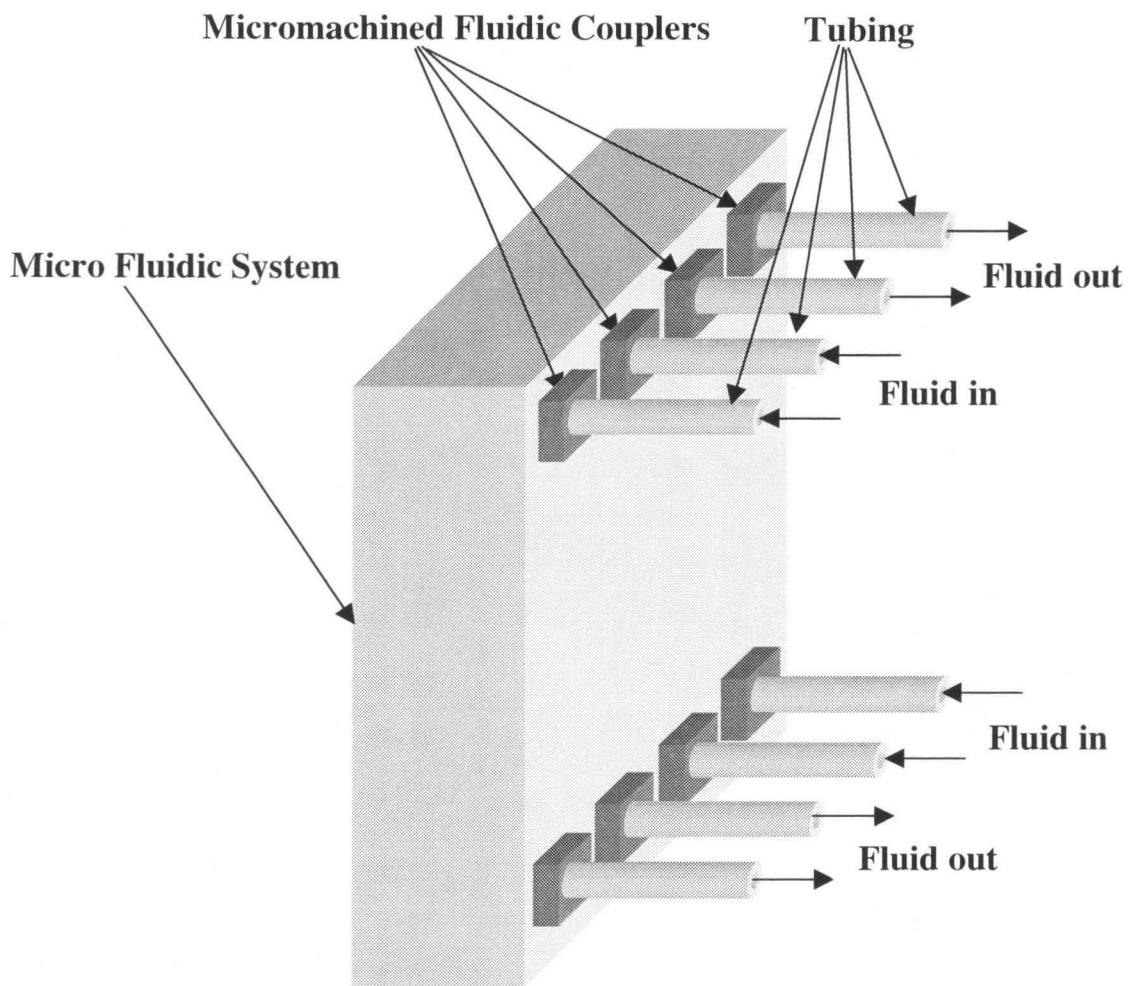


FIGURE 5.2.1 A micro fluidic system coupled with capillaries by micromachined fluidic couplers (not to scale).

In general, it is impractical to connect a fluidic capillary directly to the inlet or outlet due to their different shapes and sizes. An intermediate object, i.e., a micromachined coupler, must be introduced to achieve such a coupling. The coupler is designed in such a way that a capillary can be tightly placed into the size-matched hole in the center of the coupler and the coupler can be conformably fitted into the size-matched inlet or outlet as shown in Figure 5.2.2.

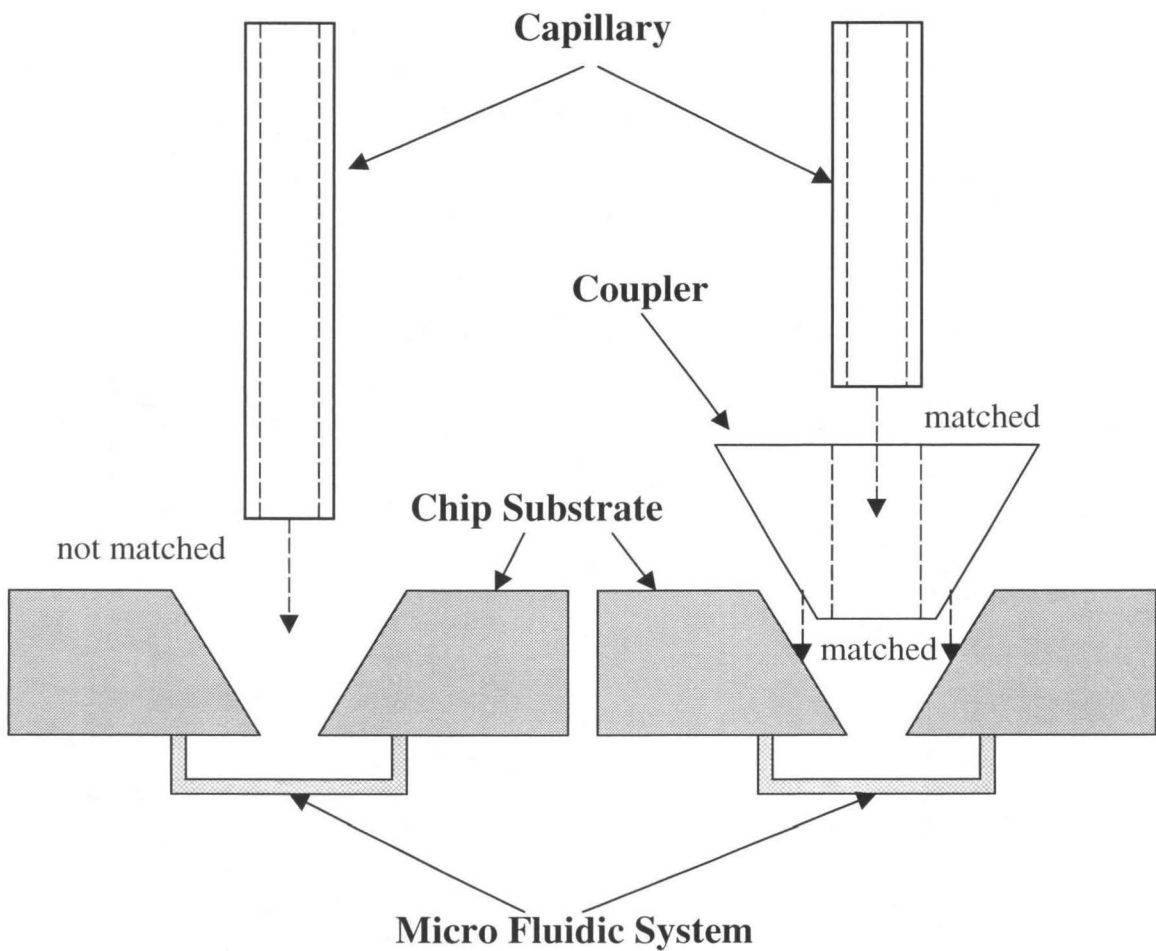


FIGURE 5.2.2 The general concept of a coupler: an intermediate fitting between the capillary and micro fluidic system (not to scale).

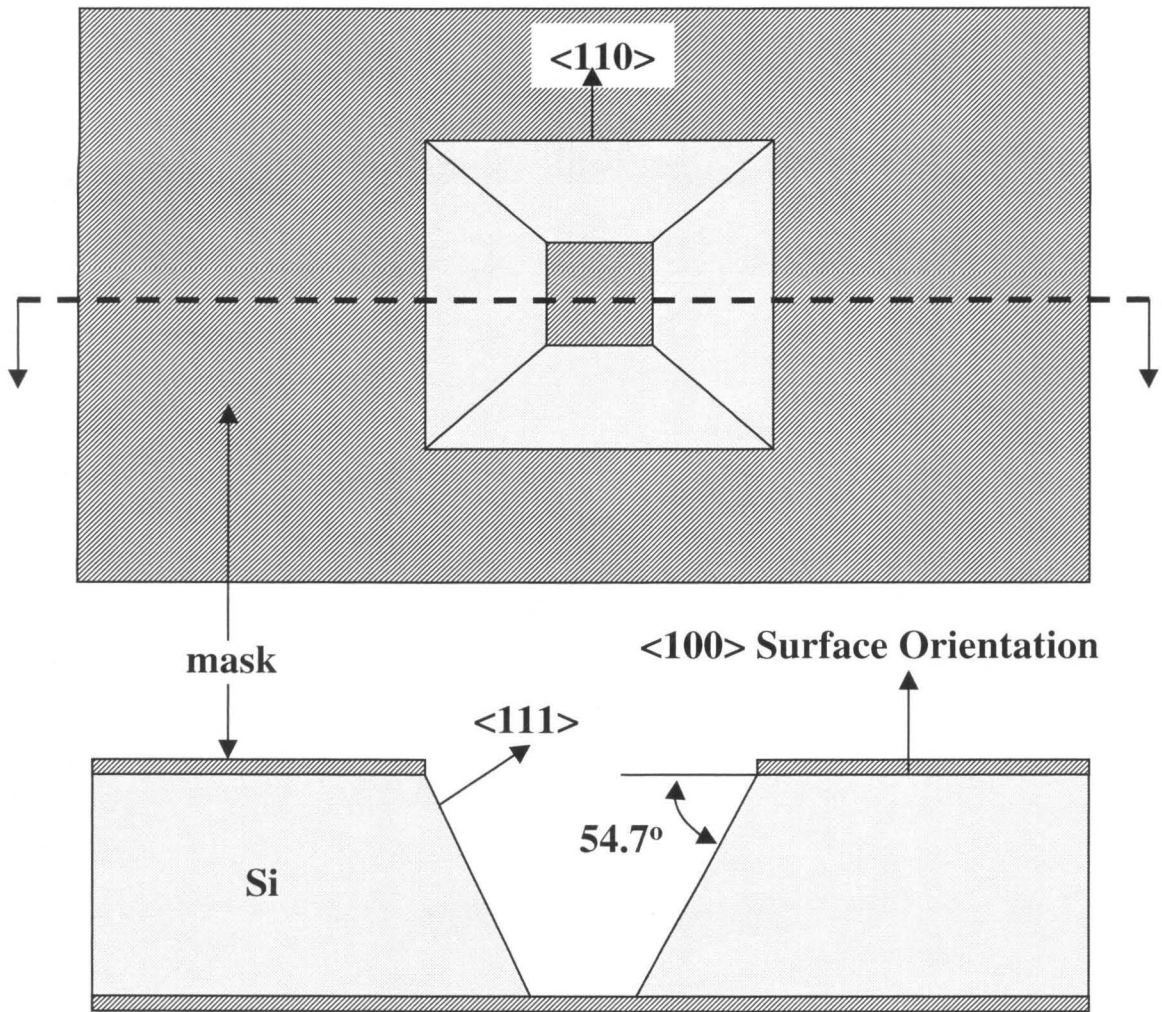


FIGURE 5.2.3 A pyramidal pit, bounded by the four- (111) planes, anisotropically etched into (100) silicon through a square opening in the mask.

For example, typical inlets and outlets in a fluidic system built on a silicon chip are pits etched into (100) silicon with an anisotropic wet etch (i.e., KOH, TMAH and EDP) through square openings in the etching mask. Such a pit has a pyramidal shape bounded by four (111) planes shown in Figure 3.2.3, and yet there is no effective way to connect a capillary directly to such an inlet or outlet. However, a coupler with the

truncated pyramidal shape bounded by four (111) sidewalls can now be applied to make such a connection, as shown in Figure 5.2.4. With the matching pyramidal shape formed by anisotropic wet etching, the coupler can be conformably fitted into the inlet or outlet. A capillary can be placed tightly in the size-matched hole etched in the center of the coupler by Deep Reactive Ion Etching (DRIE). Later they can be firmly bonded together by various techniques, such as gluing, polymer film bonding, indium solder bonding, or Au eutectic bonding. Also, as shown in Figure 5.2.5, a single coupler can be used for an inlet or outlet with various sizes by adjusting the fitting depth.

There are a few designs for a truncated pyramidal coupler as shown in Figure 5.2.6. Type A, as mentioned before, is the simplest design. Type B, with the same outside shape as type A, has a tubing stopper inside. Type C has a shoulder, which can be bonded to the chip substrate of the micro fluidic system to enforce the coupling.

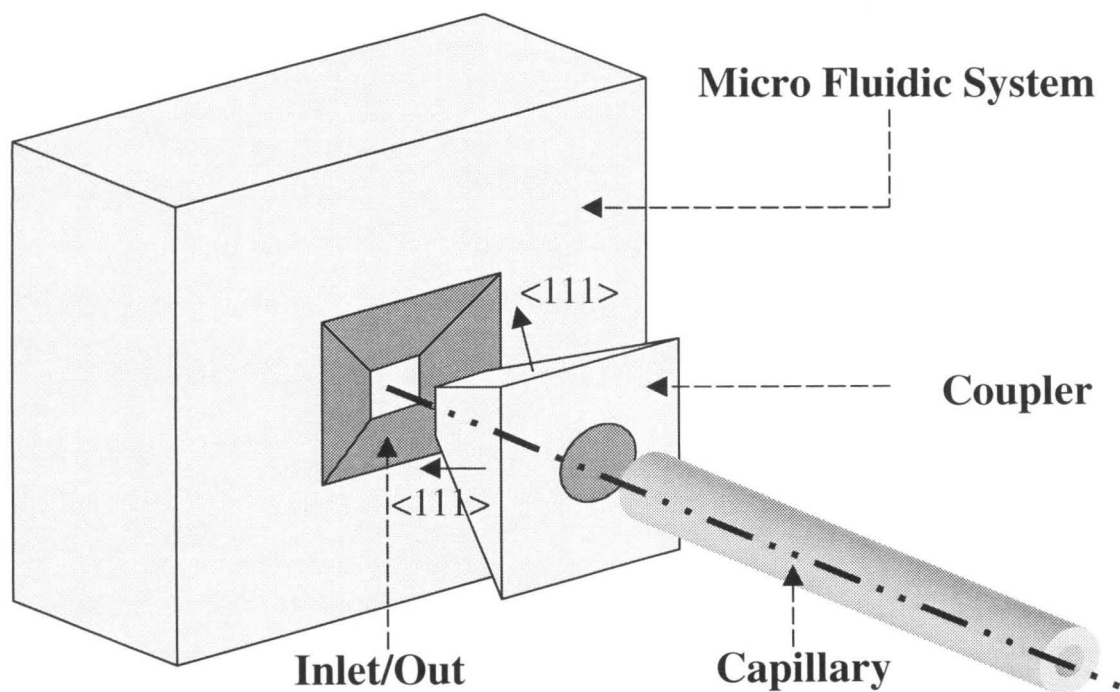


FIGURE 5.2.4 A truncated pyramidal coupler can be used to connect a capillary to an inlet or outlet (not to scale).

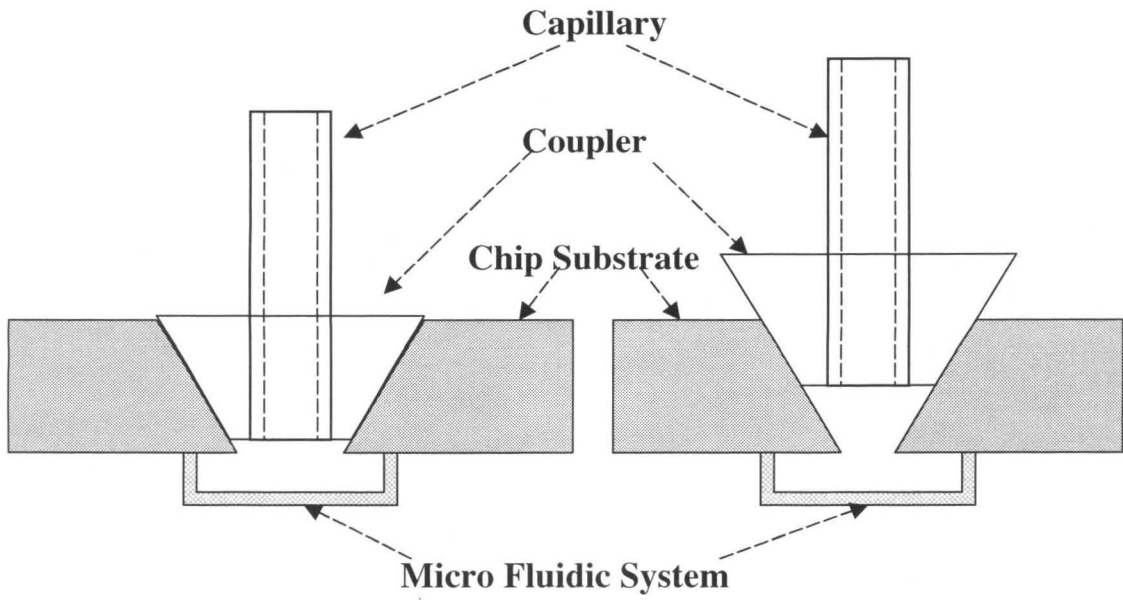


FIGURE 5.2.5. A coupler fits into an inlet or outlet of two different sizes by adjusting the fitting depth.

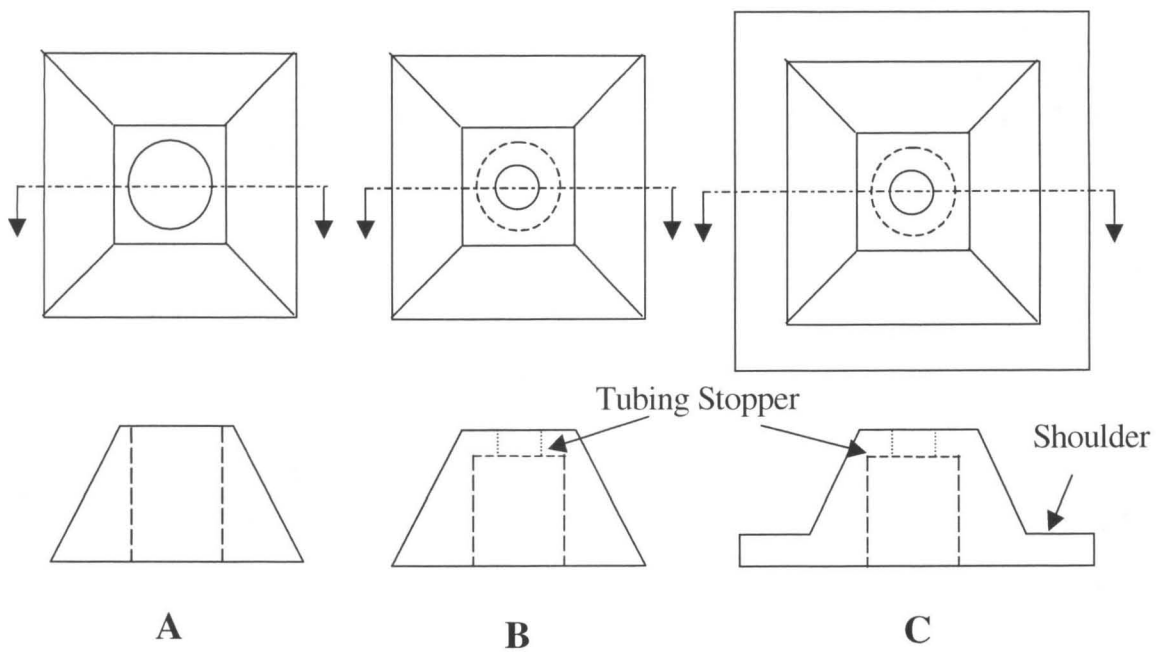


FIGURE 5.2.6. Three designs of truncated pyramidal couplers (not to scale).

The micromachined fluidic couplers can be made for inlets and outlets with any shape. As shown in Figure 5.2.7, the alignment post made in the same shape as the inlet or outlet can be fitted into the opening, and the large flat area can be bonded to the chip substrate of the micro fluidic system. As discussed before, the capillary tubing can be put into the center hole and then bonded to the coupler.

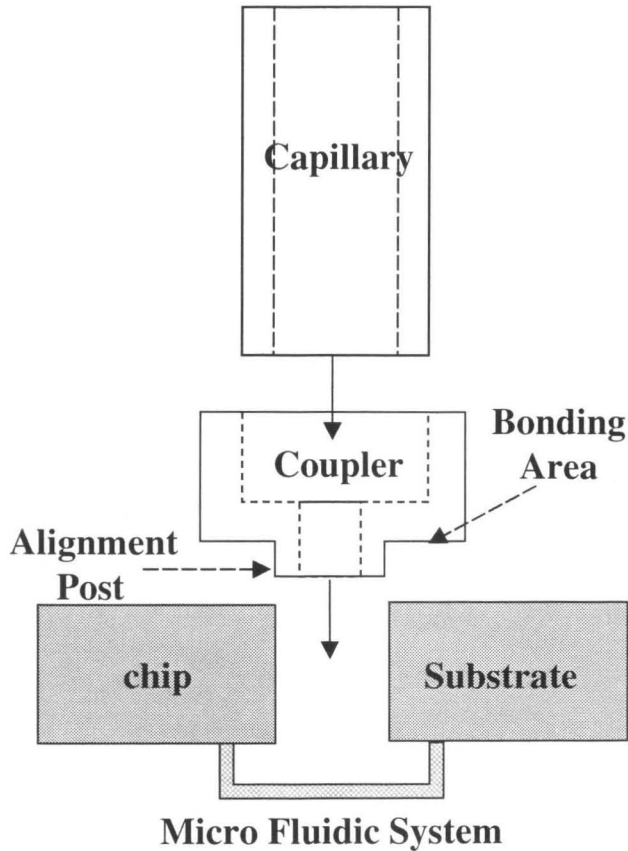


FIGURE 5.2.7 A capillary connected to an inlet or outlet by a post coupler (not to scale).

With micromachined couplers, the coupling process becomes less complicated. First, by using the specially designed micromachined couplers, small capillaries are easily aligned with the inlets/outlets of a micro fluidic system. Second, by coating a thin layer

of bonding material on their surfaces, micromachined couplers can be readily bonded to a fluidic system. Third, by applying existing bonding techniques such as gluing, polymer film bonding, indium solder bonding, or Au eutectic bonding, a strong coupling can be formed between capillaries and the micro fluidic system. Therefore, this coupling process can provide robust, high-yield fluidic interconnection with minimal preparation time and complexity.

5.3 Fabrication

The micromachined fluidic couplers can be made from different materials (i.e., silicon, metal, and even polymer plastic) that are employed in microfabrication processes. By using a batch micromachining process, a large quantity of couplers can be fabricated. Truncated couplers are designed for the inlet/outlet pits formed by silicon anisotropic wet etching. Post couplers are designed for the inlet/outlet pits with other shapes such as circular pits, rectangular pits, or even triangular pits

5.3.1 Silicon Truncated Pyramidal Coupler

As an example, we discuss the process for the type C coupler. The processes for the other two types of couplers are similar. Silicon truncated pyramidal couplers are fabricated by standard silicon anisotropic wet etching and Deep Reactive Ion Etching (DRIE). The process flow is shown in Figure 5.3.1.

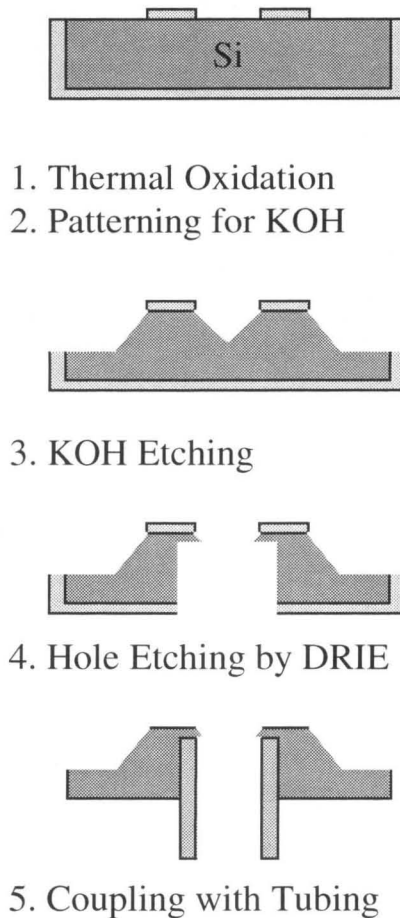


FIGURE 5.3.1 Process flow of silicon truncated pyramidal coupler.

Starting with a <100> silicon prime wafer, a layer of mask material is grown for the following silicon anisotropic wet etch and DRIE. By using a silicon anisotropic wet etch, a pyramidal island with a small pit in the center is created on the front side of the wafer. As evident from the desired geometry, corner compensation is required. Two schemes were investigated and etching results are shown in Figure 5.3.2. The merits of each method are described in [6] and [7], respectively. Using DRIE on the backside of the wafer, a circular pit is etched all the way through to meet the pit on the front side. A layer of bonding material is coated before or after DRIE. A capillary tube, coated with a

thin layer of bonding material, is placed in the size-matched pits and bonded to the coupler. Figure 5.3.3 and 5.3.4 show the pictures of fabricated silicon truncated pyramidal couplers.

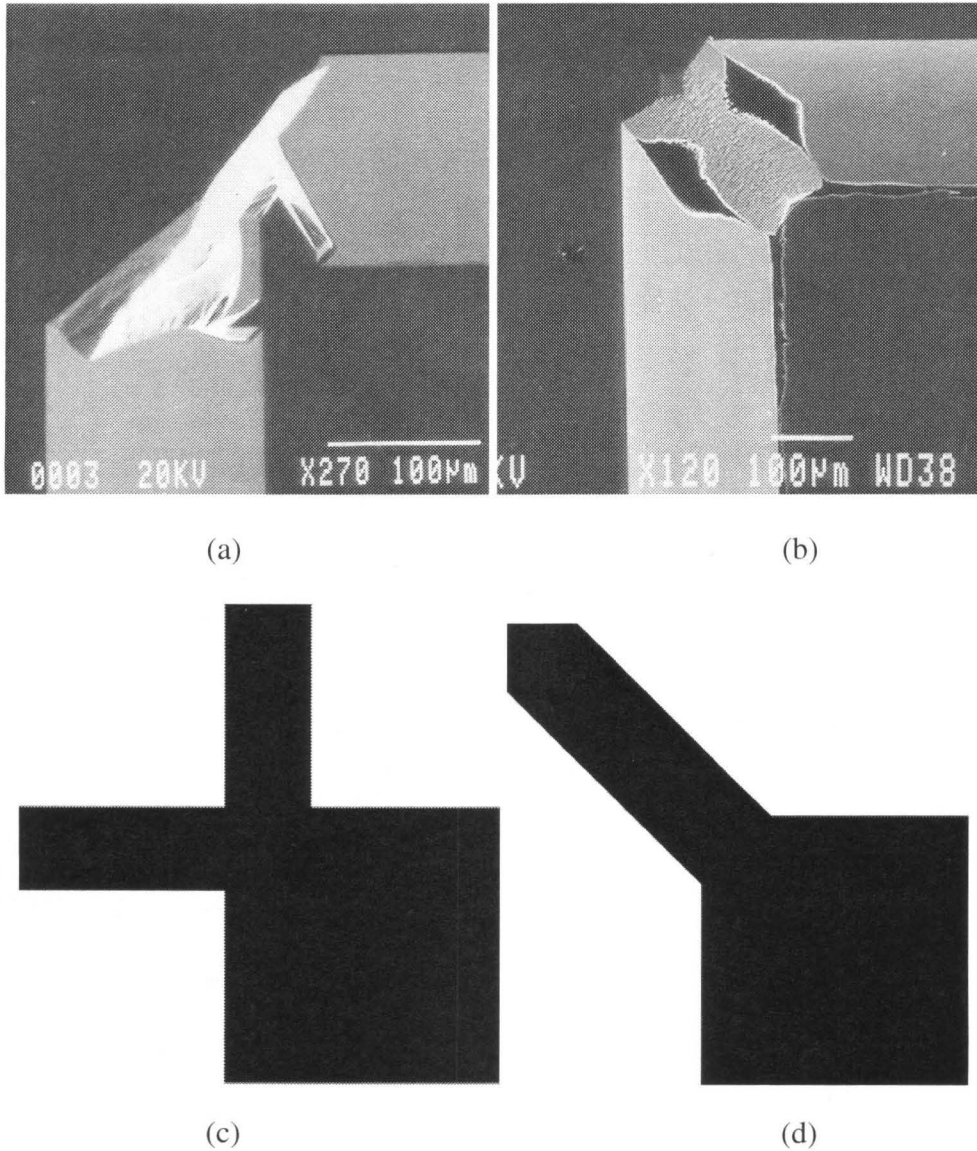


FIGURE 5.3.2 SEM corner compensation results (a) and (b) with respective masks (c) and (d).

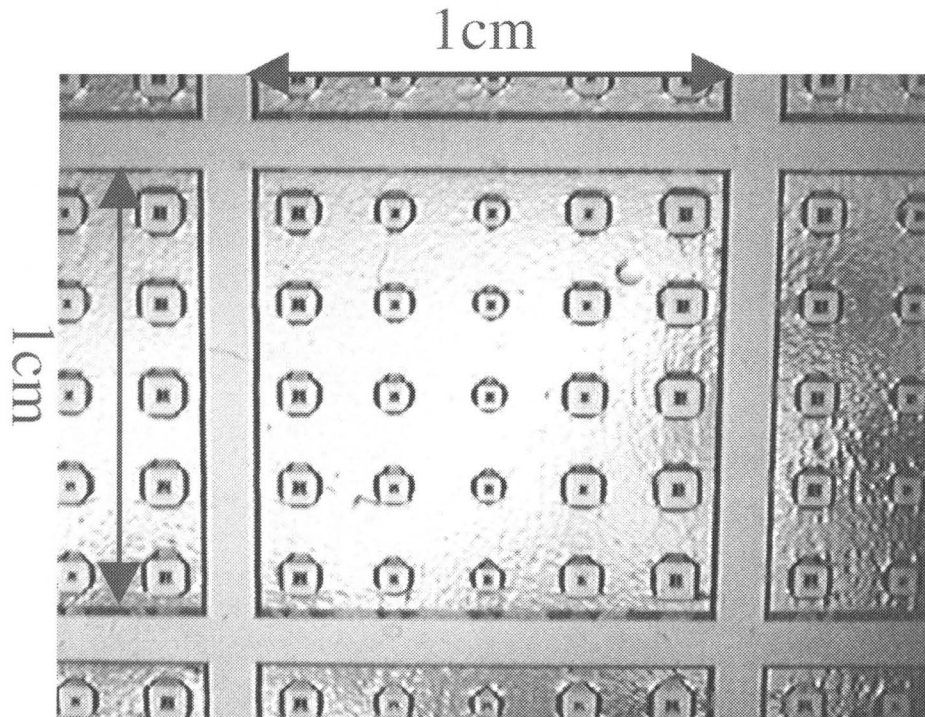


FIGURE 5.3.3 The picture of fabricated silicon truncated pyramidal couplers.

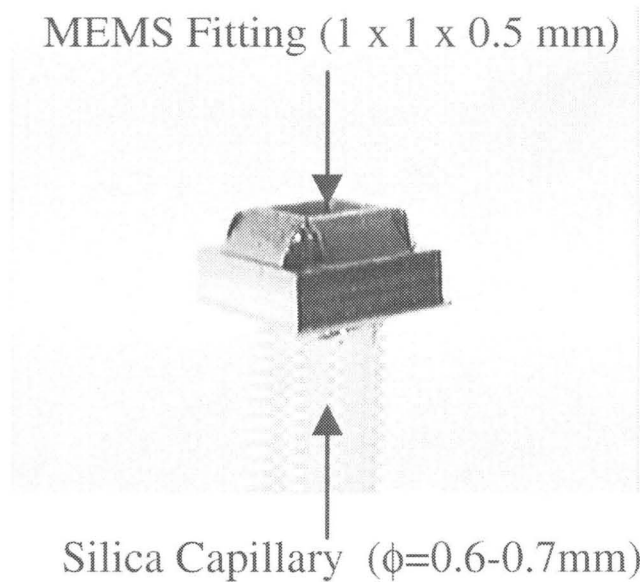


FIGURE 5.3.4 The picture of fabricated silicon truncated pyramidal couplers bonded with silica capillary tubing.

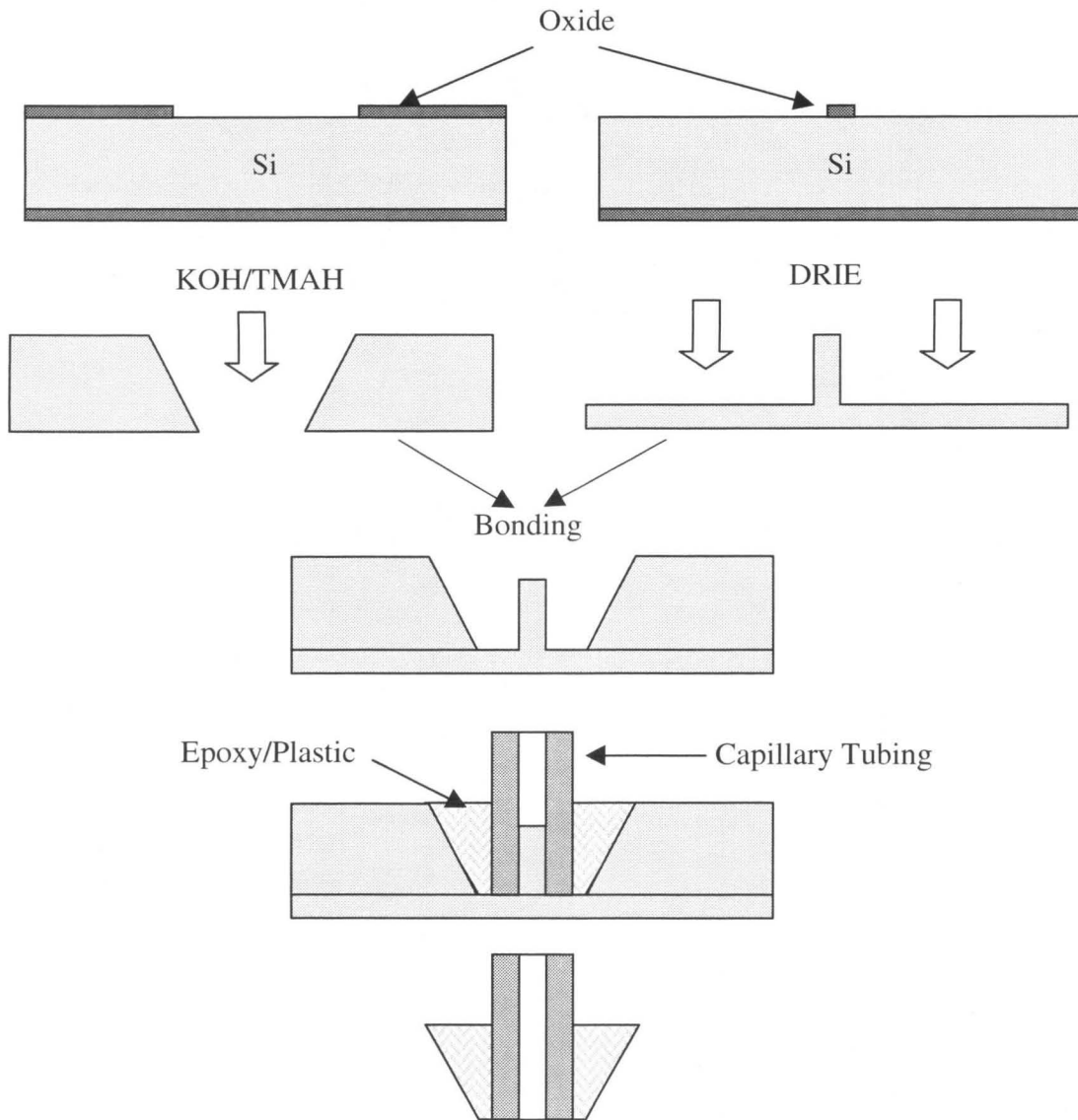


FIGURE 5.3.5 Process flow of a molded truncated pyramidal coupler.

5.3.2 Molded Truncated Pyramidal Coupler

Figure 5.3.5 shows the fabrication process flow of a molded coupler. The mold is fabricated from two bonded wafers. One is an oxidized wafer etched with KOH through opening to form truncated pyramid pits and the other wafer is etched to form an array of circular pegs by DRIE. After bonding the two wafers together, the structure is coated

with a PTFE (polytetrafluoroethylene) based mold release. Moldings are realized by fitting raw material such as a hot-melt polyolefin and epoxy around fused silica tubing fitted on mold posts and releasing when cured. Released structures are then attached to fluidic ports simply by re-heating polyolefin, allowing it to reflow and adhere to the silicon port. In applications where heating is unacceptable, adhesive joining can be used. Figure 5.3.6 shows a picture of the molded coupler.

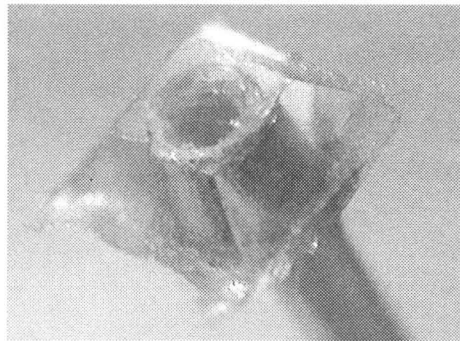


FIGURE 5.3.6 The picture of a molded coupler.

5.3.3 Post Coupler

Post coupler is fabricated on a silicon wafer by etching three times via DRIE. The process flow is shown in Figure 5.3.7. Starting from a flat wafer, 200 to 300 μm deep pits are etched on the front side, and then 50 to 100 μm high alignment posts are masked and formed on the front side by etching the unmasked area. The posts are designed such that their sizes closely match that of the inlets/outlets. On the backside, pits are etched down all the way to meet the pits on the front side. The size of the pits on the backside is chosen to closely match the size of the tubing. After coating with a bonding layer, a tube is inserted into the pit from the backside and then bonded to the coupler.

Post couplers can be used for a micro fluidic system with small straight inlets and outlets. By inserting the alignment post into an inlet or outlet of matching size, the coupler and tubing are automatically aligned to the inlet/outlet. With the strong bond formed by the bonding material and large bonding surface, the coupling can withstand very high pressures.

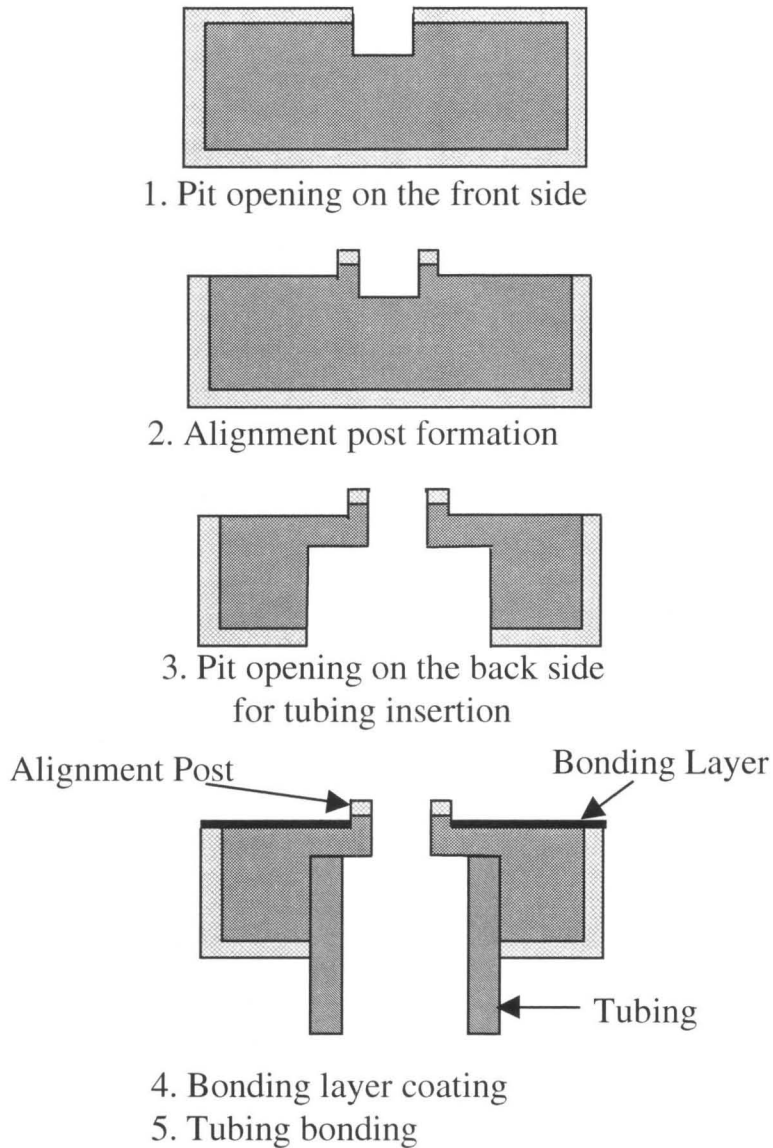


FIGURE 5.3.7 Post coupler fabrication process flow.

5.4 Test Results and Discussion

Figure 5.4.1 shows coupling with silicon fluidic couplers. The testing of the coupling under high-pressure conditions was performed using the setup shown in Figures 5.4.2 and 5.4.3. Valco stainless steel high-pressure liquid chromatography (HPLC) fittings and Vespel/graphite ferrules were used to connect a fused silica capillary to conventional Swagelok plumbing. In order to determine the failure point and the operating range, a blocked coupler was connected to fused silica capillary and pressurized using filtered (0.1 μm) nitrogen gas from a cylinder. Pressure was measured using an Omega PX120-2KGV pressure transducer in conjunction with an Omega DP25-S Strain Gage Panel Meter. The bulk coupler (with 680 μm OD fused silica tubing) was able to withstand at least 1200 psi. Table 5.4.1 provides a comparison of our work to other couplers.

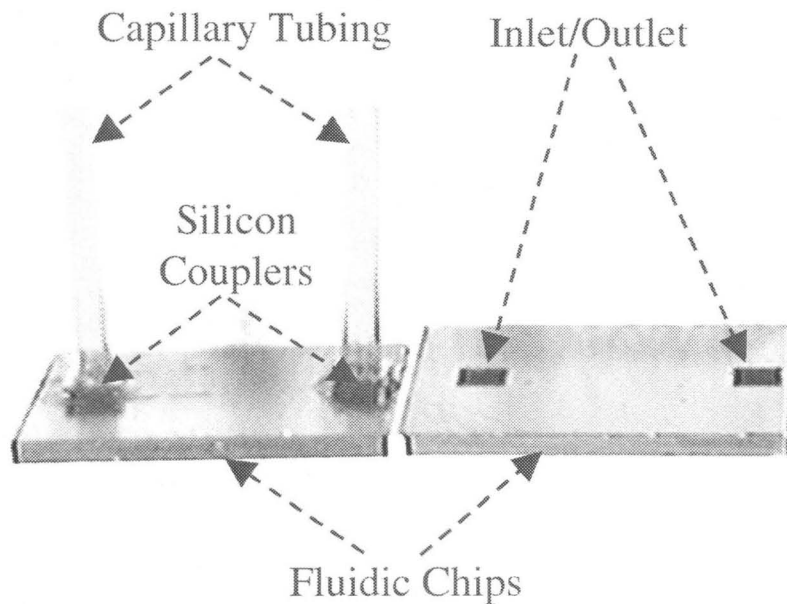


FIGURE 5.4.1 The pictures of fluidic chip with/without coupling to capillary tubing through silicon couplers.

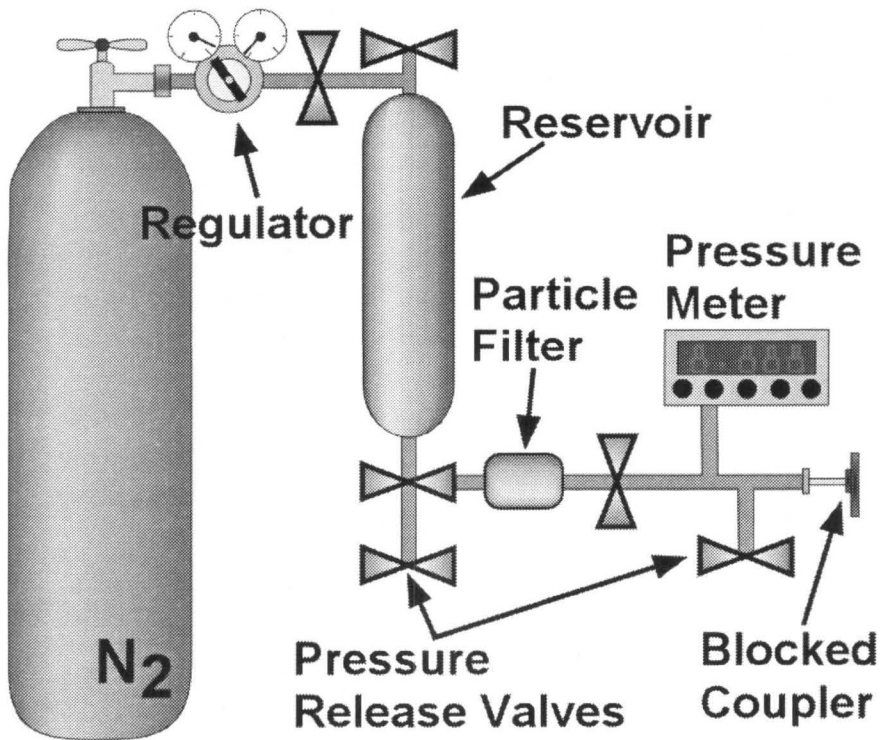


FIGURE 5.4.2 Illustration of the test setup for micro fluidic couplers.

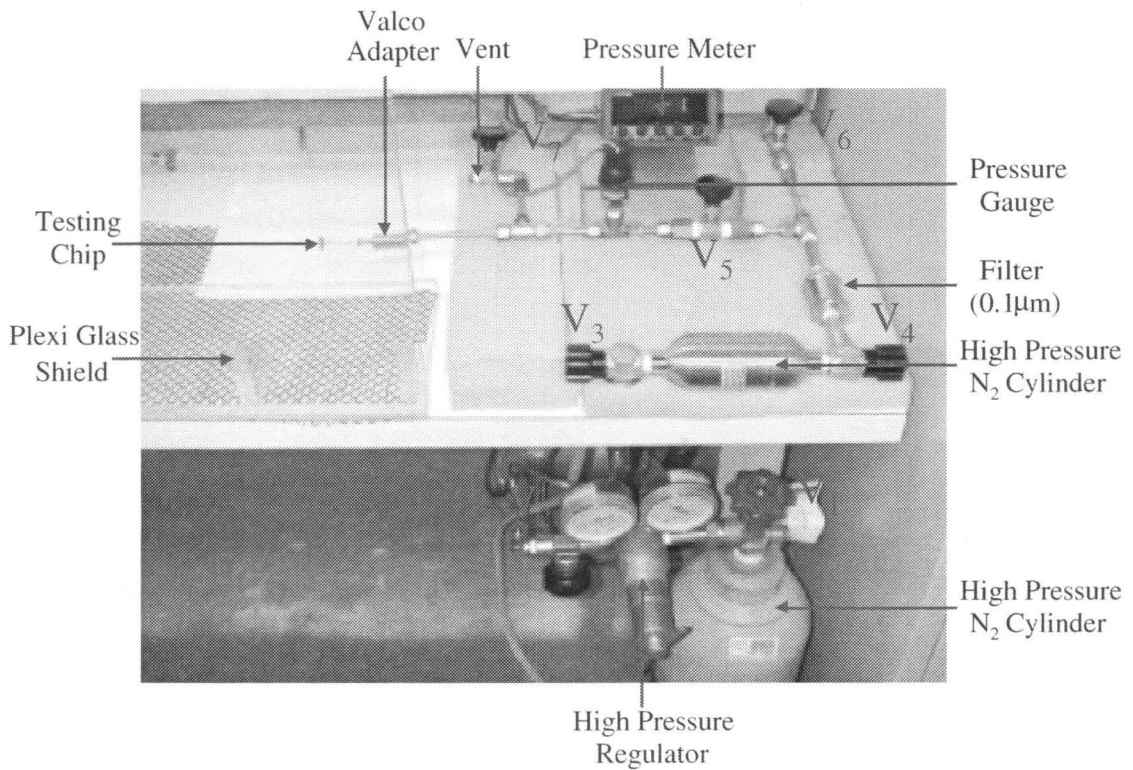


FIGURE 5.4.3 A picture of the test setup for micro fluidic couplers.

TABLE 5 A comparison of this work to other couplers.

Description of Coupler	Operation Range	References
Silicon Finger Microjoint with Silicone Gasket and Tygon Tubing	>30 psi	[8]
Silicon/Plastic Coupler with Silicone Gasket & Capillary Tubing	~60 psi	[2]
Silicone Gasket Sealed Silicon Coupler with Capillary Tubing	~80 psi	[4]
Silicon Sleeve Coupler with Capillary Tubing	~500 psi	[2]
Silicon Coupler with Fused Capillary Tubing	>1200 psi	This work
Mismatched Silicon Coupler with Capillary Tubing	~1740 psi	[3]

5.5 Conclusion

Various self-aligning micromachined fluidic couplers have been developed. Silicon couplers have been fabricated using silicon anisotropic etching (i.e., KOH) and Deep Reactive Ion Etching (DRIE). In addition, a molding technique has also been demonstrated for the molded coupler fabrication. With this novel approach, couplers can have arbitrary geometry, ensuring compatibility with most fluidic ports and providing external connections via fused silica capillaries for MEMS fluidic devices. Finally, the coupling with a silicon coupler has been tested, and no failure has been observed up to 1200 psig of pressure.

Reference:

- [1] Gonzalez, C., S.D. Collins, and R.L. Smith, "Fluidic interconnects for modular assembly of chemical microsystems," *Sensors and Actuators B*, 1998, 49: pp. 40-45.
- [2] Gray, B.L., et al., "Novel interconnection technologies for integrated microfluidic systems," *Sensors & Actuators A Physical*, 1999(1): pp. 57-65.
- [3] Spiering, V.L., et al., "Novel microstructures and technologies applied in chemical analysis techniques," *Transducers '97*, Chicago, IL, pp. 511-514, 1997.
- [4] Yao, T.J., et al., "A Micromachined Rubber O-Ring Microfluidic Coupler," *MEMS 2000*, Miyazaki, Japan, 2000.
- [5] E. Meng, S. Wu, and Y. C. Tai, "Micromachined Fluidic Couplers," *J. of Micro Total Analysis System*, 2000.
- [6] Jiang, F., et al. *A Micromachined Polysilicon Hot-Wire Anemometer in Solid-State Sensor and Actuator Workshop*. 1994. Hilton Head, SC.
- [7] Enoksson, P., *New structure for corner compensation in anisotropic KOH etching*. *Journal of Micromechanics and Microengineering*, 1997. **7**(3): pp. 141-147.
- [8] Gonzalez, C., et al., *Microjoinery: Concept, Definition, and Application to Microsystem Development*. *Sensors and Actuators A*, 1998. **66**(1-3): pp. 315-332.

CHAPTER 6

INTEGRATED MICRO FLUIDIC FLOW SENSORS

ABSTRACT

This chapter describes the application of micromachined thermistors to measuring liquid flow rates in the nanoliter-per-minute range. The sensors use a boron-doped polysilicon thin-film heater that is embedded in the silicon nitride wall of a microchannel. The boron doping is chosen to increase the heater's temperature coefficient of resistance within tolerable noise limits, and the microchannel is suspended from the substrate to improve thermal isolation. The sensors have demonstrated a flow rate resolution of 0.4 nL/min, as well as the capability of detecting micro bubbles in the liquid. Heat transfer simulation has also been performed to explain the sensor operation and yielded good agreement with experimental data.

6.1 Introduction

The emerging technology of Micro Electro Mechanical Systems (MEMS) is enabling micro fluidic systems for fluid transport in many applications. These applications include micro electrophoresis [1-4], microfluidic control (micro pumps, micro valves, micro filters, micro flow meters) [5-7], micro reaction [8], and micro total analysis [9-11]. While precise flow control is generally needed in these applications, existing commercial sensors are inadequate for this purpose because of their limited sensitivity, large size, high dead volume, and difficulties in interfacing with microfluidic devices.

To address the need for precise flow control in microfluidic systems, MEMS technology has been used to develop micro sensors for liquid flow rate measurement [12-15]. Achieving a measuring resolution up to a few microliters per minute, both thermal [12-14] and non-thermal [15] transducing principles have been used, and channels built using chip-bonding techniques have been employed as the flow-carrying device [12-13].

This work developed a class of MEMS flow sensors that demonstrate the first capability of measuring liquid flow rates below 20 nL/min with a resolution higher than 1nL/min, as well as detecting passage of micro bubbles in the flow. These thermal sensors use a boron-doped polysilicon thin-film resistor embedded within the wall of a microchannel. The microchannel, a key feature for our sensors, is fabricated using surface micromachining technology [16] (without chip-bonding), and is released from the silicon substrate using BrF_3 dry etching [17] for improved thermal isolation. The doping concentration for the polysilicon resistor is optimally chosen for an increased temperature coefficient of resistance, while keeping the noise level within tolerable limits. The

subsequent sections describe the design, fabrication, and testing, as well as heat transfer analysis of our flow sensors.

6.2 Design

The basic operating principle of the flow sensor utilizes micro convective heat transfer from a heated polysilicon thin-film sensing element (hereafter referred to as a heater) to a liquid flowing inside a microchannel. Figure 6.2.1 illustrates such a MEMS microchannel flow sensor approach. The polysilicon heater is built on the channel wall. By measuring the sensor temperature, the liquid flow rate can be calculated.

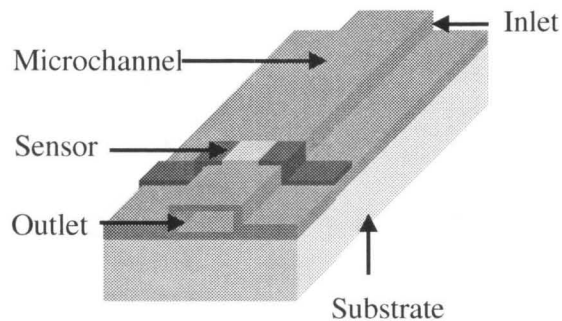


FIGURE 6.2.1 A microchannel-based flow sensing approach.

Since the channel is in direct contact with the substrate, the heat loss from the heater to the substrate may considerably reduce the sensor's sensitivity to the fluid flow. Figure 6.2.2 shows an improved approach, in which a portion of the substrate lying below the channel is removed to achieve better thermal isolation. To minimize the effect of channel wall deflection, the heater is located close to the channel outlet.

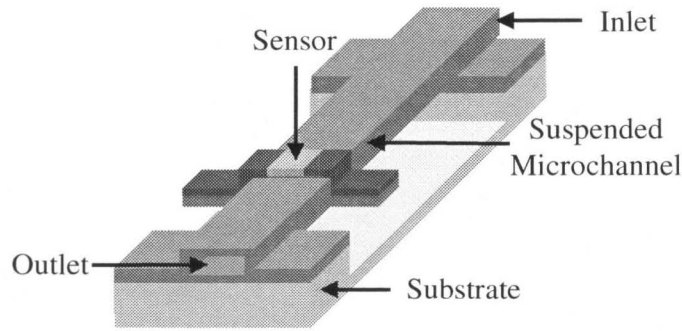


FIGURE 6.2.2 An improved flow sensing approach with a suspended microchannel.

Since the sensitivity of the sensor also depends on the heater's temperature coefficient of resistance (TCR), we investigated three sensor designs shown in Figure 6.2.3(a-c). The microchannels in all three designs have typical dimensions of $2000 \times 20 \times 2 \mu\text{m}^3$. In the first design (Figure 6.2.3(a)), the microchannel lies directly on the substrate, and the polysilicon heater is heavily doped with boron (concentration $2 \times 10^{19} \text{ cm}^{-3}$). In comparison, in the second design as shown in Figure 6.2.3(b), the doping concentration of the polysilicon thin film is reduced to $2 \times 10^{18} \text{ cm}^{-3}$. This increases the heater's TCR (while keeping the noise level within tolerable limits), and hence sensitivity to the flow. Finally, the third design, depicted in Figure 6.2.3(c), employs a suspended microchannel, which results in improved thermal isolation. Compared with Figure 6.2.3(b), the lightly doped heater length is extended to the channel's entire transverse dimension. This increases the heater's resistance and hence reduces inaccuracies arising from the resistance of the leads and wires. To summarize, these three designs allow us to investigate the effects of channel suspension and heater temperature sensitivity.

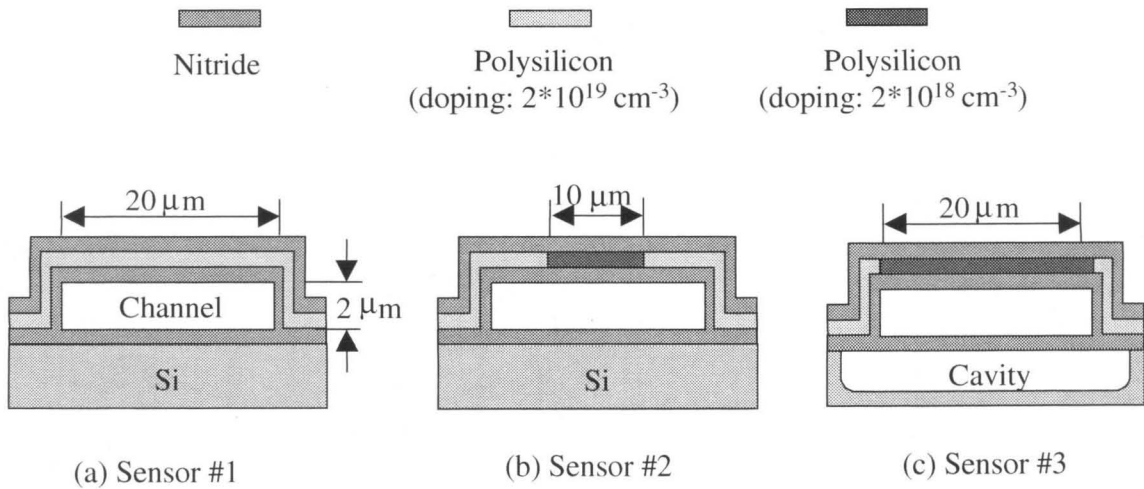


FIGURE 6.2.3 Three designs of flow sensors.

6.3 Fabrication

Figure 6.3.1 shows the fabrication process of the flow sensor, which includes the microchannel and integrated heating element. The process involves the following steps.

- (1) To start, a 1 μm -thick silicon nitride layer is deposited onto a bare silicon wafer.
- (2) A 2 μm PSG layer is then deposited on top of silicon nitride.
- (3) The PSG layer is patterned to define the microchannel geometry.
- (4) Another 0.6 μm layer of silicon nitride is deposited as the top wall of the microchannel.
- (5) The PSG is etched away by HF to form the microchannel.
- (6) 0.5 μm of polycrystalline silicon is deposited as the sensor material.
- (7) Polysilicon is doped by B^+ ion implantation, and followed by annealing at 1000°C for 30 minutes.
- (8) Polysilicon is patterned by plasma dry etching to define sensor geometry.
- (9) The sensors are sealed by uniformly depositing 0.6 μm of silicon nitride. Then the inlet and outlet are opened by KOH.
- (10) Contact opening and Al metalization form connections between the macro world and the sensing element.
- (11) Finally, thermal

isolation of the channel is achieved by BrF_3 isotropic bulk etching of the silicon underneath the channel.

Figure 6.3.2 shows a fabricated flow sensor with polysilicon resistors and a micro channel on the silicon substrate. Figure 6.3.3 shows a fabricated flow sensor with polysilicon resistors and a micro channel suspended from silicon substrate.

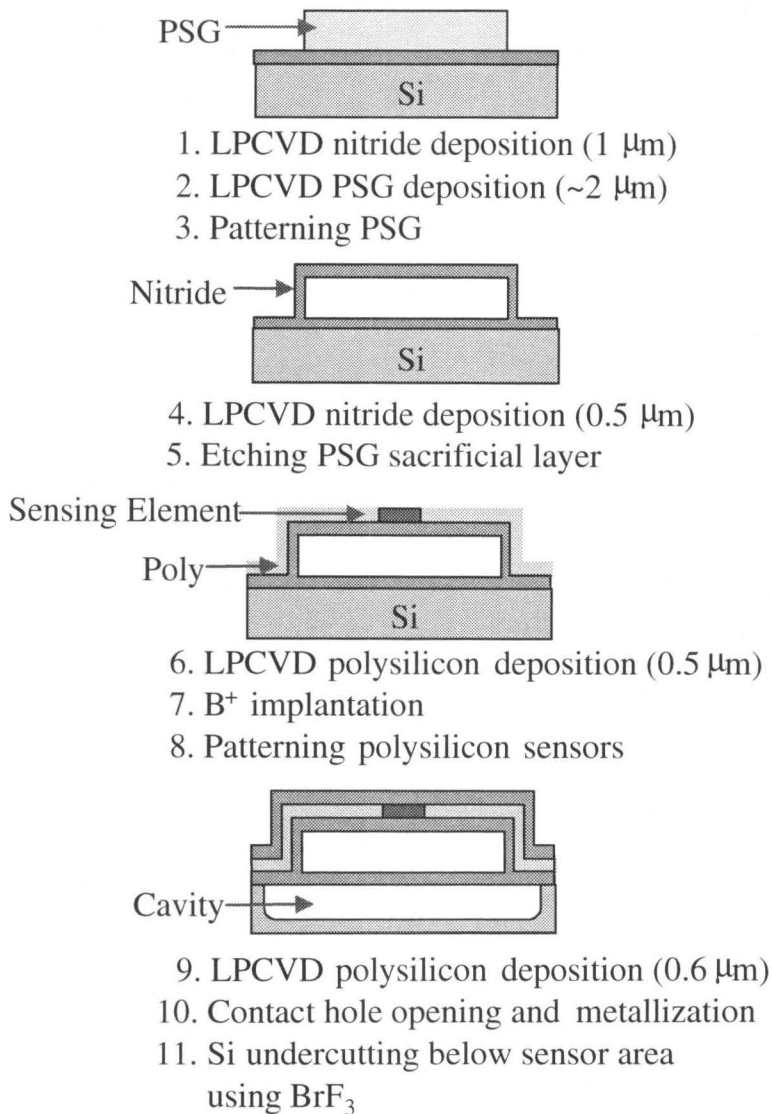


FIGURE 6.3.1 Process flow of the microchannel flow sensor with a sensing element embedded in the channel wall.

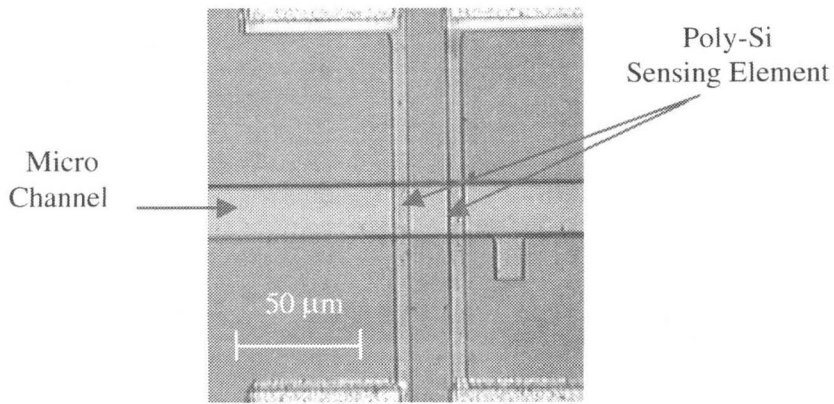


FIGURE 6.3.2 A fabricated flow sensor with polysilicon resistors and a micro channel on the silicon substrate.

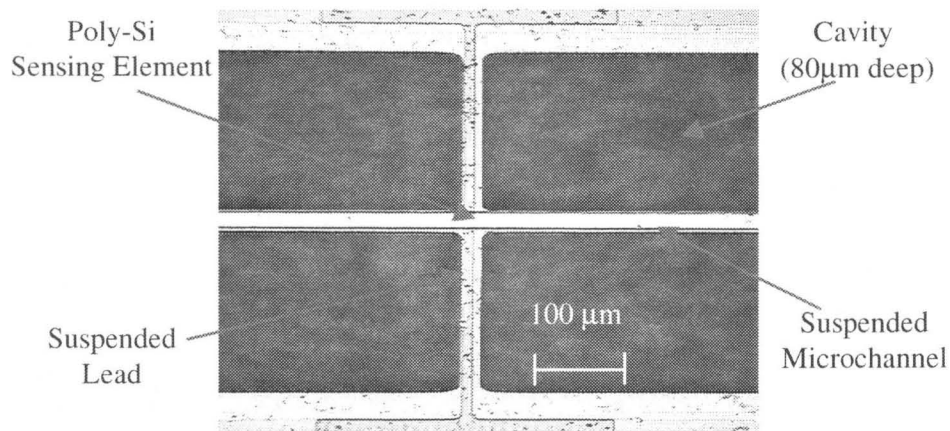


FIGURE 6.3.3 A fabricated flow sensor with polysilicon sensing element and a micro channel suspended away from silicon substrate.

6.4 Experimental Setup

A comparative study was conducted for the three types of flow sensors given in Figure 3. The package used to perform flow sensor testing is shown in in Figure 6.4.1. The sensor chip was glued to an IC package by epoxy, and electrical connection was made by wire

bonding. The inlet and outlet of the sensor's microchannel were connected to the macro world by glass tubings.

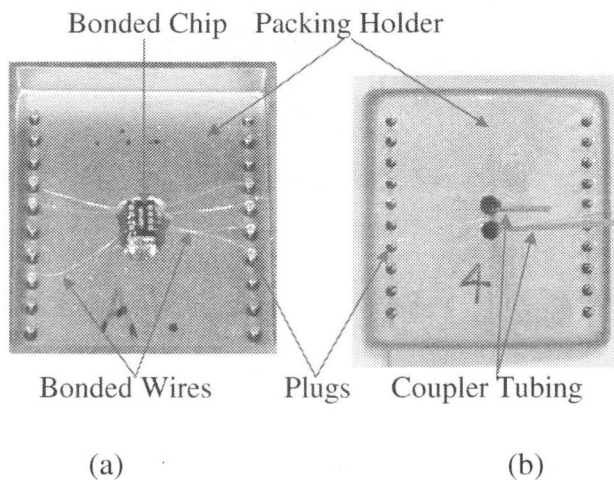


FIGURE 6.4.1 Pictures of the chip packing: (a) top view, (b) bottom view.

Figure 6.4.2 shows the experimental setup. DI water was forced into the microchannel by pressurized microelectronic grade nitrogen gas from a reservoir tank. The volumetric flow rate was then measured by timing the distance traveled by the water meniscus past marked gradations on a 10 μL glass pipette. Each flow rate data point was taken in a time period between thirty minutes and twenty-four hours, depending on the flow rate.

The sensor output was taken simultaneously with the flow measurements to give a correlation between sensor readings and flow rate. The sensor was tested and calibrated in an isothermal chamber with $\pm 0.05^\circ\text{C}$ temperature control to minimize ambient temperature fluctuations. The sensors were calibrated against an Omega DP251 Precision Temperature Meter using a resistive temperature detector (RTD) probe. With the sensors biased between $70\mu\text{A}$ to $100\mu\text{A}$, the voltage readings were taken using an HP 34970A data acquisition system, thus enabling us to track the time history of sensor readings. The

temperature calibration combined with sensor measurements provided thermal data essential for comparison to finite element simulation. Unlike the manual flow measurements, the sensor measurements were much faster ($\sim 10\text{-}60$ samples/s) and 100 data points were taken per flow rate measurement.

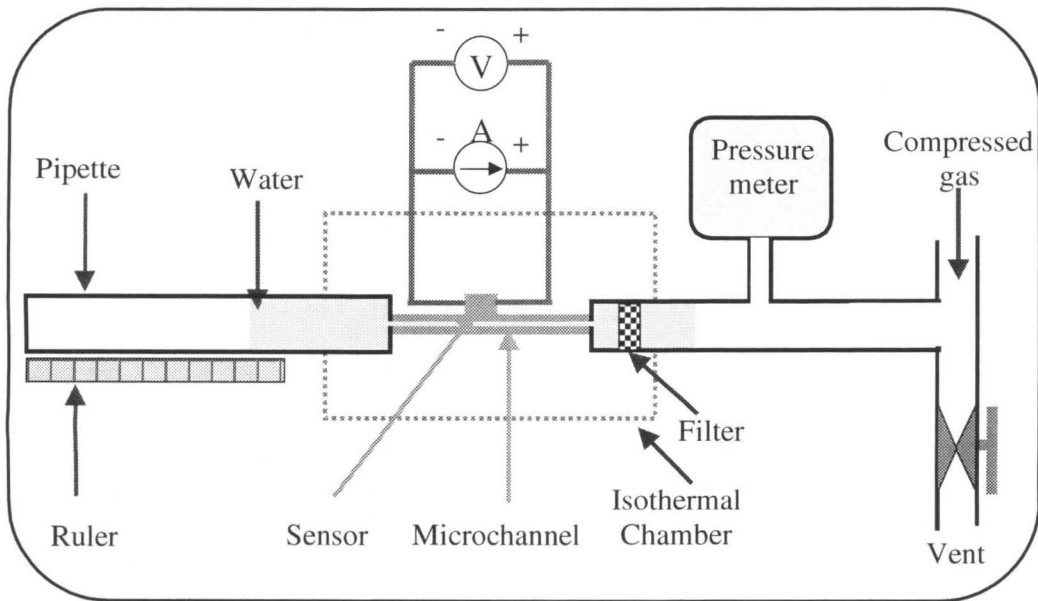


FIGURE 6.4.2 Schematic of the calibration system for MEMS flow sensors.

6.5 Test Results and Discussion

In this section, we will discuss the calibration of the heater resistance as a function of the temperature, the voltage output in response to fluid flow, and flow-induced heater temperature change.

Figure 6.5.1 shows the temperature dependence of sensor resistance for the three sensors. In the temperature calibration range the resistances decrease linearly with temperature, and thus can be characterized as follows:

$$\frac{R(T)}{R(T_0)} = 1 + \alpha(T - T_0) \quad (6.1)$$

where α is the temperature coefficient of resistance (including effects of lead and wire resistance change). For sensors #1, #2 and #3, α is found to be $-0.17\%/^{\circ}\text{C}$, $-0.56\%/^{\circ}\text{C}$ and $-0.67\%/^{\circ}\text{C}$, respectively. Sensors #2 and #3 have a higher TCR than #1 because of lower doping of the heating region. Compared to sensor #2, sensor #3 has a larger length with lower doping concentration, and hence a slightly higher TCR. According to our calibration, the temperature resolution of all three sensors is better than 0.05°C .

The sensitivity of a sensor, denoted S_V , is defined as the ratio between the changes in output voltage and flow rate, i.e.,

$$\Delta V = S_V \Delta Q_v. \quad (6.2)$$

While S_V varies for different flow rates, the sensitivity can be assessed in an average sense by the slope of a straight line fitted to the measurement data. Figure 6.5.2 shows the measured sensor response to the volumetric flow rate of DI water in the channel under constant current mode, and corresponding fitting lines. We can see that under the same constant current bias at $100\mu\text{A}$, sensor #2 is much more sensitive. Furthermore, even at $70\mu\text{A}$ bias current, sensor #3 is ten times more sensitive to flow than sensor #2.

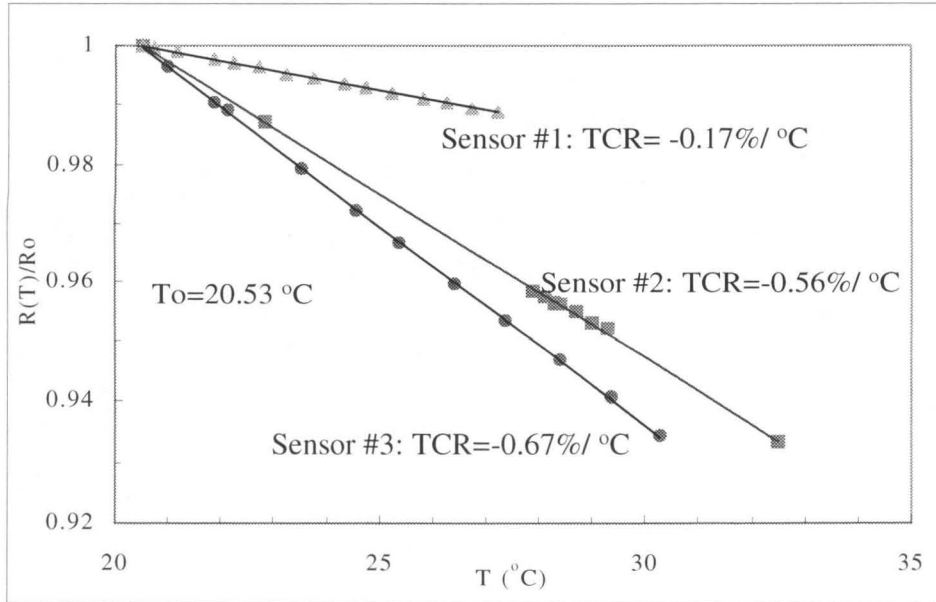


FIGURE 6.5.1 Temperature dependence of three types of sensors.

Electrically, the output voltage change can be written as

$$\Delta V = I_0 [R(T) - R(T_0)] = V_0 \alpha \Delta T \quad (6.3)$$

where $V_0 = I_0 R(T_0)$ and $\Delta T = T - T_0$. From Equations 10.2 and 10.3, we have

$$S_V = V_0 \alpha \frac{\Delta T}{\Delta Q_v} = V_0 \alpha S_T \quad (6.4)$$

where $S_T \equiv \frac{\Delta T}{\Delta Q_v}$, called temperature-to-flow ratio, is related to the structure design and fluid properties.

Although S_V is an important sensor characteristic, it involves the original bias voltage that is not related to the sensor design. Thus, it is more appropriate to normalize the sensitivity by the initial bias signal and define the relative sensitivity:

$$S_{V/V_0} = \frac{\Delta V/V_0}{\Delta Q} = \alpha \frac{\Delta T}{\Delta Q} = \alpha S_T \quad (6.5)$$

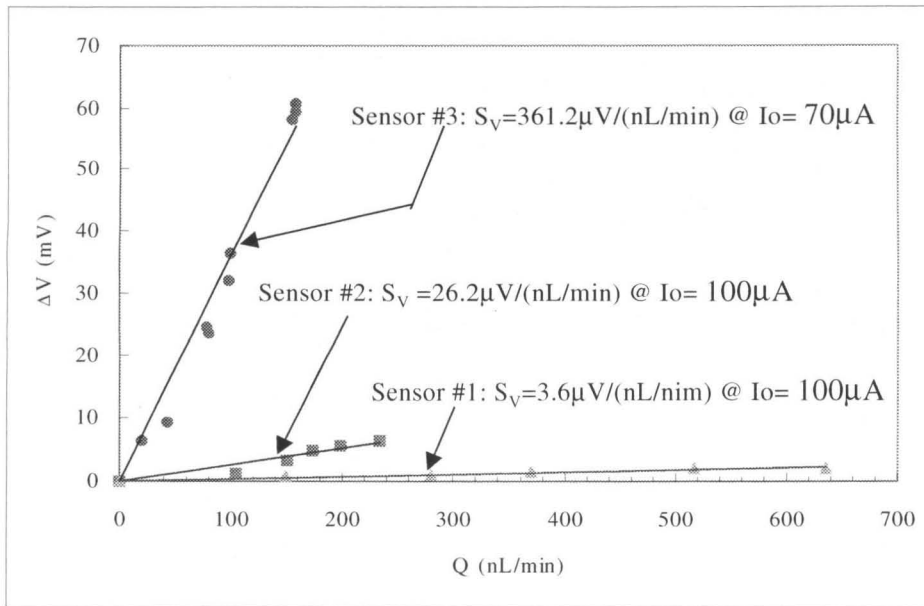


FIGURE 6.5.2 Characteristics of the flow sensors with three different designs.

From Equation 6.5, the relative sensitivity is proportional to both the TCR and S_T . Note that the former is related to the sensing material properties and the latter is related to the structure design.

Figure 6.5.3 shows the sensor temperature change versus flow rate. We see that for the same given power ($140\mu\text{W}$), the suspended flow sensor gives the best temperature-to-flow ratio ($0.026\text{ }^\circ\text{C/nL/min}$), about 5 times better than the first two sensors. This indicates that better thermal isolation offered by channel suspension achieves better sensitivity.

Table 6.1 lists the TCR's, temperature-to-flow ratios and relative sensitivities of the three sensors for an input power of $140\mu\text{W}$. Sensor #3 has the best sensitivity because of its large TCR and temperature-to-flow ratio.

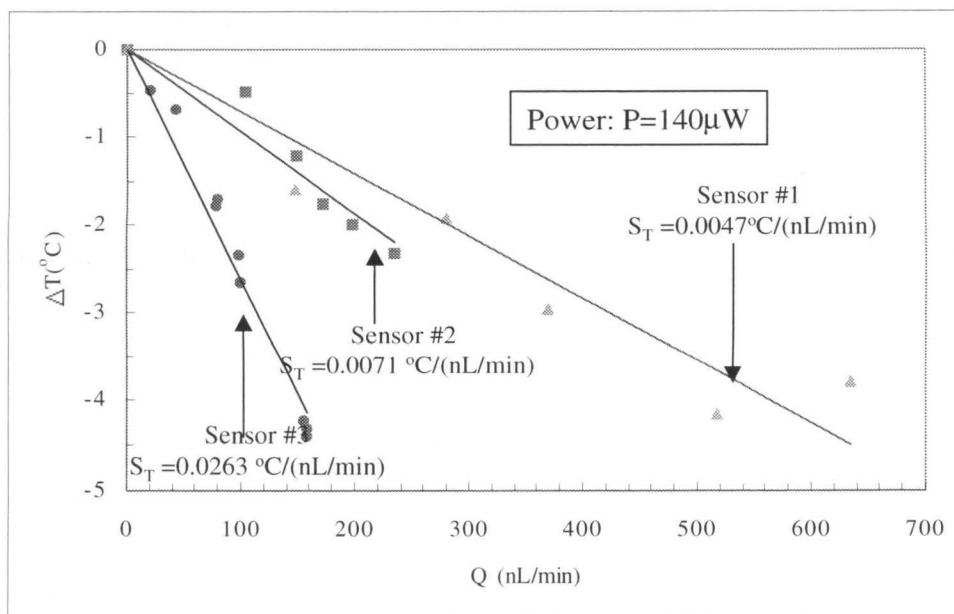


FIGURE 6.5.3 Temperature change of the sensors due to liquid flow.

TABLE 6 TCR's, temperature-to-flow ratios and relative sensitivities (power: 140μW).

Sensor	#1	#2	#3
α (%/°C)	-0.17	-0.56	-0.67
S_T (°C/nL/min)	0.0047	0.0071	0.0263
S_{V/V_0} (ppm/nL/min)	8	40	180

6.6 Error and Resolution Analysis

The resolution of the flow sensor is calculated by finding the maximum error associated with the measurements and propagating the error through curve fitting, which gives the flow rate as a function of sensor voltage. It was found that the distribution of voltages for a particular flow rate can be modeled as a two-parameter Gaussian distribution. Shown in

Figure 6.6.1 is a typical distribution of sensor readings and the fitted Gaussian distribution. About 70% of the readings lie within one standard deviation from the mean and 97% within two standard deviations. Thus, two standard deviations were taken as an adequate measure for the maximum error associated with an individual measurement. Further, according to the Central Limit Theorem in probability theory[18], this error can be reduced by \sqrt{N} through repeated measurements, where N is the number of samples.

Once the errors for each measurement are known, the corresponding error in estimating the flow rate from the calibration can be calculated. For a typical *single* measurement, $2\sigma_v$ is about 1.1mV, which corresponds to an error in flow rate measurement of about 4 nL/min. Therefore, with 100 repeated measurements, the voltage resolution is $1.1/\sqrt{100} = 0.11$ mV, while the flow rate resolution is given by $4/\sqrt{100} = 0.4$ nL/min.

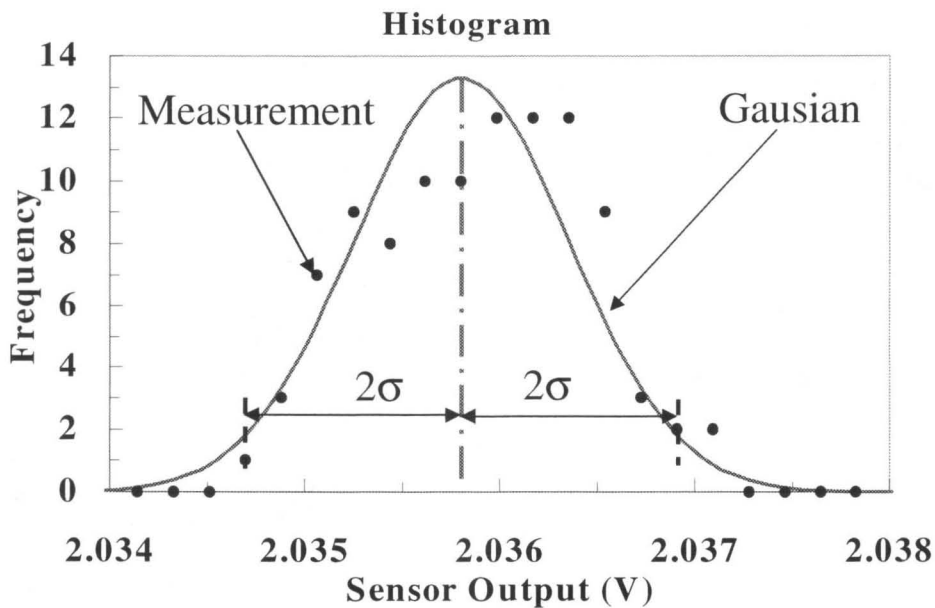


FIGURE 6.6.1 Histogram of a typical set of sensor measurements.

6.7 Micro Heat Transfer Modeling

To better understand the operation of the flow sensors, heat transfer occurring in the sensors has been investigated. As a current is passed to the polysilicon heater, heat conduction occurs within the channel's solid structure, including the nitride walls, the embedded polysilicon heater, as well as the surrounding air. This heat conduction is coupled with forced convection heat transfer in the fluid flow. Assuming a laminar incompressible flow, the flow's velocity profile was found analytically [19]. Then, the ABAQUS finite element package is employed to solve the coupled conduction-convection problem, yielding the temperature distribution in both the channel and the flow. The average temperature T for a given flow rate Q_v was then computed.

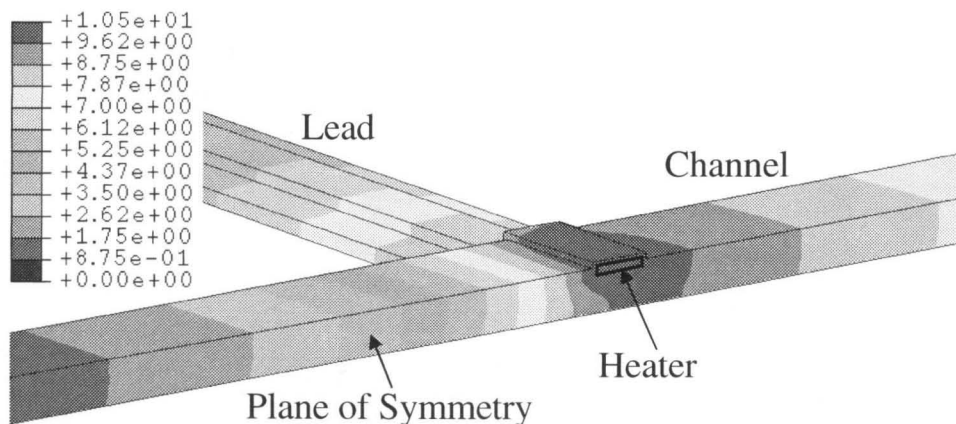


FIGURE 6.7.1 Temperature distribution along the channel (sensor #3 at a flow rate of 100nL/min and sensor input power at 140 μ W).

Figure 6.7.1 shows the temperature distribution in the flow sensor (sensor #3) at a flow rate of 0.1 μ L/min. It can be seen from this figure that the size of the heated region is comparable along all the three spatial dimensions. In contrast to typical macroscale

forced convection processes, this implies that heat conduction, in both the channel structure and the flow, in all three spatial directions is equally important for determining the heater temperature.

Figure 6.7.2 shows the plot of temperature distribution for $Q = 0, 0.05, 0.10,$ and $0.15 \mu\text{L}/\text{min}$ at the sensor input power of $140 \mu\text{W}$. As can be seen, the sensor temperature is less than 15°C above room temperature. That is, due to the low power input, the fluid temperature does not increase significantly in the sensing channel. This feature is essential to many microfluidic applications in which high temperature rise must be avoided.

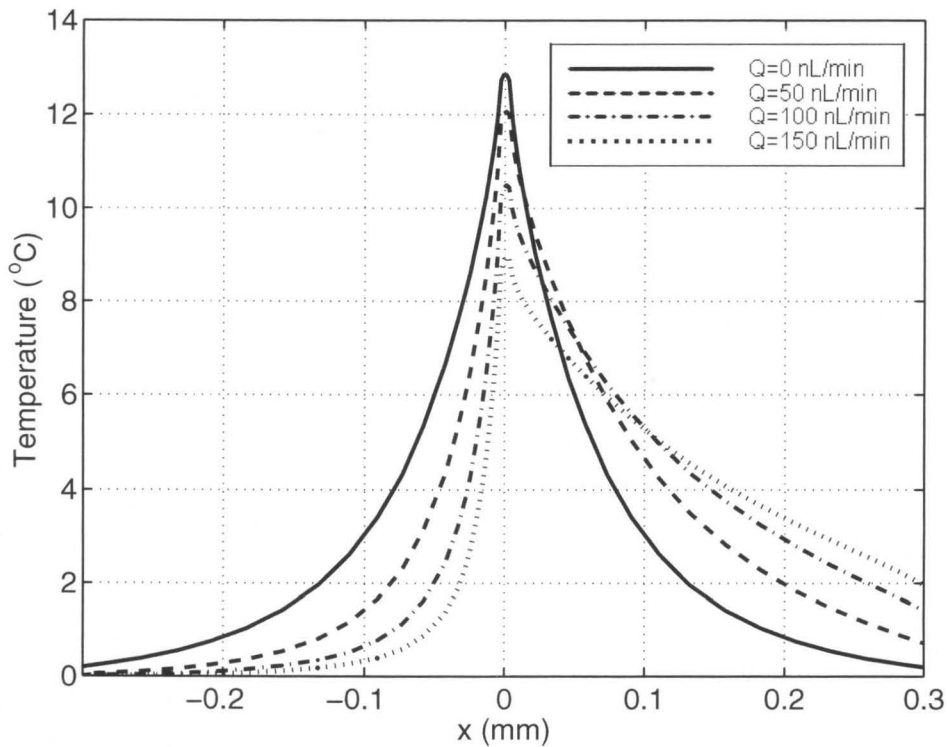


FIGURE 6.7.2 Temperature distribution along the channel for four flow conditions (0, 0.05, 0.10, and $0.15 \mu\text{L}/\text{min}$) at sensor #3 input power of $140 \mu\text{W}$.

Since the heater temperature is a function of flow rate, i.e., $T = T(Q)$, the flow rate is reflected in the flow-induced temperature change $\Delta T = T(Q_v) - T(0)$. Figure 6.7.3 displays the distribution of ΔT along the channel for sensor #3 at three different flow rates. In the figure the x -coordinate is measured along the channel with the heater at the origin. It is very interesting to observe that ΔT generally achieves its maximum away from the heater. Thus, the sensitivity of the flow sensor would be considerably improved if the flow rate is inferred from a separate temperature sensor located at an optimal distance away from the heater. Also, since the temperature change takes on opposite signs upstream and downstream of the heater, use of both upstream and downstream temperature sensors will allow the detection of flow direction.

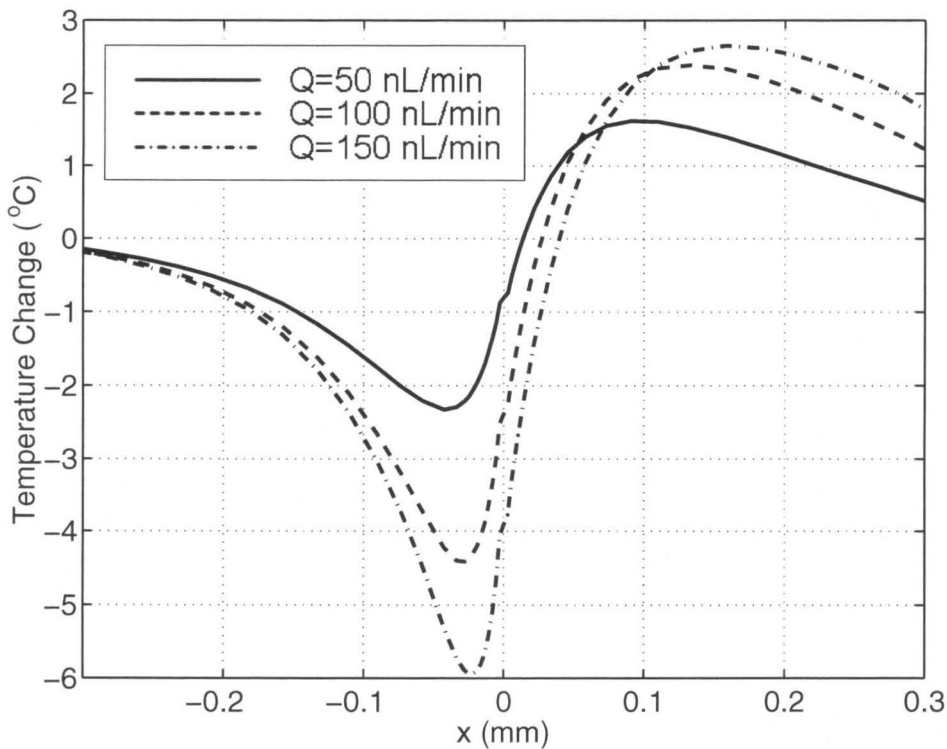


FIGURE 6.7.3 Distribution of the flow-induced temperature change along the channel for sensor #3 at input power of $140 \mu\text{W}$.

The flow-induced sensor temperature change as a function of flow rate is plotted in Figure 6.7.4 for sensor #3 along with the experimental data. From this figure it can be observed that the agreement between theory and experiment is quite good. The discrepancies may be due to uncertainties in the channel geometry and in the material properties.

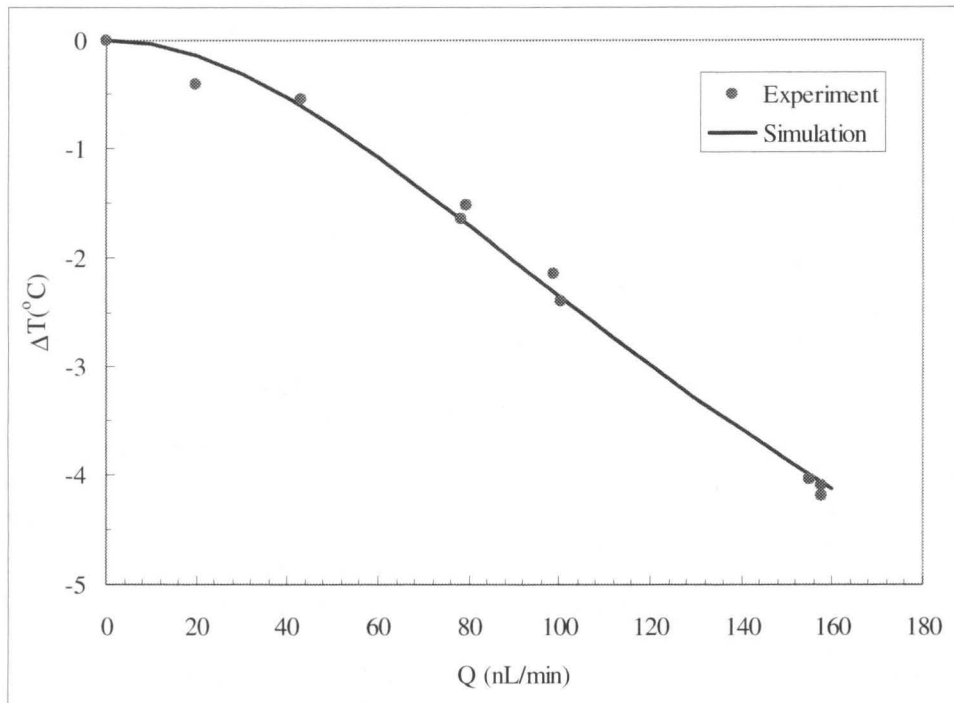


FIGURE 6.7.4 Simulated vs. measured flow-induced temperature change for sensor #3.

6.8 Bubble Detection

Finally, our flow sensors can not only measure flow rates, but also detect the presence of air bubbles. In Figure 6.8.1 the passage of air bubbles is logged using real-time data acquisition. Since air has a lower heat capacity and conductivity than water, the sensor sees a sudden temperature rise, shown as spikes in Figure 6.8.1. Further investigation is underway to investigate the possibility of detecting foreign particles other than air

bubbles. This can be particularly useful in micro-chemical reaction applications where detection of bubbles or particles is important.

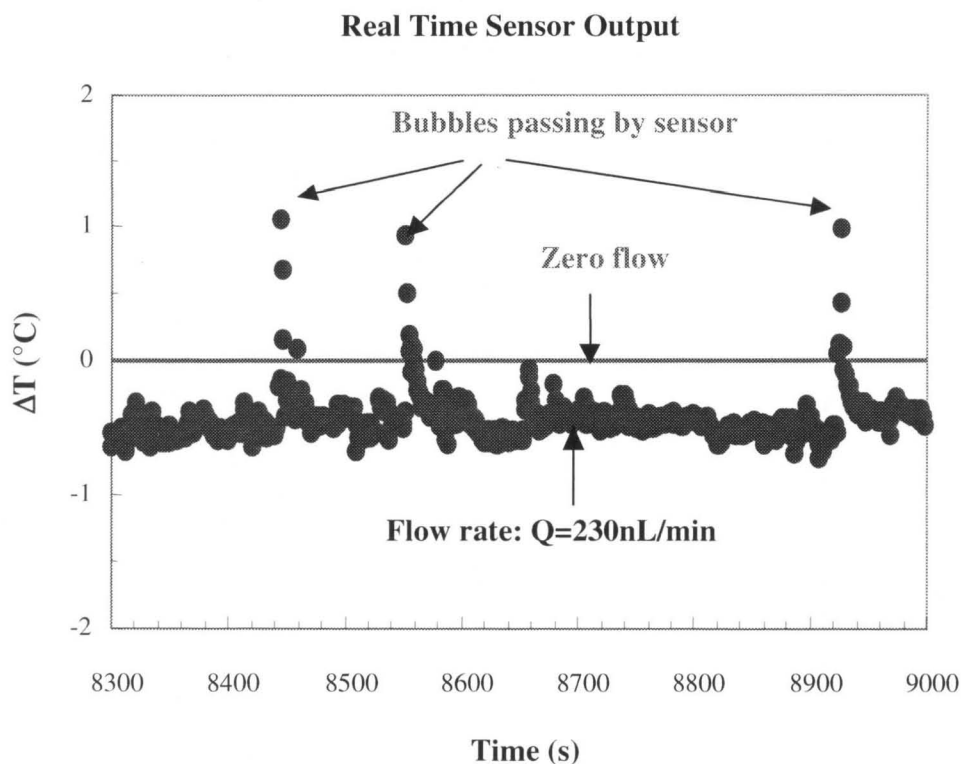


FIGURE 6.8.1 Real time output of the cold sensor next to heated sensor #1.

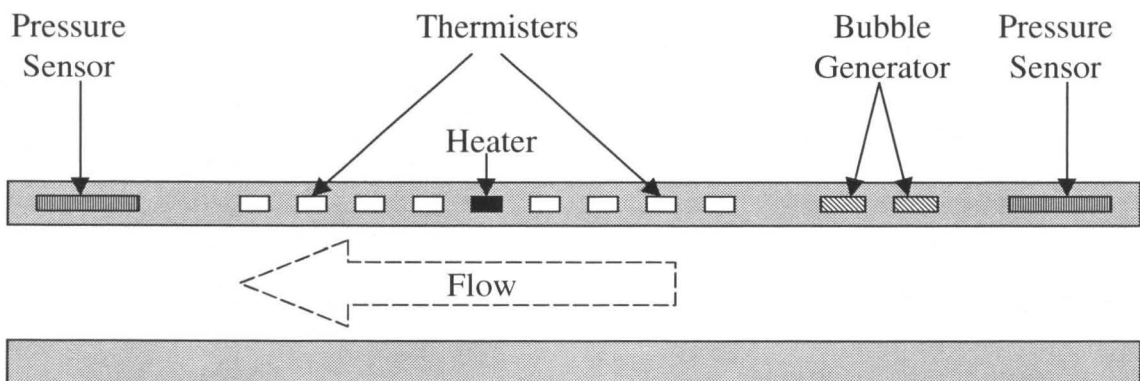
Temperature spikes indicate passage of an air bubble.

6.9 Conclusion

We have successfully developed liquid flow sensors that are integrated into a microchannel. The sensor sensitivity can be increased by switching from heavy doping ($2 \times 10^{19} \text{ cm}^{-3}$) to relatively light doping ($2 \times 10^{18} \text{ cm}^{-3}$), as well as removing a portion of the silicon substrate underneath the sensor for better thermal isolation. With such unique design, low power input (140 μW) allows the sensor to achieve a high resolution with a larger temperature rise ($< 15^\circ\text{C}$). The flow sensor has demonstrated a resolution of

4nL/min for single measurements and 0.4 nL/min for averaged multiple measurements. In addition, heat transfer simulation was performed to study the operating principle of the flow sensors, and was found to agree with experimental data. Finally, it was demonstrated that micro bubbles in the liquid flow are detectable by the real time recording of sensor output.

Our simulation results suggest several directions for future work. First, the flow sensor sensitivity can be improved by optimally arranging a temperature sensor at each side of a heater. Such an arrangement makes it possible to detect the flow direction as well. The temperature distribution along the channel can be measured experimentally by a dense array of temperature sensors as illustrated in Figure 6.9.1. In addition, a pressure sensor made of polysilicon strain gauges can be added on the diaphragms of inlet and outlet to sense the pressure difference. This provides an additional way of studying the flow sensors. Furthermore, polysilicon electrodes embedded in the channel wall can control bubble generation to calibrate bubble size detection of the sensors. Finally, the channel size can be reduced so that the sensors will detect smaller flow rates.



PICTURE 6.9.1 Temperature distribution, bubble generation, and pressure sensing capabilities for future flow sensors.

References:

- [1] A. Desai, Y. C. Tai, M. T. Davis, and T. D. Lee, "A MEMS electro spray nozzle for mass spectroscopy," 1997 International Conference on Solid-State Sensors and Actuators (Transducers '97), May 1997.
- [2] X.Q. Wang, A. Desai, Y. C. Tai, L. Licklider, and T.D. Lee, "Polymer-Based Electro spray Chips for Mass Spectroscopy," *Proc. 12th Annual International Workshop on Micro Electro Mechanical System*, pp. 523-528, January 17-21, 1999, Orlando, Florida.
- [3] C. L. Coly, T. Tang, N. Chiem, and D. J. Harrison, "Clinical potential of microchip capillary electrophoresis system," *Electrophoresis 1997*, 18, 1733-1741.
- [4] N. H. Chiem and D. J. Harrison, "Monoclonal antibody binding affinity determined by microchip-based capillary electrophoresis," *Electrophoresis 1998*, 19, 3040-3044.
- [5] S. D. Mangru and D. J. Harrison, "Chemiluminescence detection in integrated postsparation reactors for microchip-bases capillary electrophoresis and affinity electrophoresis," *Electrophoresis 1998*, 19, 3040-3044.
- [6] X. Yang, C. Grosjean, and Y. C. Tai. "A MEMS Thermopneumatic Silicone Membrane Valve," *MEMS'97*, Nagoya, Japan, Feb. 1997.
- [7] S. Wu, Q. Lin, Y. Yuen, and Y.C. Tai, "MEMS flow sensors for nano-fluidic applications," in *Proc. of The Thirteenth IEEE International Conference on Micro Electro Mechanical Systems (MEMS2000)*, Miyazaki, Japan, Jan. 23-27, 2000.
- [8] M. Koch, C. G. J. Schabmueller, A. G. R. Evans, and A. Brunnschweiler, "Micromachined chemical reaction system," *Sensor and Actuator*, 74(1999) 207-210.
- [9] K. Petersen, "From microsensors to microinstruments," *Sensor and Actuators A 56* (1996), pp. 143-149.
- [10] C. H. Mastrenghelo, M. A. Burns, and D. T. Burke, "Microfabricated devices, for genetic diagnostics," *Proceeding of the IEEE*, vol. 86, No. 8, Aug. 1998.

- [11] B. H. Weigl and P. Yager, "Microfluidic diffusion-based separation and detection," *Science*, vol. 283, pp. 46-47, Jan. 1999.
- [12] T.S.J. Lammerink, et al., "Micro-liquid flow sensor," *Sensors and Actuators*, A37-38, pp. 45-50, 1993.
- [13] T.S.J. Lammerink, et al., "Modular Concept for Fluid Handling System," *MEMS'96*, pp. 389-394, February 1996, San Diego, CA.
- [14] M. Ashauer, et al., "Thermal Flow Sensor for Liquids and Gases," *MEMS'98*, pp. 351-355, January 1998, Heidelberg, Germany.
- [15] M. Ritcher, M. Wackerle, P. Woias, and B. Hillerich, "A novel flow sensor with high time resolution based on differential pressure principle," *MEMS'99*, pp. 118-123, January 1999, Orlando, FL.
- [16] S. Wu, J. Mai, Y. Zohar, Y.C. Tai, and C.M. Ho, "A Suspended Microchannel with Integrated Temperature Sensors for High-pressure Flow Studies," *MEMS'98*, pp. 87-92, January 1998, Heidelberg, Germany.
- [17] X.Q. Wang, X. Yang, K. Walsh, and Y.C. Tai. "Gas Phase Silicon Etching with Bromine Trifluoride," *Transducer*, 97.
- [18] G. Casella and R. L. Berger, "Statistical Inference," *Duxbury Press*, pp. 216-228, 1990.
- [19] F. M. White, "Fluid Mechanics," 2nd edition, *McGraw-Hill*, 1986.

CHAPTER 7

CONCLUSION

Integrated polysilicon thermistors have been studied for microfluidic sensing. First, to study micro impinging-jet cooling, temperature imagers with integrated thermistor arrays were developed to measure the 2-D temperature distribution over the impingement surface, which was then used to compute heat transfer coefficient. Second, robust suspended microchannels with distributed polysilicon thermistors were designed and fabricated to study high-pressure channel flow including the temperature distribution along the microchannel. Third, micro fluidic couplers were developed to facilitate the interconnection of microfluidic components. Finally, micro flow sensors with polysilicon thermistors embedded in a microchannel wall were created to measure liquid flow rates and detect transient passage of micro bubbles.

The fundamental cooling characteristics and practical issues of impinging-jet cooling have been systematically studied with a MEMS-based heat transfer measurement paradigm including a technology for MEMS device fabrication, an experimental setup

well suited for micro scale thermal study, and an accurate and efficient data processing technique. Our MEMS-based temperature imager integrates sensing and heating, and allowed measurement in a significantly large area at a very high spatial resolution. The heat transfer data has demonstrated the strong local cooling capability of MEMS jets. It was found that the maximum achievable heat transfer coefficient is in the range of 0.2-0.3 W/cm² °C, several times larger than that of conventional macro scale impinging-jets. Both local heat transfer coefficient and effective cooling range increase with increasing driving pressure and are insensitive to the spacing between the nozzle and impingement surface if $H/D < 6$ (H is the spacing between the nozzle and impingement surface, and D is the nozzle diameter). The study of impinging jet arrays compared to the effective cooling range of a single jet shows average heat transfer coefficient enhancement due to the interaction of individual jets. The preliminary test results with a 10 x 10 nozzle array demonstrated a heat transfer coefficient that is almost six times higher than an equivalent macro nozzle. The experimental study of micro-impinging-jet cooling has conclusively demonstrated excellent promise and generated useful guidelines for designing impinging-jet-based micro heat exchangers.

In addition, micro channel flow has been carefully investigated. Micro channels with integrated thermistors have been successfully fabricated to investigate the basic science of micro-scale channel flow. Considerable discrepancies between existing theory and experimental data have been observed, and an improved flow model has been proposed including the effects of compressibility, slip boundary, fluid acceleration, non-parabolic fluid velocity profile, and channel-wall bulging. In addition, the temperature measurements along a high-pressure microchannel have been for the first time

performed and the isothermal assumption for a microchannel flow at the inlet pressure up to 300 psig has been validated.

Moreover, various fluidic couplers have been developed to address reliable and low-cost interconnections of microfluidic components. In the novel design, the MEMS fluidic couplers are batch fabricated and self-aligning, and minimize the use of glue. During testing, no failure was observed to the coupling formed by a silicon coupler and a thin epoxy layer for pressures up to 1200 psig.

Finally, polysilicon flow sensors have been integrated into microchannels to measure liquid flow rates. Using lightly doped polysilicon sensing elements and a suspended microchannel, the flow sensor, with a small power input of 140 μ W and operation temperature 15°C above room temperature, achieves a resolution better than 1nL/min. In addition, a simulation has been performed to understand sensor operation and is verified by experimental data. Finally, the flow sensor has demonstrated a capability of detecting micro bubbles in the liquid.

Appendix A: MOSIS Chip

The multi-channel constant current mirror was designed in the Caltech Micromachining Laboratory by Dr. Fukang Jiang et al. and then fabricated using a 2 μm CMOS process through the MOSIS service. Figures 3.6.14 and 3.6.15 are the circuit diagram and the chip photomicrograph ($2 \times 2 \text{ mm}^2$). The cascaded transistor pair is for high output impedance and the large transistor area is for minimizing V_{GS} as well as for good uniformity. The following summarizes the features of the chips.

- 2 μm CMOS process
- Chip size: 2 mm \times 2 mm
- 40-pin DIP package
- 34 channel current sources ($\pm 1\%$ uniformity)
- Maximum power supply : > 10 V

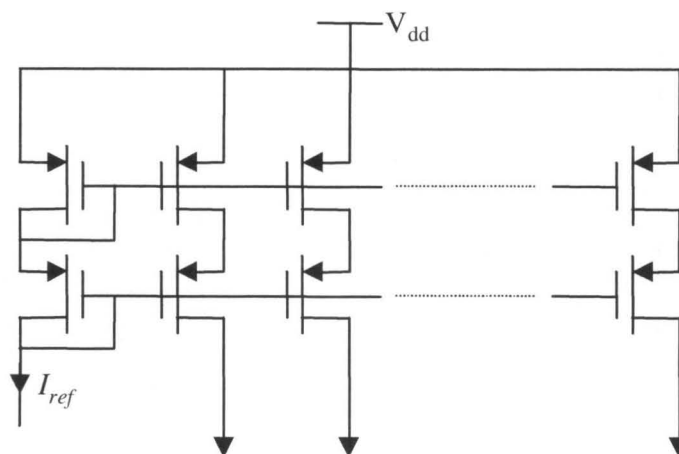


FIGURE A.1 Constant current bias circuits consisting of a MOSIS current mirror and a three terminal adjustable voltage regulator LM317.

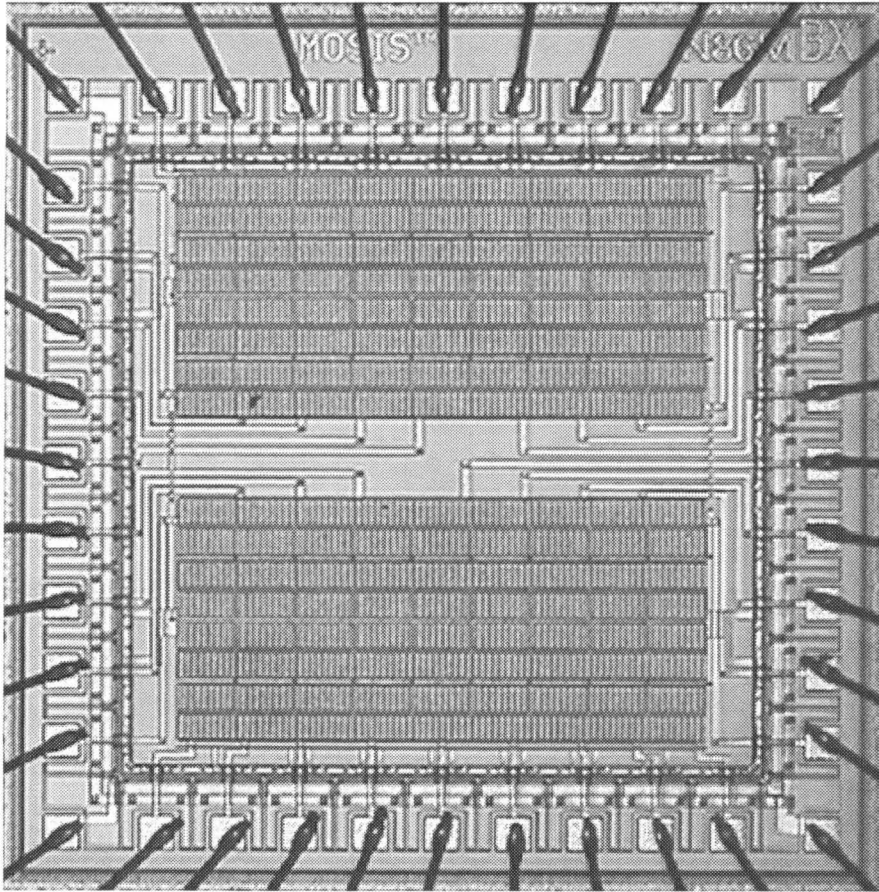


FIGURE A.2 The picture of a MOSIS constant current bias chip.

Appendix B: 200-Channel Data Acquisition System

The 200-Channel data acquisition system was built by Mr. Tianxiang Weng in the Caltech Micromachining Laboratory originally for the UAV Project [1]. Figures 3.6.16 and 3.6.17 are the block diagram and picture of the data acquisition system. As many as 200 sensor outputs are multiplexed and input to a high-resolution (14 bits) A/D converter. The digitized signal data points for each sensor are transferred to be stored in a PC which also controls the whole system. This system has a faster acquisition and provides more channels than HP 34970A data acquisition system.

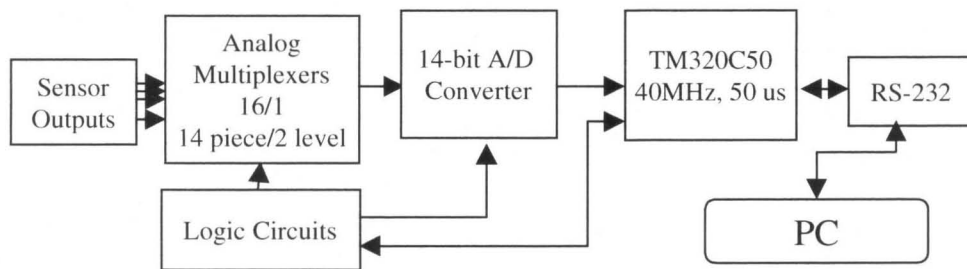


FIGURE 3.6.16 The block diagram of the 200-channel data acquisition system.

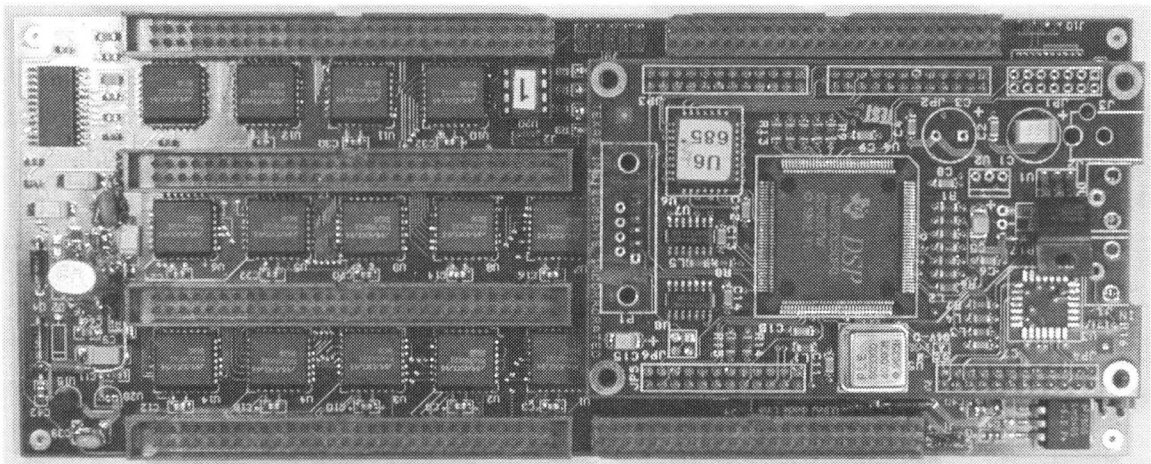


FIGURE 3.6.17 The picture of 200-channel data acquisition system.

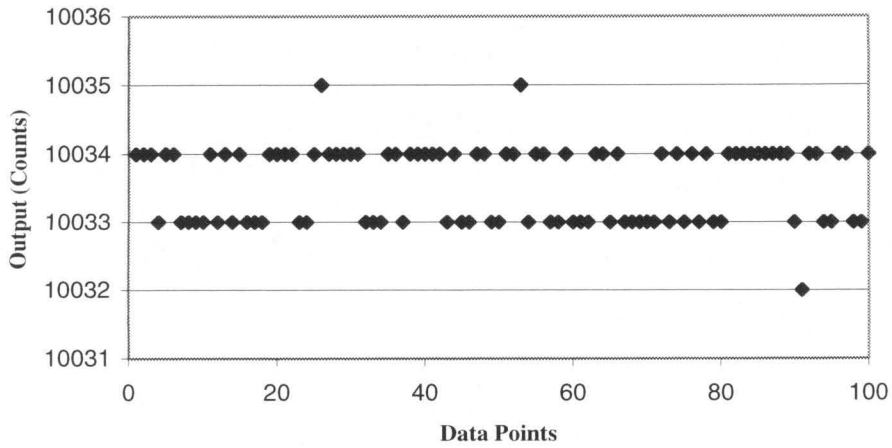


FIGURE 3.6.18 System output noise level by measuring battery voltages.

Figure 3.6.18 shows the system output noise level below $\pm 1.5\text{LSBpp}$ ($\pm 0.4\text{ mVpp}$) or 1LSBrms (0.25 mVrms) of the 14-bit A/D converter with a input range of 0 – 4 V. This is good enough to achieve the temperature resolution better than 0.1°C .

Reference:

- [1] F. Jiang, Y. Xu, T. Weng, Z. Han, Y. C. Tai, A. Huang, C. M. Ho, and S. Newbern, “Flexible shear stress sensor skin for aerodynamics applications,” *Proc. 13th Annual International Workshop on Micro Electro Mechanical System*, pp. 364-369, January 23-27, 1999, Miyazaki, Japan.